UNIVERSITY OF TRENTO - Italy

International PhD Program in Biomolecular Sciences

Centre for Integrative Biology

XXXIst Cycle

Cellulose-based BioNanoMaterials:

Structure and Properties

Tutor/Advisor

Prof. Marina SCARPA

Department of Physics

Ph.D. Thesis of

Cecilia Ada MAESTRI

Centre for Integrative Biology (CIBIO)

Department of Physics

Academic Year 2017-2018

Ogni volta che ti sentirai smarrita, confusa, pensa agli alberi,
ricordati del loro modo di crescere.
Ricordati che un albero con molta chioma e poche radici
viene sradicato al primo colpo di vento,
mentre in un albero con molte radici e poca chioma la linfa scorre a stento.
Radici e chioma devono crescere in egual misura,
devi stare nelle cose e starci sopra,
solo così potrai offrire ombra e riparo,
solo così alla stagione giusta potrai coprirti di fiori e frutti.
(Susanna Tamaro)

Declaration of Authorship

I, Cecilia Ada Maestri, declare that this thesis titled ''Cellulose-based BioNanoMaterials: Structure and Properties'' is my own work and the use of all material from other sources has been properly and fully acknowledged. I confirm that:

- This work was done while in candidature for a research degree at this University;
- Where I have consulted the published work of others, this is always clearly attributed;
- Where I have quoted from the work of others, the source is always given;
- I have properly and fully acknowledged all main sources of help;
- Where the work was done by myself jointly with others, I have made clear exactly what was done by others and what I have contributed myself.

Abstract

Biological materials such as wood show outstanding properties due to the self assembly of components from molecular to macroscopic size. An emerging nanotechnology-based strategy consists of the isolation of biological components with size in the range from nanometers to micrometers and of the design of human-driven assembly processes to obtain multifunctional materials.

The aim of this thesis was to isolate cellulose nanocrystals, with dimensions of around 4-5 nm in width and some hundred nanometers in length, and investigate their assembly processes through weak interactions among them and with small molecules, like water or ions. Knowing their interaction properties and self-assembly is indeed fundamental in order to fully exploit the potential of nanocellulose in its recently emerging applications. In particular, I focused on cellulose nanocrystals supramolecular self-organization both in absence and presence of water, studying cellulose nanocrystals-based films and hydrogels.

In dry conditions, the self-assembly of cellulose nanocrystals on a polylactic support was demonstrated to form few micrometers thick films, characterized by a densely packed arrangement of the crystals leaving elongated cavities of about 0.31 nm cross section between them. These cavities provide the pathway for gaseous $^{2}H_2$ diffusion. Conversely, these films are impermeable barriers for the transport of gaseous molecules such as O_2 and CO_2.

In aqueous solution, instead, cellulose nanocrystals undergo sonication- or cation-assisted entanglement, forming soft hydrogels. Na^{+}, Ca^{2+} and Al^{3+} crosslink the nanocrystals and produce stable hydrogels with structurally ordered domains in which water is confined. Since the gelation process is diffusion controlled, small hydrogel objects with different size and shape have been designed by the coordination-driven assembly of supramolecular rod-like cellulose crystallites, using ionotropic gelation as a methodological approach and Ca^{2+} as a gelling agent.

In parallel to material characterization, particular attention was devoted to the possible exploitation of cellulose nanocrystals-based materials in the biomedical field. In this regard, toxicity studies were performed both on the individual nanocrystals and on the films and hydrogels resulting from their assembly. Moreover, a hybrid cellulose-nanocrystals/chitosan material was developed and characterized, which shows some potential to be used as therapeutic delivery system in the gastrointestinal tract. Indeed, though a mould assisted gelation process, composite hydrogels can be produced, which are degraded by human digestive enzymes and release a model protein according to a biphasic kinetic profile.

List of Publications

The thesis is based on the following publications, which will be referred to by roman numerals:

I. Maestri, C. A.; Abrami, M.; Hazan, S.; Chistã, E.; Golan, Y.; Rohrer, J.; Bernkop-Schnürch, A.; Grassi, M.; Scarpa, M.; Bettotti, P., ''**Role of sonication pre-treatment and cation valence in the sol-gel transition of nano-cellulose suspensions''** *Scientific Reports* (2017) v. 7, n. 1, p. 11129. DOI: 10.1038/s41598-017-11649-4

II. Maestri, C. A.; Bettotti, P.; Scarpa, M., **"Fabrication of complex-shaped hydrogels by diffusion controlled gelation of nanocellulose crystallites"** *Journal of Materials Chemistry B* (2017) - DOI: 10.1039/C7TB01899A

III. Roilo, D.; Maestri, C. A.; Scarpa, M.; Bettotti, P.; Egger, W.; Koschine, T.; Brusa, R. S.; Checchetto, R., **"Cellulose Nanofibrils Films: Molecular Diffusion through Elongated Sub-Nano Cavities"** *Journal of Physical Chemistry C, Nanomaterials and Interfaces* (2018) v. 121, n. 28, p. 15437-15447 - DOI: 10.1021/acs.jpcc.7b02895

IV. Roilo, D.; Maestri, C. A.; Scarpa, M.; Bettotti, P.; Checchetto, R., **"Gas barrier and optical properties of cellulose nanofiber coatings with dispersed TiO_2 nanoparticles"** *Surface & Coatings Technology* (2018) (In press)

V. Meschini, S.; Pellegrini, E.; Maestri, C. A.; Condello, M.; Bettotti, P.; Condello, G.; Scarpa, M., **'' *In vitro* cytotoxicity of hydrogels obtained by cation-induced crosslinking of rod-like cellulose nanocrystals''** (under review)

My own contributions to the Papers and the established collaborations were the following:

I. Partial contribution to the experimental design, completion of part of the experimental work (samples preparation, optical and microscopy characterization), analysis of the results and partial writing of the paper, in collaboration with co-authors. NMR and Rheological measurements were performed by colleagues from the team coordinated by prof. Grassi at the Department of Engineering and Architecture (University of Trieste), while

SAXS analysis was performed by collaborators at the Department of Materials Engineering of the Ben Gurion University of the Negev (Israel).

II. Experimental design, achievement of the experimental work, analysis of the results and writing of the initial manuscript, on which the co-authors provided comments and corrections.

III. Partial contribution to the experimental design, completion of part of the experimental work (samples preparation, optical and AFM characterization) and writing of the paper as co-author. Gas transport measurements were performed from colleagues from the IdeA team coordinated by prof. Checchetto of the Department of Physics (University of Trento), while PALS analysis was performed by prof. Egger and prof. Koschine from the ''Institut fur Angewandte Physik und Messtechnik'' (Münich University).

IV. Partial contribution to the experimental design, completion of part of the experimental work (samples preparation, optical and AFM characterization) and writing of the paper as co-author. Gas transport measurements were performed from colleagues from the IdeA team coordinated by prof. Checchetto of the Department of Physics (University of Trento).

V. Partial contribution to the experimental design, completion of the experimental work (samples preparation and material characterization), analysis of the results and partial writing of the paper, together with co-authors. Citotoxycity tests were performed in collaboration with the team of prof. Meschini from the National Center for Drug Research and Evaluation (Istituto Superiore di Sanità, Roma).

Other publications, whose contents are not reported in this thesis, and conferences contributions:

Suárez, I.; Hassanabadi, E.; Maulu, A.; Carlino, N.; Maestri, C. A.; Latifi, M.; Bettotti, P.; Mora-Seró, I.; Martínez-Pastor, J. P.; **''Integrated Optical Amplifier–Photodetector on a Wearable Nanocellulose Substrate''** *Advanced Optical Materials* (2018) v. 6, n. 12- DOI: 10.1002/adom.201800201

Laidani, N.; Marchetti, F.; Ullah, H.; Scarpa, M.; Maestri, C. A.; Makhlouf, S.; Gottardi, G.; Bartali, R.; "**Graphene Powder Processing For Water Solar Distillation using Nanofluids**" Proceedings of: 5th Micro and Nano Flows Conference, Milan, Italy, 11-14 September 2016

Maestri, C.; Bettotti, P. Chistè, E. Rohrer, J.; Bernkop-Schnürch, A.; Scarpa, M.; **''Design and Fabrication of Nanocellulose Hyrogels''**, Poster presented at the 5th EPNOE International Polysaccharide Conference, Jena, Germany, 20-24 August 2017.

Thesis Organization and Contribution

In this PhD thesis I reported my three years of work on cellulose-based bionanomaterials. During these years, I started from the production and characterization of nanocellulose crystallites and then turned to investigate the progressively more complex structures created by them in dry conditions (films), in presence of water (hydrogels) and finally in combination with another polysaccharide material (hybrid hydrogels). Following the time-course of my research, I decided to organize the thesis in three blocks (Part 1, Part 2 and Part 3), each one corresponding to a different cellulose-based material (Films, Hydrogels and Hybrid Hydrogels). Even if all the parts are interconnected and contribute to the aim of understanding the interaction and assembly processes of nanocellulose crystallites, each block will be organized independently from the others, with its own experimental section, results and conclusions. The three blocks will be preceded by a general introduction on nanocellulose and nanocellulose-based materials in order to understand the aim of the thesis (Chapter 1) and by a chapter describing the preparation and characterization of nanocellulose crystallites, building blocks of the structures discussed in the subsequent parts (Chapter 2).

Chapter 1: Chapter 1 is a general introduction on nanocellulose. As the interest in the field and the number of publications are increasing in an astonishing manner in the last years, a detailed and exhaustive description of the topic is almost impossible in this context. For simplicity, I decided not to go into details, reporting only the essential to understand the thesis aim, and refer to recent reviews and books for insights.

Chapter 2: Chapter 2 is focused on the experimental procedure followed to obtain TEMPO-oxidized cellulose nanocrystals (TOCNs) and on their characterization. All the experiments were performed by me at the Nanolab laboratories, under the supervision of Prof. M. Scarpa, apart from TEM images, which were acquired by prof. Paolo Bettotti and prof. Yval Golan at the Department of Materials Engineering of the Ben Gurion University of the Negev (Israel).

PART 1 (Chapter 3-4): This first block concerns the study of TOCNs in the form of dry films. All the samples were prepared and optically characterized by me at the Nanolab laboratories, under the supervision of Prof. M. Scarpa. The gas permeability studies were conducted in collaboration with the IdeA team coordinated by prof. Checchetto of the Department of Physics (University of Trento)

and performed by Dr. D. Roilo. PALS analysis was performed by prof. W. Egger and prof. T. Koschine from the ''Institut fur Angewandte Physik und Messtechnik'' (Munich University). SEM images of the samples were acquired by the team of prof. Y. Golan at the Ben Gurion University of the Negev (Israel) or by Dr. N. Bazzanella at the IdEA Laboratory (University of Trento, Department of Physics). Part of the reported results are based on publications III and IV.

PART 2 (Chapter 5-8): Part 2 focuses on the investigation of TOCN hydrogels.

In particular, Chapter 6 is based on the measurements performed in collaboration with the team coordinated by prof. M. Grassi at Department of Engineering and Architecture (University of Trieste) and the Department of Materials Engineering of the Ben Gurion University of the Negev (Israel), in order to study the individual role of sonication and salt addition to promote the sol-gel transition in TOCN solutions. My personal experimental work involved samples planning, preparation and optical characterization, while NMR and rheological measurements were performed by Dr. M. Abrami from prof. M. Grassi team in Trieste. However, I had the opportunity to make a two-days visit to their laboratories and get in contact with the instrumentation and experimental techniques. SAXS measurements were performed by Prof. Y. Golan and Prof. S. Hazan from the Department of Materials Engineering (Israel). The results of Chapter 6 are published in paper I.

Chapter 7 deals instead with the study of the diffusion and coordination processes at the basis of TOCN gelation, trying to exploit a ionotropic gelation approach to fabricate hydrogel objects with tunable sizes and dimensions. My work comprised the individualization of the experimental techniques enabling to get insight on the gelation process and the realization of all the reported measurements. Chapter 7 was published with minor changes in paper II.

Finally, Chapter 8 arises from the studies performed in collaboration with the team of prof. S. Meschini from the National Center for Drug Research and Evaluation (Istituto Superiore di Sanità, Roma) to investigate the toxicity of TOCN hydrogels and their precursors. The biological part was followed by Dr. E. Pellegrini, Prof. S. Meschini and A. Condello in Rome, while samples preparation, optical and mechanical characterization was performed by me at the Nanoscience Laboratories. However, also in this case I had the opportunity to perform a two-days visit at the Istituto Superiore di Sanità (Roma) and observe MTT assay experiments. The results of this Chapter were used to write paper V, currently under review.

PART 3 (Chapter 9-10): Part 3 finally concerns some preliminary, still un-published, attempts performed to combine nanocellulose crystallites with chitosan to obtain an hybrid hydrogel material which combines the properties of both nanocellulose and chitosan. The aim was to understand the different but synergistic roles of

TOCN and Chitosan as components of a potential hydrogel delivery system, which can be digested by human enzymes and used as protein therapeutics delivery system in the gastrointestinal tract. All the experiments reported in this part 3 were planned and performed by me, under the supervision of Prof. M. Scarpa, with the exception of SEM images, which were acquired by Dr. L. Moschini at the Biotech Laboratories (Department of Materials Engineering and Industrial Technologies of the University of Trento). In particular, I performed the mechanical characterization of the hydrogels (rheological tests, compression tests, mucoadhesion measurements) during my period abroad the at the Institute of Pharmacy of the Innsbruck University in the Drug delivery and Powder Technology research Group, headed by Prof. A. Bernkop-Schnürch. Release and degradation measurements, instead, were performed at the Nanoscience Laboratories.

List of Abbreviations

AFM	Atomic force microscopy
AGU	Anhydroglucose unit
BSA	Bovine serum albumin
Cht	Chitosan
CMF	Cellulose microfibrils
CNC	Cellulose nanocrystals
CNF	Cellulose nanofibrils
FC	Flow curve
FITC	Fluorescein isothiocyanate
FS	Frequency sweep
FTIR	Fourier Transform Infrared Spectroscopy
LF-NMR	Low-field nuclear magnetic resonance
MFC	Microfibrillated cellulose
NC	Nanocellulose
PDMS	Polydimethylsiloxane
PET	Polyethylene terephthalate
PI	Propidium Iodide
PLA	Polylactic acid
SAXS	Small angle x-ray scattering
SD	Standard deviation
SEM	Scanning electron microscopy
SS	Stress sweep
STS	Staurosporine
TEM	Transmission electron microscopy
TEMPO	(2,2,6,6-Tetramethylpiperidin-1-yl)oxyl
TOCN	TEMPO-oxidized cellulose nanocrystals
TOCN-FL	TEMPO-oxidized cellulose nanocrystals film
TOCN-HM	TEMPO-oxidized cellulose nanocrystals hydrogel membrane

Contents

Chapter 4: Results and discussion

PART 2: TEMPO-oxidized Cellulose Nanocrystals Hydrogels

Chapter 5: Materials and Methods for TOCN hydrogels

Chapter 6: TOCNs sol-gel transition

Chapter 7: TOCNs Ionotropic Gelation

Chapter 8: Toxicity Studies

PART 3: Hybrid TEMPO-oxidized Cellulose Nanocrystals/Chitosan Hydrogels

Chapter 9: Materials and Methods for TOCN/Cht Hydrogels

Chapter 10: Results and Discussions

Chapter 11: Final Remarks

Chapter 1
An Introduction to Nanocellulose

1.1 Introduction

Cellulose represents the most abundant renewable polymer on Earth. Raw cellulose has been used for millennia as building material, energy source and component of clothing, and is still used nowadays for a wide spectrum of products and materials. Only in the last decades however, in concomitance with the explosion of nanotechnologies, a new form of cellulose emerged and gained a tremendous level of attention in both scientific and industry community. This new bio-nano-material is generally referred to as Nanocellulose (NC) and is the result of the isolation, by chemical and/or mechanical processes, of the nanoconstituents on which the hierarchical architecture of natural cellulose is based.

The awareness that nanocellulose is a building block with unique combination of properties has led to an extraordinary growth of research development and patenting. Moreover, the interest is now moving beyond scientific curiosity and the first commercial products are starting to reach the marketplace. Such a fast and continuously increasing interest makes sometimes difficult to keep track of all the new developments, and an exhaustive description of all the research fronts and applications concerning nanocellulose is beyond what I could achieve during my PhD and is out of the aims of this thesis.

For these reasons, in this introductory chapter, I will only provide some basic information on nanocellulose research topic, focusing on the aspects which are more relevant to understand the aim of my work. For more exhaustive descriptions it is possible to refer to the numerous existing reviews and books which supply up-to-date overviews of the fundamentals in nanocellulose materials and their utilization (Dufresne, 2012; Kargarzadeh et al., 2017; Lee, 2018).

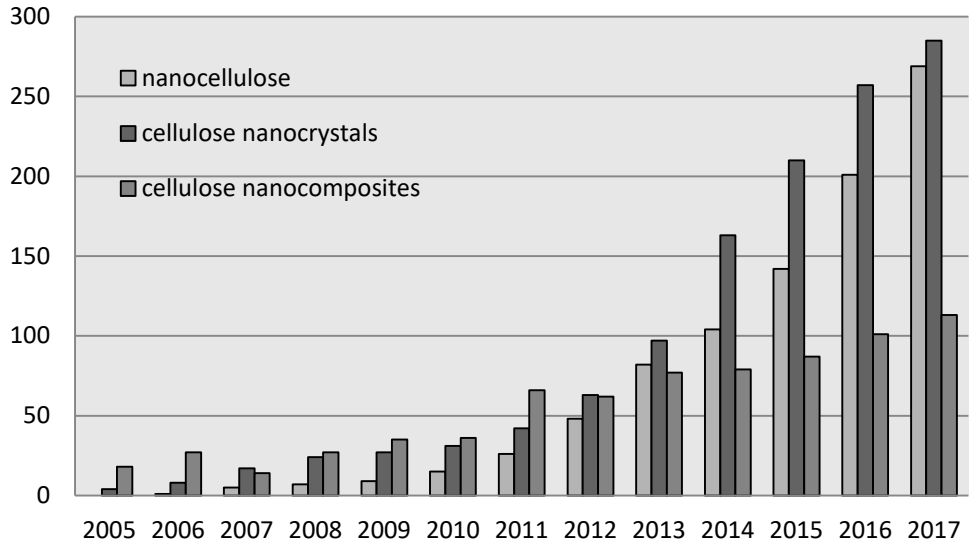

Fig. 1.1: Number of publications with respect to the publication year, obtained from Web of Science using nanocellulose, cellulose nanocrystals and cellulose nanocomposites as key words present in the publication title.

1.2 From Cellulose to Nanocellulose

Cellulose is a structural polysaccharide, composed of anhydroglucose units (AGUs) linked by chemical β(1→4) glycosidic bonds. Two repeating AGUs, having a ''chair'' conformation like that shown in Fig. 1.2 (Moon et al., 2011), represent the single cellulose repeat unit, the number of which depends on the cellulose source material and is of the order 10000-15000. Each unit comprises three hydroxyl functional groups: one primary and two secondary groups, which can form hydrogen bonds either with other cellulose units or cellulose molecules.

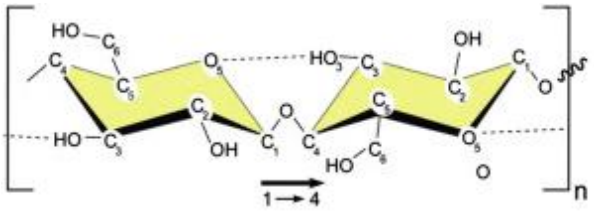

Fig.1.2: Single cellulose repeat unit composed of two anhydroglucose units (AGUs) linked by chemical β(1→4) glycosidic bonds in a ''chair'' conformation stabilized by hydrogen bonds (dotted lines).

Cellulose is synthesized through a complex pathway taking place in plants, animals and bacteria (Jr, 1996; Saxena and Brown, 2005). During cellulose biosynthesis, multiple cellulose chains are stacked via Van Der Waals and hydrogen bonds (Moon et al., 2011) forming cellulose microfibrils, like those schematically shown in Fig. 1.3. These microfibrils have diameters around 5-10 nm, lengths of several microns and

are characterized by alternating crystalline regions and amorphous domains. In nature, elementary cellulose microfibrils are further arranged in larger fibrils and fibers and represent the structural polymer that confers their mechanical properties to plants cells and other natural cellulose-based systems.

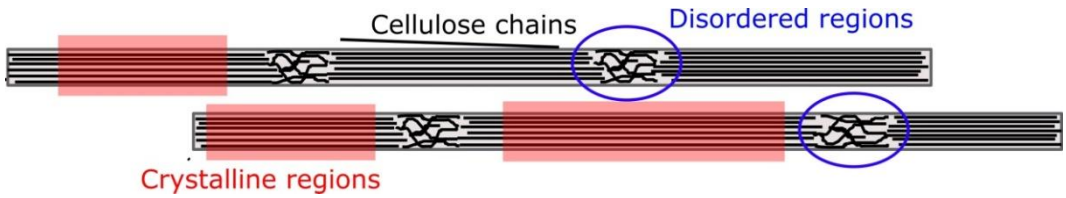

Fig. 1.3: Schematics of elementary cellulose microfibrils, showing one of the possible configurations of crystalline and amorphous domains.

Indeed, wood and plants, which represent the main source of cellulose, are basically hierarchical biocomposites formed by amorphous matrices (made by hemicellulose, lignin, waxes and trace elements) reinforced by cellulose microfibrils. A graphical representation of the hierarchical structure of wood, which spans many length scales, is shown in Fig. 1.4. Like in many other biological tissue, the hierarchical organization allows to provide maximum strength with a minimum material (Dufresne, 2012).

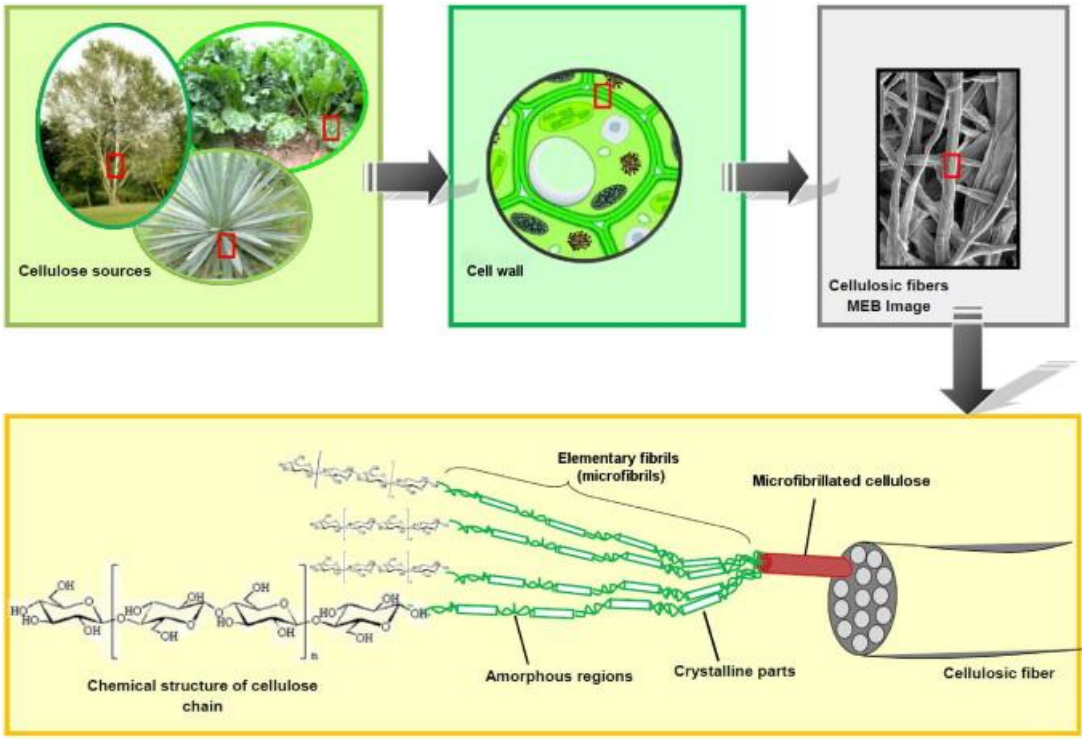

Fig. 1.4: Graphical description of the hierarchical structure of wood, from macroscopic plants down to micrometric fibrils and individual cellulose molecules. Image reproduced from (Lavoine et al., 2012) with permission of *Elsevier*.

The use and transformation as well as the ultimate properties of cellulose-based materials are dictated at molecular level by the presence, the topological distribution and strength of molecular interactions. Among them the most important are hydrogen bonds and London dispersion forces (Nishiyama, 2018). In particular, the processing of cellulose-based structures consists in loosening or overcoming the cohesive interactions in order to reshape and rearrange them.

With the general term Nanocellulose (NC), we define various types of cellulosic nanomaterials with at least one of its dimensions less than or equal to 100 nm, according to the definition of nanomaterials (Espino-Pérez et al., 2014). Nanocellulose is the result of the top-down deconstruction of the hierarchical structure of natural cellulose fibers performed in order to isolate the individual microfibrils sub-elements.
NC can be extracted from wood pulp in several ways, by using mechanical, chemical or enzymatic methods, and resulting in nanocelluloses with different crystallinities, dimensions, surface chemistry and properties (Mondal, 2017). The two most exploited techniques to obtain nanocellulose are represented by acid hydrolysis and mechanical processes eventually combined with a chemical treatment (Abitbol et al., 2016; Klemm et al., 2011).
By acid hydrolysis with sulfuric acid, cellulose fibrils are cut in correspondence of the amorphous domains obtaining highly crystalline particles usually named cellulose nanocrystals (CNC), with source dependent dimensions (5-20 nm in diameter and 100-500 nm in length for plant sources (Abitbol et al., 2016)) and negatively charged sulfate half-ester groups on particles surface.
Mechanical treatments, such as homogenization, grinding and milling, instead, enable to obtain micrometer-long entangled fibrils, known as microfibrillated cellulose (MFC), cellulose microfibrils (CMF) or cellulose nanofibrils (CNF), containing both amorphous and crystalline regions and having diameters in the range 5-60 nm and lengths of more than 1 μm (Klemm et al., 2011; Lavoine et al., 2012). The main obstacle in the individualization of MFC is the high energy required for the mechanical disintegration of the initial macrofibers. For this reason, mechanical processes are often combined with preliminary chemical treatments such as oxidation in presence of catalytic amounts of sodium bromide and 2,2,6,6-tetramethylpiperidine-1-oxyl radical (TEMPO). This procedure, known as TEMPO-mediated oxidation, allows to convert the primary hydroxyls on microfibrils' surface in carboxylate groups (negatively charged at neutral pH), decreasing in such a way the energy necessary to overcome the bonds among microfibrils.

It is important to underline that not all nanocellulose materials behave the same, as both cellulose source and production process strongly affect particles morphology and surface chemistry, resulting in materials with different structures and

properties. For this reason, and considering also the increasing number of publications in the field of NC observed in the recent years, it is often difficult to univocally address all the various kinds of nanocelluloses obtainable and the nomenclature used in the past years was not always completely uniform. Fig. 1.5 reports a recent classification of NC types with the relative standard nomenclature, as proposed by the Technical Association of the Pulp and Paper Industry (TAPPI) and based on nanocellulose dimensions (Mariano et al., 2014).

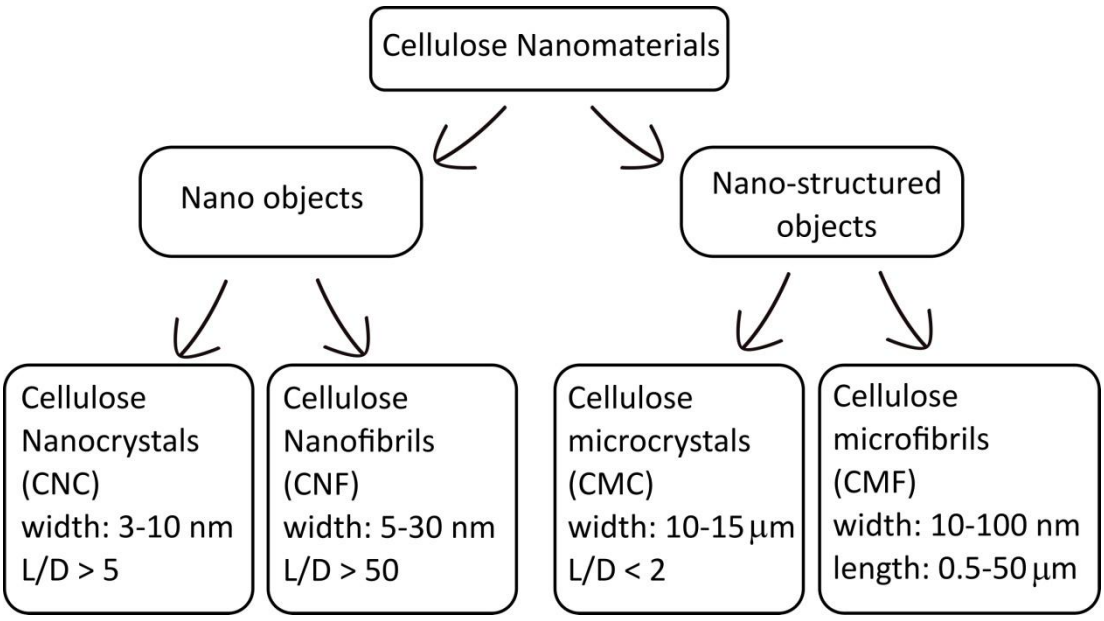

Fig. 1.5: Scheme of the standard terms for cellulose nanomaterials (with length L and diameter D), as defined by the Technical Association of the Pulp and Paper Industry (TAPPI). Image adapted from (Kargarzadeh et al., 2017).

As will be described in details in Chapter 2, the nanocellulose studied in this thesis is obtained by TEMPO-mediated oxidation followed by a mechanical sonication treatment. Considering its production process and the dimensions and morphology of the resulting nanocrystallites, it will be denoted in this thesis as TEMPO-mediated cellulose nanocrystals (TOCNs).

1.3 Why Nanocellulose

The higher and higher attention earned by nanocellulose is justified by its properties, such as special morphology, high specific surface area, mechanical reinforcement and barrier properties, low weight, alignment and orientation, biodegradability, which differentiate it from traditional materials. These properties can be generally divided in three classes (Lin and Dufresne, 2014):

I. Physical and mechanical properties, mainly related to nanocellulose morphology and degree of crystallinity;
II. Surface chemical reactivity, due to the ability of hydroxyl groups to form hydrogen bonds and to the eventual presence of charged groups. This characteristics plays a fundamental role in the interaction properties of NC both among itself and with other small molecules determining the formation of supramolecular structures and controlling their properties (Lin and Dufresne, 2014);
III. Biological properties, such as broadly biocompatibility and hemocompatibility, which makes NC-based materials good candidates for biomedical applications (Endes et al., 2016; Halib et al., 2017; Jorfi and Foster, 2015; Plackett, 2014). It is however important to underline that different results were reported for different forms of NC and further studies are required to have a comprehensive and coherent view of the biological effect of the different NC materials (Endes et al., 2016).

In addition to low cost and large availability, nanocellulose possesses the same advantages of cellulose in terms of renewability, biodegradability and environmental friendship too. Therefore, it is a suitable and promising candidate for the replacement of petroleum-based materials as a means of overcoming environmental problems.

All these properties make NC a promising material with huge potential in a wide range of applications especially in the fields of material sciences and biomedicine (Abdul Khalil et al., 2016; Abitbol et al., 2016; Almeida et al., 2018; Habibi et al., 2010; Halib et al., 2017; Lavoine et al., 2012; Lin and Dufresne, 2014; Mondal, 2017; Zheng et al., 2013).
Moreover, thanks to its nanometric dimensions, high surface area, unique morphology, low density, easiness of chemical modification and mechanical strength, NC has attracted a great interest in the field of nanocomposites. Indeed, It has already been successfully incorporated into a wide range of polymeric matrices and used to form ''smart'' hybrid materials with *ad hoc* properties for specific applications (Habibi et al., 2010; Mariano et al., 2014; Moon et al., 2011; Qiu and Hu, 2013; Salas et al., 2014).

1.4 Nanocellulose Self-assembly

With the term self-assembly we refer to the spontaneous formation of structures due to competing attractive and repulsive interactions at different length scales (Whitesides and Boncheva, 2002). The control of the molecular and supramolecular forces and the understanding of the physicochemical phenomena involved in three-

dimensional self-assembly processes is one of the goals of materials science, as it would enable to improve the performance of already existing materials and the design of novel functionalities (Kargarzadeh et al., 2017).

The self-assembly of polysaccharide chains and the hierarchical organization from the molecular to the macroscopic scale are intrinsic and striking properties of cellulose. As already said, cellulose structure is based on extensive non-covalent interactions, in particular hydrogen bonding between hydroxyl groups and their counterparts and London dispersion forces, related to temporary polarization phenomena (Klemm et al., 2005; Nishiyama et al., 2003, 2002). One of the major challenges in the processability of cellulose and its conversion to nanocellulose is overcoming these non-covalent interactions, typical of polysaccharides (Bechtold et al., 2013). Despite the numerous studies on cellulose, few quantitative information can be found on the role of the individual types of interactions to the overall properties. In a recent work (Nishiyama, 2018), the contribution of intermolecular hydroxyl hydrogen bonding to the cohesion of cellulose was estimated from the empirical correlation between heat of formation and shifts of hydroxyl groups IR stretching bands relative to the isolated molecule and reported to be approx. 20 kJ mol^{-1}. At the same time, however, molecular modeling showed that the main contribute (50-70%) for cellulose overall stabilization comes from the short-range component of additive London dispersion forces, globally estimated to correspond to an equivalent compression pressure of around 3-4 GPa (Nishiyama, 2018). Finally, also the notions of hydrophobicity and amphiphilicity of cellulose have recently been considered as important factors to explain the molecular interactions and properties of cellulose (Medronho et al., 2015; Medronho and Lindman, 2015).

Once the original cellulose interactions have been overcome and NC has been isolated from cellulose sources, NC tries to self-arrange in new structures, depending on the chemical surroundings. Also in this case, the formed structures and their properties are mainly governed by the formation of new strong interactions through London dispersion forces and hydrogen bonding, which are now exacerbated by nano-scale dimensions and high aspect ratio of nanocellulose (Mariano et al., 2014). Moreover, the eventual introduction of charged groups on cellulose microfibrils during the production of NC further increases the surface reactivity of the material.

As a consequence, the knowledge of NC molecular interactions and structural organization is fundamental in order to fully exploit the potential of NC materials in practical applications. In this sense, among the general strategic recommendations proposed by the European Polysaccharide Network of Excellence (EPNOE) for research in the field of polysaccharides, there is the theme of bio-assembly, that is

the investigation of the structures formed by polysaccharide in complex biological systems (Persin et al., 2011).
Therefore, the challenge consists in understanding the interaction occurring between NC and chemical surrounding, which can for example be represented by other NC or low molecular weight components present in the solid phase, water or other chemicals (in particular gas molecules) adsorbed from the surrounding atmosphere or aqueous solutions containing dispersed polymers, proteins, low molecular weight compounds or salts (Bechtold et al., 2013).

Many literature works and some reviews can be found in literature on the self-assembly of NC (Habibi et al., 2010; Lagerwall et al., 2014; Mariano et al., 2014), but most of them are focused on cellulose nanocrystals (CNC) obtained by acid hydrolysis and on their arrangement in lyotropic liquid crystallite assembly and chiral nematic films (Chen et al., 2014; Dumanli et al., 2014; Liu et al., 2014; Picard et al., 2012). However, the TOCN crystallites investigated in this thesis were not observed to form such regular and periodic structures. This fact can be ascribed to the particular preparation procedure of TOCN crystallites, which will be described in Chapter 2. As already said, nanocelluloses are objects with nanometer-scale lateral dimensions but variable lengths, morphology and surface charge, depending on the production method and cellulose source. These differences are reflected in different interaction properties and assembly structures. Also the extraction processes often result in a broad size distribution, especially in the case of NC not obtained by acid hydrolysis, which does not allow the formation of well-defined or even periodic three-dimensional structures (Kargarzadeh et al., 2017).
Apart from liquid crystals, other self-assembly processes reported for NC are the formation of layered structures (films) by coalescence processes and the arrangement in networks (solvent swollen hydrogels or dried areogels). It is well known that both cellulose and nanocellulose have a strong affinity to materials like water which contain hydroxyls and are thus excellent competitors for inter-crystallites hydrogen bonds. Moreover, as already seen, also London dispersion forces are known to play an important role for the stabilization of the structures formed between the two reactive entities (Chami Khazraji and Robert, 2013). As a consequence, it is expected that NC self-assembly strongly depend on the presence of water and on the formation of molecular associations with it (Kamida et al., 1984; Li et al., 2012; Liu et al., 2011). Important advances have been recently achieved in the understanding of NC aggregation behavior (Nyström, 2018) and in the control of NC assembly by different methods like flow assisted techniques (Mittal et al., 2018) or interfacial complexation (Zhang and Liimatainen, 2018). Different scaled-up processing strategies have been developed too, for the application of NC in the fields of biomedicine (Yang and Li, 2018), energy (Chen et al., 2018; Wang et al., 2017), printed electronics (Hoeng et al., 2016) and infrastructures (Vo and Navard,

2016). Moreover, experimental measurements are being recently combined with multiscale models and atomistic simulations to better understand the mechanisms that determine NC structure and behavior at different length scales (Martin-Martinez, 2018). Nevertheless, many questions about NC interaction-driven structural organization are still open. For example details about the structures created in terms of porosity, crosslinking and voids among NC are often missing.

1.5 Aim of the Thesis

The aim of this thesis was to isolate cellulose nanocrystals exploiting TEMPO-mediated oxidation followed by a mechanical sonication treatment and investigate their assembly processes through weak interactions among them and with small molecules, like water or ions.
With the purpose of getting more information on the structures formed by TEMPO-oxidized cellulose nanocrystals both in dry conditions and in presence of water, I focused, after a preliminary characterization of TOCNs, on the study of TOCN films (PART 1) and TOCN hydrogels (PART 2). Finally, the last part of my work (PART 3) was devoted to the investigation of the hybrid hydrogel structures resulting from the combination of nanocellulose with low molecular weight chitosan.

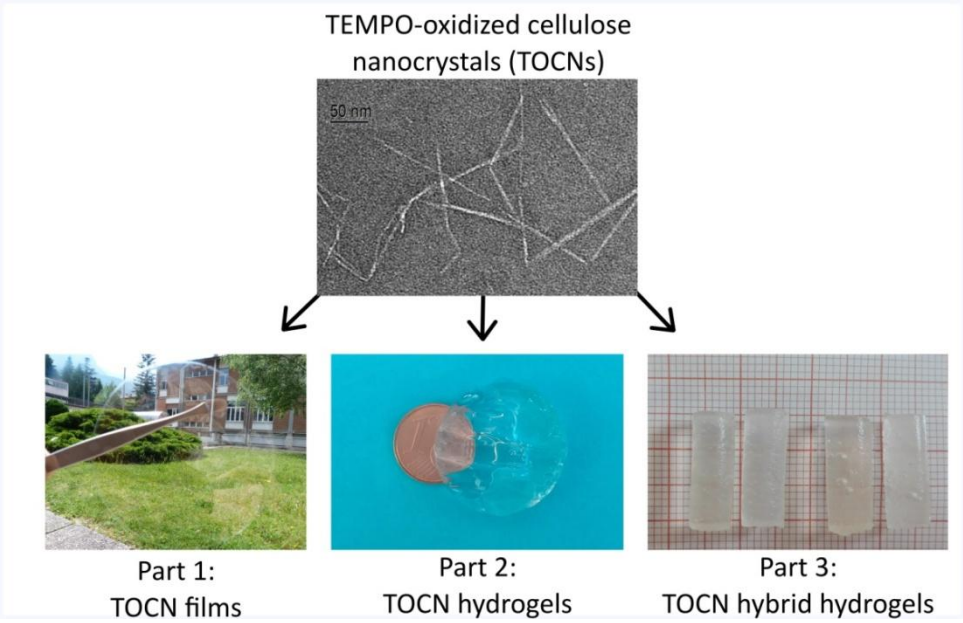

Fig. 1.6: Scheme showing the rational under both my research and this thesis organization. I started from the isolation and characterization of TOCNs (showed in the TEM image in figure) and then turned to investigate their assembly processes through weak interactions to produce films, hydrogels and hybrid materials (which will be treated in three separate parts of this thesis).

In parallel to material characterization, I focused my attention also to the possible exploitation of TOCNs-based materials in the biomedical field. In this regard, a specific chapter (Chapter 8) was dedicated to the investigation of TOCN crystallites and hydrogels toxicity and all the investigations reported in PART 3 were performed in view of a possible exploitation of hybrid nanocellulose hydrogels as therapeutics delivery system in the gastrointestinal tract.

In the following subsections I will briefly provide the state of the art of nanocellulose research on the specific topics of nanocellulose films, hydrogels and hybrid hydrogels and introduce more into details my specific research work on these topics.

1.5.1 Nanocellulose Films

Transparent, self-standing nanocellulose films can be obtained starting from nanocellulose solutions by vacuum assisted drying or simply casting evaporation techniques. Nanocellulose-based films have caught much attention in the recent years, thanks to their peculiar properties. The large aspect ratio of nanocellulose fibrils/crystallites and their ability to form intra- and inter- fibrillar hydrogen bonds permit them to assemble in dense films exhibiting high optical transparency and low gas permeability (Moon et al., 2011). Beyond transparency and barrier properties, also their thermal, mechanical and swelling properties have being largely investigated (Fukuzumi et al., 2013a; Klemm et al., 2011) and make NC films a promising material for disparate applications, among which printed electronics (Hoeng et al., 2016), packaging (Abdul Khalil et al., 2016; F. Li et al., 2015b), and photonics (Abitbol et al., 2016).
In a previous work, I collaborated to an investigation concerning the actuation mechanism induced in TOCN films by their exposure to water gradients: these films are able quantitatively convert the intensity of the gaseous water flux into a fast, reversible bending movement. The actuation is due to the interaction between TOCN crystallites and adsorbed water molecules, which induces a structural rearrangement of the of TOCNs on the exposed surface layers of the film (Bettotti et al., 2016). The ability of cellulose-based films to interact with water at molecular level and consequently change shape or dimensions has been recently exploited to design moisture-responsive cellulose-based materials, miming the humidity-driven bending, unbending, curling and twisting movements observed in plants (Almeida et al., 2018).

Considering the structure investigation of nanocellulose-based films, many efforts were devoted to understand the liquid-crystalline self-assembly of CNC in ordered

helical structures, which enables to obtain iridescent films with unique and tunable optical properties (Giese et al., 2015; Lagerwall et al., 2014; Majoinen et al., 2012; Usov et al., 2015). At the same time, it is known that both the morphology and dimensions of nanocellulose fibers/crystals (Fukuzumi et al., 2013b) and the process leading to films formation, that is the drying process (Klemm et al., 2011; Müller et al., 2014; Ul-Islam et al., 2013), heavily affects the structure and properties of the resulting material. Indeed, the coalescence of nanocellulose fibers/crystals is a not fully understood phenomenon, as a number of different interactions can occur during the drying (such as cross-linking between adjacent nanofibers/crystals) and many processes can contribute to it (Pönni et al., 2012). The first part of my research on nanocellulose films was devoted to the investigation of the self-organization of TOCNs in absence of water, with the purpose of better understanding the specific arrangement of TOCNs and the structures created as a consequence of the casting and drying process.

Among the possible applications, nanocellulose films are being much studied nowadays as green alternatives to petroleum-derived polymer materials in the packaging technology, thanks to their gas barrier properties. Indeed, different literature works (Aulin et al., 2010; Rodionova et al., 2011; Syverud and Stenius, 2009) report O_2 permeability values for nanocellulose films with thicknesses in the micrometer range similar to those achievable with the synthetic polymers commonly used in packaging applications (ethylene vinyl alcohol EVOH, poly(vinyl alcohol) PVA). Moreover, CNF have been demonstrated also to act as gas permeation barrier when deposited as sub-micrometer thick coating on commercial polymers (Fukuzumi et al., 2009). The performance of nanocellulose films as gas barrier was reported to depend on a series of factors, among which not only the temperature (Bayer et al., 2016) and nature of penetrant molecules (Fukuzumi et al., 2011) but also nanocellulose structure and chemical properties such as entanglement (Belbekhouche et al., 2011), length (Fukuzumi et al., 2013b) and surface functionalization (Fukuzumi et al., 2013a). The second part of my research on nanocellulose films was thus focused on the study of the permeation properties of hybrid TOCN/ polylactic acid (PLA) films, where PLA was used as a substrate to enable gas permeation studies. Also in this case, my aim was the extrapolation of important structural information from permeation studies as well as the practical possible exploitation of TOCN/PLA films as gas barrier films.

1.5.2 Nanocellulose Hydrogels

A hydrogel can be defined as a three-dimensional matrix, produced by chemical or physical crosslinking of soluble building blocks (usually polymers), able to retain

large amounts of water in a swollen state. Thanks to their simplicity of fabrication, tunable 3D structure, versatile physical characteristics and wide range of applications, hydrogels are considered nowadays among the materials of the future (Buwalda et al., 2017; Kopeček, 2007; Milroy and Manthiram, 2016). In particular, their hydrophilic nature, adequate flexibility and viscoelastic properties similar to those of native tissues suggest them as promising candidates for biomedical applications (Khademhosseini et al., 2009.; Gauvin et al., 2012).

Polysaccharides are important hydrogel precursors (Pasqui et al., 2012): indeed gel formation is facilitated by their high hydrophilicity and by the presence or introduction by chemical modification of different charged functional groups on the native polymer chains, which are involved in the gelation process (d'Ayala et al., 2008; Nie et al., 2016). In particular, nanocellulose, thanks to its surface properties, can easily form hydrogel structures, even at low concentrations and many literature studies report the self-assembly of NC or NC-composites into soft hydrogels (McKee et al., 2014; Pääkkö et al., 2007), characterizing them in terms of macroscopic parameters such as mesh size, charge density, gelation rate, mechanical performances, or stability (Bonilla et al., 2016; Lasseuguette et al., 2008; Li et al., 2016; Yang et al., 2017). However, differently from common polysaccharides, NC fibers and crystallites cannot be considered as ''conventional polymers'' (de Greef and Meijer, 2008) as they belong to the class of supramolecular structures, able to self organize and generate macroscopic objects stabilized by networks of weak bonds (Ikkala and ten Brinke, 2002). Moreover, while flexible NC fibers containing amorphous regions are described as excellent hydrogel precursors, NC rod-like crystallites are often considered ill-suited as single components of gels, due to their intrinsic rigidity and reduced ability to entangle into a network (De France et al., 2017). In this context, rheology experiments show that the behavior of NC suspensions is strongly dependent on NC production: mechanical fibrillation without chemical modification produces suspensions with flocculated structure, while NC which underwent chemical processes produces suspensions with better colloidal stability (Nechyporchuk et al., 2016b). Static and dynamic rheological experiments on rod-like TOCNs hydrogels suggest that liquid crystal domains consisting of self-organized ordered structures are present in TOCNs (Wu et al., 2014). It is also known that divalent or trivalent cations (Ca^{2+}, Zn^{2+}, Cu^{2+}, Al^{3+}, and Fe^{3+}) induce gelation of negatively charged TOCNs and form interconnected porous nanofibril networks (Dong et al., 2013b). Dynamic viscoelastic measurements performed on these gels and SEM images measured on dried samples (Zander et al., 2014) reveal storage moduli and mesh sizes strongly related to the valence of the metal cations and their binding strength with carboxylate groups. Despite the large interest on NC hydrogels and their applications, several basic aspects regulating NC properties and its interaction with the environment are still unclear. In particular, little is known about its interaction with water molecules and the contribution of

hydrogen bonds. Moreover, as the number of hydrogels potential applications increases, it is important to be able to control the local structure of the hydrogels and develop strategies to tune their sizes and shapes in a precise and reproducible manner. In this general context are located my investigations of TOCN hydrogels, which will be reported in Chapter 6 and Chapter 7.

More into details, the aim of the studies reported in **Chapter 6** is the better understanding of the mechanical and chemical sol-gel transition process from TOCN solutions to TOCN hydrogels induced by sonication and salt addition. As already said, hydrogels are materials which contain huge amounts of water and water is an excellent competitor for intra- and inter- fibril hydrogen bonds. Different dynamic regimes of the water molecules have been observed within and on the surface of polysaccharide-based or synthetic hydrogels: free interstitial water which does not take part in hydrogen bonds with hydrogel molecules; bound water, which is directly bound to the chains and semi-bound water, with intermediate properties (Jhon and Andrade, 1973; Pasqui et al., 2012). In this regard, TOCNs behave as a typical polysaccharide and their structure and dynamics in solution are expected to strongly depend on electrostatic bonds and on the surface available for their occurrence. However, being TOCN hydrogels formed by the assembly of rigid nanostructures rather than polymer chains, the behavior of water molecules inside them could substantially differ from that in more traditional hydrogels. For this reason, during our investigations, particular attention was given to the presence and the dynamic behavior of water molecules inside TOCN hydrogels.

The studies reported in **Chapter 7** are focused on the dynamics of the gelation process. It is based on the coordination-driven assembly of TOCN crystallites in aqueous solutions and on the use of ionotropic gelation as methodological approach to fabricate small hydrogel objects, in an easy, fast and reproducible manner. Ca^{2+} was chosen as gelling agent for the possibility to monitor its concentration and presence by colorimetric methods. The control of the local structure of the hydrogels and the development of strategies to tune their sizes and shapes in a precise and reproducible manner are indeed fundamental in order to increase the possibilities of TOCN hydrogels applications.
Ionotropic gelation is a commonly used method to form polyelectrolytes hydrogels, and in particular polysaccharides hydrogels, exploiting the diffusion of multivalent counter ions (Patil et al., 2010). Two main different types of ionotropic gelation processes exist: external ionotropic gelation and inverse ionotropic gelation. In the first case, a polyelectrolyte suspension is dropped in a solution containing the counter ion, which gradually moves inward from the outer counter ion reservoir to the inner hydrogel meanwhile it is formed. Instead, in inverse ionotropic gelation the counter ions diffuse outward from an inner discrete core into an external

polyelectrolyte pool (Patil et al., 2012). Despite being a largely used technique, especially for pharmaceutical preparations, the dynamics underlying the gelation process is still poorly understood, since diffusion, osmotic swelling, electrostatic interactions, coordination complexes and polyvalent hydrogen bonding networks contribute to the gel formation (Leong et al., 2016; Pasqui et al., 2012). As a consequence, the understanding of mechanism and kinetic of gelation are fundamental if complex hydrogel microstructures such as fibres, hollow beads, scaffolds or anisotropic and compartmentalized particles are required.

Finally, the last part of my researches on TOCN hydrogels (**Chapter 8**) was devoted to study the toxicity of TOCN hydrogel membranes in view of their possible application as skin patches, in particular for the photodynamic therapy of melanoma. Indeed, hydrogels are good candidate materials for patches production, because their high water content, softness and flexibility properties preserve skin hydration, avoiding dryness and depletion of epidermal barrier properties, which are often associated to skin diseases or are side effects of the therapy. NC offers several advantages with respect to other hydrogel precursors of natural origin, such as the easy production process and the quite low cost (De France et al., 2017; García et al., 2016).
However, the toxicity topic still remains an open question. Hazard assessment studies have been performed mainly for nanocellulose fibers (NCF) (Catalan et al., 2017) and NCF hydrogels (Basu et al., 2017), reporting low cytotoxicity and no DNA or chromosome damage in the first case and good cell viability and no adverse immunological response in the second. Conversely, considering nanocellulose in the form of nanocrystals (CNC), only few cell cultivation experiments consisting in the monitoring of growth propagation and activity of cells in CNC hydrogel scaffolds have been reported (Lin and Dufresne, 2014). In the context of toxicity studies, the correctness of the methodologies used to probe the safety of a medical device is an important concern, as opposite results can be obtained using two different assays (Hua et al., 2014). In this regard, the International Standard protocol ISO 10993-1 and DIN EN ISO 10993-5:2009 (STANDARD, 2009), which was originally developed for the biological evaluation of non-degradable materials in medical devices, suggests to test each component material, including impurities, and constituents associated with processing together with the device, both in direct and indirect contact. Following these suggestions, we evaluated the biosafety not only of the hydrogel device (produced by crosslinking TOCNs with mono and divalent cations) but also of each component material (in particular, TOCN solutions and salt solutions) in cultures of malignant melanoma cells A375.

1.5.3 Hybrid Nanocellulose-chitosan hydrogels

As already said, NC hydrogels possess unique and interesting properties which make them promising materials in several fields. However, while these properties well meet the requirements of some applications, they are not optimal (or not enough) for others. As an example, the high stability of NC hydrogels in common solvents can become an obstacle if materials that degrade in time are required. Recently, many attempts have been done to produce hybrid materials, made of NC and other precursors (natural or synthetic polymers or particles) in such a way to take advantage from the characteristic properties of both of them and obtain materials with ad-hoc properties for specific applications (Chang and Zhang, 2011; De France et al., 2017; Salas et al., 2014).

In order to obtain a hydrogel material which can be digested by human enzymes and used as protein therapeutics delivery system in the gastrointestinal tract, we combined TOCN with low molecular weight Chitosan. Chitosan is a linear polysaccharide derived by deacetylation of chitin and composed of randomly distributed N-acetyl-D-glucosamine and D-glucosamine units, the latter containing primary amines, which are positively charged at acidic-neutral pH (pK_a 6.4). Chitosan is a biocompatible, biodegradable material much used in the biomedical field (Anjum et al., 2016; Kong et al., 2010; Kumar et al., 2004; Shahidi et al., 1999), however its poor mechanical stability and low mechanical strength limit its fields of applications as pure material (Zhou et al., 2014). The combination of chitosan and TOCNs allows the development of a new biomaterial, which could exhibit properties not achievable by the two individual components. In our case, TOCN/Cht nanocomposite hydrogels are expected to be mechanically strong and stable in Phosphate Buffered Saline (PBS), but at the same time undergo digestion by human enzymes such as lysozyme (Muzzarelli, 1997).
Moreover, chitosan could eventually confer interesting mucoadhesive properties to the hybrid hydrogel material. Indeed, chitosan mucoadhesion properties have been widely studied and documented (Bonferoni et al., 2009; Ganguly and Dash, 2004). Mucoadhesive materials, that is synthetic or natural macromolecules capable of attaching to mucosal surfaces, are nowadays gaining more and more attention as promising drug delivery strategies for various administration routes, such as nasal, ocular, vaginal and oral (Boddupalli et al., 2010; Peppas et al., 2006; Peppas and Sahlin, 1996). This interest is due to the fact that they are able to prolong the residence time of the material and to improve the specific localization of drug delivery systems on various membranes (Grabovac et al., 2005; Lee et al., 2016). In particular, the use of mucoadhesive intestinal devices appears as a novel delivery technique for the effective administration of peptide/protein-based therapeutics, whose instability in the gastrointestinal tract and poor permeability across

biological membranes would otherwise necessitate their parental administration (Banerjee et al., 2016).
Even though several recent literature works report the use of chitosan and cellulose-based materials to produce hybrid composites (Borysiak and Grząbka-Zasadzińska, 2016; Grande et al., 2017; Riva et al., 2015), most of them are focused on the formation of films (Poonguzhali et al., 2017; Toivonen et al., 2015), or hydrogels produced from commercial cellulose acetate or carboxymethyl cellulose (Duan et al., 2015; Singh et al., 2017) or CNC obtained through acid hydrolysis (Sampath et al., 2017; Udeni Gunathilake et al., 2017). Very little can be found instead on the combination between TOCNs and chitosan (Toivonen et al., 2015; Zhou et al., 2014).

With the aim of understanding the different but synergistic role of TOCN and Cht as components of a potential hydrogel delivery system, the last part of my PhD studies was devoted to set up a procedure to obtain TOCN/Cht hydrogels with cylindrical shape, characterize their structural and mechanical properties and investigate the drug release and hydrogel matrix degradation *in vitro*. A medium-sized protein such as bovine serum albumin (BSA) was chosen as protein drug model, while lysozyme was utilized as a representative example of human digestive enzymes, since chitosan is thought to be degraded in vertebrates predominantly by lysozyme and by bacterial enzymes in the colon (Kean and Thanou, 2010). As in the previous parts of the thesis, particular attention was devoted to the characterization of the material itself, envisaged as the starting point to understand the properties of the final product.

1.6 Characterization techniques

The study of TOCN interaction and assembly processes required the combination of a wide number of techniques, which investigated and characterized the resulting materials from different perspectives: structurally, chemically, mechanically and biologically. Here I briefly report the main experimental methodologies exploited, with particular focus on the structural characterization techniques.

1.6.1 Structural characterization

A first category of techniques traditionally used to characterize the structure of materials is represented by microscopy. Apart from more traditional methods like optical microscopy, in these thesis electron microscopy (scanning electron microscopy SEM and transmission electron microscopy TEM) and atomic force

microscopy (AFM) were used to investigate TOCN-based structures. By these techniques, high resolution images can be obtained, whose analysis allowed to get information about crystals morphology, their arrangement and the porosity and surface properties of the structures created. However, SEM and TEM require a significant sample manipulation. While this is not a problem in the case of dried samples like fibrils or films, the drying procedure can cause a partial shrinkage or collapse of 3D aqueous structures, like hydrogels, hindering a quantitative analysis. On the other hand, AFM does not require complex samples preparation procedures but enables the mechanical characterization and imaging only of surfaces. Moreover, the structural and morphological information supplied by all these microscopy techniques is restricted to the local area/volume where the analysis is performed.

For these reasons, in parallel to structural characterization by electron and atomic force microscopy, other techniques were used to indirectly get information about the assembly of nanocellulose crystallites.
The structural investigation of the compact assembly of TOCNs in films required techniques which enable to get information about the low porosity of the material. Positron annihilation lifetime spectroscopy (PALS) analysis and gas permeation tests were performed to indirectly get insight on the voids present in the films, through the behavior of positrons and gas molecules inside them.
Turning instead to consider hydrogels, the main problem encountered in the study of their structures was their high water content. Indeed, the presence of water is strongly related to the properties of the material but, at the same time, is incompatible with many instrumental techniques that require vacuum conditions and/or absence of water. The methods here exploited to investigate the nanometric structure of the hydrogels networks and get information about their porous assembly were rheology, low-field nuclear magnetic resonance (LF-NMR) and small angle x-ray scattering (SAXS).

1.6.2 Other characterization techniques

Among the other experimental approaches utilized in this thesis work, there were optical and spectroscopic techniques like UV-Vis spectroscopy (to evaluate the transparency and homogeneity of the materials), Fourier-Transform Infrared Spectroscopy (FTIR) (to monitor the presence and coordination of functional groups) and Fluorescence Spectroscopy (to follow release kinetics from hydrogels). Moreover, the mechanical characterization of hydrogel samples was performed by compression tests and mucoadhesion experiments (in addition to the already cited rheological measurements) and colorimetric methods were used to study the diffusion processes inside hydrogel structures.

Finally, the bio-compatibility and toxicity properties of TOCNs and TOCN based materials were evaluated studying their influence on cell viability *in vitro* through MTT assays, phase contrast microscopy and confocal laser scanning microscopy.

1.7 Conclusions

As briefly introduced in this chapter, NC appears nowadays as a promising material with possible applications in a wide range of fields. Despite the increasing interest on the topic, many aspects regulating NC self-assembly and interaction properties are still unclear. The knowledge of these properties is however fundamental as they determine the final structure and behavior of NC-based materials.
The aim of my work was therefore the investigation of the assembly processes of cellulose nanocrystals, obtained from TEMPO-mediated oxidation of cellulose pulp followed by sonication, in different environments. In particular, I considered TOCNs assembly:

- in absence of water, with the purpose of getting information about the dense structure of TOCN films,
- in presence of water, in order to better understand TOCNs-water supramolecular interaction through hydrogen bonds and weak forces and be able to control the properties, size and shape of the resulting hydrogels,
- in combination with chitosan, obtaining a hybrid polysaccharide material.

The influence of assembly/interactions processes on the final properties of TOCN-based structures was exploited to evaluate some possible applications of TOCN-based materials. In particular, I focused on:

- permeation studies of TOCN films, envisaged as possible gas barrier materials,
- toxicity studies on TOCN hydrogel membranes and precursors, in view of their possible usage as skin patches,
- development of hybrid TOCN-chitosan hydrogels, which could be used as delivery system in the gastrointestinal tract.

CHAPTER 2:
TEMPO-oxidized cellulose Nanocrystals

The aim of this Chapter 2 is to describe the methods used in this thesis work to produce TEMPO-oxidized cellulose nanocrystals (TOCNs) and provide a basis characterization of them, in terms of morphology, dimensions and chemical composition. It is important to underline here that TOCNs are the fundamental building block from which both films and hydrogels are assembled. In this sense, their characterization is the starting point from which all the subsequent investigations can move on and differentiate.

The procedure exploited to obtain cellulose nanocrystals is a slightly modified version of the method developed by Saito et al. in 2006 (Saito et al., 2007, 2006). It consists of two-steps: the first one is the oxidation of cellulose soft pulp, while the second one is a sonication process, which enables the individualization of the TOCNs.

Considering the Chapter organization, in Section 2.1 a general description of the oxidation process, known as TEMPO-mediated oxidiation, will be reported. Section 2.2 will be focused on the details of the experimental procedure exploited to obtain TOCNs and on the techniques used to characterize them. Finally, in Section 2.3 the results of TOCNs preparation and characterization will be presented.

2.1 Generalities on TEMPO-mediated oxidation of cellulose

Different top-down strategies exist to deconstruct the hierarchical structure of cellulose natural fibers and extract its structural micro-nano sub-elements (Jonoobi et al., 2015; Mondal, 2017; Nechyporchuk et al., 2016a). The main obstacle in the conversion from pure cellulose to its constituting micro-nano elements is represented by the presence of numerous hydrogen bonds between microfibrils, which hinder the isolation of nano-sized structures. Among the different approaches, there are preprocessing tricks which facilitate the separation by weakening the interfibrillar hydrogen bonds. An efficient and increasingly used strategy is the oxidation of cellulose with 2,2,6,6-tetramethyl piperidine -1-oxyl

(TEMPO) in aqueous solution (Isogai et al., 2018). The main advantage of TEMPO-mediated oxidation with respect to other methods of microfibrils separation is that it introduces carboxylic groups negatively charged at pH > 4. In this way, an electrostatic repulsion between microfibrils is created. This repulsion overcomes the interfibrillar hydrogen bonds that otherwise held the microfibrils together, decreases the energy consumption otherwise required to defibrillate cellulose (Lavoine et al., 2012) and guarantees high weight recovery ratios (higher than 80%).
More into details, by the TEMPO-mediated oxidation process catalytic amounts of TEMPO and sodium bromide (NaBr) are dissolved in cellulose solution at pH 10.5-11 and oxidation starts by the addition of sodium hypochlorite (NaClO) as a primary oxidant. The primary oxidant is required because TEMPO radical, although its not negligible oxidation potential, needs to be converted into the more powerful nitrosonium salt in order to function as an efficient oxidant of organic substances. As long as the reaction goes on, carboxylic groups are generated and are in equilibrium with their anionic form (carboxylates) depending on the pH of the solution. A scheme of the oxidation process of the C6 primary hydroxyl groups of cellulose by TEMPO/NaBr/NaClO in water is reported in fig 2.1. Only the C6 primary hydroxyls exposed on the surface of crystalline cellulose microfibrils are expected to be converted to sodium carboxylates groups (Moon et al., 2011).

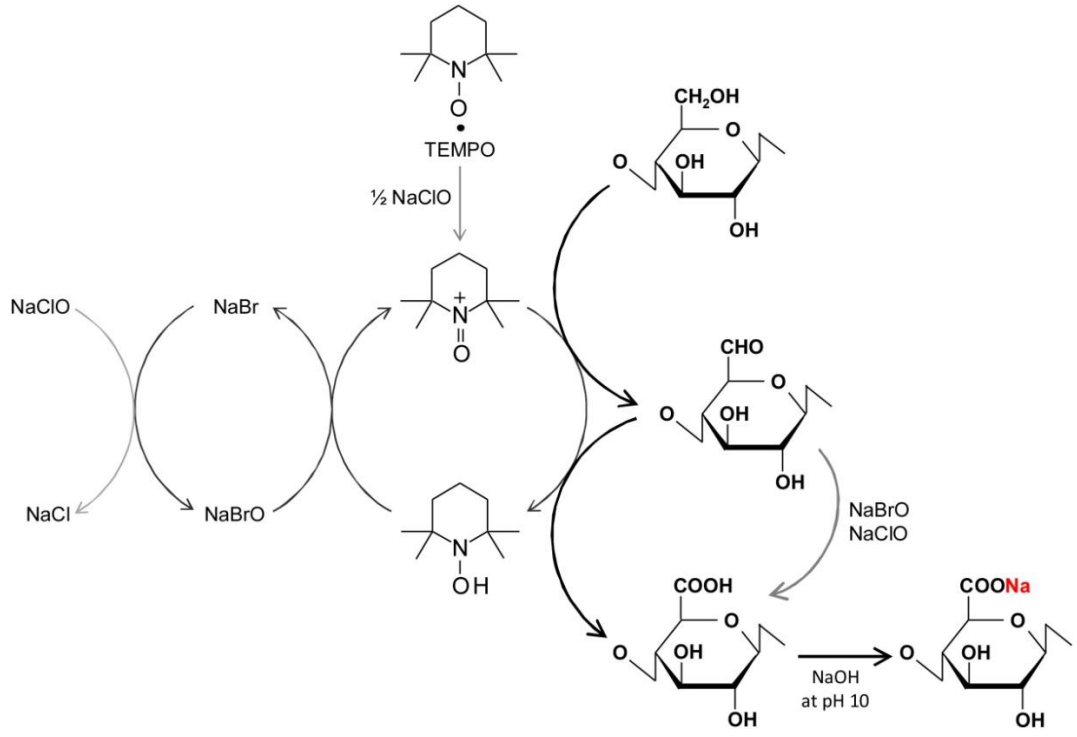

Fig. 2.1: Scheme of TEMPO/NaBr/NaClO oxidation of the C6 primary hydroxyls of cellulose in water at pH 10.5-11. The nitrosonium ion is continuously regenerated in situ by the primary oxidant, as shown in the central part. Image taken from (Isogai et al., 2018) with permission of *Elsevier*.

2.2 Materials and Methods for TOCNs preparation and characterization

2.1.1 TOCNs preparation

The starting material from which the cellulose nanocrystals produced and studied in this work were prepared is never dried soft bleach pulp (Celeste90), which we received from SCA-Ostrand (Sweden).
As already introduced, TOCNs were obtained following a two-steps procedure consisting firstly in the TEMPO-mediated oxidation of cellulose soft pulp and then in a sonication process.
Going more into details and starting from the first step, 1 g of cellulose was suspended in 100 mL distilled water, stirred with a magnetic stirrer at room temperature for 1 hour and then sonicated for 30 min in a 350 Watt ultrasonic bath in order to obtain a more homogeneous suspension of cellulose. After that, 0.016 g of TEMPO, 0.1 g of NaBr and 1.75 mL of NaClO (6-14% active basis) were added to the slurry under vigorous stirring. 1 M NaOH was continuously added to the reaction mixture to maintain the pH between 10.5 and 11 during the reaction. Oxidation ended when no more NaOH was consumed and the pH of the solution did not change anymore, meaning that no further consumption of alkali was taking place. At this point the pH was lowered to 7.0 by washing the slurry with distilled water (400 mL) for at least 10 times, ending up with an aqueous suspension of cellulose oxidized nanofibers with concentration around 3 mg mL^{-1}.
Once TEMPO-mediated oxidation has taken place, the second step consisted in the mechanical disintegration of the oxidized cellulose through an ultrasonic treatment, by which transparent TOCN aqueous solutions were obtained. For this purpose, a Bandelin Sonopuls HD 2200 ultrasonic homogenizer with a 13 mm diameter ultrasonic tip was used. The oxidized cellulose slurries were divided in 50 mL aliquots and sonicated for 4 min at 20 kHz frequency and 100 W output power. The sonicated solution was then vacuum filtered over a 1.2 μm cellulose ester Millipore filter to remove residual coarse fibrils. To obtain the desired concentrations, TOCN solutions were concentrated by a rotary evaporator (Laborota 4000 efficient, Heidolph) connected to a vacuum pump.

2.1.2 TOCNs characterization

Fourier Transform Infrared (FTIR) spectra of TOCNs were acquired using a micro-FTIR Nicolet iN10 spectrophotometer equipped with a liquid nitrogen cooled detector. Samples were prepared by casting TOCN solutions on Petri dishes and

drying them at 60°C in an oven obtaining, after water evaporation, free standing films (whose preparation and properties will be described in detail in Part 1 of this thesis), which were placed on a perforated metal disk and scanned in transmittance mode in the range 750-4000 cm^{-1} with a 4 cm^{-1} resolution.

The carboxylic content of TOCNs was evaluated by conductometric titration using a HD 2256.2 (Delta Ohm) conductimeter. Procedure parameters and data analysis were chosen and done according to Saito *et al.* (Saito and Isogai, 2004) and Fras *et al*. (Fras et al., 2004). The conductance of 100 mL of TOCN aqueous solution (1 mg mL^{-1}) was measured as a function of the volume of 0.1 M NaOH added solution, considering that an increase or decrease of conductance is primarily due to the concentration of H^+ and OH^- ions. 50 μL of 1 M NaCl were added to the TOCN solution in order to have an equal distribution of mobile ions between the fibers and in the bulk solution and have a better accuracy in the determination of the number of carboxylic groups. The TOCN solution was initially brought to pH 2.7 by addition of 1 M HCl to neutralize all the carboxylic groups. After that, the pH was gradually raised adding 0.1 M NaOH and the values of conductance registered.

The morphology and dimensions of TOCNs were investigated by microscopy techniques. In particular, we used both atomic force microscopy (AFM) and transmission electron microscopy (TEM). AFM images were acquired using an AFM NT-MDT P47H scanning probe microscope operated in semi-contact mode and elaborated with the software Gwyddion (Nečas and Klapetek, 2012). For the sample preparation, two different techniques were used. In one case, a drop of diluted TOCN solution was deposited on a silicon substrate and dried in oven at 60°C. In alternative, TOCNs were deposited on glass slides (previously treated in an ozone cleaner) by a dip coating procedure. By this technique, the cleaned and vertically aligned slides were immersed in a diluted TOCN solution (0.25 mg mL^{-1}) and then raised up at a constant speed (27 mm min^{-1}). Also in this case, samples were dried in oven at 60°C before measurements. TEM images were acquired by a FEI Tecnai 12 G2 TEM operated at 120 kV. For this purpose, 5 μL of an aqueous TOCN solution were placed on a 300-mesh copper grid coated by a support carbon film (Ted Pella Inc.). After 1 min the excess fluid was removed and the grids were negatively stained with 2% uranyl acetate in water for 1 min. TEM images were then analyzed with the software ImageJ to determine TOCNs dimensions.

Transmission Electron Measurements were performed at the Ben Gurion University of the Negev (Israel).

2.3 TEMPO-oxidized cellulose nanocrystals (TOCNs) characterization

Fig. 2.2 schematically summarizes the process used to prepare TOCNs starting from cellulose pulp. A detailed description of the procedure is reported in Subsection 2.1.1, here we just recall that it consisted of two steps, the first being a chemical oxidation reaction by which carboxylic groups are introduced on fibrils surface, the second consisting in a mechanical treatment that exploits the energy supplied by ultrasounds to individualize TOCNs.

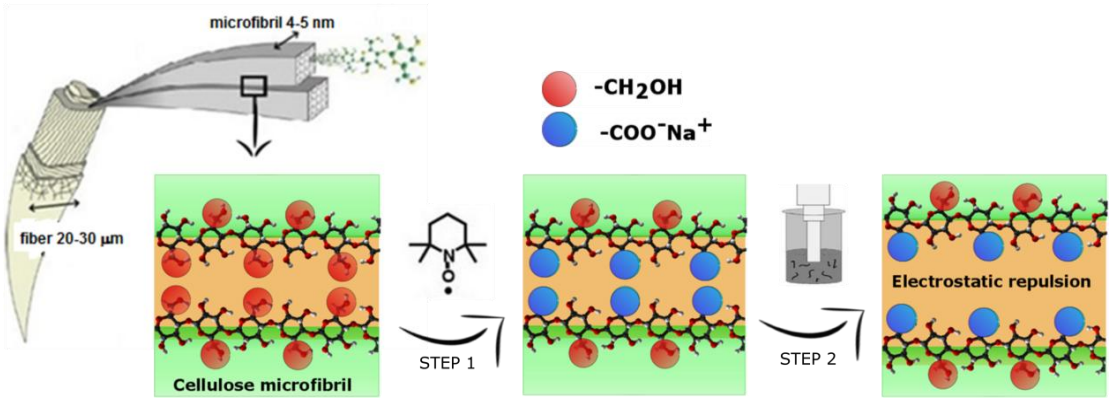

Fig. 2.2: Sketch of the two steps process, which leads to the individualization of TOCNs starting from soft cellulose pulp. The two steps consist respectively of an oxidation reaction, which introduces carboxylic groups on cellulose fibrils surface, and an ultrasonication treatment which breaks the fibrils and separate TOCNs.

In Fig. 2.3, instead, some pictures showing the visual appearance of the starting cellulose pulp material (Fig. 2.3a), of the microfibrils suspension after TEMPO-mediated oxidation and subsequent extensive washing (Fig. 2.3b) and of the transparent TOCN solutions finally obtained after sonication (Fig. 2.3c) are reported.

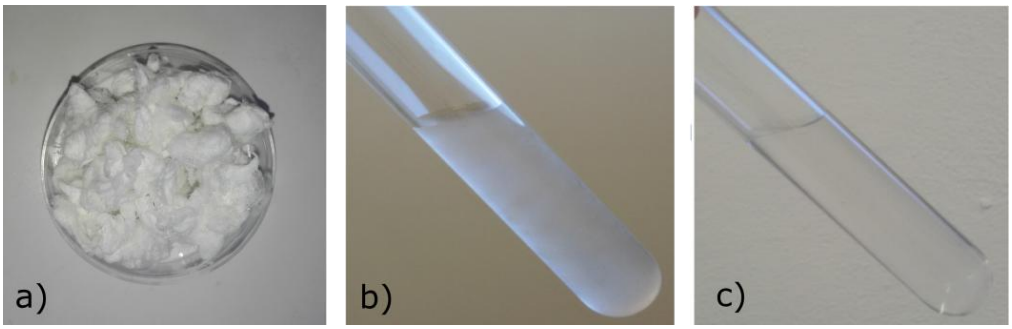

Fig. 2.3: Pictures of cellulose-based materials at the different stages of the process leading to TOCNs: a) starting cellulose bleached pulp; b) 3 mg mL^{-1} aqueous suspension of cellulose microfibrils after TEMPO-mediated oxidation and subsequent extensive washing; c) 3 mg mL^{-1} transparent TOCN solutions obtained after sonication.

2.3.1 TOCNs morphology

The structure and dimensions of TOCNs were evaluated by microscopy techniques, in particular AFM and TEM. Fig. 2.4 shows two representative TEM images of TOCNs, while an AFM image is reported in Fig. 2.5:

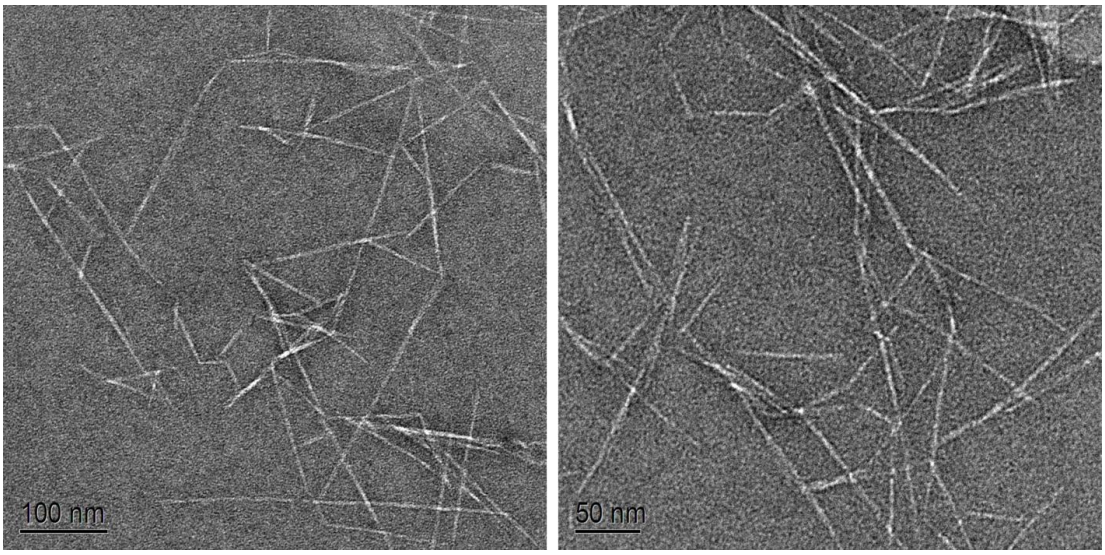

Fig. 2.4: TEM images of TOCNs, showing the straight crystalline regions connected by less frequent flexible amorphous domains. Samples were prepared by depositing 5 μL of TOCN solution on a copper grid coated by a support carbon film, removing the excess fluid and negatively staining the grids with 2% uranyl acetate in water for 1 min.

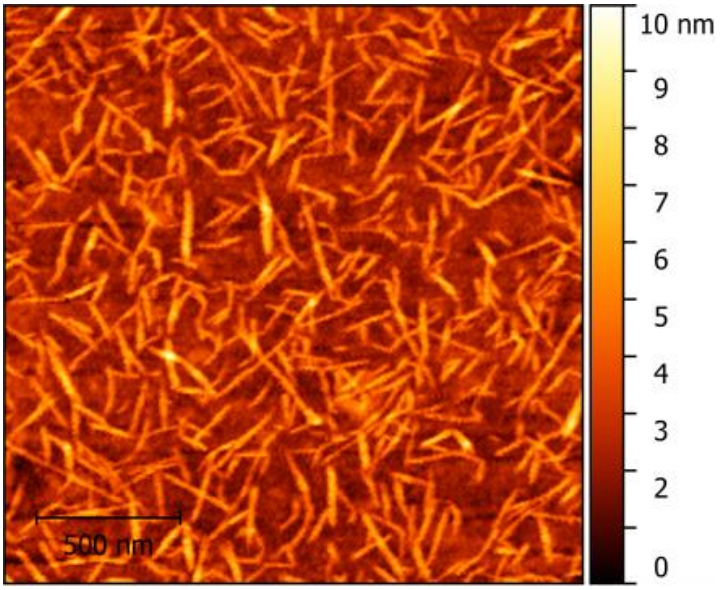

Fig. 2.5: AFM image to TOCNs, from which the rod-like nature of TOCNs can be observed. Samples were prepared by a dip coating procedure, immersing cleaned and vertically aligned glass slides in a diluted TOCN solution, raising them up at a constant speed and then drying them at 60°C.

Both TEM and AFM images show that the nanometric structures obtained by TEMPO-mediated oxidation and subsequent sonication process consist of crystalline domains (straight tracts in the images) bound by rare, flexible amorphous domains. These latter are less frequent because they are more reactive than crystalline regions toward oxidation and more easily broken by sonication. Because of this observed crystalline, rod-like nature, we decided to denote the obtained nanometric material as TEMPO-oxidized cellulose nanocrystals (TOCNs) to distinguish it both from cellulose nanocrystals (CNC), usually obtained by acid hydrolysis, and from microfibrillated cellulose (MFC), a less crystalline material which can be obtained by TEMPO-mediated oxidation without a subsequent extensive mechanical disintegration (See Section 1.2 for nanocellulose nomenclature).

The dimensions of the TOCNs were evaluated by statistical analysis on several TEM images. As visible in Fig. 2.6, TOCNs width is centered at about 4 nm, while TOCNs length is of the order of some hundred nanometers (100-200 nm). Interestingly, the TOCNs diameter is compatible with that of an elementary fibril of wood cellulose nanocrystal (Moon et al., 2011).

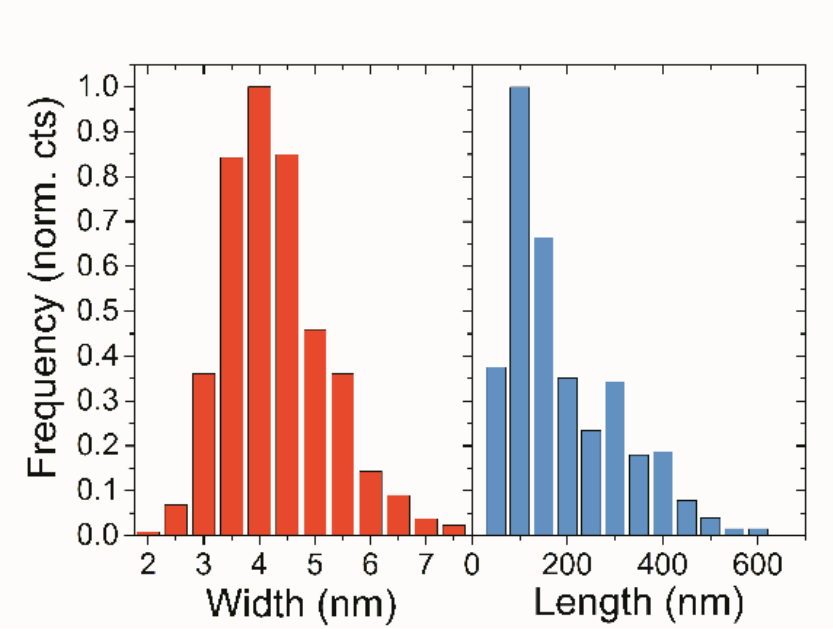

Fig. 2.6: Statistical distribution of TOCNs width and length, measured from several TEM images by using the software ImageJ. Published figure (Bettotti et al., 2016)

2.3.2 TOCNs carboxylic content

As already pointed out, a characteristic feature of TOCNs is the presence of carboxylic groups, introduced on the surface of cellulose fibrils by the TEMPO-mediated oxidation process. These groups are fundamental not only for the individualization of the TOCNs during the sonication treatment but also in the

determination of their reactivity and assembling properties. Fig. 2.7 shows the typical FTIR spectrum of TOCNs: the sharp peak at around 1605 cm^{-1} is related to the stretching vibration of carboxylate functional groups. The assignations of the other main vibrational bands present in the spectrum are summarized in Table 3.1 (Li et al., 2015a).

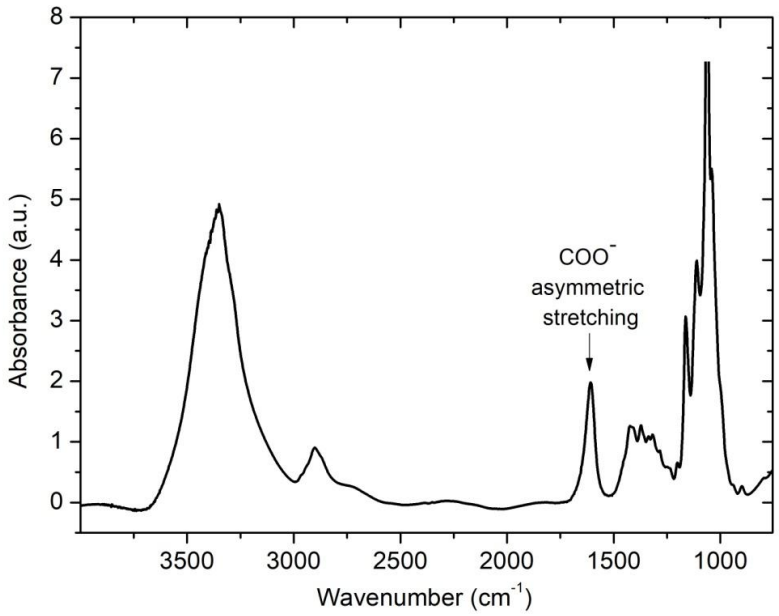

Fig. 2.7: FTIR spectrum of TOCNs, in the form of film obtained by casting a solution of TOCNs in a Petri dish and peeling-off the resulting self standing film after incubation at 60 °C. Spectra were acquired in transmission mode with a 4 cm^{-1} spectral resolution. The stretching vibrational band of carboxylic groups introduced on cellulose fibrils by the TEMPO-mediated oxidation process is well visible at 1605 cm^{-1}.

Table 2.1: Assignments of the main vibrational bands characterizing TOCNs spectra and visible in Fig. 2.7.

Vibrational band assignation	**peak position**
O-H stretching	3300-3400 cm^{-1}
C-H stretching (CH_2)	2900 cm^{-1}
O-H bending of adsorbed water	1640 cm^{-1}
COO^- asymmetric stretching	1600-1610 cm^{-1}
HCH and OCH in-plane bending	1425 cm^{-1}
COO^- symmetric stretching	1410-1420 cm^{-1}
CH in-plane bending	1370 cm^{-1}
CH_2 rocking at C_6	1317 cm^{-1}
C-O-C stretching	1161 cm^{-1}
C-C stretching	1112 cm^{-1}

A quantitative evaluation of the TOCNs carboxylate content was performed by the conductometric titration method, as explained in Section 2.1.2. Fig. 2.8 shows on example of the obtained conductivity versus added NaOH curve, from which the number of carboxyls can be determined (Fras et al., 2004; Saito and Isogai, 2004).

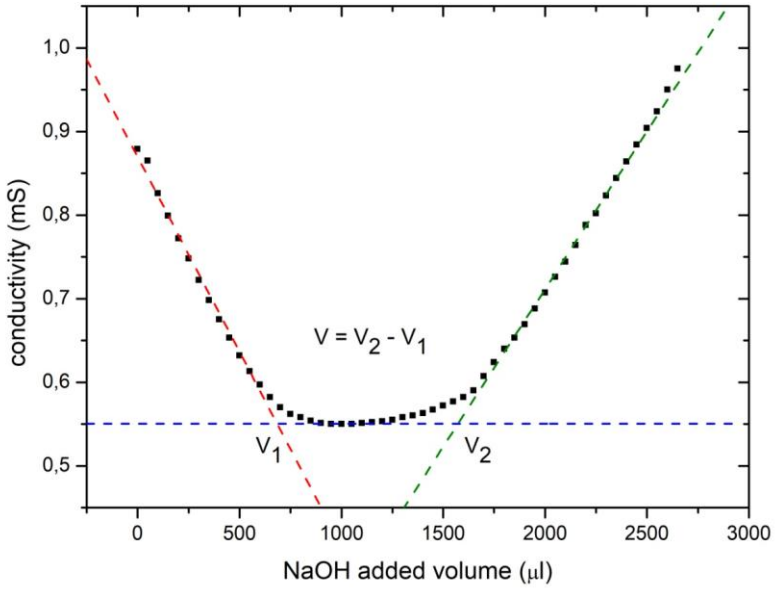

Fig. 2.8: Titration curve showing the conductivity of TOCN solution as a function of NaOH volume added. Measurements were performed using a HD 2256.2 (Delta Ohm) conductimeter, starting from 100 mL of TOCN aqueous solution (1 mg mL^{-1}) to which 50 µL 1 M NaCl were added in order to have a better accuracy. The pH of the solution was initially brought to 2.7 by addition of 1 M HCl to neutralize all the carboxylic groups. After that, the pH was gradually raised adding 0.1 M NaOH and the values of conductance registered. The reported points are the experimental values measured, while the dashed lines are linear fits performed on the different curve parts.

The curve can be divided into three parts: in the first part the conductivity decreases because of the neutralization of free protons by OH^-. In the second part, Na^+ ions are absorbed by the carboxylic groups and H^+ are neutralized by OH^-: the carboxylic groups are titrated and the conductivity is constant. In the third part, there is an excess of OH^- and the conductivity increases. Red, blue and green dashed lines in Fig. 2.8 are linear fits of the three parts respectively, while V_1 and V_2 are the intersection points between the lines. Knowing the V_1 and V_2 values the TOCNs carboxylic content X can be estimated through the following formula (Fras et al., 2004):

$$X = \frac{v\,c}{m} \qquad \text{(Eq. 2.1)}$$

where *m* is the dry mass of the sample, *c* the concentration of NaOH solution used and *v* the NaOH volume necessary for the titration of the carboxylic groups, calculated from the plot as $V=V_2-V_1$. By this procedure, the carboxylic content of TOCNs was estimated to be 0.9 ± 0.2 mmol/g corresponding to 0.30 ± 0.07 carboxylate groups per cellobiose unit.

2.4 Conclusions

TEMPO-mediated cellulose nanocrystals were obtained by a two-steps procedure, the first being a chemical oxidation reaction by which carboxylic groups are introduced on fibrils surface, the second consisting in a mechanical treatment that exploits the energy supplied by ultrasounds to individualize TOCNs.
The resulting nanocrystals were observed by microscopy techniques and show a rod-like shape with dimensions around 3-5 nm in diameter and some hundred nanometers in length. Their carboxylic content, determined by conductimetric titration, was estimated to be around 0.30 ± 0.07 carboxylate groups per cellobiose unit.

In the next chapters, I will use the term TOCN ''solutions'' to denote the homogeneous aqueous suspensions of TOCN crystallites after the two-steps procedure. I will use instead the term ''suspensions'' to denote the turbid, non homogeneous suspensions of cellulose fibrils after oxidation but before extensive sonication, that is before complete individualization and separation of the nanometric constituents.

PART 1

TEMPO-oxidized Cellulose Nanocrystals Films

CHAPTER 3
Materials and Methods for TOCN films

In this Chapter I will describe the methods used to prepare TOCN films starting from TOCN solutions and the techniques used to characterize them. Both pure TOCN films and bilayered TOCN/polylactic acid (PLA) films were studied. Moreover, hybrid nanocomposite films formed by TiO_2 nanoparticles dispersed among TOCN crystallites were considered too.
The starting material, from which TOCN films were prepared, was represented by aqueous solutions of TOCN crystallites prepared and characterized as reported in Chapter 2.

3.1 TOCN films preparation

TOCN films were obtained casting sonicated TOCN solutions on Petri dishes and drying them at 60°C in an oven, over a flat copper foil to maintain homogeneous temperature over the whole film surface. The thickness of the films was controlled by casting variable amounts of the starting TOCN solution and/or by changing its concentration. After water evaporation, the resulting free standing films could be easily peeled off from the Petri dishes and were conserved at Room Temperature (RT) in a desiccator until use.
TOCN/PLA double layer films were prepared by depositing TOCN solutions on 6.2 cm^2 PLA disks, which in turn were laid on a hydrophobic polydimethylsiloxane (PDMS) substrate to confine the aqueous TOCN solution. The films were then dried at 60°C for 24 h in oven. Also in this case, the thickness of the TOCN layer was changed by casting different amounts of TOCN solution.
Finally, nanocomposite hybrid TOCN-TiO_2 films were obtained casting in Petri dishes or on PLA disks TOCN solutions in which TiO_2 nanoparticles were previously dispersed. To get an homogeneous distribution, TiO_2 nanoparticles were added to diluted TOCN solutions obtaining a weight ratio between TiO_2 and TOCNs equal to 1:20 and the resulting TOCN-TiO_2 suspensions were sonicated and vortexed previously to casting. Also in this case the films were dried at 60°C. Degussa Aeroxide® TiO_2 p25 nanoparticles were purchased from Evonik (Germany). These nanoparticles have a average diameter of 25 nm and are made by a combination of rutile and anatase crystal structure.

The thickness of self supporting TOCN films was measured analyzing their UV-Vis spectra (Poelman and Smet, 2003), as will be explained in Section 3.2, to obtain a calibration curve between the TOCN amount (in mg cm^{-2}) and the film thickness. Thicknesses in the range 2-20 μm were obtained for TOCN films/ TOCN layers, while the PLA substrate thickness was fixed and equal to 23 ± 1 μm.
The density of TOCN films was estimated from 7 films with surface (4.0 ± 0.2)cm^2. The thickness of each film was measured in three different areas and a mean value was considered for each film. Knowing the volume of each film and measuring its weight, the density of TOCN films was estimated to be (1.57 ± 0.06) g cm^{-3}.

3.2 Films optical characterization

Transmittance spectra of TOCN self-standing films in the UV-VIS region were acquired by a Varian Cary 5000 UV-Vis-NIR spectrophotometer operated in %T mode. For this purpose, film fragments were vertically fixed in the spectrophotometer cell compartment, perpendicularly to the beam path, and scanned in the range 190-900 nm with a 1 nm resolution.
The interference pattern created by light impinging and being reflected from the two faces of TOCN films was used to estimate the thickness of the film through the following formula (Poelman et al., 2003; Padera, 2013):

$$d = \frac{N(\lambda_1\lambda_2)}{2(\lambda_1-\lambda_2)}\frac{1}{\sqrt{n^2-(\sin\theta)^2}} \qquad \text{(Eq. 3.1)}$$

where d is the film thickness in nm, λ_1 and λ_2 the maximum and minimum wavelengths considered, N the number of fringes in the considered wavelength range, θ the light incident angle (equal to zero in our geometry) and n the film material refractive index (assumed to be constant in the examined wavelength range and equal to 1.58 (Nogi et al., 2005)).

3.3 Films structural characterization

The morphology of TOCN films and bilayered TOCN/PLA films was investigated by scanning electron microscopy (SEM). A first set of images was acquired using a FEI Quanta 200 scanning electron microscope operating at 2.5 kV accelerating voltage by the team of prof. Y. Golan at the Ben Gurion University of the Negev (Israel). Film fragments were sputter coated with an ultrathin layer of gold before measurements and cross sectional images were acquired by embedding the film fragments in a resin. A second set of samples were instead imaged using a JEOL JSM-7001F microscope operating at 2 kV by dr. N. Bazzanella at the IdEA Laboratory (University of Trento, Department of Physics). Also in this case, film samples were metalized.

3.4 Positron Annihilation Lifetime Spectroscopy measurements

Depth-profiled positron annihilation lifetime spectroscopy (PALS) measurements were performed with a pulsed low energy positron system apparatus at the high intensity positron source NEPOMUC (Hugenschmidt et al., 2008; Sperr et al., 2008) by prof. W. Egger and prof. T. Koschine from the ''Institut fur Angewandte Physik und Messtechnik'' (Munich University). The energy of the accelerated positrons was between 4 and 12 keV, corresponding to mean implantation depth values $\bar{x}$ between 27 and 1.4 × 10^3 nm as shown by the relation (Mills and Wilson, 1982):

$$\bar{x} = \frac{40}{\rho} E^{1.6} \qquad \text{(Eq. 3.2)}$$

where *E* is the positron implantation energy in keV and ρ TOCNs density, assumed equal to 1.5 g cm^{-3} (Sehaqui et al., 2011). The overall time resolution of the apparatus was 230-240 ps and the beam diameter was < 1 mm at all energies.

Lifetime spectra containing 4 × 10^6 counts were acquired, deconvolved and the resulting curves were decomposed in the sum of three exponential decay functions using the PATFIT package (Kirkegaard et al., 1989) (fit chi square around 1). The obtained lifetimes τ_i and intensities I_i give information about the positrons annihilation processes in the material. In particular, the longer relaxation time τ_3 and its relative intensity I_3 are related to the annihilation of *ortho*-positronium *o-Ps* (triplet state of the electron-positron bound state) entrapped in nanometric-sized regions of low electron density, such as voids, with surrounding electrons having opposite spin. This process, known as *pick-off* process, reduces *o-Ps* vacuum lifetime from around 125 ps to few nanoseconds and can be related to the size of the cavities where annihilation takes place (Eldrup et al., 1981; Tao, 1972). More into details, the intensities I_3 of the signal are proportional to the cavity number density, while the τ_3 values allow to evaluate their average size (Mallon, 2003; Consolati et al., 2010)

In the case of TOCNs, we assume the film voids to be formed by elongated cavities having TOCNs as walls and geometrically described as prisms with square cross section of size d_p and length $L=md_p$.

In this particular geometry, the τ_3 and d_p values are related by the following equation (Jasińska et al., 1996):

$$\tau_3^{-1} = \lambda_0 \left[1 - \left(\frac{d_p}{d_p+2\Delta R} + \frac{1}{\pi} sin \frac{\pi d_p}{d_p+2\Delta R} \right)^2 + \left(\frac{md_p}{md_p+2\Delta R} + \frac{1}{\pi} sin \frac{\pi md_p}{md_p+2\Delta R} \right) \right] \qquad \text{(Eq. 3.3)}$$

where $\lambda_0 \approx 0.5$ ns^{-1} is the *o-Ps* annihilation rate in the bulk state and ΔR = 0.166 nm the empirical electron layer thickness.

3.5 Gas Transport Measurements

To evaluate the transport of gas molecules through TOCN films, gas phase permeation tests were performed, using gases with different molecular sizes and condensation properties. In particular, dry nitrogen (N_2), carbon dioxyde (CO_2), helium (He) and deuterium ($^2H_2$) were considered. Measurements were performed also using ambient air at relative humidity values ranging from 20 to 50% (humidity was measured using a Delta Ohm HD2301 thermo-hygrometer). The tests were carried out on disc-shaped TOCN/PLA films (diameter around 1.3 cm) with different TOCN thicknesses in the range 2-12 µm and at sample temperature in the range 293-324 K. Before measurements, the films were outgassed by keeping them in high vacuum conditions for 12 hours.

Measurements were performed by colleagues from the IdeA team coordinated by prof. R. Checchetto of the Department of Physics (University of Trento) using a home-made apparatus (Checchetto et al., 1995). Briefly, at time t = 0 one side of the film (high pressure side: HPS) was exposed to the gas kept at fixed pressure and temperature. During the permeation process, gas molecules are absorbed by the film surface layers, diffuse through the film and are desorbed by the opposite side (low pressure side: LPS) in a high vacuum chamber (continuously pumped and with background pressure in the low 10^{-6} Pa order).

The partial pressure of the permeating gas $P_{LPS}(t)$ in the analysis chamber was measured as a function of time by a calibrated quadrupole mass spectrometer (QMS: Balzers QMG 420). In the considered experimental conditions, the permeation flux $J_{PERM}(t)$ can be calculated from pressure measurements through the following formula (Checchetto et al., 1995):

$$J_{perm}(t) = \frac{1}{A} S_P P_{LPS}(t) \qquad \text{(Eq. 3.4)}$$

where A is the surface area of the film and S_p is the pumping speed of the vacuum sysytem (in the 10^{-2} m^3 s^{-1} range, depending on the permeant gas).

The background pressure present in the analysis chamber, due to small leaks or outgassing effects from the chamber walls, was measured before each test (setting P_{HPS}=0) and then subtracted from the measured signal $P_{LPS}(t)$. The detection limit of the apparatus was related to the fluctuations of background partial pressure in the chamber and estimated to be $\delta J \sim 10^{-2} mL\ m^{-2}\ day^{-1}$.

Fig. 2.3 shows an example of the permeation curves obtained for PLA films (without TOCN coating) at T= 293 ± 1 K and P_{HPS} = (3.5 ± 0.1) × 10^4 Pa for different gases. As visible, the curves show an initial transient state, during which the permeation flux $J_{perm}(t)$ increases with time, and a subsequent stationary state, for which the flux is constant meaning that stationary transport conditions have been reached.

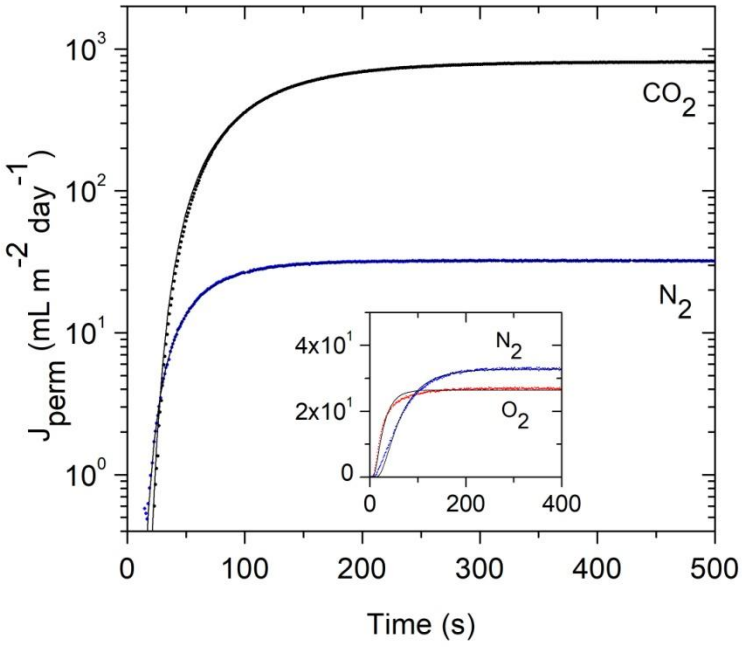

Fig.3.1 : Permeation curves for 23 ± 1 μm PLA films at T = 293 ± 1 °C and P_{HPS} = (3.5 ± 0.1) × 10^4 Pa using CO_2 and N_2 as testing gases. In the inset the permeation curves obtained using ambient air at RH = 37%, T = 293 ± 1 °C and P_{HPS} = (3.5 ± 0.1) × 10^4 Pa are reported. Points refer to experimental values, while the lines are numerical fits performed using Eq. 3.4.

The process of gas transport in polymers is controlled by the solution-diffusion mechanism (Yampolskii and Shantarovich, 2006) according to which the gas permeability ϕ can be expressed by the product of solubility S and diffusivity D in the film layers: ϕ= S*D. From the experimental permeation curves it is possible to determine the main gas transport parameters of the materials. In particular, the permeability value ϕ can be obtained from the permeation flux in stationary conditions (stc) using the following relation:

$$J_{perm}(stc) = D\frac{S\,P_{HPS} - SP_{LPS}}{d} \cong DS\frac{P_{HPS}}{d} \qquad \text{(Eq. 3.5)}$$

where *d* is the film thickness and SP_{HPS} and SP_{LPS} the concentrations of gas molecules dissolved in the high pressure side (HPS) and low pressure side (LPS) film layers respectively. We can assume $P_{HPS} \gg P_{LPS}$ because the analysis chamber is continuously pumped in our experimental conditions.

The gas diffusivity D can be instead determined from the temporal evolution of the permeation flux by fitting it with the following Eq 3.6, which is valid for planar geometry films with thickness *d* much smaller than the lateral size (Crank and Crank, 1979):

$$J_{perm}(t) = J_{perm}(stc)\left[1 + 2\sum_{n=1}^{\infty}(-1)^n \exp\left(-\frac{Dn^2\pi^2 t}{d^2}\right)\right] \qquad \text{(Eq. 3.6)}$$

CHAPTER 4
Results and Discussion

TOCNs films were obtained by a casting procedure, by which the crystallites self-arrange originating thin, transparent and flexible films. A first qualitative evaluation of our TOCN films showed an amazing stability: once formed, they are stable in water for months without losing their compact structure. Not even the energy supplied by ultrasonication (using an ultrasonic tip delivering 100 W output power at 20 kHz frequency in a 30-50 mL aqueous solution containing the TOCN film) enables to disrupt the densely packed TOCNs and re-disperse the crystallites, suggesting the presence of a strong network of weak interactions between TOCNs.

It is known that nanocellulose is able to assemble in films exhibiting high optical transparency and low gas permeability, thanks to their large aspect ratio and their ability to form intra- and inter- fibrillar hydrogen bonds (Moon et al., 2011). The results reported in this Chapter were obtained through measurements aimed at investigating this spontaneous self-organization of TOCNs in absence of water. The first part of the Chapter (Section 4.1), in particular, concerns the structural characterization of pure TOCN films through optical measurements, microscopy techniques and PALS analysis with the purpose of better understanding the arrangement of TOCNs and the structures created as a consequence of the casting and drying process. Section 4.2, instead, is focused on TOCN/PLA films, where PLA was used as a substrate to enable gas permeation studies. Also in this case, the aim was (more than the practical possible exploitation of TOCN/PLA films as gas barrier films) the extrapolation of important structural information from permeation studies. Finally, in Section 4.3, the possibility of forming hybrid nanocomposite TOCN-TiO_2 films is briefly shown.

4.1 TOCN films

4.1.1 Optical and morphological characterization

The transparency of TOCN films to nearUV-Vis radiation can be seen in Fig. 4.1a, both from the film picture shown in the inset and, in a more quantitative manner, from the reported UV-Vis spectrum of a 12 μm thick film fragment. In particular, the light transmittance is almost zero in the low UV range and gradually increases: at 300 nm transmittance is around 85%, while at 600nm more than 90% of light is transmitted, in agreement with literature data (Shimizu et al., 2014).

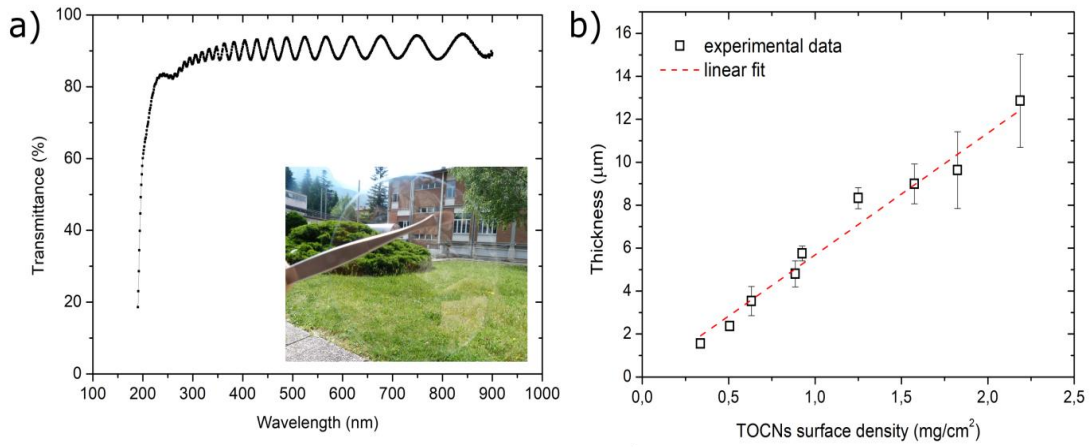

Fig. 4.1: (a) Transmittance spectrum of a TOCN film, showing the high transparency of the material in the Vis-nearUV range and the interference fringes, from which the thickness of the films can be estimated. In the inset a picture of a transparent, self-standing TOCN film is reported. (b) Calibration curve for the evaluation of film thickness knowing the amount of TOCNs casted. Thicknesses were estimated from transmittance spectra and the error bars are the SD over different measurements on different fragments of the same film, to account for thickness inhomogeneity. The red dotted line is a linear fit of the experimental data.

The interference fringes visible in the spectrum are due to the reflection and refraction of light impinging on the air/film interfaces and allow to estimate the film thickness through Eq. 3.1 (Poelman and Smet, 2003). To account for the fact that film thickness is not perfectly uniform because of the casting procedure, different spectra were acquired on different fragments of the same film and the standard deviation (SD) of the thicknesses estimated from the spectra for each fragment was calculated. The resulting uncertainty on TOCN film thickness, due to film inhomogeneity, was estimated to be between 5% and 15%. The accuracy of the method was demonstrated by (Bettotti et al., 2016) comparing the film thickness calculated through transmittance spectra with SEM cross section measurements.
Starting from transmittance spectra of films obtained casting different known volumes of TOCNs solutions on a 20 cm^2 surface Petri dish, a calibration curve was obtained to directly relate films thickness to the amount of casted TOCN solution. The results are reported in Fig. 4.1b, where the red dotted line is a linear fit of experimental data with intercept fixed to zero. The proportionality constant between film thickness in μm and TOCN surface density in mg/cm^2 resulted equal to 5.7 ± 0.3 μm/(mg cm^{-2}).
In Fig. 4.2, the transmittance values of TOCN films in the visible and UV regions (at 600 and 300 nm respectively) as a function of film thickness are reported. Light transmittance values are around 90% even for films thicker than 10 μm, while

transmittance in the UV region slightly decreases from (88.2 ± 0.1)% to (70 ± 3)% increasing the thickness from (1.6 ± 0.2) µm to (13 ± 2) µm.

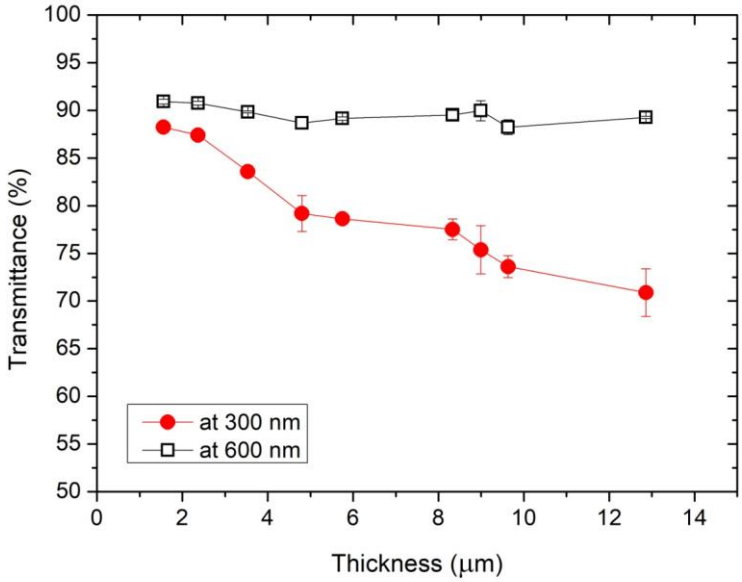

Fig. 4.2: Transmittance values at 300 nm and 600 nm for TOCN films as a function of film thickness. Experimental values and indetermination are the average value and SD of at least four measurements. Indetermination on thickness due to samples inhomogeneity was estimated to be between 5% and 15%.

Starting from the transmittance values for different film thicknesses, and assuming that the film-air interface causes negligible light scattering, it is possible to estimate the optical absorption coefficient α through Lambert's law (Young, 2000):

$$I \sim I_0(1-R)^2 \exp(-\propto d) \qquad \text{(Eq. 4.1)}$$

where *I* is the intensity of transmitted light, I_0 the intensity of the incident beam, *d* the thickness of the TOCN film, *R* the reflectivity (for normal incidence of the light beam) and α the optical absorption coefficient. Considering that the measured transmittance values are defined as $\%T = 100\, I/I_0$, the coefficients α and *R* can be determined from the slope and intercept of the straight lines, which best fit the values of the $\ln\left(\frac{100}{\%T}\right)$ versus thickness *d* curves, respectively. The obtained values are reported in Table 4.1.

The estimated reflectivity value is in agreement with that resulting from Fresnel equation for normal incidence (R ≈ 0.05) and assuming a refractive index equal to that of pure cellulose:

$$R = \left|\frac{n_1 - n_2}{n_1 + n_2}\right|^2 \qquad \text{(Eq. 4.2)}$$

where n_1= 1 and n_2= 1.58 are the refractive indexes of air and cellulose respectively (Nogi et al., 2005). The fact that the refractive index of pure cellulose can be used

for TOCN films as well, suggests that the porosity of the films is very low. Moreover, the absence of scattering effects and the transparency of the material suggest the absence of specific structures like fibrils aggregates.

Table 4.1: Optical absorption coefficient α and reflectivity R of TOCN films as estimated from transmittance spectra at different film thicknesses and exploiting Lambert's law (Eq.4.1).

	at 300nm	at 600nm
α (μm^{-1})	$(25 \pm 1) \times 10^{-3}$	$(1{,}0 \pm 0{,}4) \times 10^{-3}$
R	$(4{,}2 \pm 0{,}2) \times 10^{-2}$	$(5{,}0 \pm 0{,}2) \times 10^{-2}$

The dense network structure of TOCN films is confirmed by microscopy. Fig. 4.3a and Fig 4.3b are respectively an AFM and a SEM image of the surface of a film. From the figures it is possible to see that the nanocrystallites are oriented in a dense random network, with their long axis parallel to the film surface, originating an uniform morphology.

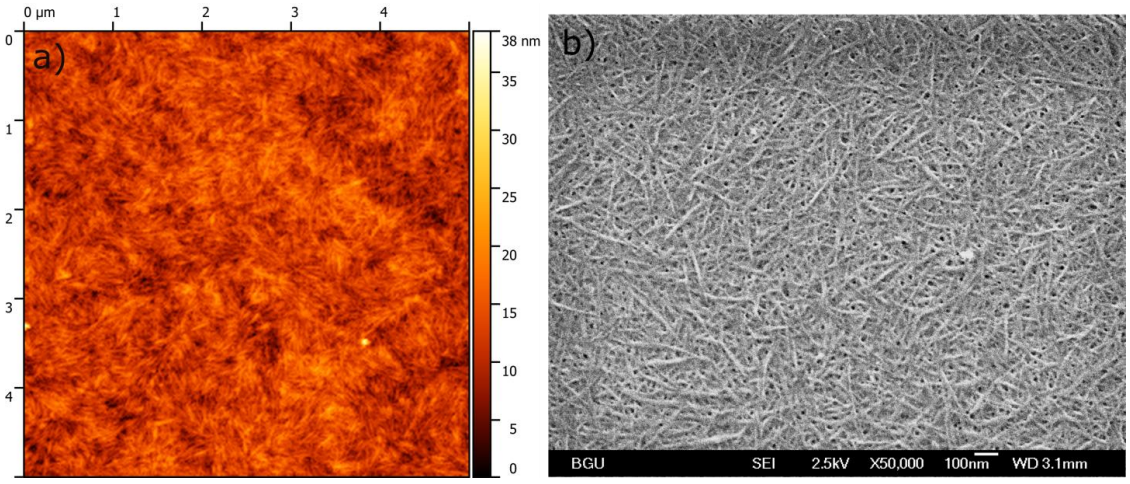

Fig. 4.3: Surface morphology of TOCN films. (a) AFM image, (b) SEM image

4.1.2 PALS analysis

The results of depth-profiled positron annihilation lifetime spectroscopy (PALS) performed on TOCN films are reported in Fig. 4.4, which shows the lifetime τ_3 and Intensity I_3 of the annihilation signal coming from *o-Ps* entrapped in the film voids as a function of the positrons mean implantation depth.

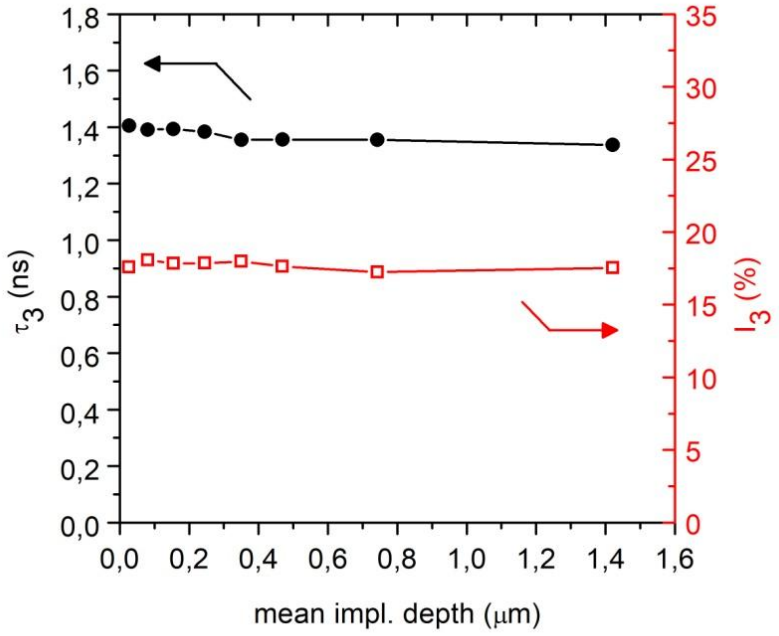

Fig. 4.4: (a) Lifetime τ_3 (black, filled circles, left axis) and intensity I_3 (red, empty squares, right axis) of the *o-Ps* annihilation signal obtained from PALS spectra measurements on TOCN films as a function of positrons mean implantation depth.

As explained in Chapter 3, τ_3 is related to the average size of the voids: the smaller the cavity volume, the shorter the lifetime τ_3. I_3 is related instead to their density number, that is to the number of voids per unit of volume. We can observe that both τ_3 and I_3 are constant and with average values of 1.37 ± 0.02 ns and 17.7 ± 0.3 % respectively. The fact that these values do not depend on the implantation depth suggests that the cavities present in the TOCN film have an uniform size and are distributed with constant concentration in the film.

Several models exist to predict the cavity dimensions from the obtained τ_3 values knowing the shape of the holes (Mallon, 2003; Consolati et al., 2010). Here, we assumed that the voids in the films are represented by elongated cavities between TOCNs, having the packed crystallites as walls, and can be geometrically described as prisms with square cross section of size d_p and length $L = md_p$. Fig. 4.5 reports the d_p values, obtained from the mean τ_3 value (1.37 ± 0.02 ns) through Eq. 3.3 and assuming the just explained cavity geometry (schematically shown in the figure inset), as a function of the *m* value, which is the ratio between cavity length and section.

It is possible to observe that, when the cavity length is a factor 5 larger than its cross sectional size (m=5), a saturation value is obtained for the section $d_p \approx 0.31$ nm. For our TOCN films and in the geometrical model of prism-shaped cavities, the condition $m > 5$ can be considered fully satisfied as the cavity length *L* is of the same order of the TOCN length, which is around some hundred nanometers (as seen in Section 2.3.1).

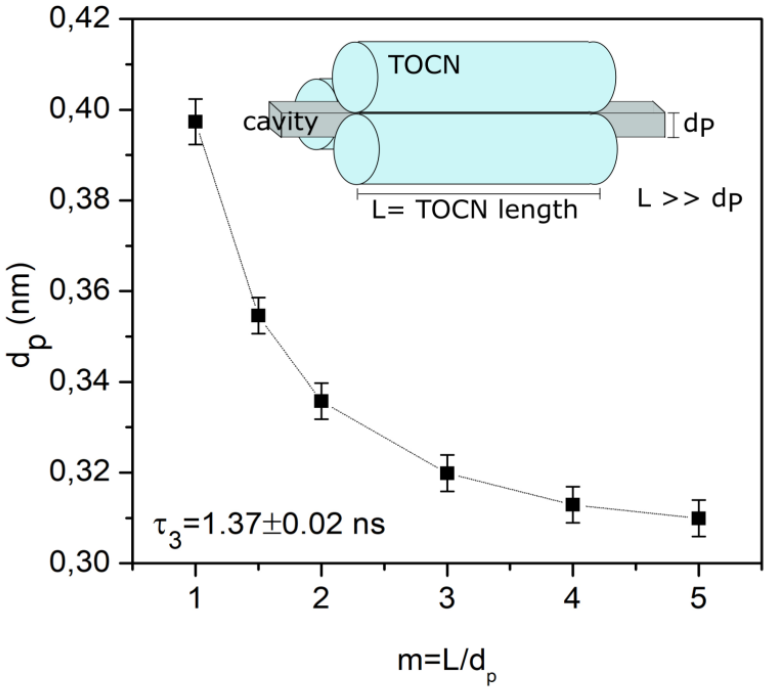

Fig. 4.5: Cavity section dimension d_p obtained from PALS measurements, assuming a mean τ_3 value equal to 1.37 ns and exploiting Eq. 3.3, as a function of the ratio m between cavity length and cross section dimension. In the inset a sketch of the assumed cavity geometry is shown.

The cavity dimension value estimated through PALS analysis strengthens and confirms the hypothesis, supported also by optical measurements and microscopy images, of TOCN films being formed by a densely packed network of nanocrystals, strongly interacting among them and letting only tiny holes (0.31 nm) in between.

4.2 TOCN/PLA films

TOCN/PLA films were prepared by coating PLA disks (thickness 23 ± 1 μm and diameter 3 cm) with few micron thick TOCN layers.

4.2.1. Optical and SEM characterization

The UV-Vis spectra of both uncoated PLA and a TOCN/PLA film are reported in Fig. 4.6a, while Fig. 4.6b shows the transmission values at two selected wavelengths as a function of the TOCN coating thickness. As visible in Figure 4.6 the transmittance of pure PLA is around 95% at 600 nm and around 86% and 300 nm. These values are slightly reduced by the presence of TOCN layer but remain higher than 87% and

73% for TOCN coatings up to 13 μm. Moreover, the transmittance values are coherent with those obtained for pure TOCN films (reported in Fig. 4.6b as empty squares and circles).

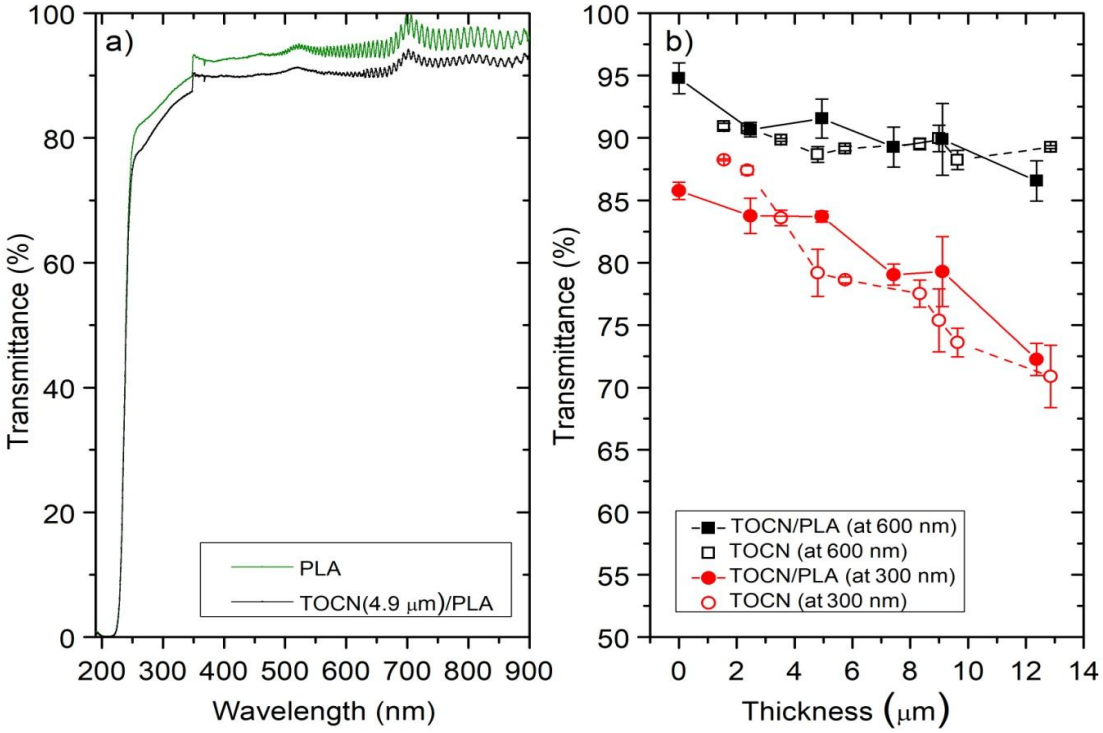

Fig. 4.6: (a) UV-Vis spectra of a 23±1 μm thick PLA film (green line) and a 23±1 μm thick PLA film covered with a 4.9±0.5 μm thick TOCN layer. (b) Transmittance values of TOCN/PLA films in the UV (at 300 nm wavelength) and visible (at 600 nm wavelength) regions as a function of TOCN coating thickness. As a comparison the values obtained for pure TOCN films are reported too (empty symbols). Values and uncertainty are respectively the mean values and SD over at least 4 measurements on different areas of the same sample.

The structure and morphology of TOCN/PLA films were investigated by SEM microscopy. Some representative images are reported in Fig. 4.7. In particular, panel (a) shows a cross-sectional view of the TOCN/PLA double layer, while panel (b) reports images of the TOCN coating. For cross-section observations, the samples were freezed-cut in liquid nitrogen. As visible in figure, the film surface has a uniform morphology, without cracks or defects. Moreover, the TOCN coating appears to be formed by layers of cellulose nanocrystals, which are not 3D entangled but preferentially aligned one parallel to another with the main axis parallel to the film surface. This is more evident observing the inset of Fig. 4.7b, which allows to distinguish individual TOCNs and their assembly.

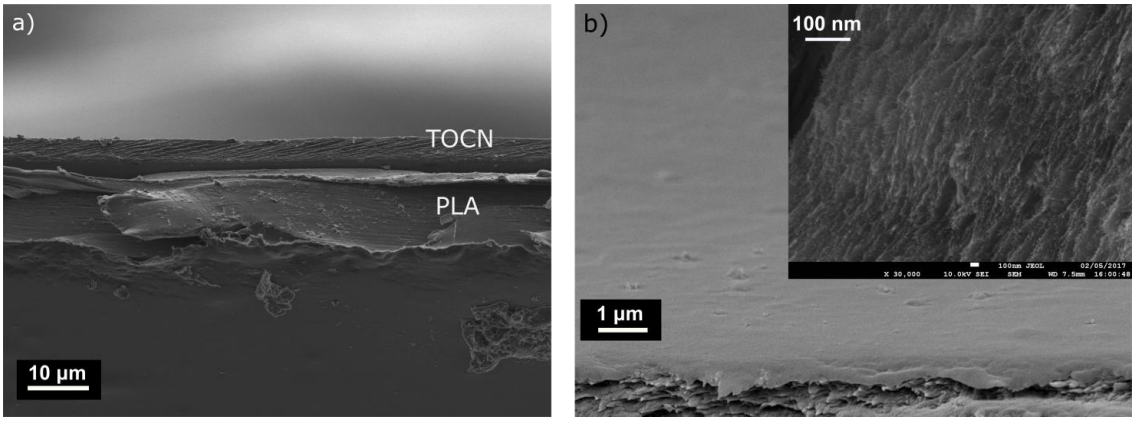

Fig. 4.7: SEM images of TOCN/PLA films. (a) Cross sectional image enabling to distinguish the PLA substrate and TOCN coating, (b) Surface and the cross section view of TOCN coating, showing the assembly of TOCNs in a layer by layer structure. In the inset a more magnified image is reported, enabling to distinguish the alignment of individual TOCNs parallel to each other and with the main axis parallel to the film surface.

4.2.2 Permeation tests

The morphological characterization suggests that the tight packing of the TOCNs could give gas barrier properties to the films. Some literature works already studied the permeability of nanocellulose films (Aulin et al., 2010; Fukuzumi et al., 2009; Rodionova et al., 2011; Syverud and Stenius, 2009) and showed that the gas barrier performances of the films strongly depend not only on the kind of penetrant molecules (Fukuzumi et al., 2011) but also on structural factors of the starting cellulose nanofibrils/nanocrystals material, such as fibril entanglement (Belbekhouche et al., 2011), surface functionalization (Fukuzumi et al., 2013a) and length (Fukuzumi et al., 2013b).
Here we used TOCN/PLA films to evaluate the gas permeability of TOCN films to CO_2, N_2, $^2H_2$ He gases and ambient air and to investigate their gas transport kinetics. Permeation tests were performed at fixed PLA substrate thickness (23 ± 1 µm), and TOCN coating thicknesses in the range 2.6-6.5 µm. PLA was used as substrate for its renewability and biodegradability. Indeed, it is commonly considered a promising alternative to petroleum-based materials in packaging applications and several literature works have already reported its use as substrate for the deposition of thin coatings with gas-barrier properties by both solvent-casting (Fukuzumi et al., 2009) or layer-by-layer deposition techniques (Aulin et al., 2013a, 2013b; Laufer et al., 2012).

Using CO_2, N_2 and ambient air (at different relative humidity values) as test gases, no permeation signal was detected in hours-lasting experiments performed at T= 293 K and pressures P_{HPS} up to 10^5 Pa, meaning that the permeation flux was lower

than the detection limit of the experimental apparatus (around 10^{-2} mL m^{-2} day^{-1}). Under these conditions, and assuming that the gas barrier properties of the double-layer film can be attributed only to the TOCN coating (with thickness *d*), we can evaluate an upper limit for the gas permeability through the equation:

$$\Phi_{max} = J_{perm}(stc) \cdot d/P_{HPS} \quad \text{(Eq. 4.3)}$$

Using P_{HPS} = 10^5 Pa and *d* ≈ 1 μm, it results Φ_{max} ≈ 10^{-4} mL μm m^{-2} day^{-1} kPa^{-1}.
This value is orders of magnitude lower than the oxygen permeability values reported by Aulin *et. al.* (Aulin et al., 2013a, 2013b) studying the gas barrier properties of multilayer thin films of anionic nanofibrillated cellulose and cationic polyethyleneimine(PEI) deposited on PLA substrates by a layer-by-layer procedure. The significantly reduced permeability observed in our experiments could be related to the different NC production method, which produces a NC material with different dimensions and assembly properties. Indeed, the nanofibrillated cellulose used by Aulin *et al.* is obtained by a carboxymethylation reaction followed by a mechanical treatment through an high pressure homogenizer and shows both higher dimensions (diameter and length of the nanofibers) and lower carboxylic content with respect to TOCNs. Carboxyl groups have a double hydrogen bonding possibility. It is expected that the presence of a stronger hydrogen bond network, together with the smaller dimensions of TOCNs, lead to an increased capability of the impermeable TOCN crystallites to organize in densely packed film structures, leading to smaller void volumes between them and thus to a decreased capability of gas molecules to permeate through the films.

The permeation curves obtained using test gases with smaller kinetic diameters are reported in Fig. 4.8. In particular panel (a) refers to deuterium $^2H_2$ and panel (b) to helium He. In both cases the flux for a TOCN/PLA film with TOCN coating thickness 6.5 μm is compared with the flux measured for pure PLA (without TOCN coating). It is possible to observe that few micrometers thick TOCN coatings reduce the permeation flux in stationary transport conditions by at least 3 orders of magnitude for both deuterium and helium gases. Moreover, the presence of TOCN coatings slow down the kinetics: while in the case of pure PLA stationary transport conditions are reached in 1-2 seconds, in the case of TOCN/PLA films longer times are required (around 30 s for He and 15 min for deuterium).
The transient time interval increases and the value of the permeation flux in stationary conditions decreases increasing the TOCN coating thickness, as shown in Fig. 4.9 for the case of deuterium at T= 301 ± 2 K.

Figures 4.8 and 4.9 allow to say that the transport properties of TOCN/PLA films are determined by the TOCN coating both in the transient and stationary conditions and that the PLA layer only acts as permeable mechanical support. For this reason we

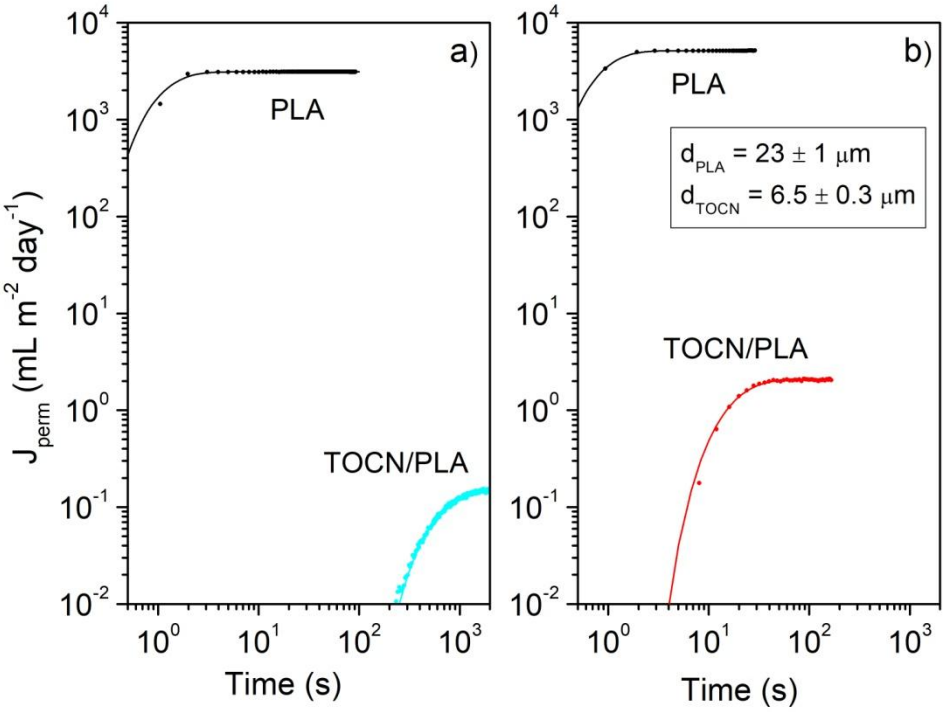

Fig. 4.8: Permeation curves of pure PLA (23±1 μm thick) and TOCN/PLA films (TOCN coating 6.5±0.3 μm thick) for (a) deuterium $^2H_2$ and (b) helium He testing gases. Points are experimental values, while lines are fits of the experimental values according to Eq. 3.6. Measurements were performed at T = 301 ± 2 K and P_{HPS} = (3.5 ± 0.1) × 10^4 Pa.

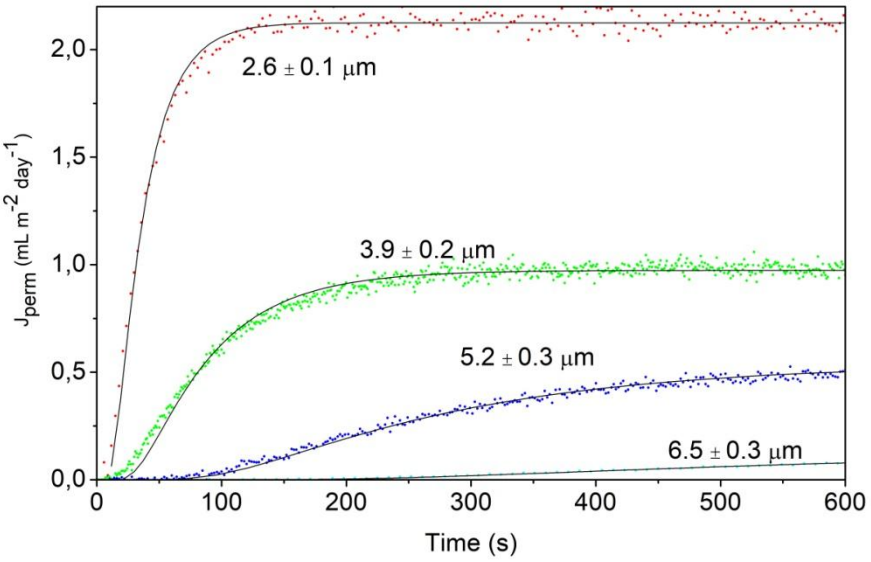

Fig. 4.9: Permeation curves of TOCN/PLA films for different thicknesses of the TOCN coating layer (in the range 2.6-6.5 μm). Points are experimental values, while continuous lines are fits of the experimental values according to Eq. 3.6. Measurements were performed at T = 301 ± 2 K and P_{HPS} = (3.5 ± 0.1) × 10^4 Pa.

used the experimental curves obtained for TOCN/PLA films together with Eq. 3.5 and Eq. 3.6 to evaluate the penetrant transport parameters of TOCN layers. The results in terms of permeability ϕ and diffusivity *D* (averaged over the different TOCN thicknesses samples measured at ambient T) are reported in Table 4.2 and compared with those obtained for the PLA substrate. The solubility S was estimated from the equation $S = \phi/D$ and the obtained values are reported in Table 4.2 too. As a comparison, the vacuum solubility of a perfect gas at standard temperature is equal to $S_{vac} = \frac{n}{PV} = \frac{1}{RT} = 1\ mL\ cm^{-3} atm^{-1}$.

Table 4.2: Permeability ϕ, Diffusivity *D* and Solubility S of PLA (23±1 μm thick) and TOCN/PLA films (TOCN coating layer thickness in the range 2.6-6.5 μm) estimated from deuterium ($^2H_2$) and helium (He) permeation curves at T = 301 ± 2 K and P_{HPS} = (3.5 ± 0.1) × 10^4 Pa.

	Deuterium $^2H_2$		Helium He	
	PLA	TOCN/PLA	PLA	TOCN/PLA
$\phi\ \left(\frac{mL\ \mu m}{m^2\ day\ kPa}\right)$	(2.01 ± 0.06) × 10^3	0.10 ± 0.03	(2.6 ± 0.1) × 10^3	0.4 ± 0.1
D ($cm^2\ s^{-1}$)	(7 ± 3) × 10^{-7}	(2.2 ± 0.4) × 10^{-10}	≈ 10^{-6}	(4.3 ± 0.8) × 10^{-9}
$S\ \left(\frac{mL}{cm^3 atm}\right)$	(3 ± 1) × 10^{-5}	(5 ± 3) × 10^{-3}	≈ 10^{-5}	(0.9 ± 0.4) × 10^{-3}

The permeability values obtained for $^2H_2$ are two orders of magnitude lower than those reported in literature for membranes composed by cellulose nanocrystals obtained from acid hydrolysis (Bayer et al., 2016) and comparable to those reported for films made using TEMPO-oxidized cellulose nanofibers (Fukuzumi et al., 2013a). Their permeability values for O_2, CO_2 and N_2 are however slightly larger than those obtained with our samples, probably because of different preparation procedures leading to different packing conditions. Indeed, the process of nanocellulose coalescence during drying strongly affects the structure of the material (Klemm et al., 2011; Müller et al., 2014; Ul-Islam et al., 2013), even if the process is not fully understood as a number of different effects can contribute to it (Pönni et al., 2012). The main difference between our TOCN preparation procedure and those reported in literature is that we neutralize the oxidized fibrils solution by thoroughly washing it instead of adding HCl. This leads to a reduced presence of ions between the TOCNs and thus to a decreased shielding of their partial charges. Moreover, it avoids the formation of salt aggregates during the drying. All these facts can favor TOCNs coalescence and the formation of a planar, parallel and dense arrangement enhancing the gas barrier properties.

The comparison between the measured gas transport parameters D and S for TOCN coatings and those reported in literature for commercial polymers used for gas barrier applications suggests that TOCN films act as diffusive barriers for penetrant gas molecules. In fact, the measured $^2H_2$ solubility is similar to those reported for PET, PS or PVA films (around $10^{-2}\ mL\ cm^{-3} atm^{-1}$ (Paterson et al., 1999)), while the diffusivity is orders of magnitude lower (being D around 10^{-7} cm^2 s^{-1} for PET and around 10^{-5} cm^2 s^{-1} for Teflon (Alentiev et al., 2002)).

4.3 Hybrid TOCN-TiO_2 films

In this last Section, I will briefly report some results regarding the possibility of forming hybrid nanocomposite film combining TOCNs with inorganic materials. In particular, we studied TOCN-TiO_2 films and double-layered TOCN-TiO_2/PLA films, obtained dispersing TiO_2 nanoparticles (25 nm in diameter, combination of rutile and anatase crystal structure) in TOCN solutions to a weight ratio 1:20 between TiO_2 and TOCNs and casting them in Petri dishes or on PLA disks. The interest on TiO_2 nanoparticles is related to their antimicrobial properties, as, when they are irradiated with UV light, they produce reactive oxygen species able to kill microorganisms (He and Hwang, 2016; Rhim et al., 2013).
Fig. 4.10a and Fig. 4.10b report two SEM images respectively of the surface and cross section of a TOCN-TiO_2 film. Observing panel (a), it appears that the surface morphology of the film is uniform and without cracks or imperfections, even if TiO_2 nanoparticles agglomerates are clearly visible. Moreover, the cross-sectional view (panel b) enables to distinguish both TOCNs, aligned to each other and with the main axis parallel to the film surface, and TiO_2 nanoparticles agglomerates, which interrupt the TOCN layers.

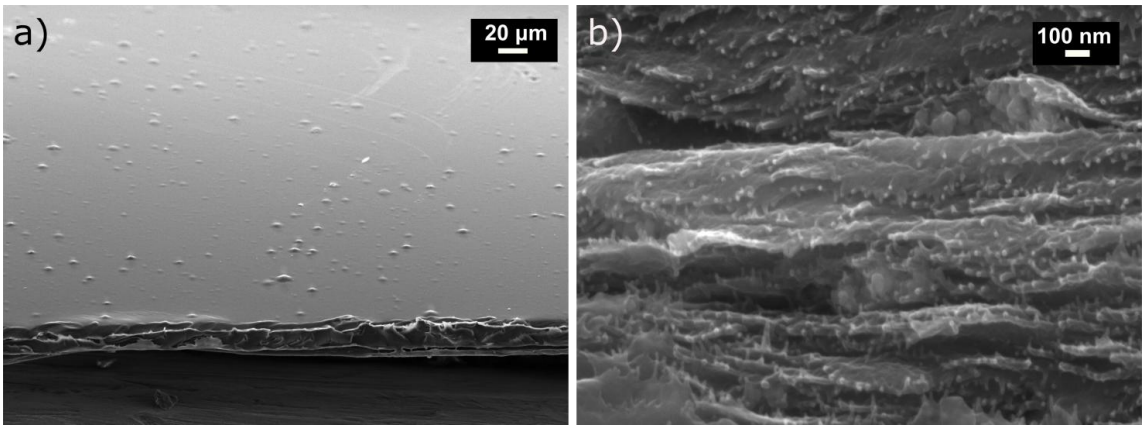

Fig. 4.10: SEM images of hybrid TOCN-TiO_2 films. (a) Surface image showing the uniform morphology of the film and the presence of TiO_2 agglomerates. (b) Cross-sectional view enabling to distinguish both individual TOCNs and TiO_2 agglomerates.

In Fig. 4.11 the results of an optical characterization of TOCN-TiO_2 films are reported. In particular, Panel (a) compares the UV-Vis spectrum of a 2.5 μm thick TOCN-TiO_2 film with the spectrum of a same-thickness pure TOCN film. It can be seen that the transmission is reduced by the dispersion of TiO_2 nanoparticles both in the UV and visible region. The reduction in the UV range can be attributed to the absorption of UV light from TiO_2 nanoparticles, which have a bandgap at 3.0-3.2 eV (Chen and Mao, 2007). The decreased transmission in the Visible range, instead, can be ascribed to light scattering effects due to the presence of TiO_2 agglomerates, as seen also in the SEM image (Fig. 4.10b). Aeroxide nanoparticles usually produce quite stable water dispersions (EVONIK Industries, 2015), however agglomeration takes place at pH near neutrality and at high nanoparticle concentration (like during the casting process), which enhances the collision frequency (Suttiponparnit et al., 2010). In our experimental conditions, only small particle clusters were observed, however agglomeration could be further reduced by using nanoparticles with different morphologies (such as TiO_2 small size nanotubes, which are expected to present a more hydrophilic character on their surface (Zennaro et al., 2013)) or by introducing functional groups on the TiO_2 surface.

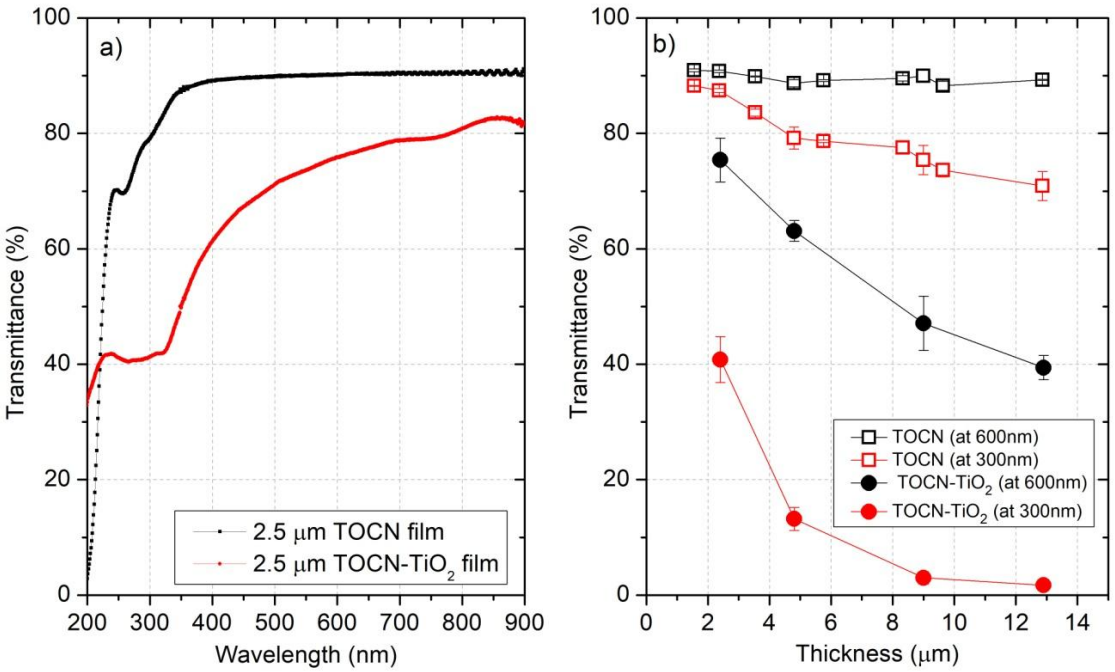

Fig. 4.11: Optical characterization of TOCN-TiO_2 films. (a) UV-Vis spectra of a pure TOCN film and of a hybrid TOCN-TiO_2 film. As visible, the transmission is reduced by the presence of TiO_2 nanoparticles both in the UV and visible region. (b) Comparison between the transmittance values of pure TOCN films and TOCN-TiO_2 films in the UV (at 300nm) and visible (at 600nm) region as a function of film thickness. Measurements were repeated at least on 4 different film fragments and the reported values and error bars are the obtained mean values and SD, respectively.

Panel (b) shows the transmittance of pure TOCN films and hybrid TOCN-TiO_2 films in the UV (at 300nm) and visible (at 600nm) region as a function of film thickness. Increasing film thickness, the transmission is decreased both in the UV and visible regions, in a more marked extent for TOCN-TiO_2 films with respect to pure TOCN films. Indeed, it becomes almost zero at 300 nm for a 13 μm thickness in the case of TOCN-TiO_2 films, while remaining higher than 70% in the case of TOCN films.

4.4 Conclusions

In this Chapter the self-arrangement of TOCN crystallites in absence of water was studied and the structure of the thin, transparent and flexible films obtained by the casting of TOCN solutions was investigated.

1) The structural characterization of pure, self-standing TOCN films (Section 4.1) showed that nanocellulose crystallites are arranged in highly packed layered structures. The low porosity of the films was suggested by both optical measurements and microscopy observations. Moreover, PALS analysis enabled to estimate the dimensions of the cavities present in TOCN films, confirming the fact that, in absence of water competitor for hydrogen bonds, TOCNs strongly interact among them and assemble in dense networks leaving only tiny holes (0.31 nm).

2) The dense structure of TOCN films is at the origin of the gas barrier properties of TOCN coatings for CO_2, N_2 and O_2 gases and their selective transport of $^2H_2$ and He, described in Subsection 4.2.
   As cellulose nanocrystals are gas-impermeable, the only way for gas molecules to diffuse through the TOCN layers is migrating through empty regions between the crystallites. The observed selective transport is in agreement with the results of PALS analysis, from which the cross section size of the cavities was estimated to be around 0.31 nm. In fact, the obtained cavity size value is comparable with the kinetic diameters of deuterium and helium molecules, but smaller than those of CO_2, N_2 and O_2 suggesting that the selective transport properties of TOCN coatings are due to a size-sieving effect.

3) Finally, in Subsection 4.3, the possibility of combining TOCNs with inorganic materials, like TiO_2 nanoparticles, to obtain hybrid nanocomposite films was briefly explored. Hybrid TOCN-TiO_2 films with tunable thicknesses were successfully prepared. They showed an uniform surface morphology and

very low transmission values in the UV region. The presence of particles clusters, due to the agglomeration of TiO_2 nanoparticles, was directly observed in SEM images and indirectly suggested by the reduced transmittance measured in the visible region.

PART 2

TEMPO-oxidized Cellulose Nanocrystals Hydrogels

CHAPTER 5:
Materials and Methods for TOCN hydrogels

In this section I report the different techniques used to characterize TOCN hydrogels. In particular the first section focuses on the experimental techniques exploited to characterize the bulk sol-gel transition of TOCN aqueous solution as a consequence of sonication and salt addition. The second section, concerns the methods utilized to study the ionotropic gelation of TOCN as a consequence of Ca^{2+} diffusion and to control the gelation process obtaining TOCN-Ca^{2+} hydrogel structures with tunable sizes and shapes. Finally the third section reports the experimental techniques used to investigate the toxicity of TOCN hydrogels. The results of the measurements explained in Section 5.1, Section 5.2 and Section 5.3 will be reported respectively in Chapter 6, Chapter 7 and Chapter 8.

All the TOCN hydrogels studied in this PART 2 are obtained starting from aqueous solutions of NC crystallites (TOCNs) obtained from TEMPO-mediated oxidation as explained in Chapter 2.

5.1 TOCN sol-gel transition

The role of sonication treatment and salt addition on the formation of TOCN hydrogels starting from TOCNs aqueous suspensions was investigated combining rheology, microscopy and spectroscopy (UV-Vis, SAXS and NMR). Sonication was performed using an ultrasonic homogenizer (HD2200 Bandelin Sonoplus, Berlin, Germany) equipped with a 13 mm titanium tip. An output power of W_{eff} = 160W was delivered in 40 mL of TOCNs suspensions for a variable time. Salt addition was performed by simply adding a known volume of multivalent 1M salt solution (NaCl, $CaCl_2$, $AlCl_3$) to a known volume of TOCNs solution and hand-shaking them.

SAXS measurements were performed by collaborators at the Department of Materials Engineering of the Ben Gurion University of the Negev (Israel), while Rheological and NMR tests were carried out by prof. M. Grassi's group at the Department of Engineering and Architecture (University of Trieste).

5.1.1 UV-Vis Spectroscopy

A Varian Cary 5000 UV-VIS-NIR spectrophotometer was used to acquire the transmittance spectra of TOCNs suspensions after different sonication times. The suspensions were placed in a 1 cm optical path cuvette and scanned in the range 200-800 nm with a 1 nm resolution. The signal of the empty cuvette was used as baseline correction.

5.1.2 SAXS Spectroscopy

SAXS measurements on TOCNs hydrogels were performed using a SAXSLAB GANESHA 300-XL. Cu Kα radiation was generated by a Genix 3D Cusource with integrated Monochromator, 3 pinholes collimation and two-dimensional Pilatus 300K detector. The scattering intensity was recorded in the interval $0.003 < q < 0.21$ $Å^{-1}$. Measurements were performed under vacuum at ambient temperature. The scattering curves were corrected for counting time and sample absorption. The gel under study were placed in stainless steel sample cells with entrance and exit window made of mica. The scattered intensity I(q) was modeled as the sum of an exponential decay at low-q values plus a lorentzian term at high q-values:

$$I(q) = I_G(0)exp\left(-\frac{q^2\Xi^2}{2}\right) + \frac{I_L(0)}{(1+q^2\xi^2)} \qquad \text{(Eq. 5.1)}$$

where $I_G(0)$ and $I_L(0)$ are the scaling factors for each of the two terms, while Ξ and ξ are respectively the static and dynamic correlation lengths. This model, assumed to be valid for gel structures, is known as Gauss-Lorentz Gel Model (Evmenenko et al., 2001) and attributes the static correlation length to the 'frozen-in' crosslinks of some gels and the dynamic correlation length to the fluctuating polymer chains between crosslinks.

5.1.3 NMR Spectroscopy

The interaction between water and the three-dimensional network of TOCNs hydrogels was investigated by Low-field ^{1}H-NMR, measuring the response of water proton spin to a magnetic excitation. In particular, the water proton transverse relaxation rate T_2^{-1} (and relaxation time $T_2 = 1/T_2^{-1}$) was measured using a Bruker Minispec mq20, operating at 20.1 MHz that is at $B_0 \approx 0.47$T for ^{1}H Larmor precession frequency (Karlsruhe, Germany). CPMG (Carr-Purcell-Meiboom-Gill) pulse sequence $\{90°[-\tau-180°-\tau(echo)]_n-T_R\}$, with a 8.36 μs wide 90° pulse, τ=250 μs and the sequence repetition rate T_R equal to 5 s, was used. The result of the measurement is a transient signal known as Free Induction Decay (FID) (Atta-Ur-Rahman, 1986). The

number of repetitions n (approximately equal to 700) was chosen in such a way to ensure that the final signal FID intensity was about 2% of the initial FID intensity.
In the simplest situation, the relaxation process can be modeled by a single exponential decay and thus characterized by only one value of T_2^{-1}. However, in general, and in particular for water entrapped in porous materials like hydrogels, more than one relaxation time is required to describe the process, as the T_2^{-1} depends on the environment surrounding the protons (Vanhamme et al., 2001). In such a way, LF-NMR analysis on hydrogel samples allows to distinguish different states of water, i.e. free water or water trapped in meshes of different sizes and interacting with the hydrogel solid components.
To obtain the so-called discrete relaxation times spectrum of the sample, represented by m couples (A_i, T_{2i}), the experimental FID time decay was fitted by a sum of exponential decays (Chui et al., 1995):

$$I(t) = \sum_{i=1}^{m} A_i e^{-\frac{t}{T_{2i}}} \qquad \text{(Eq. 5.2)}$$

where t is time, T_{2i} relaxation time and A_i is an amplitude factor proportional to the number of protons relaxing with relaxation time T_{2i}. The number of exponentials m was determined by minimizing the product χ^{2*} (2m), where χ^2 is the sum of the squared errors and m represents the number of fitting parameters of Eq. 5.2 (Draper and Smith, 1966).

5.1.4 Rheology Measurements

Rheology is the science that studies the deformation and flow of matter in real systems and tries to correlate the observed stress-strain relationships with the structural properties of the material (Lapasin and Pricl, 1995).
Rheology measurements were performed using a stress controlled rotational rheometer (Haake Mars Rheometer, 379-0200 Thermo Electron GmbH, Karlsruhe, Germany) equipped by parallel plate geometry (C35/1° phi=35mm) The gap was fixed at 0.5mm. Three kinds of measurements were performed on hydrogel samples: stress sweep tests (SS), frequency sweep tests (FS) and steady value tests (SV).
In stress sweep tests a sinusoidal deformation, characterized by an increasing deformation γ_0 and a constant frequency f or pulsation ω, is applied to the sample: $\gamma = \gamma_0 \sin(\omega t)$. In order to have such a sinusoidal deformation it is necessary to apply the following sinusoidal stress field:

$$\tau = \tau_0 cos\delta \sin(\omega t) + \tau_0 sin\delta \cos(\omega t) = G' \gamma_0 \sin(\omega t) + G'' \gamma_0 \cos(\omega t) \qquad \text{(Eq. 5.3)}$$

where τ_0 is the maximum stress, δ the loss angle between stress and deformation, G' the elastic or storage modulus, connected to the elastic energy stored in the material, and G'' the loss or viscous modulus, related to the energy dissipated due to internal friction. In our case, stress sweep tests were performed in the range 0.01-500 Pa, keeping the frequency constant (1 Hz), with the purpose to find the linear viscoelastic region (LVR), that is the region of small deformations/stresses where G' and G'' do not depend on τ_0 or γ_0.
Frequency sweep tests consist in the application of a sinusoidal stress, with constant amplitude τ_0 and variable frequency. We chose a constant shear stress of 1 Pa (within the linear viscoelastic field) and performed measurements in the frequency range 0.01-10Hz. The temperature was set to 25±1 °C for all the measurements.
Finally, in steady value tests, an increasing stress τ is applied to the sample and the shear viscosity $\eta(\dot{\gamma})$ is determined from the measured shear rate $(\dot{\gamma})$ exploiting the Newton law:

$$\tau = -\eta(\dot{\gamma})\dot{\gamma} \qquad \text{(Eq. 5.4)}$$

The result is the so-called flow curve, showing the dependence of the sample viscosity on the applied shear stress. Steady value tests were performed in the shear stress range 0.1-100 Pa.

Rheological data were elaborated on the basis of Flory theory (Flory, 1953) in order to evaluate the average mesh size ξ of the TOCN hydrogels. The first step was the determination of the polymeric network crosslink density ρ_x, that is the moles of junctions between different polymeric chains per hydrogel unit volume:

$$\rho_x = \frac{G}{RT} \qquad \text{(Eq. 5.5)}$$

where R is the universal gas constant, T the absolute temperature and G is the shear modulus of the hydrogel, estimated from FS tests as the average G' value over the considered frequency range.
ξ can be determined from ρ_x according to the equivalent network theory (Schurz, 1991). As in most cases a detailed description of a real polymeric network is rather complicated, the equivalent network theory suggests to replace the real network topology by an idealized one (cubical arrangement of the meshes) sharing the same average ρ_x. According to this model, the empty volume associated to each crosslink point is that of a sphere centered in the crosslink point and having a diameter equal to the average mesh size ξ. Considering the definition of crosslink density and the Avogadro Number N_A, the volume competing to each cross-link in the real network is $1/N_A\rho_x$ and is equal to the volume of a sphere with diameter ξ in the ideal network:

$$\frac{1}{\rho_x N_A} = \frac{4}{3}\pi\left(\frac{\xi}{2}\right)^3 \qquad \text{(Eq. 5.6)}$$

from which it is possible to obtain the relation between ξ and ρ_x: $\xi = \sqrt[3]{\frac{6}{\pi\rho_x N_A}}$

5.1.5 Microscopy

The morphology and dimensions of TOCN at different sonication times was evaluated through microscopy techniques. In particular, an optical microscope Olympus IX70 equipped with a digital camera Moticam 2.0 MP was used in the case of small sonication times (that is for fibers with length major than 1 mm). In this case images were analyzed with the software ImageJ. For longer sonication times (and thus nanometric TOCNs) atomic force microscopy was used. Images of the crystallites were acquired by an AFM NT-MDT P47H scanning probe microscope operated in semi-contact mode and elaborated with the software Gwyddion (Nečas and Klapetek, 2012). We recall here that images of TOCNs at fixed 240 sec sonication time were acquired with TEM microscopy too, as reported in Chapter 3.

5.2 TOCN ionotropic gelation

5.2.1 Gelling procedures

Ionotropic gels were obtained using $CaCl_2$ as gelling agent and following external and inverse gelation procedures.

In the case of external gelation concentrate TOCN solutions (8 mg mL^{-1}) were extruded inside a $CaCl_2$ (0.1-2 M) gelling aqueous solution. A microfluidic flow system, consisting of a compressor (JUN-AIR oil-lubricated compressor), a flow control system (Elveflow OB1 pressure controller and Elveflow software) and an output nozzle (400 μm diameter), was used to obtain TOCN-Ca^{2+} hydrogel wires and beads with different sizes. The wires were obtained by extruding the TOCN solution from the nozzle directly inside the $CaCl_2$ pool, while the beads were obtained by dropping the TOCN solution. Wires and beads of different sizes were obtained changing the pressure or the duration of the pressure pulse impressed by the system. Hydrogel disks were obtained using a spin-coater (spin-coater SPS 150) by pouring TOCN solution (8 mg mL^{-1}) on a rotating $CaCl_2$ (0.1-2 M) aqueous solution.

In the case of inverse gelation, instead, an aqueous solution of $CaCl_2$ (0.1-2 M), was dropped into a TOCN solution (8 mg mL^{-1}). The outward diffusion of the Ca^{2+} ions from the drop to the outer TOCN solution led to the formation of capsules with a liquid aqueous-core and a jelly TOCN-Ca^{2+} shell. In order to enable $CaCl_2$ drop to break the TOCN solution surface, when impinging on it, and to penetrate in the

solution with minimal deformations, obtaining an almost spherical core, TiO_2 nanoparticles (Aeroxide® TiO_2 P25, 5 mg mL^{-1}) were added to the $CaCl_2$ solution in some experiments. After several attempts, a TiO_2 concentration equal to 5 mg mL^{-1} was chosen as it enables to increase $CaCl_2$ solution viscosity and density, reducing drop deformation, without altering the inverse gelation process. Moreover, the presence of TiO_2 nanoparticles, which remain in the core and do not diffuse in the jelly TOCN-Ca^{2+} shell, makes the aqueous core opaque, increasing the contrast with the surrounding hydrogel and enabling to better identify the core-shell interface in capsule images. The volumes of core-shell microcapsules were measured with calibrated cylinders (with either 0.05 cm^3 or 0.25 cm^3 volume resolution). Individual particle images were obtained by a digital camera (Moticam CMOS 2) connected to a microscope Olympus IX70. The size of the beads and of the microcapsule core, together with the shell thickness were analyzed with the software ImageJ.

5.2.2 Ca^{2+} determination and monitoring

In order to study both the amount of calcium ions necessary to maintain the TOCN-Ca^{2+} hydrogel structure and the diffusion of calcium ions leading to hydrogel formation, a method was required to quantitatively detect the presence of calcium ions and monitor their position in time. It was chosen to use a colorimetric method exploiting the capability of murexide dye (5,5'-Nitrilodibarbituric acid monoammonium salt) absorption peak to shift, turning from purple to yellow, upon complexation with Ca^{2+} (Pollard and Martin, 1956; Tammelin and Mogensen, 1952).

Ca^{2+} determination in TOCN-Ca^{2+} hydrogels in steady state conditions

The concentration of Ca^{2+} strongly bound inside hydrogels incubated in water under steady-state conditions was determined on the basis of the amount of excess Ca^{2+} ions released in water by TOCN-Ca^{2+} hydrogels incubated in aqueous solution after the gelation process. To this purpose, hydrogel disks obtained by adding 1 mL $CaCl_2$ (1 M) to 5 mL of TOCN (9 mg mL^{-1}) suspension were used. The $CaCl_2$ solution was let diffuse between TOCN crystallites and a compact hydrogel disk was formed. The coarse excess of Ca^{2+} not interacting with the hydrogel was removed by rinsing with 50 mL distilled water for two minutes. Then the disk was incubated into 50 mL of water. At selected times, 2 μL of the incubation solution were transferred into 500 μL of the assay solution containing 0.2 mM murexide buffered at pH 11.3 and the wavelength shift of the absorption peak of murexide was used to obtain Ca^{2+} concentration, according to a calibration curve . At the end of the release kinetic, the hydrogel disk was disrupted using an ultrasonic tip in order to release all the Ca^{2+} ions still trapped in the hydrogel. The Ca^{2+} of the sonicated TOCN suspension was measured by the murexide assay as above reported. The experiment was repeated three times under the same experimental conditions. The spectra were

acquired by a Varian-Cary 5000 UV-VIS-NIR spectrophotometer operated in %T mode in the range 200-900 nm with a 1 nm resolution.

Ca^{2+} diffusion in external and inverse ionotropic gelation

The dynamics of Ca^{2+} diffusion in the incipient hydrogels obtained by external ionotropic gelation was investigated by monitoring the advancement of the front of color change of murexide dye upon Ca^{2+} complexation. A similar approach was used by G. Skjak-Braek *et al.* to visualize the migration of the gelling zone in calcium-alginate gels (Skjåk-Bræk et al., 1989). The experimental set-up consisted of a plastic cuvette (square 12.5 mm base and 45 mm length) filled with a solution containing murexide (20 μM) and TOCN (8 mg mL^{-1}), as shown in Fig. 5.1a. The opened extremity of the cuvette was closed with a dialysis membrane (MW cut-off 10000) and the cuvette was placed in a solution containing $CaCl_2$. The experiment was repeated at various concentrations (0.1 M, 1 M and 2 M) of Ca^{2+} in the diffusing gelling solution. By this set-up, the diffusion of Ca^{2+} occurs in one dimension along the cuvette axis. The temperature of the solutions was kept fixed at (25.0 ± 0.5) °C by using a heating immersion circulator (Julabo MD). Images were taken at different times from the beginning of the gelation process (moment at which the cuvettes were placed in the $CaCl_2$ solutions bath) with a digital camera. The software ImageJ was used to analyze the images and obtain the distance of the yellow-purple interface from the dialysis membrane. For each image three distances were measured (at the centre of the cuvette and near the two walls, as shown in Fig. 5.1b) and the sol-gel front was then expressed as the mean value of the three measurements. As the distance measurement uncertainty, we considered the maximum value between the standard deviation over the three measurements and the half-thickness of solution color front (0.5 mm).

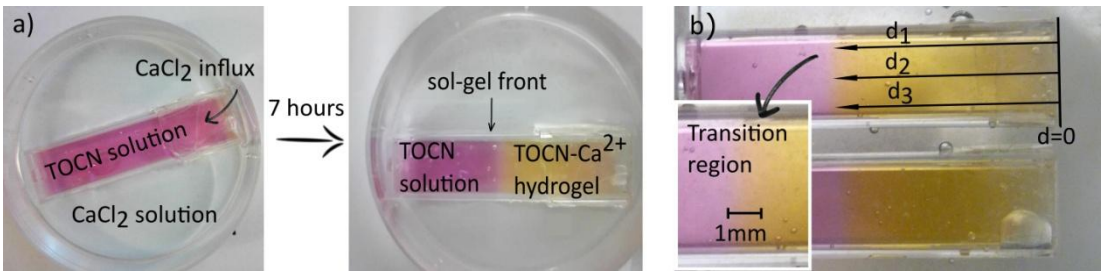

Fig. 5.1: Pictures of the experimental set-up used to visualize the diffusion front of Ca^{2+} ion in the incipient TOCN-Ca^{2+} hydrogel obtained by external ionotropic gelation. (a) Pictures of a cuvette filled with TOCN (8 mg mL^{-1}) and murexide (20 μM) after 5 min and 7 hours immersion in 1 M $CaCl_2$ solution; the cuvette containing the TOCN-murexide solution is closed at the opened extremity with a dialysis membrane to allow only Ca^{2+} diffusion from outside to inside the cuvette. (b) Advancement of the diffusion front. The inset shows that a transition region of the change in color of murexide is present. The arrows indicate the three distances (d_1, d_2 and d_3) used to calculate the average value of the diffusion front.

Also for the case of inverse ionotropic gelation process, the dynamics of Ca^{2+} diffusion was investigated by monitoring the advancement of the front of color change of murexide dye added to the TOCN solution. However, in this case a spherical geometry was adopted: 7 μL droplets of aqueous solution containing $CaCl_2$ and TiO_2 nanoparticles ($CaCl_2$ concentration 0.1 M, 0.5 M, 1 M and 2 M, TiO_2 concentration 5 mg mL^{-1}) were dropped in a TOCN-murexide solution (8 mg mL^{-1} TOCN and 20 μM murexide). Images of the samples were taken at different times from the beginning of the gelation process (that is the time $CaCl_2$-TiO_2 drop comes in contact with the TOCN-murexide solution) with a digital camera. The software ImageJ was used to analyze the images and obtain the diameter of the capsules by exploiting the color change of murexide from purple to yellow in presence of Ca^{2+} ions. To account for deviations from a spherical shape, three diameters (D_1, D_2 and D_3, as shown in the central panel of Fig. 5.2) were measured in the three spatial dimensions and an average value was considered. The uncertainty on diameter measurements was related to the not sharp sol-gel interface (about 1 mm along the gel growth direction) and to image contrast and calibration and was estimated to be around 20%. Knowing the microcapsule radius $R = D/2$ and the liquid core radius r, we determined the gel shell thickness as a function of time as the distance $r = R - r$.

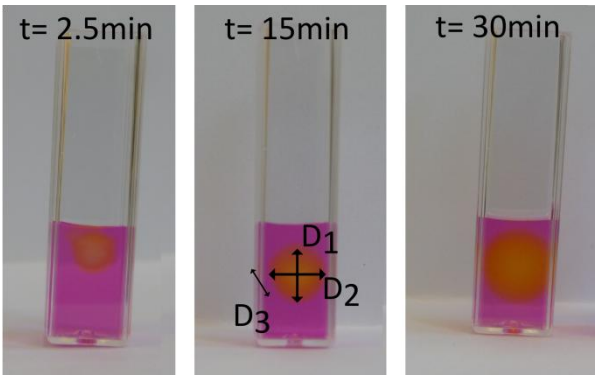

Fig. 5.2: Representative pictures of the measurements performed to visualize the diffusion front of Ca^{2+} ions in an incipient TOCN-Ca^{2+} core-shell capsule obtained by inverse ionotropic gelation. The images show the core-shell capsule growth induced by Ca^{2+} diffusion from the aqueous core. The pictures of the same sample were taken at 2.5 min, 15 min and 30 min (from left to right) after the contact between the $CaCl_2$-TiO_2 drop and the TOCN-murexide bulk solution (purple in the three images). The annulus, enlarging from left to right images, is the ionotropic gel shell formed upon diffusion of Ca^{2+} ions between TOCN crystallites.

5.2.3 FTIR spectra and maps of dried TOCN-Ca^{2+} hydrogels

Fourier Transform Infrared (FTIR) spectroscopy was used to monitor the coordination between Ca^{2+} ions and carboxylic groups in TOCN-Ca^{2+} hydrogels, as it induces a shift of the vibrational frequency of these groups (Deacon, 1980; Nakamoto, 1989; Nara et al., 1996). In particular, changes in FTIR features of TOCN carboxylic group in TOCN-Ca^{2+} hydrogels with respect to those of TOCN crystallites at pH 7 (where the counter ion is Na^{+}) were used to monitor the presence and the homogeneity of distribution of Ca^{2+} inside TOCN-Ca^{2+} hydrogels.

FTIR spectra of TOCN-Ca^{2+} samples were acquired using a micro-FTIR Nicolet iN10 instrument equipped with a liquid nitrogen cooled detector. For these measurements, TOCN-Ca^{2+} hydrogel beads were produced by external ionotropic gelation, left in water for 3 days to let them release the non-coordinated Ca^{2+}. The beads were then cut in transversal slices and a central slice was dried in an oven at 60 °C for 24 h before measurements to minimize the water feature in the spectra. Dried samples were scanned in %T mode in the range 750-4000 cm^{-1} with a 4 cm^{-1} spectral resolution or 1200-2500 cm^{-1} with a 1 cm^{-1} spectral resolution. Spectra of TOCN films (without Ca^{2+}) obtained by casting TOCN suspensions on a Petri dish were acquired under the same conditions and used as a reference for assignment of vibration features and peak wavenumbers. The position of the symmetric and asymmetric carboxylate peaks (at 1410 cm^{-1} and 1608 cm^{-1} in TOCN films, where the counter ion of the carboxylate groups is Na^{+} and at 1420 cm^{-1} and 1600 cm^{-1} in TOCN-Ca^{2+} hydrogels, where the counter ion is Ca^{2+} respectively) and their relative shift upon Ca^{2+} complexation were used to monitor the presence of Ca^{2+} in the hydrogel (Papageorgiou et al., 2010). To investigate the Ca^{2+} distribution inside the TOCN-Ca^{2+} gels, spatial maps were automatically acquired by selecting a given number of points per area over different parts of a bead slice. In particular, a surface of 300 × 1300 μm^2 was mapped with 100 μm spacing for both a central and an edge zone of the sample. In the case of the edge zone, spectra related to points closer than 400 μm from bead edge were not reported because of artifacts due to surface effects on the acquisition.

To perform a rigorous spectral analysis and to get the precise position of the symmetric and asymmetric carboxylate peaks we followed a two steps procedure consisting in 1) the deconvolution of the partially overlapping peaks and 2) the normalization of the intensities with respect to the 1372 cm^{-1} peak, which is related to the in-plane alkane -C-H bending vibration in TOCN and can be assumed to be constant for all the samples and not altered by the ionotropic gelation. In particular, the bands at around 1610 cm^{-1} were analyzed performing a double gaussian fit procedure to separate the contribution of the asymmetric carboxylate stretching vibration from that of water (at 1640 cm^{-1}). The bands at around 1420 cm^{-1} were analyzed in TOCNs films performing a double gaussian fit procedure to separate the

contribution of the symmetric carboxylate stretching vibration from that of alkane -C-H vibrations (at 1425 cm^{-1}). The obtained alkane peaks were then subtracted from TOCNs-Ca^{2+} spectra to isolate the symmetric carboxylate stretching vibration peak.

5.3 TOCN Hydrogels toxicity studies

In order to perform toxicology studies on TOCN hydrogels, the hints of the International Standard protocol ISO 10993-1 and DIN EN ISO 10993-5:2009 (STANDARD, 2009) were considered. They suggest to test each component material, including impurities and constituents associated with processing together with the device, both in direct and indirect contact. For this reason, not only TOCN hydrogels were evaluated, but also TOCN films, TOCNs in solution and salts used to prepare the hydrogels. Moreover, the toxicity of TOCN hydrogels was evaluated *in vitro* both placing them in direct contact with cell cultures and using a support to avoid mechanical stress (indirect contact test).
The cell cultures used to performed the toxicity studies were human malignant melanoma cells (A375), provided by the American Type Culture Collection, (ATCC, Virginia, USA), CRL-1619. Cell were grown in monolayer in RPMI 1640 medium (Euroclone Pero MI, Italy) supplemented with 10% fetal bovine serum (FBS) (Euroclone), 1% penicillin (50 U/mL) - streptomycin (50µg/ml) (Euroclone), and 1% non-essential aminoacids (Euroclone) in a humidified atmosphere of 5% CO_2 in a water-jacketed incubator at 37 °C.
TOCN hydrogels were prepared in Trento, while toxicity measurements were performed by collaborators from the National Center for Drug Research and Evaluation (Istituto Superiore di Sanità, Roma).

5.3.1 TOCN hydrogel membranes (TOCN-HM) and films (TOCN-FL) preparation

TOCN hydrogels were obtained by cation-induced gelation using different cations (Na^+, Ca^{2+}, Mg^{2+}). Moreover, different washing procedures after the gelation process were tested in order to remove the excess of salt and increase TOCN hydrogels stability in water solutions.
Among the different shapes achievable, I decided to use disk-shapes TOCN hydrogels (referred to as TOCN hydrogel membranes: TOCN-HM) with height and diameter around 4-5 mm and 9 mm, respectively. To prepare them, 25 mL of 8 mg mL^{-1} TOCN solution were transferred into an 85 mm diameter Petri dish over which 10 mL of 1M salt solution ($CaCl_2$, $MgCl_2$, NaCl) were poured under gentle agitation.

The resulting 85 mm diameter hydrogel membrane was shaped in smaller TOCN-HM disks using a cylindrical 9 mm diameter die and placed in 20 mL of 1M salt solution ($CaCl_2$, $MgCl_2$, NaCl) for 24 hours.
At this point, four different post-gelation processing strategies were evaluated: a) short washings (5 min) in water to remove the excess of salt solution from the surface (rinsed TOCN-HM), b) washing by incubation in water (50 mL) for 5 days, changing the 50 mL water once a day (water TOCN-HM), c) conversion to alchoolgel by incubation in ethanol (50 mL) for 5 days, changing the 50 mL ethanol once a day, followed by rinsing in aqueous solution (ethanol TOCN-HM), d) 2h washing in water followed by 1h drying at 60°C (60°C TOCN-HM).
To obtain TOCN films (TOCN-FL), the TOCN suspension was casted on a Petri dish and left to dry at 60°C for 24 hours in an oven. The thickness of the film was in the range 10-12 μm.

5.3.2 Direct and Indirect contact toxicity tests

To determine the 2D cell culture response to the direct contact between the TOCN-HM and melanoma cells, the cells (4×10^5) were initially placed in a 35 mm tissue culture dish and allowed to grow in culture medium as a confluent monolayer. After 24 h of growing, the TOCN-HM was laid down on the monolayer cells, the well plate was filled with the culture broth and cell proliferation and morphology were monitored for 24h.
The indirect toxicity tests were performed by protecting the cell layer from possible mechanical stress damage induced from TOCN-HM contact using a cell culture insert with a microporous (8 μm), permeable polyethylene terephthalate (PET) membrane (FalconTM Cell culture insert, Corning inc. North Carolina). The insert housing was laid over 0.5 cm from the confluent cell monolayer avoiding the direct contact but favoring the molecules diffusion. Then, the TOCN-HM was laid over the PET membrane and the well plate was filled with the culture broth up to the TOCN hydrogel membrane. A sketch of the experimental set-up is shown in Fig. 5.3: it allows diffusion of molecules through the PET membrane, however it avoids the mechanical stress due to contact between cells and TOCN-HM.

The toxicity of TOCN-HM both in direct and indirect contact with melanoma cells was evaluated, in a qualitative way, observing the cells after the treatment by phase contrast microscopy and, in a more quantitative manner, by performing MTT assays.

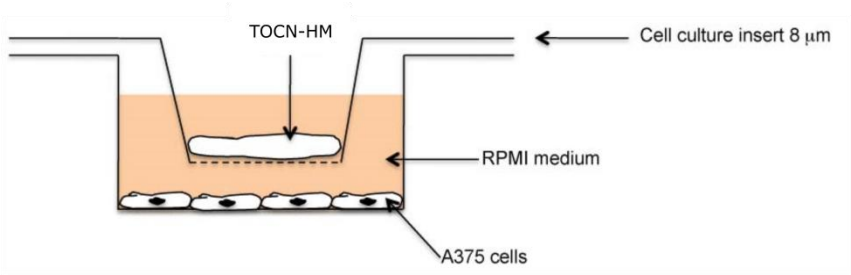

Fig. 5.3: Sketch of the experimental set-up used for indirect contact toxicity tests, consisting of a cell culture insert with a microporous (8 μm), permeable PET membrane laid over 0.5 cm from the confluent cell monolayer. To perform the tests, the TOCN-HM was laid over the PET membrane and the well plate was filled with the culture broth up to the TOCN hydrogel membrane.

MTT assay

Cell viability was assessed by (3-[4, 5-dimethylthiazol-2-yl] -2,5-diphenyltetrazolium bromide) MTT assay (Sigma Aldrich, Milan, Italy). This test measures the activity of the enzymes, above all mitochondrial enzymes, which reduce MTT to formazan, imparting a blue/purple color to the dye.

After removing cell medium, untreated and treated cells with TOCN-HMs were washed with phosphate buffered saline (PBS) solution and incubated with 0.5 mg mL^{-1} MTT solution for 2 h at 37 °C. After removing the MTT solution, the samples were lysed by 100 μL DMSO, and analyzed by a microplate reader (Bio-Rad, California) at 570 nm. As positive control, 1 μM staurosporine (STM) from Sigma Aldrich for 24 h was used. Three absorbance measurements were done for each sample and the cell viability (%) was expressed as the percentage ratio between the absorbance mean value of the treated sample and absorbance mean value of the control sample.

In the same way, MTT assays were performed also for cells treated with TOCNs, TOCN-FLs and salts. In these cases the use of the support for indirect contact was not necessary, as TOCNs, TOCN-FLs and salts are not heavy or macroscopic devices able to cause mechanical damage to the cell layer.

The experiments were performed at least in duplicate and all the data are reported as the sample mean ± the standard deviation (SD).

Phase contrast microscopy

A375 cells untreated and treated with TOCN-HM were observed by phase contrast microscope (Zeiss, Axiovert200, Gottingen, Germany).

Confocal laser scanning microscopy (CLSM)

The toxicity of TOCNs was evaluated by incubating cells with FITC-labeled TOCNs and observing their intracellular distribution with a confocal laser scanning microscope.

To obtain FITC-labeled TOCNs, 0.75 mL of 2 mM fluorescein isothiocyanate (FITC) were added to 5 mL of a 0.1 M NaOH aqueous suspension of TOCNs (3 mg mL^{-1}) and then stirred for 6 days in the dark at RT (Nielsen et al., 2010). The suspension was dialyzed against 400 mL NaOH (0.05 M) for 7 days by changing the dialysis solution 4 times and then dialyzed against deionized water until pH 7.0 was reached.

Cells ($4x10^5$) were seeded in completed RPMI 1640 medium for 24 h prior to the experiment. After carefully removing the growth medium, cells were washed with PBS and incubated with FITC-labeled TOCNs at different concentrations (0.13±0.03 mg mL^{-1}; 0.4±0.1 mg mL^{-1}; 0.53±0.13 mg mL^{-1}) for 24h of treatment. At the end of incubation, slides were washed in PBS and fixed in 3.7% paraformaldehyde in PBS for 30 min at RT. After washing with PBS, cells were permeabilized in Triton-X-100 (0.5% in PBS) and then incubated with propidium iodide (PI) nuclear staining (1 µg mL^{-1}) for 30 minutes, after that, mounted on glass microscope slides.

The analysis of the intracellular distribution of FITC-TOCNs and PI for nuclear counterstain was carried out using a Leica TCS SP2 spectral confocal microscopy equipped with argon-helium neon (Ar-HeNe) lasers. FITC-labeled TOCNs were excited at a wavelength of 488 nm and PI at 594 nm; emission lines were collected after passage through a DD488/543 filter in a spectral window ranging from 515 to 700 nm. Signals from different fluorescent probes were taken in sequential scan mode, which allows the elimination of channel cross talk and colocalization was detected in an overlay model. The acquisition parameters were: 63.0/1.4 NA objective, 1024x1024 image size, 1 Airy pinhole size; 0.5 µm step size. Images were processed by using LCS (Leica Microsystems. Heidelberg GmbH, Germany) and Photoshop (Adobe System Inc. Mountain View, CA, USA) software programs.

Chapter 6:
TOCNs SOL-GEL TRANSITION

The studies reported in this Chapter 6 were performed after the observation, during routine lab-practices, that TOCN aqueous solutions at concentrations higher than a threshold value (around 5 mg mL^{-1}) are very prone to undergo sol-gel transitions. This transition was observed to happen in different situations, in particular during the sonication treatment, for appropriate sonication times, and when cations were added to the TOCN solutions. The combined use of ultrasonication and salt addition enabled to obtain strong, macroscopic, transparent TOCN hydrogels in some conditions but not in others. For example TOCN hydrogels were obtained if a prolonged sonication was followed by the addition of salts, while inhomogeneous suspensions were obtained if salts were added before sonication. The will of better understanding the mechanical and chemical sol-gel transition process led us to perform measurements to unveil the individual roles of sonication and salt addition. Particular attention was given, during our investigations, to the presence and the dynamic behavior of water molecules inside TOCN hydrogels, as the material structures and properties are expected to be strongly dependent on the presence of hydrogen bonds and interaction between TOCNs and water.

Here we report the results obtained by the combined use of spectroscopic (NMR, SAXS, UV-VIS) and rheological techniques. In particular, the first section is focused on the role of sonication in the transition process, reporting the changes in optical, morphological, rheological properties and water relaxation spectra of TOCN solutions as a function of the sonication time. The second section investigates the effect of salt addition and sonication order, trying to understand the reasons why sonication has to precede salt addition in order to observe a sol-gel transition. Finally, the last section reports the results obtained investigating the sol-gel transition in the case of salts added after sonication. In particular, the results of rheological, NMR and SAXS measurements were combined to understand the changes in TOCN hydrogels structures and properties due to different sonication times, salt type and salt concentration.

6.1 Sol-Gel transition of TOCN solutions: the effect of sonication

In this Section we report the results obtained investigating the effect of sonication on TOCN aqueous suspensions. In particular, 40 mL of aqueous slurry containing 6 mg mL^{-1} TOCN at pH 7 was sonicated for variable times and the resulting suspensions were analyzed combining different techniques.
From a qualitative point of view, before sonication the solution appears highly heterogeneous and formed by macroscopic aggregates of fibers. This turbid and flocculent suspension becomes progressively a homogeneous and viscous jelly solution increasing the sonication time. As a representative example, Fig. 6.1 shows a TOCN suspension before and after a 240 s sonication treatment. The whitish appearance of the non- sonicated suspension is due to aggregates of cellulose fibers, which are disrupted and transformed in TOCNs upon sonication, giving rise to a transparent, homogeneous solution.

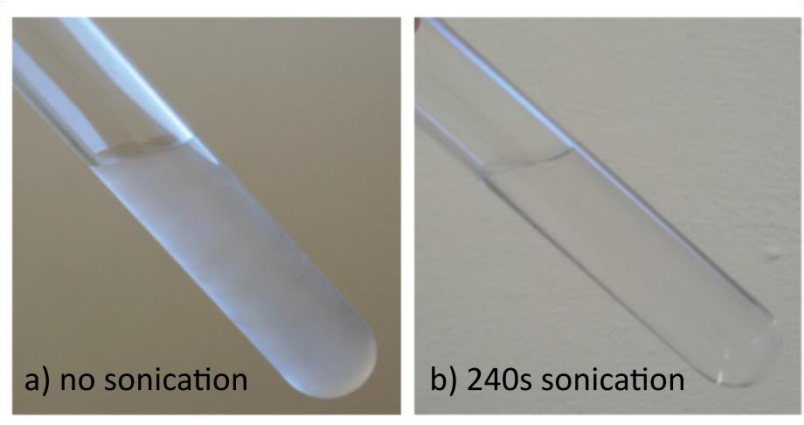

Fig. 6.1: Visual appearance of (a) a non sonicated TOCN slurry and (b) a sonicated one. Macroscopic aggregates of cellulose fibers induces the whitish appearance of the non sonicated slurry. Upon sonication, fibers are disrupted and transformed in TOCNs leading to transparent, homogeneous solutions.

6.1.1 Morphological changes and optical properties

The morphology changes induced by sonication were investigated by optical and AFM microscopy. Fig. 6.2a and Fig 6.2b report respectively an optical microscope image of TOCNs after 30 s sonication and an AFM image obtained after 480 s sonication. It is visible that branched fibrils are converted into rod-like crystallites. The morphology of and dimensions of TOCNs after extensive sonication were evaluated through TEM microscopy and the results were reported in Chapter 2, Section 2.3.1.

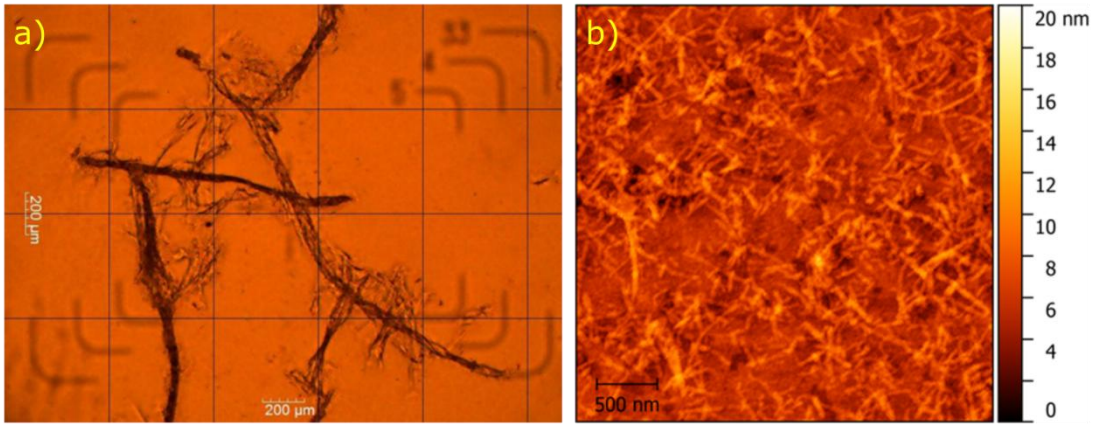

Fig. 6.2:. (a) Optical microscopy image of macroscopic cellulose fibers after a short sonication treatment (30 s); (b) Atomic force microscopy of TOCNs after a prolonged sonication treatment (480 s).

A further demonstration that large aggregates disappear upon sonication is given by optical transmission measurements. As shown in Fig. 6.3, optical transmission is low for short sonication time (< 120 s) and reaches a plateau value after 120 s sonication. The high transmission values (97% at 500 nm and 89% at 300 nm) and thus the absence of significant scattering for solutions sonicated for more than 120 s rules out the presence of meso- to macroscopic aggregates.

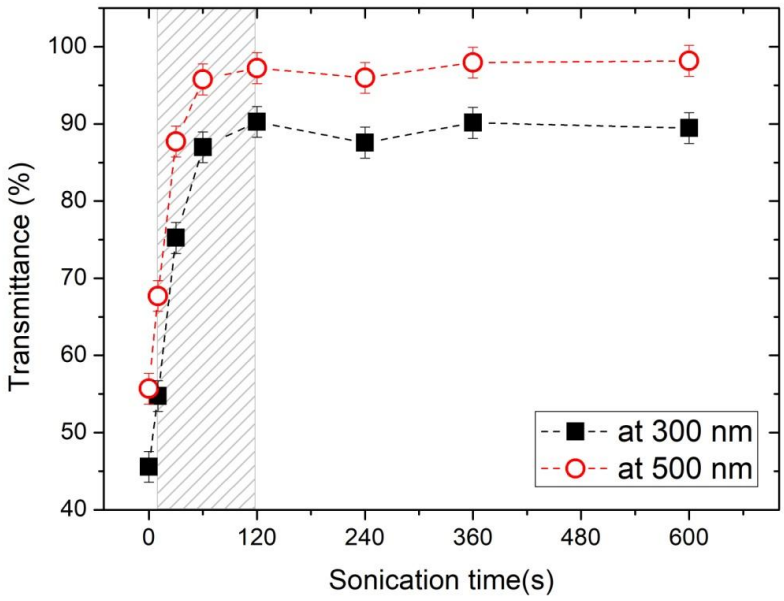

Fig 6.3: Transmittance of TOCN suspensions as a function of sonication time. Black squares refer to UV wavelength (300 nm) and red empty circles to visible wavelength (500 nm). Values and error bars refer to mean value and SD over at least three measurements.

Both microscopy images and optical measurements show that the transition from fibrils to nanocrystals is almost completed after 120 s sonication (for 6 mg mL^{-1} TOCN solutions). The dispersion of the TOCNs is driven by their polyelectrolytes nature. In fact, at pH 7 they bear an average negative charge on the 29% of the cellobiose units, as determined by conductometric titrations (Chapter 2, Section 2.3.2).

6.1.2 Rheological behaviour

Frequency sweep tests (in the linear viscoelastic range) and flow curves were performed to investigate the dynamic rheological behavior of TOCN solutions characterized by different sonication times (0-480 s). Fig 6.4a and Fig. 6.4b report respectively the G' and G'' values obtained from frequency sweep tests, while Fig. 6.5 shows the flow curves.

Observing Fig 6.4, it appears that the only case for which G''>G' is for 0 s sonication, confirming again that the non-sonicated slurry is an inhomogeneous suspension of fibers agglomerates without cohesion. For sonication times in the interval 30-360 s, instead, G'>>G'' and G' and G'' are roughly independent of frequency, indicating a gel-like behavior of the samples. Assuming that Flory theory holds (Flory, 1953) and that the shear modulus of the hydrogels is the average G' value over the considered frequency range, the resulting mesh size was estimated to be around 50-70 nm. This is a considerable wide value, meaning that the connectivity within these hydrogels is not very high and suggesting the presence of a tenuous transient network (statistical network) involving non-covalent associations among polymeric chains, typical of weak polysaccharides gels (Coviello et al., 2013; Grassi et al., 1996). The gels show a reversible behavior as, for sonication times higher than 360 s, they tend to revert to a viscous solution: G' decreases, approaches G'' and both of them are frequency dependent. We are in the condition of incipient weak gel (sol-gel transition). Considering an average shear modulus around 5 Pa and applying Flory theory, a wide average mesh size can be estimated for these systems (≈ 120 nm) showing their scarce connectivity.

The same trend (as a function of sonication time) can be observed in the viscosity curves of Fig. 6.5. While in the case of 0 s sonication the viscosity is low and nearly constant (0.01-0.1 Pa s), for sonication times lying in the range 30-360 s a sudden drop of viscosity (from 1-10 kPa s to 0.1-1 Pa s) happens at stress around 20-60 Pa, indicating a fracture of the internal structure. Finally, in the case of 480 s sonication time, the weaker connectivity is confirmed by the lower viscosity values (around 100 Pa s) and by the fact that the abrupt viscosity drop is substituted by a smooth decrease starting from 5 Pa stresses.

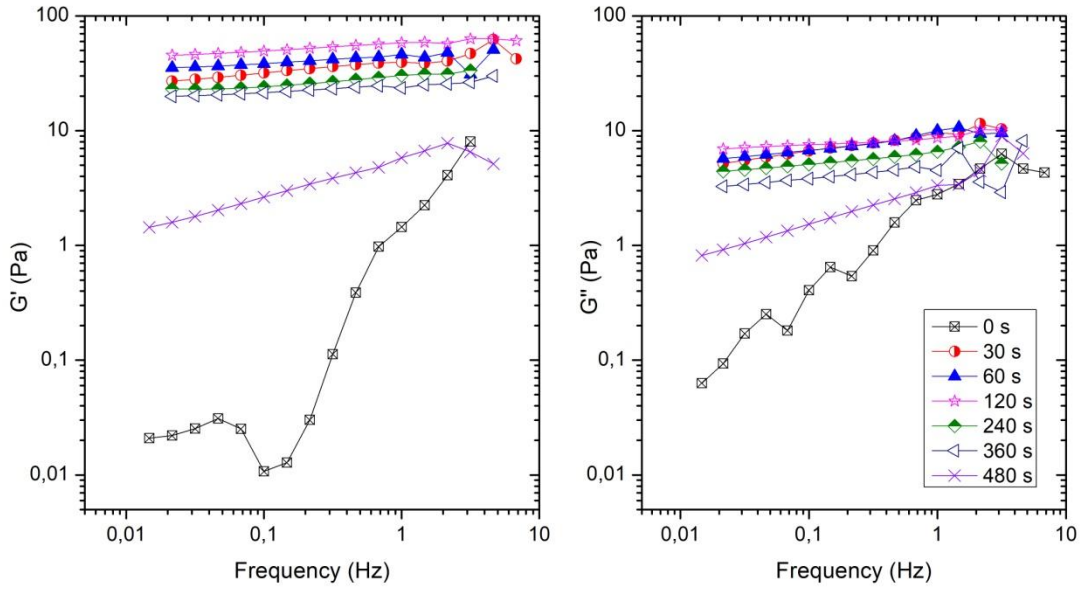

Fig 6.4: Results of Frequency Sweep tests for TOCN suspensions non-sonicated (0 s) and sonicated at variable times (30-480 s). Elastic modulus G' and viscous modulus G'' are reported respectively in Panel a and Panel b. Measurements were performed at 25±1 °C and 1 Pa shear stress.

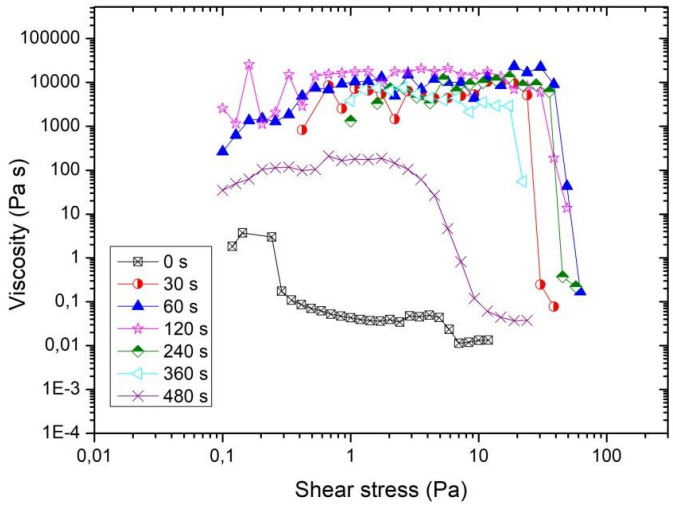

Fig 6.5: Flow curves for TOCN suspensions at different sonication times (0-480 s). The maximum viscosity value is obtained for sonication times in the range 30-360 s and it drops, in all cases, for shear stresses higher than 30 Pa, indicating a fracture of the internal structure. Measurements were performed at 25±1 °C.

The effect of sonication on the dynamic rheological behavior of TOCN suspensions/solutions obtained by frequency sweep tests is summarized in Fig 6.6, which reports the dependence of the elastic modulus G' (conventionally evaluated at 1 Hz) versus sonication time. Despite a gel-like behavior is observed for every

sonication time different from zero (with the limit situation of G'≈G'' at 480 s), it appears again that the gel strength (i.e. the elastic component) increases up to 120 s and then gradually decreases, suggesting a reduction of the interaction points among different TOCN crystallites.

The reduction of crosslinks is probably due to the efficient nano-fibrils detachment induced by sonication and to the high rigidity and limited length of TOCNs, which hinder the formation of a three dimensional network. This interpretation is in agreement with the results of the optical and morphological characterization reported in Subsection 6.1.1, showing that the transition from fibrils to nanocrystals is almost completed after 120 s sonication.

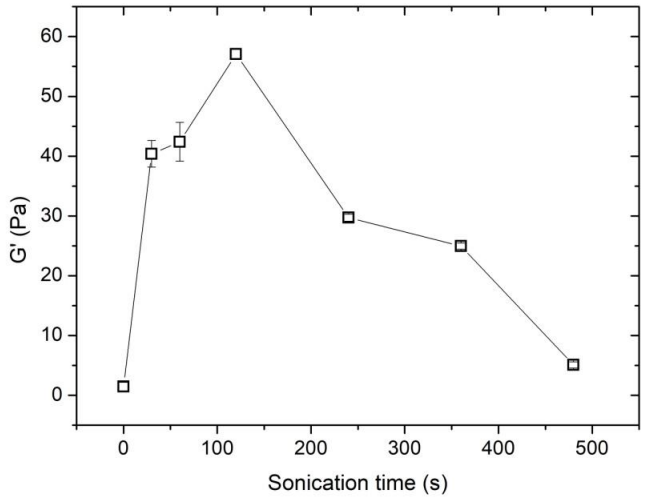

Fig 6.6: Elastic modulus G' (conventionally evaluated at 1 Hz) of 6 mg mL^{-1} TOCN solutions as a function of sonication time. The reported values and errors were evaluated performing a linear fit on FS curves in the frequency range 0.02-2Hz and extrapolating from them the G' value at 1 Hz. Gel strength increases up to 120 s and then decreases, suggesting a reduction of the crosslinks among TOCN crystallites.

6.1.3 State and dynamics of water in TOCNs solutions

Transversal nuclear magnetic relaxation rate (T_2^{-1}) of water was used to better understand the organization of TOCNs and the state and dynamics of water in the TOCN suspensions at different sonication times. Table 6.1 reports the results of multi-exponential analysis of the magnetization decays in terms of average water relaxation times (T_{2m}), individual relaxation rates (T_{2i}^{-1}) and respective relative abundances (A_i). The average relaxation time is calculated as the weighted average of the individual relaxation times (T_{2i}). It appears that, for short sonication times (30-60 s) two relaxation rates are required to describe the process, suggesting the coexistence of two different proton environments. The slower relaxation rate (more similar to that of pure water: 0.3 s^{-1} (Koenig et. al., 1975)) can be associated to

macroscopic dispersed fibrils, while the faster rates are compatible with TOCN nanocrystals. For sonication times longer than 120 s, a single relaxation time is sufficient to describe the system, supporting the idea of a homogeneous structure of the material.

Table 6.1: Relaxation rates (T_{2i}^{-1}) and respective relative abundances (A_1) and average water relaxation times (T_{2m}) of TOCN suspensions at different sonication times. A single relaxation time is always enough to describe the systems apart from the case of 30 s and 60 s sonication times, indicating quite homogeneous materials.

Sonication time (s)	T_{21}^{-1} (s^{-1})	A_1 (%)	T_{22}^{-1} (s^{-1})	A_2 (%)	T_{2m} (ms)
0	0.57	100			1747
30	0.65	71	0.90	29	1531
60	0.61	76	0.74	25	1651
120	0.68	100			1476
240	0.69	100			1448
360	0.71	100			1412
480	0.73	100			1360

Fig. 6.7 shows the trend of the average relaxation time (T_{2m}) as a function of sonication.

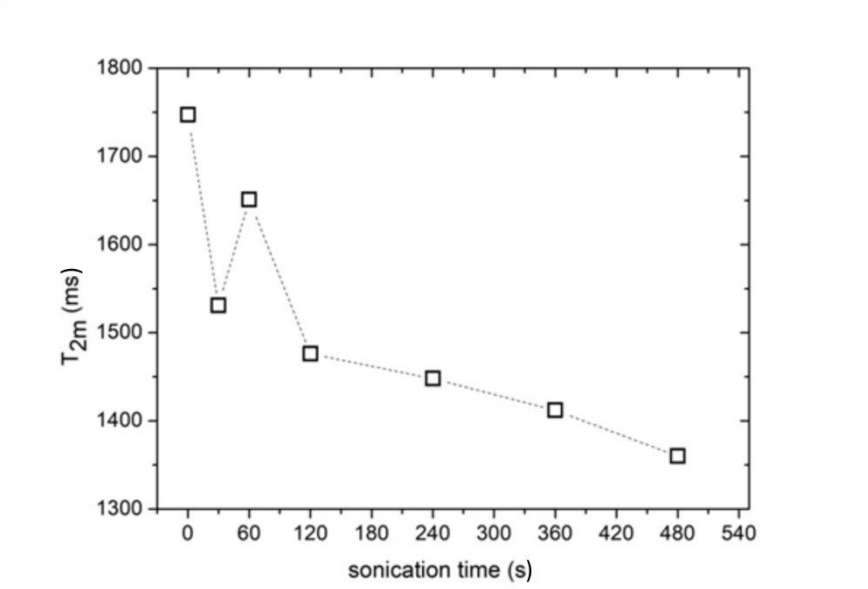

Fig. 6.7: Average relaxation times for TOCN suspensions as a function of sonication time. The decreasing trend suggests that fibers progressively detach from each other increasing the polymeric surface available for the interaction.

It is possible to see that T_{2m} decreases increasing the sonication time, indicating that fibers progressively detach from each other so that the polymeric surface available for the interaction with water molecules increases. Indeed, an higher solid surface

available for water interaction is known to cause a lower water ^{1}H relaxation time (Chui, 1995). Comparing Fig 6.7 with Fig. 6.6, it is possible to see the complementarity of rheological and NMR measurements. While NMR, through T_{2m}, shows the attitude of TOCNs to detach from each other, rheology, through G', gives information about the attitude of TOCNs to form a three-dimensional network. Up to 120 s, T_{2m} and G' are inversely proportional, possibly because fibers detachment favors their interaction to form a 3D network. However, larger sonication times cause a further detachment but reduce the attitude to form a gel structure.

To have a complete and summary picture of the effect of sonication on the behavior of aqueous suspensions of TOCNs, the results of transmittance, rheological and NMR measurements are reported together in Fig. 6.8, in terms of Transmittance values (Fig 6.8a), Elastic modulus (Fig 6.8b filled black circles, left axis) and relaxation rates (Fig 6.8b red squared symbols, right axis).

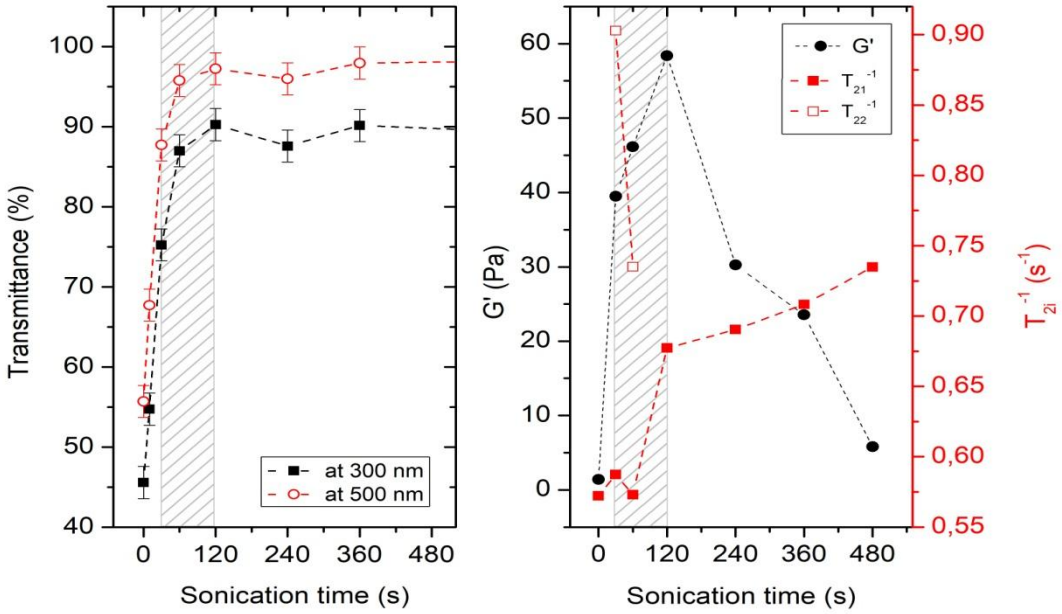

Fig 6.8: (a) Transmittance values of TOCN suspensions at 300 nm and 500nm as a function of sonication time. (b) Elastic modulus G' (filled black circles, left axis) and relaxation rates T_{2i}^{-1} (red squared symbols, right axis) as a function of sonication time. The shaded region underlines the sonication times for which gel-like structure forms.

To sum up, experimental measurements suggests that a 30-120 s sonication time breaks the fibrils in correspondence of the amorphous domains producing isolated TOCN crystallites which form a weak physical gel (shaded region in Fig. 6.8). This interpretation is supported by %T values, showing the disappearance of meso-macroscopic aggregates, by rheological data, reporting higher G' values, and by NMR measurements, indicating the presence of two different relaxation rates and thus two different water environments, which is typical of gel-like entangled

structures. Increasing the sonication time, a solution state is reached, as shown by the reduction of the G' values and by the presence of a single relaxation rate. This is probably due to the energy supplied by sonication, which breaks the hydrogen bridges between the TOCNs.

6.2 Sol-Gel transition of TOCN solutions: the effect of sonication and salt addition order

As already mentioned and similarly to what happens for other polyelectrolyte systems like alginates (Stokke et al., 2000) , cations increase the interactions among fibrils/TOCNs and can drastically change the properties of TOCN solutions. However, in our case, the effect is different if salts are added previously or after sonication.

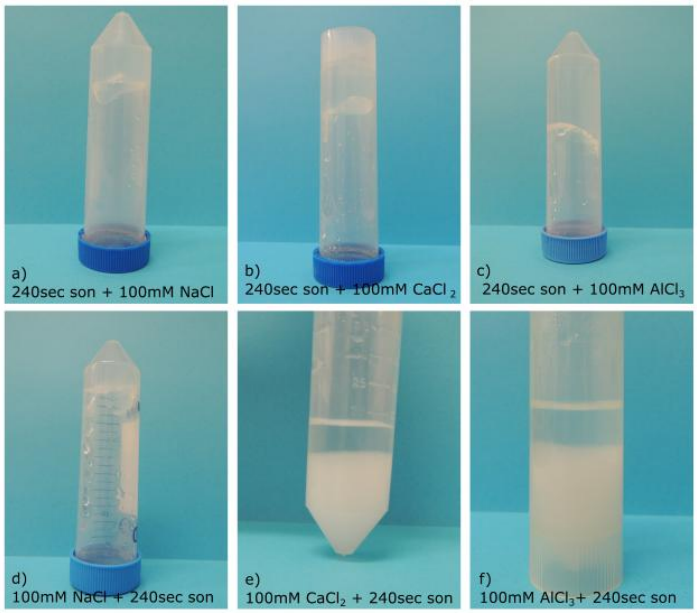

Fig. 6.9: Visual appearance of TOCNs solution/hydrogels. Panels a-b-c show the homogeneous and transparent hydrogels formed by 240 s sonication followed by the addition of cations (Na, Ca^{2+} and Al^{3+}), while panels c-d-e show samples obtained by first adding the cations and then sonicating. In this second case, only NaCl forms a weak and homogeneous hydrogel, while $CaCl_2$ and $AlCl_3$ form inhomogeneous materials.

In particular, sonication to disperse TOCNs followed by salt addition (sony+salt), produces homogeneous hydrogels, while sonication performed on TOCNs solutions already containing cations (salt+sony) produces visually inhomogeneous suspensions, with macroscopic compact structures surrounded by water. To have an idea of the phenomenon, Fig. 6.9 reports some pictures of the samples as they appear in the two cases, that is sonication followed by salt addition (Fig. 6.9 a-b-c) and salt addition followed by sonication (Fig. 6.9 d-e-f).

Here we focus on the comparison between the two procedures, while in the next section the case of sonication followed by salt addition will be treated more into details.

6.2.1 Rheological behavior

Fig. 6.10 compares the results of frequency sweep tests performed on samples obtained by the salt+sony and sony+salt procedures using 10 mM sodium chloride (panel a), 100 mM sodium chloride (panel b), 10 mM calcium chloride (panel c) and 100 mM calcium chloride (panel d). The sonication time was 240 s for every sample.

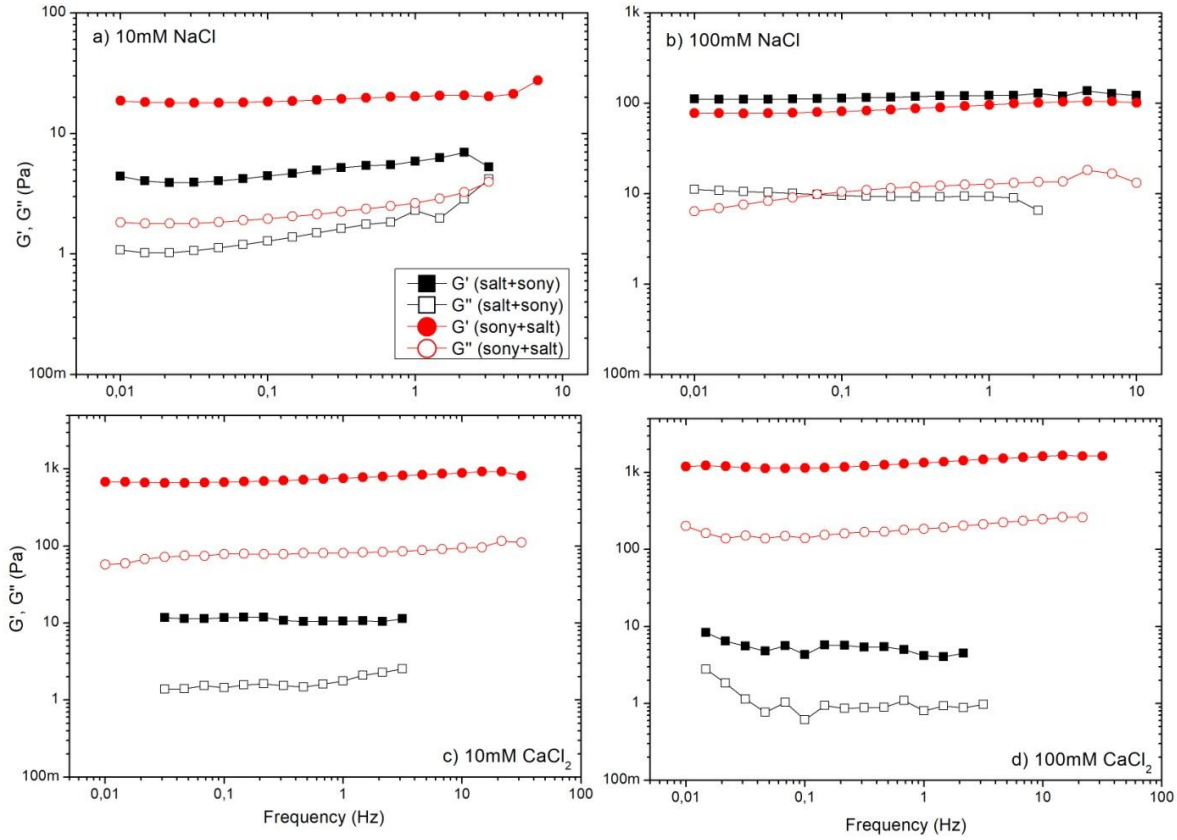

Fig 6.10: Frequency sweep test performed in the LVR (at stress equal to 1 Pa) on TOCN solutions/hydrogels (concentration 5 mg mL^{-1}) obtained by the sony+salt and salt+sony procedures. Sodium chloride and calcium chloride were used as salt types and their concentration in the TOCN solutions/hydrogels was 10 mM (panel a and panel c for NaCl and $CaCl_2$ respectively) and 100 mM (panel b and panel d for NaCl and $CaCl_2$ respectively). Sonication time was fixed to 240 s for every sample and measurements were performed at 25±1 °C.

The mechanical spectra of Fig 6.10 show that, apart from the case of 100 mM NaCl, the sony+salt procedure produces a higher increase of the mechanical properties

with respect to the salt+sony procedure. This is particularly evident in the case calcium chloride, for which the elastic modulus increases around two orders of magnitude (from 10 Pa to nearly 1 kPa) passing from the salt+sony to the sony+salt situation.

This trend is in agreement with the visual observation of the samples and is confirmed also by the flow curves shown in Fig. 6.11. While in the case of NaCl, the procedure (sony+salt or salt+sony) does not have a strong impact on the mechanical properties of the samples, in the case of divalent $CaCl_2$ salt, flow curves show a clear increase of both viscosity values and inflection point in the case the salt is added after sonication. Moreover, considering the sony+salt procedure, it is visible that the mechanical properties of the samples are stronger using $CaCl_2$ with respect to NaCl and using a 100 mM concentration in comparison to the 10 mM concentration (these effects will be considered in details in Section 6.3).

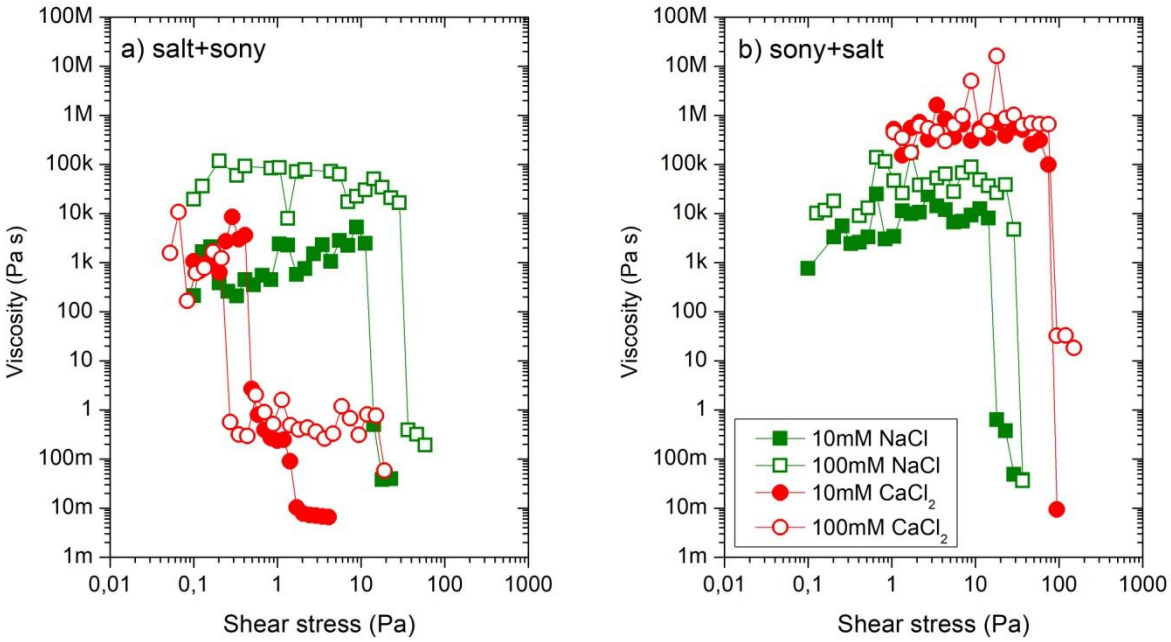

Fig. 6.11: Flow curves for TOCN solutions/hydrogels (concentration 5 mg mL^{-1}) obtained by two different procedure: (a) addition of salts followed by 240 s sonication and (b) 240 s sonication followed by salt addition. Measurements were performed at 25±1 °C.

The different behavior of sodium chloride with respect to calcium chloride can be ascribed to the different dimensions of the two cations. While Na^+ is smaller and able to reach all the interaction sites of TOCN fibrils without sonication, Ca^{2+} is bigger and unable to get the less exposed interaction sites and induce an homogeneous gelation, unless a previous sonication promotes fibers detachment. In this way, Ca^{2+} probably induce a gelation only of the outer surface of the macroscopic fibers aggregates and this prevents a subsequent effective sonication and dispersion of TOCNs, leading to inhomogeneous turbid suspensions.

6.2.2 NMR measurements

In Table 6.2 water relaxation rates (T_{2i}^{-1}) with the relative abundances (A_i) and the average relaxation times (T_{2m}) resulting from ^{1}HNMR measurements on TOCN solutions/hydrogels obtained following the salt+sony and sony+salt procedures are reported. All samples were sonicated for 240 s and sodium chloride or calcium chloride were added to the TOCN solutions at a 10 mM or 100 mM concentration. What appears of particular interest in this context is the increase of the number of relaxation rates necessary to fit the relaxation profile of the sony+salt procedure. Although the increase of polynomial terms for the fit reduces its quantitative reliability, we can argue that the sony+salt procedure forms more complex three-dimensional architectures, where the TOCNs are coordinated in a more intricate way which is in accord with visual observation and rheological data.

Table 6.2: Results of NMR measurements performed on samples obtained adding 10 mM or 100mM salt solution (NaCl or $CaCl_2$) to TOCN solution (concentration 5 mg mL^{-1}) previously or after a 240 s sonication treatment (series salt+sony and sony+salt respectively). In particular, the results are expressed in terms of water average relaxation times (T_{2m}) and relaxation rates (T_{2i}^{-1}) with relative abundances(A_i).

	salt	conc [mM]	T_{21}^{-1} (s^{-1})	A_1 (%)	T_{22}^{-1} (s^{-1})	A_2 (%)	T_{23}^{-1} (s^{-1})	A_3 (%)
salt+sony	NaCl	10	1.01	100				
	NaCl	100	0.88	24	1.09	76		
	$CaCl_2$	10	0.77	100				
	$CaCl_2$	100	0.70	100				
sony+salt	NaCl	10	1.14	7	1.18	93		
	NaCl	100	0.72	36	0.78	45	1.63	19
	$CaCl_2$	10	0.89	24	1.17	66	1.95	10
	$CaCl_2$	100	0.76	32	0.89	37	1.66	31

6.3 Sol-Gel transition of TOCN solutions: the effect of sonication + salt addition

In this Section we focus on the effect of salt addition to TOCN solutions after the sonication process. In particular, I was interested in evaluating the dependence of TOCN hydrogels structural properties on the combined effect of sonication time and salt addition and on the valence and concentration of the added salt. The measurements reported in this Subsection were performed on 6 mg mL^{-1} TOCN solutions sonicated for times in the range 30-480 s and to which different chloride salts were added (NaCl, $CaCl_2$, $AlCl_3$) at concentrations 10 mM or 100 mM.

6.3.1 Rheological behavior

FS tests were performed on samples obtained adding 100 mM NaCl, $CaCl_2$ and $AlCl_3$ salts to TOCN solutions after different sonication times (30-480 s). The results in terms of elastic modulus G' and viscous modulus G'' are reported if Fig. 6.12. They show that G' > G'' and both of them are frequency independent for all the samples, indicating that the addition of Na^+ Ca^{2+} and Al^{3+} produces sol-gel transition for every sonication time.

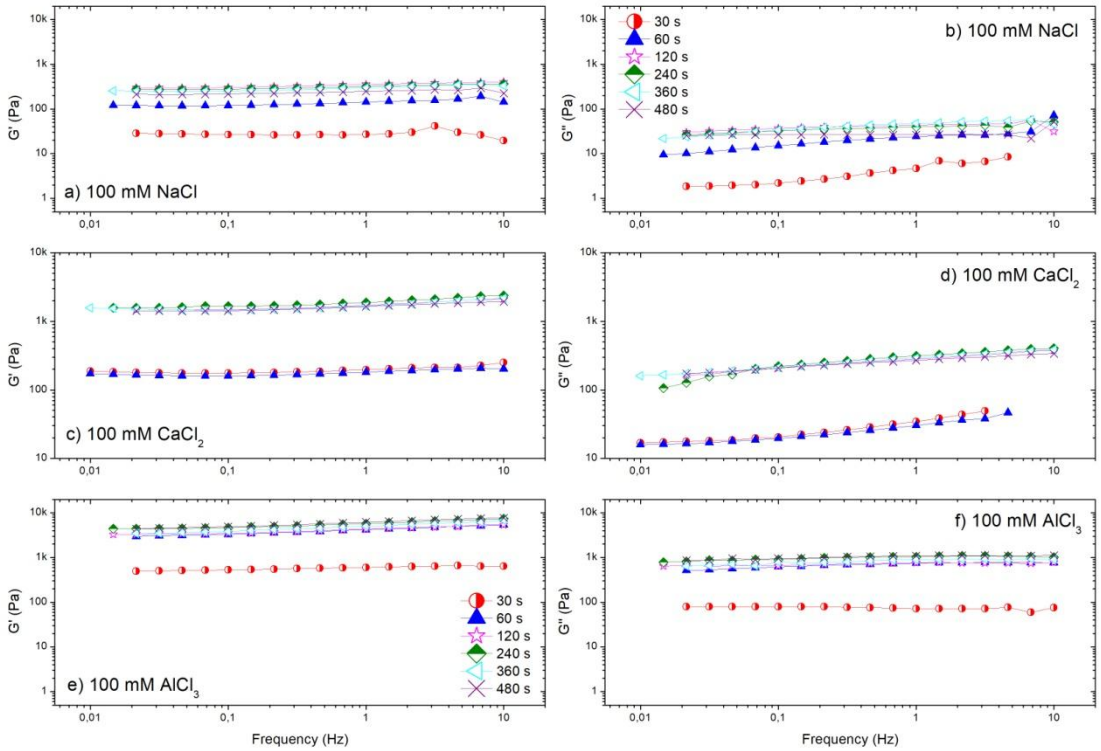

Fig 6.12: Results of FS tests performed on TOCN suspensions (6 mg mL^{-1}) sonicated for different times (30-480 s) and to which 100 mM NaCl (panels a-b), $CaCl_2$ (panels c-d) and $AlCl_3$ (panels e-f) were added after sonication. Panels a-c-e and panels b-d-f report respectively the Elastic Modulus G' and the viscous Modulus G'' values. Measurements were performed at 25±1 °C.

The G' values at 1 Hz as a function of sonication time for NaCl, $CaCl_2$ and $AlCl_3$ are compared in Fig. 6.13. It can be observed that G' increases up to 120 s sonication time and then shows a small reduction (in the case of NaCl) or remains constant (in the case of $CaCl_2$ and $AlCl_3$). The increase of G' is probably due to the fact that the sonication process un-packages the TOCNs exposing more and more carboxylic groups, which act as sites for ion-TOCNs interaction. Moreover it appears that, once

the TOCNs are fully un-packed, Ca^{2+} and, even more, Al^{3+} guarantee much better jelly-like properties than Na^{+}.

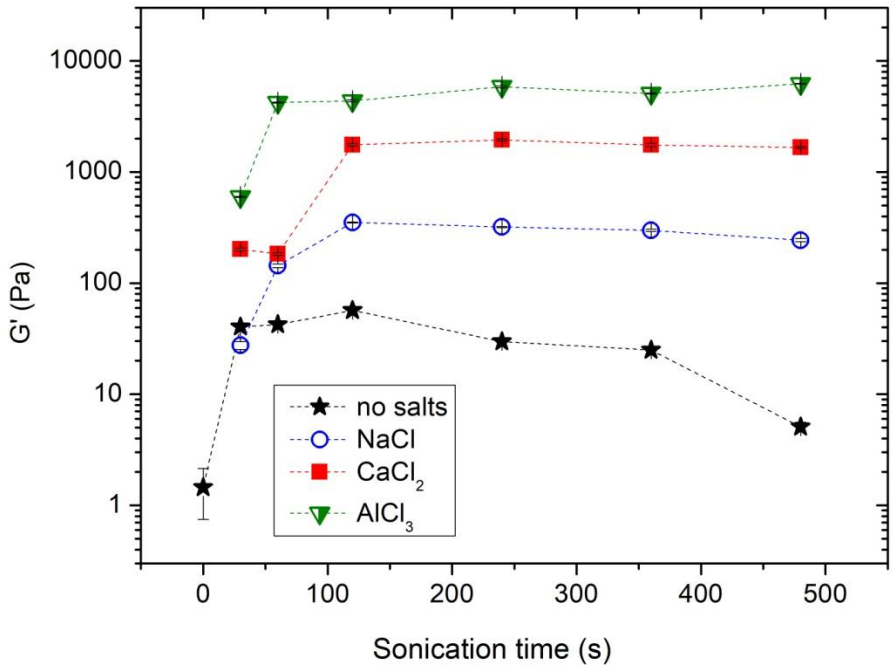

Fig 6.13: Storage modulus G' measured at 1Hz for TOCN hydrogels formed adding 100mM of sodium chloride, calcium chloride and aluminum chloride to TOCN solutions sonicated for variable times. The reported values and error bars (not visible in figure) were evaluated performing a linear fit on FS curves in the frequency range 0.02-2Hz and extrapolating from them the G' value at 1 Hz. As a comparison, also the case of no salt addition is reported (see Section 6.1 for details).

From these measurements it appears that a sonication pre-treatment of at least 120 s is required to form a homogeneous hydrogel with a nearly stabilized G' value. For this reason we compared TOCN hydrogels obtained at a fixed sonication time (equal to 240 s) and adding NaCl (10 mM and 100 mM), $CaCl_2$ (10 mM and 100 mM) and $AlCl_3$ (100 mM) in order to evaluate the effect of salt type and concentrations.

Fig. 6.14 shows the results of frequency sweep tests (panel a and panel b) and flow curves (panel c). It is possible to observe that mechanical properties (in terms of G', G'', viscosity values and viscosity drop points) increase proportionally to cations valence and concentration.

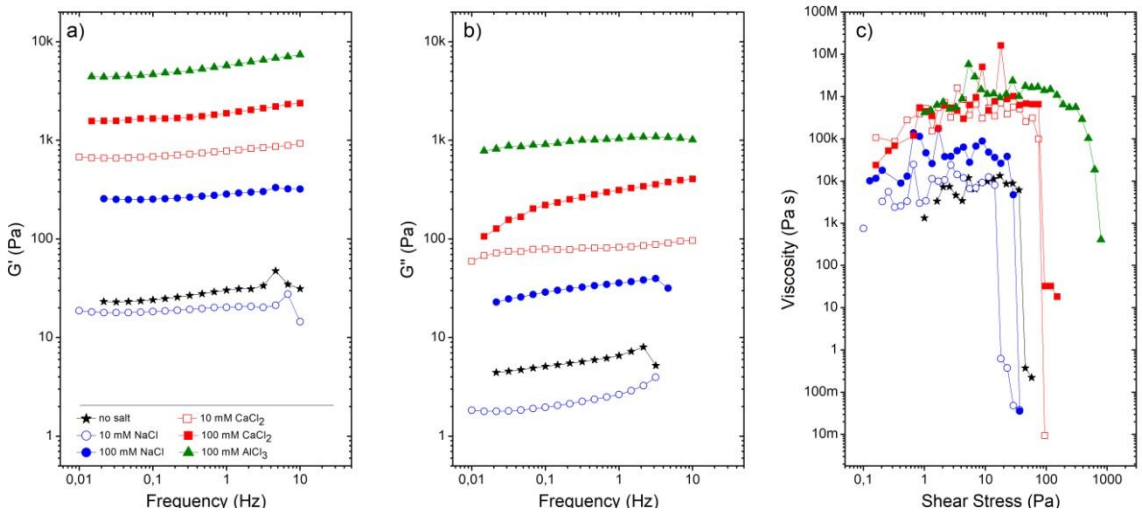

Fig. 6.14: Elastic modulus G' (a) and viscous modulus G'' (b) obtained through frequency sweep tests and flow curves (c) of TOCN hydrogels realized adding different cations (Na, Ca^{2+}, Al^{3+}) and concentrations (10 mM and 100 mM) to suspensions of 6 $mgmL^{-1}$ TOCNs sonicated for 240 s. As a comparison the G', G'' and viscosity values for TOCN solutions, without added salts, are reported too. Sonication time was fixed to 240 s for every sample and measurements were performed at 25±1 °C.

In particular, as shown in Fig. 6.15 (where the G' value at 1 Hz is reported), G' increases linearly with the ratio of cation valence over cation radius (assuming 116 pm Na^{+}, 114 pm for Ca^{2+} and 67.5 pm for Al^{3+}) at a fixed 100 mM cation concentration. The linear trend is typical also of polymeric systems (Yang et al., 2013) and the main difference is the reduced G' modulus achievable with TOCNs, due to their limited capability to entangle.

While the cation valence has a profound influence on the gel stiffness, for a given cation, modest changes appear between the 10 mM and the 100 mM concentrations. The relatively small difference between the 10 mM and the 100 mM $CaCl_2$ TOCN hydrogels might be due to a saturation of the TOCNs sites available for crosslinks.

Applying Flory theory and assuming that the shear modulus G of the system is the G' value over the frequency range explored, the mesh size of the TOCN hydrogels was estimated to be around (28 ± 3) nm, (16 ± 1) nm and (11 ± 1) nm for 100 mM NaCl, $CaCl_2$ and $AlCl_3$ addition, respectively. As a comparison we recall that the mesh size in the case of no salt addition was estimated to be (63 ± 2) nm. As expected, mesh size is inversely proportional to the G' module of the hydrogels.

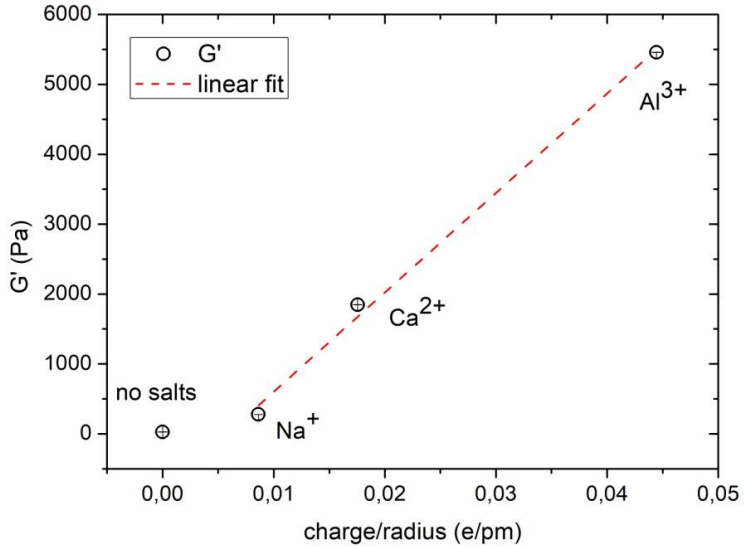

Fig. 6.15: Elastic modulus, evaluated at 1 Hz, for TOCN hydrogels obtained adding 100 mM of different cations to TOCN solutions sonicated for 240 s as a function of cation valence over cation radius. The red line is a linear fit of the experimental data (X=0.999). Error bars (not visible in figure) are in the range 1.5%-5%.

Finally, to better investigate how the combined role of sonication and salt addition (NaCl, $CaCl_2$ and $AlCl_3$) influence the properties of TOCN hydrogels, the dependence of the G' value on the sonication time was analyzed more into details. As already seen, the maximum G' depends on the duration of the sonication pre-treatment and reaches a quite stable value after 120 s sonication. However, looking more closely at the trend of the G' values for longer sonication times, it appears that they can either slightly decrease or increase depending on cation and cation type addition. The dynamics of G' are reported in Fig 6.16a. Assuming the G' value at 120 s of sonication (G'_{120}) to be the highest achievable in each hydrogel, the G' variations ($\Delta G'$) for different sonication times were normalized against G'_{120} as follows: $\Delta G' = \frac{G'_{120} - G'}{G'_{120}}\ 100$.

As visible in Fig. 6.16b, ΔG' scales inversely proportional to the valence of the crosslinking cations, showing that the duration of the sonication pretreatment required to bring the TOCN hydrogel in the most stable state scales proportionally to the cation valence. This evidence is coherent with the results reported in Fig. 6.8, showing that a prolonged sonication treatment reduces the density of crosslink points and, in turn, the G' values. This means that above an optimal sonication treatment, the material tends to liquefy again and the duration of the optimal sonication depends on the ion valence.

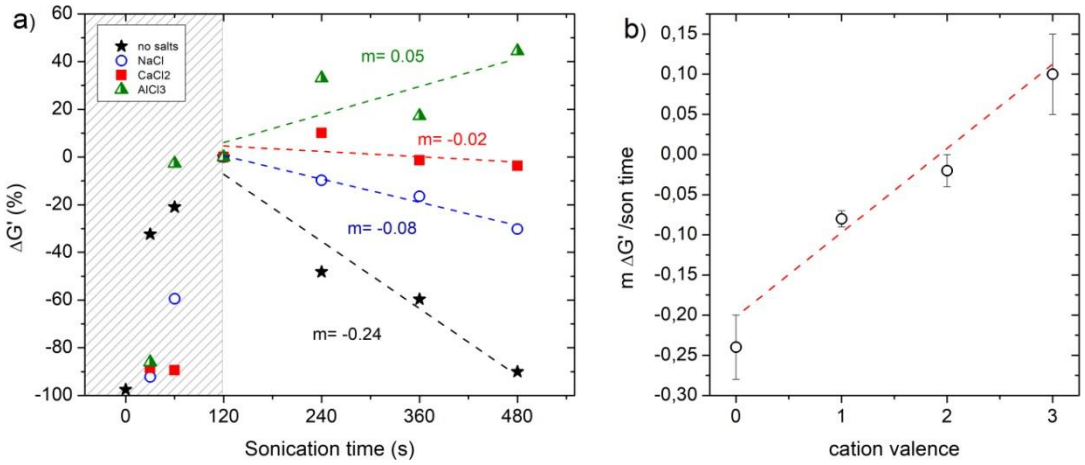

Fig. 6.16: (a) Variation of G'(conventionally evaluated at 1 Hz), expressed in percentage with respect to the G' value at 120 s sonication, as a function of sonication time for TOCN solutions and TOCN hydrogels obtained adding 100 mM NaCl, $CaCl_2$ and $AlCl_3$ to 6 mg mL^{-1} TOCN solutions after sonication. The dotted lines are linear fits. (b) Slope m of the variation of G' versus sonication time (ΔG'/son time) curves as a function of cation valence.

6.3.2 Small angle X-ray scattering measurements

TOCN hydrogels obtained adding 100 mM NaCl, $CaCl_2$ and $AlCl_3$ to TOCN solutions after 240 s sonication were investigated also by SAXS measurements. The SAXS profiles (reported in Fig. 6.17) do not reveal any peak indicating the presence of structurally ordered domains.

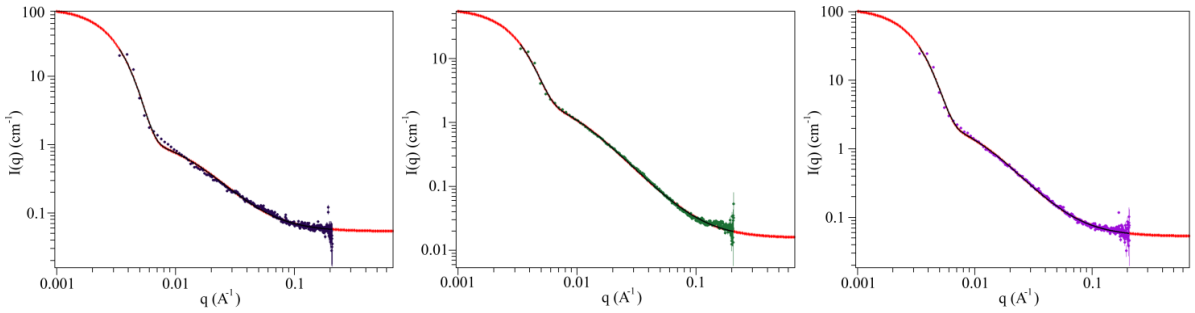

Figure 6.17: SAXS profile of TOCN hydrogels obtained adding 100 mM NaCl (a), $CaCl_2$ (b) and $AlCl_3$ (c) to TOCN solutions (concentration 6 mg mL^{-1}) after 240 s sonication. The dots are the experimental points, while the red line is the fit of the experimental points with the Gauss-Lorentz Gel Model (see Eq. 5.1).

Spectra were fitted with the Gauss-Lorentz model, obtaining two characteristic lengths corresponding to two structural length scales. The resulting values are reported in Table 6.3. While the static correlation length is attributed to the average

size of long-lived entanglements, the dynamic correlation length is correlated to the fluctuation amplitudes between crosslinks (Cohen et al., 1992; Horkay et al., 1996).
A first observation is the fact that both static and dynamic correlation lengths do not easily correlate with the characteristic TOCN nanocrystal size (about 300 x 5 x 5 nm). Moreover, it can be observed that the static correlation length is independent of the crosslinking cation. In the assumption that the static correlation length describes the typical size of high density regions formed by the overlapping TOCNs, it follows that the size of these regions is constant across all samples, irrespectively from the cations. On the other hand, the dynamic correlation length is affected by the strength of the crosslinks created by the different cations and thus it might be correlated with the G' of the hydrogels. The last column of Table 6.4 reports the values of the mesh sizes as estimated from the Flory theory. While there is a large discrepancy between SAXS and Flory theory predictions for gels formed using NaCl, the values reasonably agree for gels formed using multivalent cations.

Table 6.3: Characteristic lengths for TOCN hydrogels obtained by the addition of 100 mM chloride solutions to TOCN solutions after 240 s sonication. Column 2 and 3 report the static and dynamic correlation lengths resulting from SAXS profiles: the reported values and errors are respectively the mean value and standard deviation of measurements over at least 3 different samples. The mesh size values, estimated through rheological measurements, are reported in column 4.

Salt (100 mM)	**Static length (Å)**	**Dynamic length (Å)**	**Mesh size (Å)**
NaCl	416 ± 144	77 ± 7	280 ± 30
$CaCl_2$	474 ± 28	127 ± 11	160 ± 10
$AlCl_3$	469 ± 51	106 ± 13	110 ± 10

6.3.3 State and dynamics of water in TOCNs solutions

Table 6.4 reports the relaxation rates in TOCN hydrogels obtained with 100 mM NaCl (a), $CaCl_2$ (b) and $AlCl_3$ (c) after a sonication treatment lasting different times. The last column reports the mean relaxation time.
Comparing Table 6.4 with Table 6.1 (representing the case of no salt addition), it appears that the number of relaxation rates for sonication longer than 60 s increases from one to two in presence of Na^+ and Ca^{2+} (becoming even three or four in the case of Al^{3+}) suggesting a more complex structure with respect to the un-salted systems. This is coherent with the increase of the G' values reported in the rheological measurements section.

Table 6.4: Relaxation rates with relative abundances (T_{2i}^{-1}, A_i) for TOCN hydrogels obtained adding 100mM of sodium chloride (a) and calcium chloride (b) and aluminum chloride (c) to TOCN solutions sonicated for variable times (30-480 s). The last, gray column shows the mean relaxation time.

a) NaCl

Sonication time (s)	T_{21}^{-1} (s^{-1})	A_1 (%)	T_{22}^{-1} (s^{-1})	A_2 (%)	T_{2m} (ms)
30	0.75	82.2	1.29	17.8	1331
60	0.52	79	0.87	21	1906
120	0.65	76	0.93	24	1548
240	0.64	57	0.79	43	1569
360	0.72	60	1.04	40	1386
480	0.67	34	0.75	66	1503

b) $CaCl_2$

Sonication time (s)	T_{21}^{-1} (s^{-1})	A_1 (%)	T_{22}^{-1} (s^{-1})	A_2 (%)	T_{2m} (ms)
30	0.56	80	1.23	20	1590
60	0.54	74	1.27	26	1581
120	0.51	48	1.06	52	1423
240	0.58	33	1.10	67	1179
360	0.58	33	1.17	67	1145
480	0.67	38	1.20	62	1090

c) $AlCl_3$

Sonication time (s)	T_{21}^{-1} (s^{-1})	A_1 (%)	T_{22}^{-1} (s^{-1})	A_2 (%)	T_{23}^{-1} (s^{-1})	A_3 (%)	T_{24}^{-1} (s^{-1})	A_4 (%)	T_{2m} (ms)
30	0.79	12	1.39	46	3.32	32	10.17	9	592
60	0.67	14	1.39	15	4.39	41	8.62	30	446
120	0.95	9	3.62	34	7.02	58			265
240	0.66	10	1.63	13	5.04	54	8.88	22	371
360	0.73	11	2.46	21	5.90	68			351
480	0.59	12	1.48	13	4.28	55	7.83	20	439

We focus now on NaCl and $CaCl_2$ hydrogels which show two relaxation rates. It is possible to observe that, for sonication times longer than 120 s (that is upon gelation), T_{21}^{-1} and T_{22}^{-1} assume quite constant values irrespectively of the sonication time. Moreover, while T_{21}^{-1} is quite similar for NaCl and $CaCl_2$, T_{22}^{-1} assumes different values for hydrogels produced with either mono- and bi-valent cations. These data are summarized in table 6.5 (column two and three) together with the single component representing the relaxation in TOCN solutions without

salts. We can see that the value of the T_{22}^{-1} component increases passing from NaCl to $CaCl_2$ and is thus correlated with the G' modulus of the hydrogels (values reported in the last column), indicating a strong dependence of the elastic properties of the hydrogel on its local structure, mediated by both the presence of cations as well as hydrogen interactions.
As the T_{22}^{-1} component seems not to change significantly with sonication time, it is possible to compare their relative amplitudes A_{22}, as shown in Fig. 6.18.

Table 6.5: Water relaxation rates T_{21}^{-1} and T_{22}^{-1} and Elastic modulus G' for TOCN solutions (no salts) and TOCN hydrogels obtained adding 100 mM NaCl and $CaCl_2$ salts after sonication of 6 mg mL^{-1} TOCN solutions. The reported relaxation rates value and error refer respectively to the mean value and SD over measurements performed for sonication times longer than 120 s (that is upon gelation in the case of TOCN hydrogels). The Elastic modulus G' is the value at 1Hz in the case of 240 s sonication, evaluated performing a linear fit on FS curves in the frequency range 0.02-2Hz.

salt	T_{21}^{-1} (s^{-1})	T_{22}^{-1} (s^{-1})	G' (Pa)
no salts	0.70 ± 0.02	-	30 ± 2
NaCl	0.67 ± 0.04	0.88 ± 0.13	290 ± 5
$CaCl_2$	0.59 ± 0.06	1.13 ± 0.06	1945 ± 40

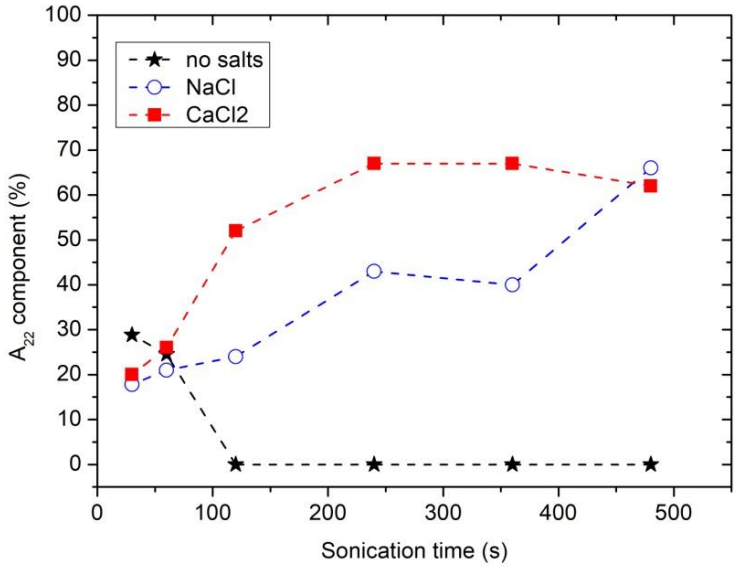

Fig. 6.18: Amplitudes of the A_{22} components as a function of sonication time for 6 mg mL^{-1} TOCN solutions (black stars) and TOCN hydrogels obtained adding 100 mM NaCl (blue circles) and $CaCl_2$ (red squares) after sonication.

It is possible to observe that the A_{22}^{Ca2+} component saturates for times longer than 120 s, suggesting that the TOCNs have reached a stable configuration. On the contrary, the A_{22}^{Na+} component increases supporting the idea that the structure of TOCN hydrogels obtained using NaCl is weak and dependent on the initial conditions, probably because the electrostatic interaction of Na^+ is not strong enough to structure the hydrogel. These evidences correlate with the results reported in Fig. 6.16, showing that the duration of the sonication pretreatment required to bring the TOCN hydrogel in the most stable state (corresponding to higher G' values) depend on cation valence. Finally, as already seen previously, the A_{22}^{sol} component of TOCN solutions disappears for sonication times longer than 120s.

6.4 Conclusions

In this Chapter, we investigated the sol-gel transition of TOCN solutions. In particular the effects of the two factors that strongly affect the assembly of TOCNs in gel-like supramolecular structures (i.e. the energy release by sonication and the addition of cations) were analyzed in details. Measurements were performed combining predominantly Rheology and LF-NMR and highlighted the following results:

1) TOCN solutions at concentrations higher than 5 mg mL^{-1} undergo a sol-gel transition apparently similar to that observed for flexible polymer chains. Even if a weak hydrogel results from non exhaustive sonication, a clearer gel-like behavior is obtained if sonication is followed by salt addition. Compared to truly polymeric systems formed by long, entangled chains, short and rigid TOCNs yet form gels thanks to the strong electrostatic interactions generated by hydrogen bonds and between cations and carboxyl groups.

2) The gelation mechanism depends on the cation. In particular, a different behavior was observed for hydrogels formed by adding mono- or multi-valent cations. Monovalent NaCl gives rise to softer hydrogels with wider meshes. The weaker interactions created by monovalent cations permit them to disperse homogeneously in the hydrogel phase independently on the order of salt addition and sonication. On the contrary, multivalent $CaCl_2$ and $AlCl_3$ produce homogeneous hydrogel phases only if cations are added to solutions where TOCNs are already well dispersed by the sonication and thus are free to diffuse around isolated TOCNs. This suggests that a strong interaction takes place between the multivalent cations and the non-sonicated fibres that form inhomogeneous macroscopic aggregates. These

aggregates limit the efficacy of the sonication treatment, contrast the dispersion of isolated nanocrystals and hinder the formation of a homogeneous gel phase.

3) Considering TOCN hydrogels obtained adding chloride salts with different valences (NaCl, $CaCl_2$ and $AlCl_3$) after a fixed 240 s sonication pre-treatment, it appears that the rheological properties (G', viscosity and viscosity drop point) increase proportionally to cations valence and concentration. Moreover the number of relaxation rates required to describe the water relaxation increases with respect to the un-salted systems, showing the formation of more complex three-dimensional architectures. Finally, SAXS analysis shows the presence of high density domains with dimensions of around 40-50nm (static correlation length), which are independent of the added cation and where water is confined. The water confined in these regions exchanges slowly with the less structured regions, giving rise to a compartmentalized relaxation behavior, as confirmed by NMR.

4) Evaluating the effect of the sonication pre-treatment, it results that the stability and elasticity of the TOCN hydrogels depends on its duration, being Ca^{2+} more effective than Na^{+} in creating strong and stable hydrogels. This fact is confirmed by both NMR and rheological data. In particular, the amplitude of the magnetization component relaxing with rate T_{22}^{-1} (related to the overall number of water molecules confined in the rigid domains) reaches its maximum after 120 s sonication in the case of Ca^{2+}, while requires longer times in the case of Na^{+} for confining the same amount of water. These findings suggest that, in the case of Na^{+}, non-specific electrostatic interactions take place, which necessitate of extensive sonication to break the hydrogen bonds between the TOCNs and forms weaker gels. On the contrary, in the case of Ca^{2+}, a specific coordination between TOCN carboxylic groups and calcium ions contributes, in line with the interaction models of cations with nanocellulose fibres proposed by (Dong et al., 2013a) and with the stability of metal carboxylate complexes (Stendahl et al., 2006).

In conclusion, despite their non-polymeric and rigid nature, TOCNs undergo a sol-gel transition process similarly to polymers and produce hydrogels with good mechanical properties. The transition is very fast (few seconds) thanks to the short length of the TOCNs and the mechanical properties of the hydrogels can be tuned by changing both cation valence and sonication pre-treatment.

Chapter 7:
TOCNs IONOTROPIC GELATION

As seen in Chapter 6, TOCNs are excellent building blocks for hydrogels formation, particularly in presence of multivalent counter ions, being able to form physical or chemical cross-linked 3D networks entrapping large amount of water. However, in order to increase their possibilities and broader their fields of application, it is important to control the local structure of the hydrogels and develop strategies to tune their sizes and shapes in a precise and reproducible manner.

A commonly used method to form polyelectrolytes hydrogels, and in particular polysaccharides hydrogels, exploiting the diffusion of multivalent counter ions, is ionotropic gelation (Patil et al., 2010, 2012). In the external ionotropic gelation process, a polyelectrolyte suspension is dropped in a solution containing the counter ion, which gradually moves inward from the outer counter ion reservoir to the inner hydrogel meanwhile it is formed. In inverse ionotropic gelation, instead, the counter ions diffuse outward from an inner discrete core into an external polyelectrolyte pool (Leong et al., 2016).

The aim of the work reported in this Chapter 7 is to investigate the mechanism and dynamics of TOCNs solutions ionotropic gelation in presence of calcium ions. While in Chapter 6, the attention was mainly devoted to the bulk properties of hydrogels obtained by simple mixing of TOCNs and cations, here we focus on the spontaneous mechanism and kinetics of hydrogel formation with the aim of using this water-in-water strategy to fabricate microstructures with tunable size and shape. More into details, the two processes controlling the gelation, that is Ca^{2+} diffusion and interaction between Ca^{2+} ions and TOCNs, were investigated respectively using a Ca^{2+} sensitive indicator and exploiting FTIR spectroscopy. Section 7.1 is focused on the case of external ionotropic gelation, while section 7.2 concerns the inverse ionotropic gelation process.

7.1 External Ionotropic Gelation

External gelation of TOCNs solutions can be performed by extruding concentrate TOCNs solutions (8 mg mL^{-1}) inside a $CaCl_2$ (0.1-2 M) gelling aqueous solution. Various TOCNs-Ca^{2+} hydrogel shapes (beads, wires, disks) and sizes were obtained by changing the pouring method and the amount of TOCNs solution and Ca^{2+} concentration, as shown if Fig. 7.1.

In particular, a microfluidic flow system, with a pressure controller and an output nozzle (400 μm diameter) was used to obtain TOCNs gel wires and beads with different sizes. The wires (Fig. 7.1a) were obtained by extruding the TOCNs solution from the nozzle directly inside the $CaCl_2$ pool, while the beads (Fig 7.1b) were obtained by dropping the TOCNs solution. Wires and beads of different sizes were obtained changing the pressure or the duration of the pressure pulse impressed by the system. Hydrogel disks were instead obtained using a spin-coater by pouring the TOCNs solution (8 mg mL^{-1}) on a rotating $CaCl_2$ (0.1-2 M) aqueous solution (Fig 7.1c).

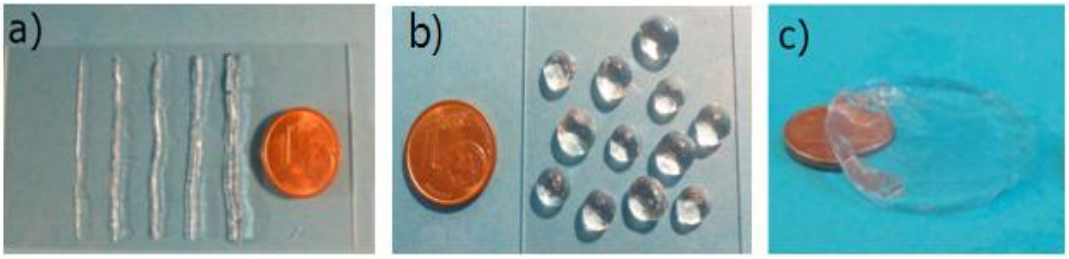

Fig 7.1: TOCNs-Ca^{2+} hydrogel structures obtained via external ionotropic gelation: (a) wires obtained by extruding a selected amount of 8 mg mL^{-1} TOCNs solution from a nozzle directly in 1 M $CaCl_2$ solution at different pressures, (b) beads obtained by dropping the TOCNs from a nozzle in $CaCl_2$ solution, (c) disk obtained by pouring TOCN solution onto a rotating 1 M $CaCl_2$ solution.

The dynamics of external ionotropic gelation indicates that the process starts from the interface with the Ca^{2+} solution and proceeds towards the inner part of the incipient TOCNs-Ca^{2+} hydrogels. The attention is focused now on the specific case of TOCNs-Ca^{2+} hydrogel beads, as shown schematically in Fig. 7.2a, but the reasoning is the same for the other hydrogel structures produced by external ionotropic gelation. The time course of hydrogel formation is qualitatively shown in Fig. 7.2b and Fig 7.2c: the bead (diameter 1 cm) left for 30 s in Ca^{2+} solution appears to be constituted of an outer gel-like shell and an inner liquid core (Fig. 7.2b) and the liquid core is progressively reduced obtaining, after 10 min, a macroscopically homogeneous, self-standing TOCNs-Ca^{2+} hydrogel bead, as shown in Fig. 7.2c.

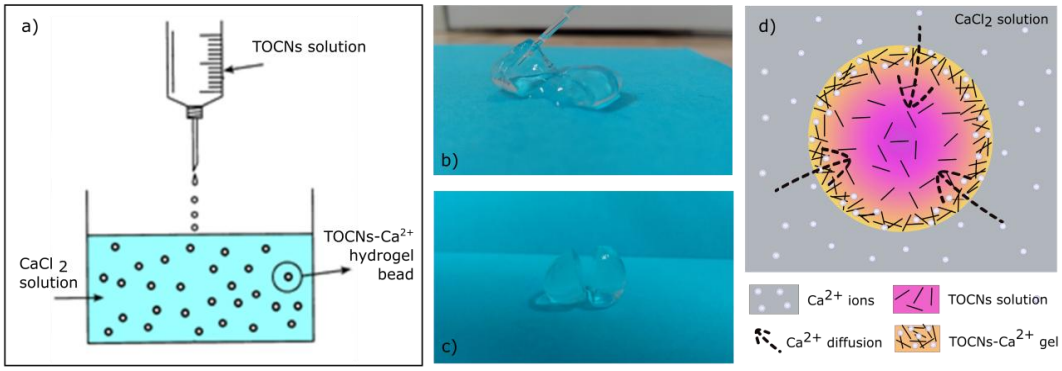

Fig 7.2: (a) Simplified scheme of the external ionotropic gelation procedure used to obtain TOCNs-Ca^{2+} hydrogel beads. TOCNs-Ca^{2+} hydrogel bead after (b) 30 s and (c) 10 min in 1M $CaCl_2$ solution. (d) Sketch view of the external gelation process mechanism.

The observed immediateness of the sol-gel transition upon contact of TOCNs with Ca^{2+} ions indicates that the spatiotemporal events are driven by the diffusion of the small Ca^{2+} ion in the TOCNs solution and the transition process occurs where Ca^{2+} and TOCNs meet, as shown in the sketch figure (Fig 7.2d). The interaction between Ca^{2+} ions and TOCNs was investigated by FTIR spectroscopy as reported in Sub-Section 7.1.1, while the results of the diffusion kinetics studied, performed using a Ca^{2+} sensitive indicator, will be shown in Sub-Section 7.1.2. Finally, in Sub-Section 7.1.3 the results of the studies performed to determine the steady-state concentration of Ca^{2+} required to maintain the gel network are reported.

7.1.1 FTIR Spectra Analysis

FTIR spectroscopy was used to monitor the interaction between calcium ions and carboxylate groups on the surface of TOCNs, exploiting the fact that the coordination between metal ions and carboxylate groups induces a shift of the vibrational frequency of these groups (Deacon, 1980; Nakamoto, 1986; Nara et al., 1996). Spectra of TOCNs-Ca^{2+} hydrogel samples were compared with those of TOCNs films at pH 7 (where the counter ion is Na^{+}) and changes in the features were used to monitor the presence and the distribution homogeneity of Ca^{2+} inside TOCNs-Ca^{2+} hydrogels (Papageorgiou et al., 2010). Before spectra acquisition, TOCNs-Ca^{2+} hydrogel samples were left in water for 3 days to let them release the non-coordinated Ca^{2+} and then dried in an oven at 60°C to for 24 h to minimize the water feature in the spectra.

As visible in Fig. 7.3, both asymmetric and symmetric carboxylate bands undergo a wavenumber shift in TOCNs-Ca^{2+} hydrogels, the first band (asymmetric) moving to smaller wavenumbers, the second one (symmetric) to higher wavenumbers.

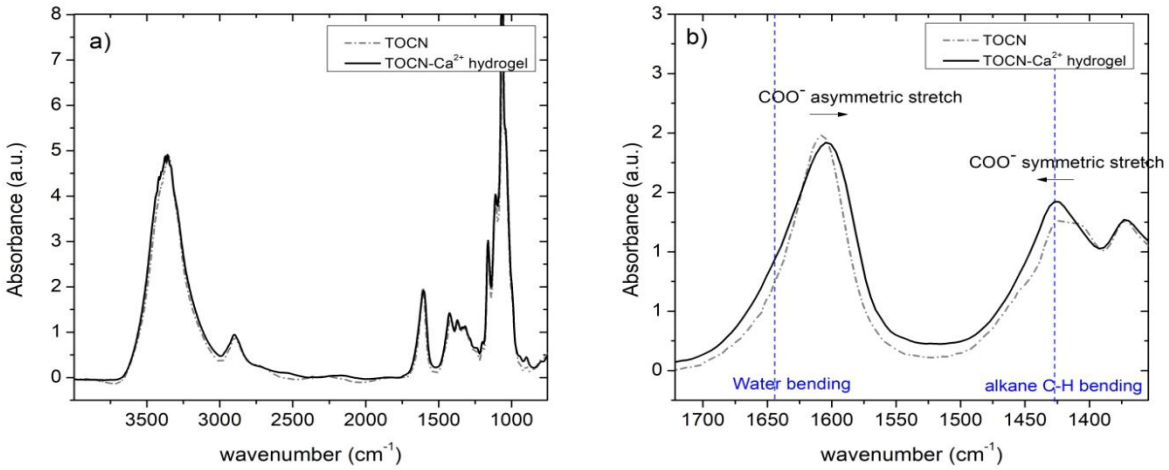

Fig. 7.3: (a) FTIR spectra of a TOCN film (gray dotted line) prepared by casting a solution of TOCNs at pH 7.0 and of a dried TOCN-Ca^{2+} gel bead fragment obtained by external ionotropic gelation (black continuous line) (b) Zoom on the 1300-1750 cm^{-1} range where the carboxylate stretching bands are located, with assignation of the main vibrational bands present in the region. The dashed vertical lines indicate the wavenumbers where water bending vibration mode and alkane C-H bending mode are located. The spectra were acquired in transmission mode with 1 cm^{-1} spectral resolution on a micro-FTIR Nicolet iN10 instrument equipped with a liquid nitrogen cooled detector.

The analysis of FTIR spectra was performed after intensity normalization and deconvolution of partially overlapping peaks as explained in Chapter 5. Here we recall that the bands at around 1610 cm^{-1} were analyzed performing a double gaussian fit procedure to separate the contribution of the asymmetric carboxylate stretching vibration from that of water (at 1640 cm^{-1}). Moreover, the bands at around 1420 cm^{-1} were analyzed in TOCNs films performing a double gaussian fit procedure to separate the contribution of the symmetric carboxylate stretching vibration from that of alkane -C-H vibrations (at 1425 cm^{-1}). The obtained alkane peaks were then subtracted from TOCNs-Ca^{2+} spectra to isolate the symmetric carboxylate stretching vibration peak. Fig. 7.4 shows an example of the deconvolution procedure result for both TOCN films (gray dots and lines in figure) and TOCN-Ca^{2+} (black dots and lines in figure). In particular, the points refer to experimental data, while the lines are the results of the deconvolution fitting procedure (dashed lines for deconvolved peaks and continuos lines for their sum).

The results, in terms of peak centre, peak intensity and separation $\Delta\nu$ between asymmetric and symmetric peaks are reported in Table 7.1.

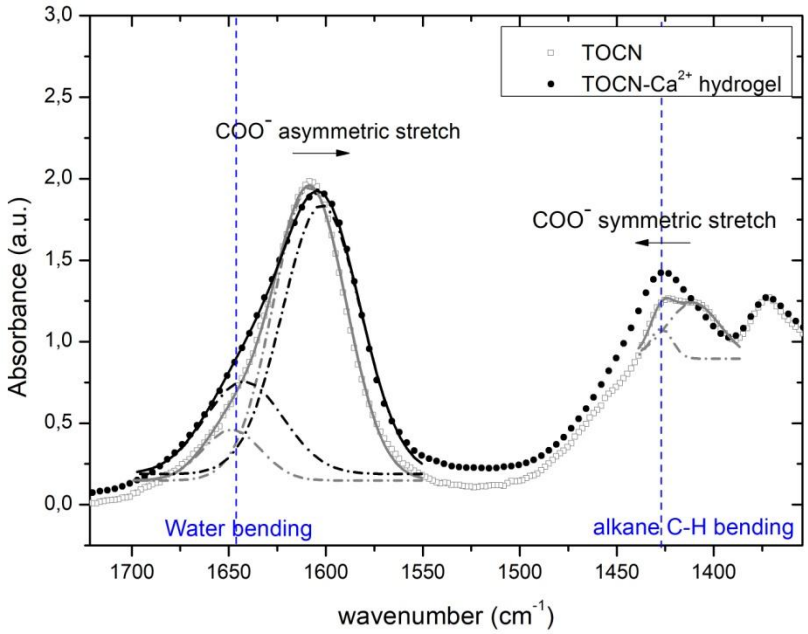

Fig. 7.4: Example of the deconvolution of carboxylic groups bands for both TOCN films (gray dots and lines) and TOCN-Ca^{2+} hydrogels (black dots and lines). Points refer to experimental data, while the lines are the results of the deconvolution fitting procedure (dashed lines for deconvolved peaks and continuos lines for their sum). The bands at around 1610 cm^{-1} were analyzed performing a double gaussian fit procedure for both films and hydrogels to separate the contribution of the asymmetric carboxylate stretching vibration from that of water (at 1640 cm^{-1}). Instead, the bands at around 1420 cm^{-1} were analyzed in TOCNs films performing a double gaussian fit procedure to separate the contribution of the symmetric carboxylate stretching vibration from that of alkane -C-H vibrations (at 1425 cm^{-1}) and the obtained alkane peaks were then subtracted from TOCNs-Ca^{2+} spectra to isolate the symmetric carboxylate stretching vibration peak.

Table 7.1: Results of spectral analysis performed on TOCN films and TOCN-Ca^{2+} hydrogels. Peak centers, peak absorbance intensity for both COO^- asymmetric and symmetric bands and separation $\Delta\nu$ between asymmetric and symmetric peak are reported. Values and errors refer to mean values and standard deviation over at least 10 measurements.

	TOCN-film	TOCN-Ca^{2+} hydrogels
ν (COO^- asymm) [cm^{-1}]	1608. 3 ± 0.3	1601 ± 1
ν (COO^- symm) [cm^{-1}]	1410 ± 3	1419 ± 2
I (COO^- asymm) [a.u.]	2.0 ± 0.2	1.8 ± 0.1
I (COO^- symm) [a.u.]	1.2 ± 0.3	1.05 ± 0.05
$\Delta\nu$ [cm^{-1}]	198 ± 3	182 ± 3

It is possible to see that the separation between the stretching vibrations of carboxylates decreases from 198 cm^{-1} to 182 cm^{-1} when Ca^{2+} substitutes Na^{+}. Similar values were reported in literature for Ca^{2+}-alginate complexes (Papageorgiou et al., 2010) and related to a ''pseudo-bridged'' unidentate arrangement between Ca^{2+} ions and alginic acid.

To investigate the Ca^{2+} distribution inside the TOCN-Ca^{2+} gels, spatial maps were automatically acquired by selecting a given number of points per area over different parts of a bead. In particular, a slice of hydrogel bead was cut, left in water for 3 days to release the non-coordinated Ca^{2+}, dried and then a surface of 300 × 1300 μm^2 was mapped with 100 μm spacing for both a central and an edge zone of the dried NC-Ca^{2+} gel bead slide. In the case of the edge zone, spectra related to points closer than 400 μm from bead edge were not reported because of artifacts due to surface effects on the acquisition.

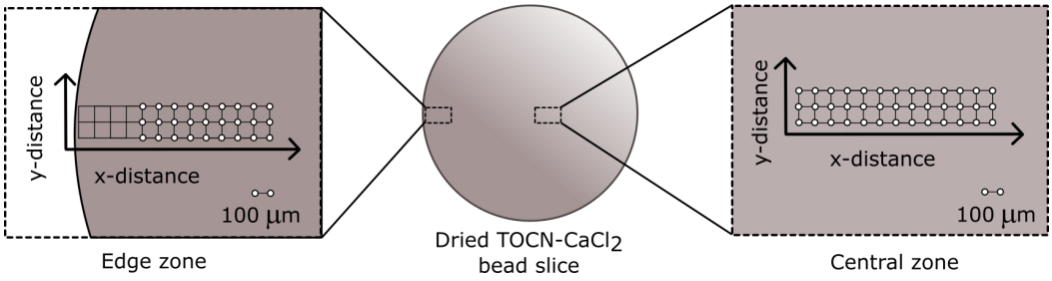

Fig 7.5: Sketch of the grid for acquisition of FTIR spectra maps on an edge zone and on a central zone of a dried NC-Ca^{2+} hydrogel bead slice. In both cases a surface of 300 × 1300 μm^2 was mapped with 100 μm spacing. In the case of the edge zone, spectra related to points closer than 400 μm from bead edge were not reported because of artefacts due to surface effects on the acquisition.

The map of the wavenumber separation between the two carboxylate bands is reported in Fig. 7.6 for both the edge area (Fig 7.6a) and the central area (Fig 7.6b) of the sample. As a comparison, the wavenumber separation of a TOCN film is shown as the black bold line on the z- axis.

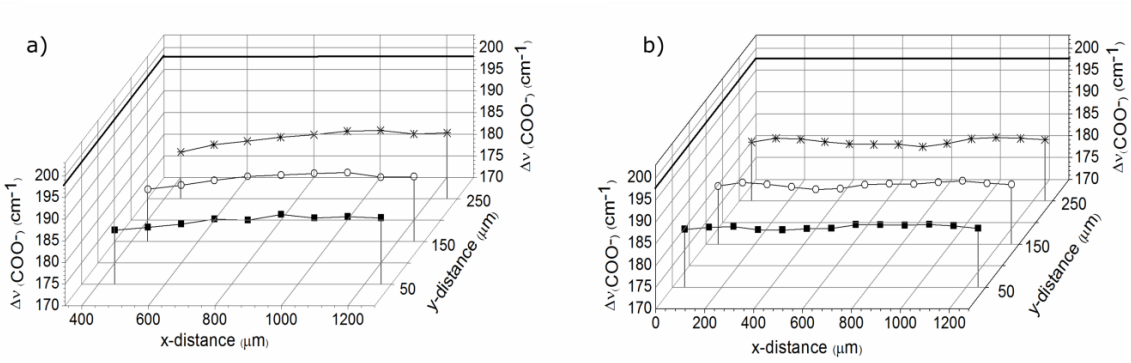

Fig 7.6: Separation between the centers of COO^- asymmetric and COO^- symmetric peaks for an area (a) near the surface and (b) at the center of the sample. x- and y-distances refer to the spatial coordinates of the 300 × 1300 μm^2 area mapped. As a reference, the same distance for TOCN films was found to be 198 ± 3 cm^{-1} (black bold line on the z- axis in Fig.).

The presence of a shift in the carboxylic bands of TOCN-Ca^{2+} samples with respect of those in TOCN films and the persistence of this shift for all the mapped points (Fig. 7.6) is a confirmation that the phenomenon at the basis of ionotropic gelation is the coordination between Ca^{2+} ions and TOCN carboxylic groups and that this coordination occurs both in edge and central areas. Moreover, the persistence of the shift after 3 days of TOCN-Ca^{2+} beads incubation in water shows that the coordination between calcium ions and TOCN crystallites is not disrupted by a long permanence in water.

The intensity of the symmetric and asymmetric COO^- vibrational bands for each experimental point of Fig. 7.6 is reported in Fig. 7.7.

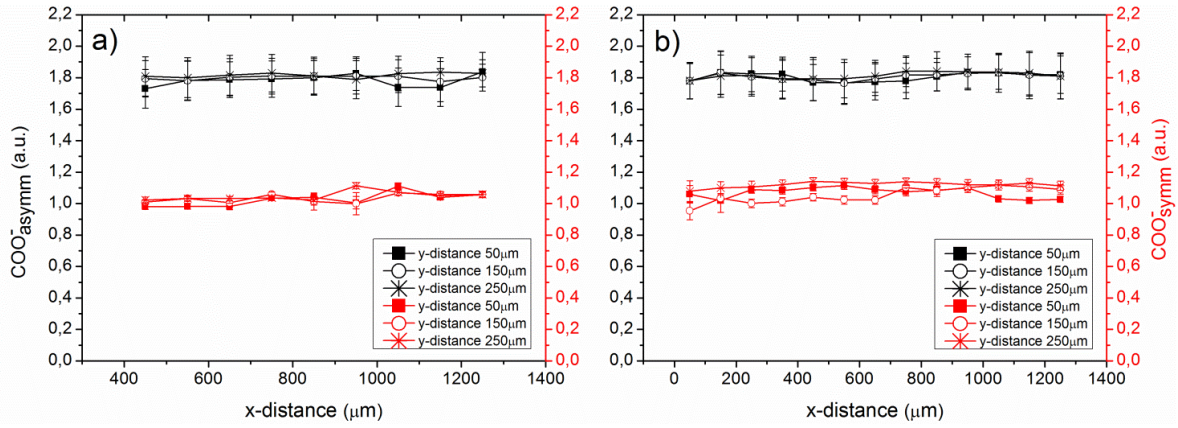

Fig 7.7: Intensity of COO^- asymmetric (black traces) and COO^- symmetric (red traces) absorption peaks. The x and y distances reported on the x-axis and in the legend refer, respectively, to the xy center position of the 100 × 100 μm area corresponding to each map point spectrum. Left panel and right panel refer to an area near the surface and at the center of the dried sample, respectively.

It is visible that the intensity values are constant for both the mapped areas and comparable with the intensities of pure TOCN films (see Table 7.1). The constant values of peak heights for the different mapped points suggest that the Ca^{2+}-COO^- coordination is uniform in the whole bead volume. Moreover, a peak height of Ca^{2+}-COO^- comparable with that of carboxylic bands in TOCN films suggests that the majority of the COO^- groups are involved in the Ca^{2+}-COO^- interaction.

7.1.2 Ca^{2+} diffusion and external ionotropic gelation kinetics

The dynamics of Ca^{2+} diffusion in the incipient hydrogels obtained by external ionotropic gelation was investigated by monitoring the advancement of the sol-gel front through the change in color (from purple to yellow) of murexide dye upon Ca^{2+} complexation. A similar approach was used by G. Skjak-Braek *et al*. to visualize the migration of the gelling zone in calcium-alginate gels (Skjåk-Bræk et al., 1989). Fig. 7.8 shows the experimental set-up used to visualize the Ca^{2+} reaction front propagation. It consists of a plastic cuvette filled with NC (8 mg mL^{-1}) and murexide (20 μM), closed at the opened extremity with a low cut-off dialysis membrane and immersed into a Ca^{2+} solution. Only Ca^{2+} diffusion from outside to inside the cuvette is allowed and the diffusion of Ca^{2+} occurs in one dimension along the cuvette axis. The experiment was repeated at various concentrations (0.1 M, 1 M and 2 M) of Ca^{2+} in the diffusing gelling solution and at fixed temperature (25.0 ± 0.5) °C. The advancement of the Ca^{2+} diffusion front was measured recording the distance of the yellow-purple interface from the dialysis membrane (see Fig. 7.8b).

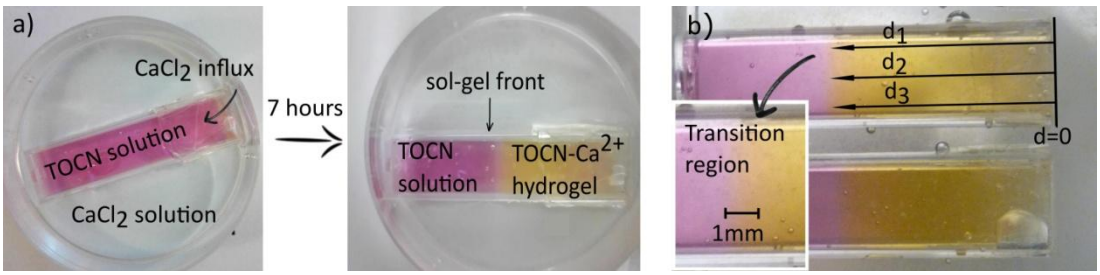

Fig 7.8: Pictures of the experimental set-up used to visualize the diffusion front of Ca^{2+} ion in the incipient TOCN-Ca^{2+} hydrogel obtained by external ionotropic gelation. (a) Pictures of a cuvette filled with NC (8 mg mL^{-1}) and murexide (20 μM) after 5 min and 7 hours immersion in 1 M $CaCl_2$ solution; the cuvette containing the TOCN-murexide solution is closed at the opened extremity with a dialysis membrane to allow only Ca^{2+} diffusion from outside to inside the cuvette. (b) Advancement of the diffusion front. The inset shows that a transition region of the change in color of murexide is present. The arrows indicate the three distances (d_1, d_2 and d_3) used to calculate the average value of the diffusion front.

The images of the reaction front revealed that a narrow region (about 1 mm) of gradual change of the solution color is present (as shown in the inset of Fig. 7.8b). In the image analysis, we measured the distance from the membrane to the middle of this transition region. For each image three distances were measured and the sol-gel front was then expressed as the mean value of the three measurements. As the distance measurement uncertainty, we considered the maximum value between the standard deviation over the three measurements and the half-thickness of solution color front (0.5 mm). The advancement of the color change is considered a reliable estimation of the flux of the Ca^{2+} ions through the gel. In fact, a negligible Ca^{2+} amount reacts inside the gel, due to the low concentration of the carboxylate groups (6.7 mM) and of murexide (20 μM) and the large amount of Ca^{2+} ions present in the external $CaCl_2$ reservoir that can be considered constant.

The linear relationship obtained between the advancement of color change profile (that is the distance d) and the square root of time ($t^{1/2}$) reported in Fig. 7.9a confirms that gelation is controlled by the diffusion of Ca^{2+} ions (Braschler et al., 2011; Nobe et al., 2005; Wu et al., 2011).

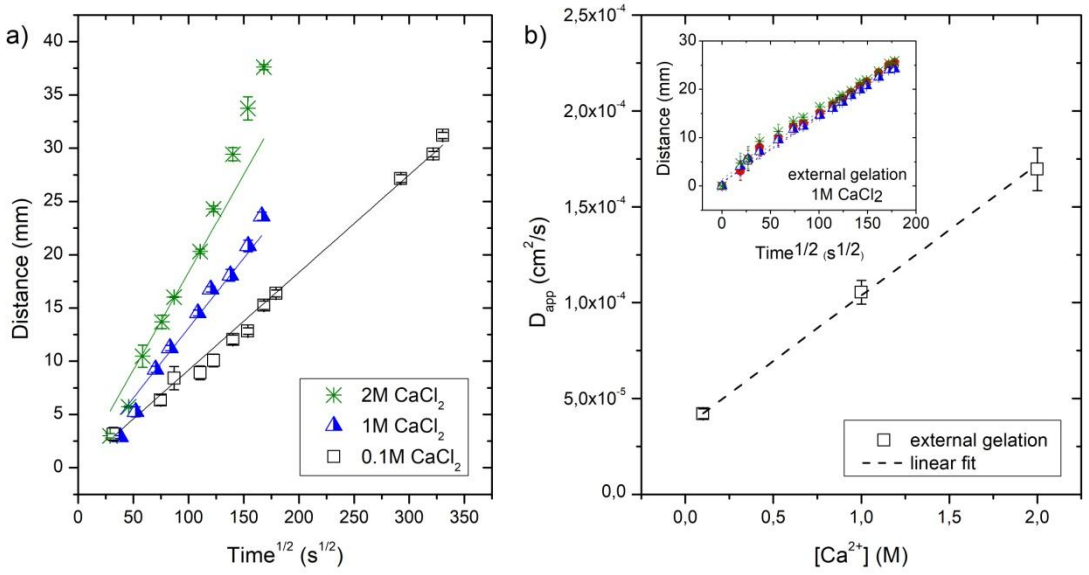

Fig 7.9: a) Sol-gel front distance from dyalisis membrane as a function of square root of time for constant concentration of TOCN solution (8 mg mL^{-1}) and murexide (20 μM) and different $CaCl_2$ concentrations in the external bath solution. The points and errors are the mean value and SD, respectively. The lines are linear fits (with intercept fixed to 0) performed on each set of data. The slopes resulting from the linear fits are (92 ± 1) μm $s^{-1/2}$, (139 ± 6) μm $s^{-1/2}$ and (184 ± 6) μm $s^{-1/2}$ respectively for 0.1 M, 1 M and 2 M $CaCl_2$ solutions. b) Apparent diffusion coefficients (D_{app}) of Ca^{2+} in the incipient gels at T = 25 °C and variable Ca^{2+} concentration. All the experiments were performed in triplicate and example of the three sets of data is shown in the inset for the case of 1 M $CaCl_2$ solution.

By fitting the experimental data to a straight line $d = St^{1/2}$, we obtained the slope S from which the apparent diffusion coefficient (D_{app}) for each sample can be calculated according to the Einstein-Stoke equation $d = (2D_{app})^{1/2}$ (details about the reaction–diffusion kinetics are reported in the Appendix "Reaction-diffusion models"). The results are reported in Fig. 7.9b.
The obtained D_{app} values are comparable with those found by Z. L. Wu *et al*. (2.4 × 10^{-5} cm^2 s^{-1}) studying gelation of a PBDT polyanion 2 wt % solution induced by a 0.5 M Ca^{2+} solution and M. Nobe *et a*l. (1.62 × 10^{-5} cm^2 s^{-1}) studying liquid crystalline gel formation upon Ca^{2+} ion diffusion in Curdlan 5 wt % solutions from a 0.7 M $CaCl_2$ solution (Nobe et al., 2005; Wu et al., 2011). Differently from these materials, which consist in gels made of flexile polymer chains, TOCN-Ca^{2+} hydrogels are due to the assembly of supra-macromolecular rigid structures, that is NC crystallites. The similarity of the diffusion coefficients suggests that in this regard the behavior of NC crystallites is similar to that of polymeric materials.

To evaluate the real diffusion coefficient of Ca^{2+} ions through the TOCN-Ca^{2+} hydrogel, the experimental data were analyzed according to a model that relates front propagation kinetics and Ca^{2+} diffusion (Braschler et al., 2011; Nobe et al., 2005). The diffusion coefficient of this cation inside the gels was estimated through the formula (details are reported in the Appendix ''Reaction-diffusion system models''):

$$D \approx \frac{\rho_G}{\rho_S} D_{app} \qquad \text{(Eq. 7.1)}$$

where D_{app} is the experimental apparent diffusion coefficient, ρ_G the critical salt concentration for forming the gel (dependent on TOCN-Ca^{2+} interaction and TOCN concentration) and ρ_s the salt concentration in the external $CaCl_2$ solution. Since a ρ_G value of 39 ± 6 mM (for TOCN concentration 9 ± 1 mg mL^{-1}) is estimated from the Ca^{2+} release measurements as the steady-state Ca^{2+} concentration in the hydrogels (as will be explained in Sub-Section 7.1.3) the true diffusion coefficient of Ca^{2+} ions in TOCN-Ca^{2+} gels (NC concentration 8 ± 1 mg mL^{-1}) is (4.5 ± 1.1) × 10^{-6} cm^2 s^{-1}.
The calculated D value is of the same order of the self-diffusion coefficient of Ca^{2+} ions in free water (7.9 × 10^{-6} cm^2 s^{-1}) (Haynes, in Handbook of Chemistry and Physics, 2014-2015), showing that the Ca^{2+} ions can freely diffuse through the gel. The value is moreover compatible with those found by T. Braschler *et al*. for Ca^{2+} ions in alginate gels (8 ± 1 × 10^{-6} cm^2 s^{-1}) and by M. Nobe et al. for Ca^{2+} in Curdlan (≈ 5.0 × 10^{-6} cm^2 s^{-1}) (Braschler et al., 2011; Nobe et al., 2005).

7.1.3 Steady-state Ca^{2+} concentration

The steady-state concentration of Ca^{2+} required to maintain the gel network of TOCN-Ca^{2+} hydrogels was estimated on the basis of the amount of excess Ca^{2+} ions released in water by TOCN-Ca^{2+} hydrogels incubated in aqueous solution after the gelation process. To this purpose, disk-shaped hydrogels were produced by adding excess Ca^{2+} to a known volume of 9 mg mL^{-1} TOCN solution. The $CaCl_2$ solution was let diffuse between TOCN crystallites and a compact hydrogel disk was formed. The coarse excess of Ca^{2+} not interacting with the hydrogel was removed by rinsing with distilled water for two minutes. Then the disk was incubated into 50 mL of water. The Ca^{2+} release was monitored over time and the Ca^{2+} retained by the hydrogel was calculated as difference from the starting Ca^{2+} amount. At the end of the kinetic, the Ca^{2+} retained in the gel was measured after gel disruption by sonication. Since a quantitative determination of the released Ca^{2+} is necessary, a colorimetric method based on the shift of the absorbance peak (from purple to yellow) of murexide dye (5,5'-Nitrilodibarbituric acid monoammonium salt) upon complexation with Ca^{2+} was used. The method is well assessed, however some preliminary tests were performed to check its reliability under our experimental conditions (Pollard and Martin, 1956; Tammelin and Mogensen, 1952).

Fig. 7.10 shows the changes of murexide absorption peak at different Ca^{2+} concentrations. In particular, Fig. 7.10b reports the measured peak shift as a function of calcium concentration. It appears that, for Ca^{2+} concentration in the range 0-60 μM, which is the concentration range involved in our experiment, a linear relationship between the shift of murexide absorbance peak and Ca^{2+} concentration holds. The experimental points of Fig. 7.10b were fitted to a Hill curve:

$$Peak\ shift = V_{max} \frac{[Ca^{2+}]\, n}{k \cdot n + [Ca^{2+}]\, n} \qquad \text{(Eq. 7.2)}$$

and the resulting V_{max}, k and n parameters were used to determine Ca^{2+} concentration released into aqueous solutions by TOCN-Ca^{2+} hydrogels.

Moreover, we checked that a small amount of TOCNs, which could be released by the hydrogels in the incubation bath, does not interfere with the Ca^{2+} detection. The results are reported in Fig. 7.11, where it is possible to see that the presence of TOCNs in the murexide-Ca^{2+} solution (TOCNs concentration up to 45 μg mL^{-1}) does not alter the peak shift.

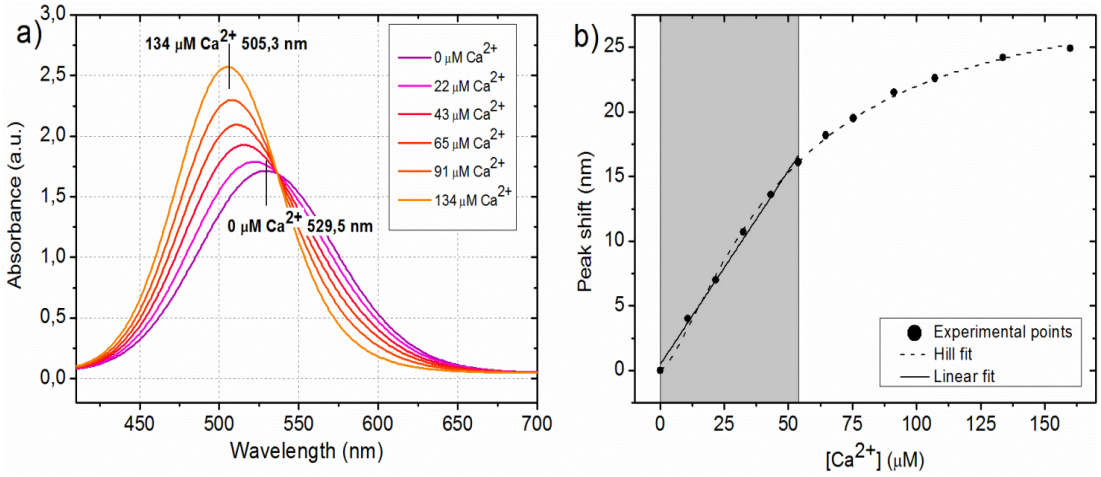

Fig 7.10: (a) Murexide absorption peak in the presence of increasing Ca^{2+} concentrations. The absorption peak of 0.2 mM murexide at pH 11.3 is centered at around 529.5 nm in absence of Ca^{2+} and progressively moves to shorter wavelengths by adding Ca^{2+}. (b) Peak shift versus Ca^{2+} concentration. The experimental points were fitted to a Hill curve $y=V_{max}x_n/(k_n+x_n)$ and the resulting V_{max}, k and n parameters were used to determine Ca^{2+} concentration released into aqueous solutions by TOCN-Ca^{2+} hydrogels. The gray area highlights the concentration range involved in the Ca^{2+} release of the measurements performed in the present work. The spectra were acquired by a Varian-Cary 5000 UV-VIS-NIR spectrophotometer operated in the range 200-900 nm with a 1 nm resolution.

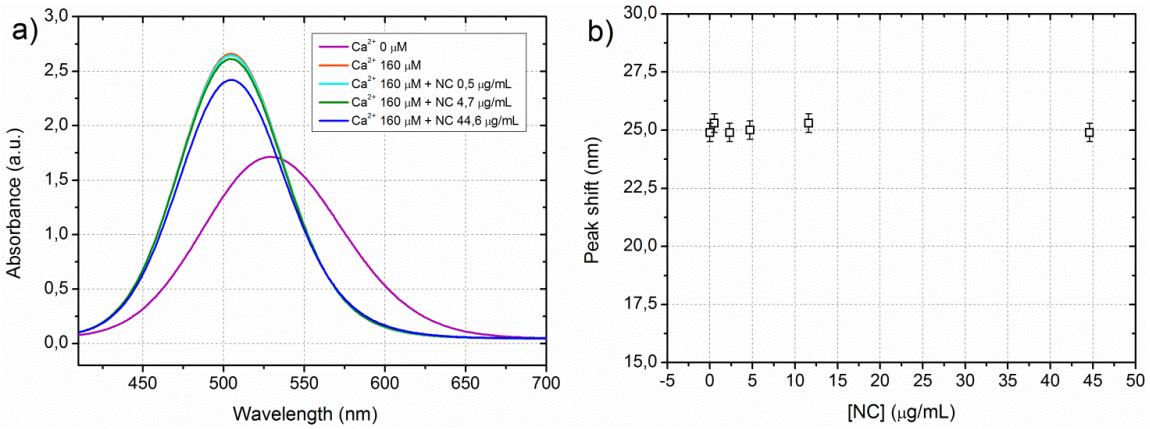

Fig. 7.11: Effect of TOCNs on murexide-Ca^{2+} peak position. Various concentrations of TOCNs (from 0.5 to 45 μg mL^{-1}) were added to a solution containing murexide (0.2 mM) and Ca^{2+} (160 μM) to check that TOCN crystallites do not interfere with Ca^{2+} determination. a) Absorbance spectra of murexide-Ca^{2+} solutions after addition of different amounts of TOCN crystallites (from 0.5 μM to 45 μM). As a comparison, the spectrum of murexide in the absence of Ca^{2+} is reported (purple trace). b) Shift of absorbance peak of murexide-Ca^{2+} solutions (murexide 0.2 mM, Ca^{2+} 160 μM) after addition of different amounts of TOCN. Peak shift was calculated with respect to the maximum absorbance of murexide in the absence of Ca^{2+} (peak at 529.5 nm).

Once the preliminary tests were performed and the calibration curve obtained, the Ca^{2+} release measurements from TOCN-Ca^{2+} hydrogel disks could be done. The experiment consisted in the transfer, at selected times, of 2 μL of the incubation solution into 500 μL of the assay solution containing 0.2 mM murexide buffered at pH 11.3 and in the acquisition the UV-Vis spectrum. The Ca^{2+} concentration was then calculated from the observed peak shift according to the murexide-Ca^{2+} calibration curve. At the end of the release kinetic, the hydrogel disk was disrupted using an ultrasonic tip in order to release all the Ca^{2+} ions still trapped in the hydrogel and the Ca^{2+} of the sonicated TOCN suspension was measured.

The histograms of Fig. 7.12 show the Ca^{2+} concentration inside the hydrogel after few minutes (column A), after 2 days incubation (column B) and after 2 days incubation followed by gel disruption by sonication (column C). Fig. 7.12b shows the kinetic of release of Ca^{2+} during hydrogel incubation in water. It can be noticed that about 20% of the expected Ca^{2+} is not detected even after hydrogel sonication, probably because small TOCN clusters containing coordinated Ca^{2+} are still present. Moreover, the maximum release is reached in the first 2 days of gel incubation in water and then stabilizes.

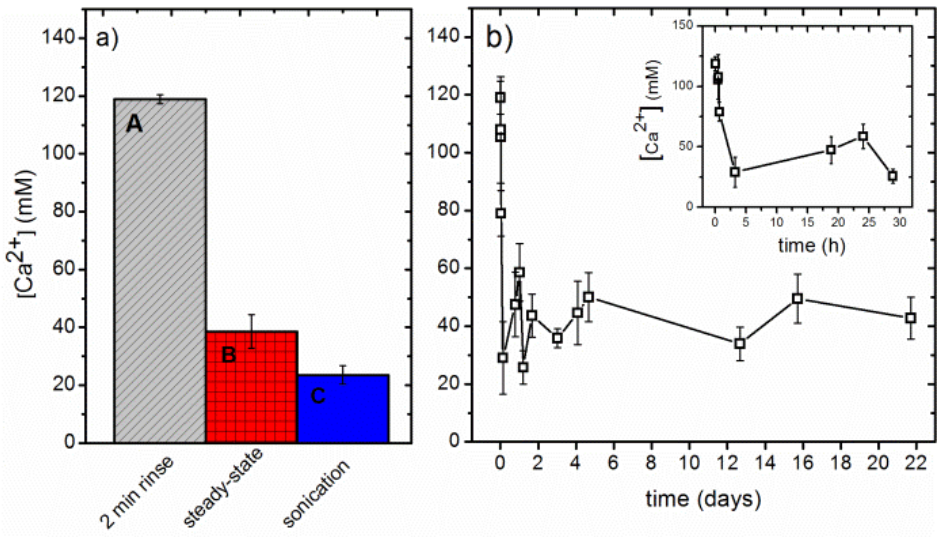

Fig 7.12: Measurements of Ca^{2+} in TOCN-Ca^{2+} hydrogel disks suspended in water. (a) Ca^{2+} concentration in the disk at different stages of the experiment. Columns A refers to the concentration after the disk was rinsed in water for two minutes. Columns B refers to the steady-state Ca^{2+} concentration measured before disk disintegration. Columns C refers to Ca^{2+} concentration after disk disintegration. Concentration values and error bars are respectively mean values and SD over three repetitions of the experiment. (b) Ca^{2+} concentration inside TOCN-Ca^{2+} hydrogel disks as a function of incubation time in water. In the inset a zoom on the small times region is reported. The experiment was performed three times and the each experimental point is the mean of 2-4 measurements, the error bar is the SD.

Assuming that this time of incubation in fresh water is enough to remove the Ca^{2+} in excess, it was estimated that 39 ± 6 mM Ca^{2+} (column B in Fig. 7.12a) is strongly bound to the hydrogel containing 22 mM cellobiose units and 6.7 mM carboxylate groups and can thus be considered the Ca^{2+} steady-state concentration in the TOCN-Ca^{2+} hydrogels. This datum indicates that a large amount of Ca^{2+} is not coordinated by carboxylates but is embedded among the polar cellobiose units. Hoverer, it is important to note that, in spite of the large amount of Ca^{2+} released, TOCN-Ca^{2+} disks or beads can survive for months in water without being disrupted.

7.2 Inverse Ionotropic Gelation

Differently from external ionotropic gelation, in inverse ionotropic gelation the calcium ions diffuse outward from an inner discrete core into an external TOCN solution. In our case, inverse gelation was performed by dropping an aqueous solution of $CaCl_2$ (0.1-2 M), into a TOCN solution (8 mg mL^{-1}), as shown in Fig 7.13a.

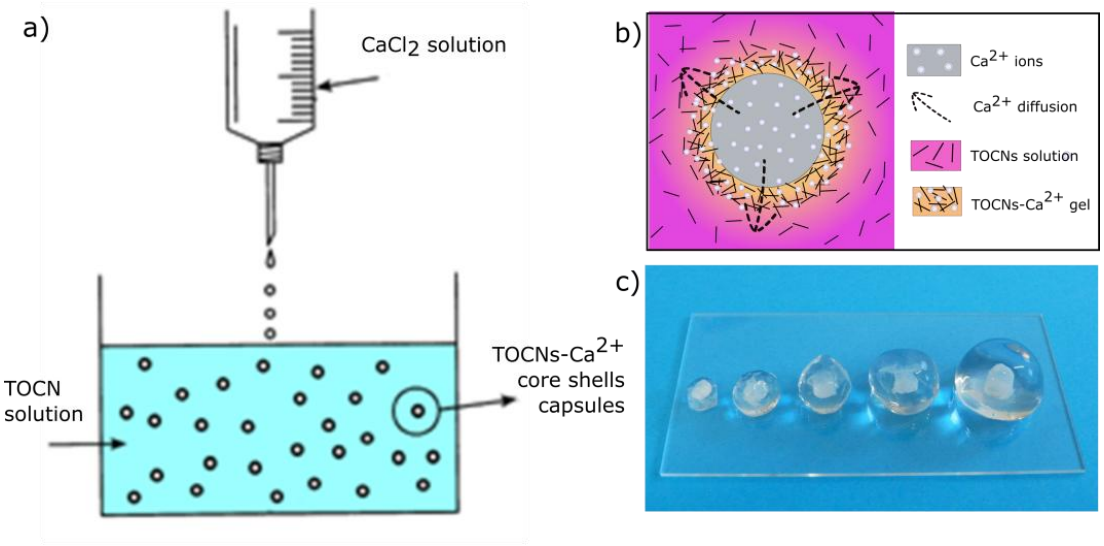

Fig. 7.13: a) simplified sketch view of the set-up used in inverse ionotropic gelation. b) Scheme of the diffusion mechanism at the basis of the inverse ionotropic gelation process. c) TOCN-Ca^{2+} microcapsules of tunable dimensions obtained by inverse ionotropic gelation. 7 μL of a solution of $CaCl_2$ with variable concentration (from 0.1 to 2 M, from left to right) were dropped inside the TOCN solution (8 mg mL^{-1}). The white liquid core is due to the opaque TiO_2 nanoparticles, which do not permeate through the incipient hydrogel network, and were added to the $CaCl_2$ drop to contrast the aqueous core with respect to the surrounding transparent shell of hydrogel.

The outward diffusion of the Ca^{2+} ions from the drop to the outer TOCN solution led to the formation of capsules with a liquid aqueous-core and a jelly TOCN-Ca^{2+} shell (see Fig. 7.13c). The size of the core depends on the $CaCl_2$ drop volume, while the size and thickness of the shell depend on the dropped $CaCl_2$ amount, provided that the diffusion of Ca^{2+} is left to go to completion.

Some representative pictures of core-shell capsules obtained by inverse gelation are reported in Fig. 7.13c, from which it appears that, for a constant 7 μL $CaCl_2$ drop volume, larger shells are produced by increasing Ca^{2+} concentration. In some experiments, TiO_2 nanoparticles (Aeroxide® TiO_2 P25, 5 mg mL^{-1}) were added to the $CaCl_2$ solution to increase its viscosity and weight and reduce drop deformation upon impact with the surface of the TOCN solution. Moreover, the TiO_2 nanoparticles do not diffuse in the jelly TOCN-Ca^{2+} shell, make the aqueous core opaque and increase the contrast with the surrounding hydrogel in the capsule images.

Measuring the final volume of the capsule (using calibrated cylinders with either 0.05 cm^3 or 0.25 cm^3 volume resolution) and considering that at the end of the diffusion process Ca^{2+} is homogeneously distributed, it was estimated that the mean Ca^{2+} concentration in the shells is (9 ± 1) mM independently of the dropped Ca^{2+} amount, as shown in Fig. 7.14.

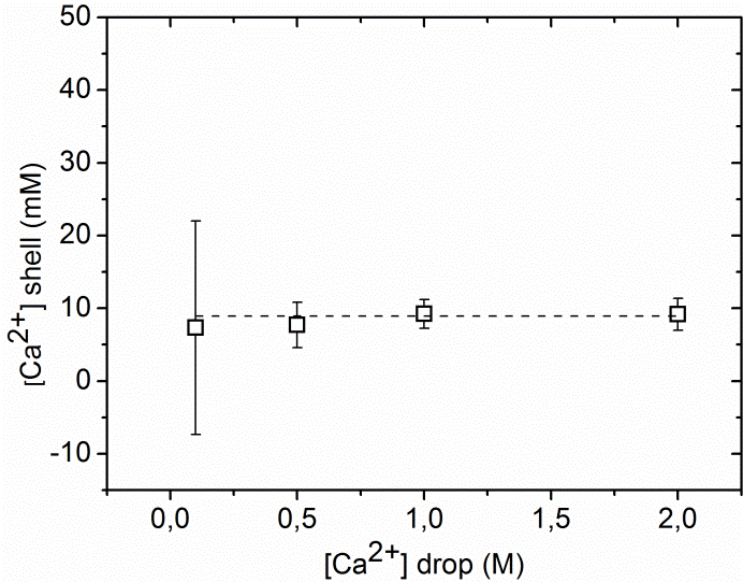

Fig. 7.14: Concentration of Ca^{2+} ions in the shell of TOCN-Ca^{2+} capsules obtained by inverse ionotropic gelation as a function of Ca^{2+} concentration in the starting $CaCl_2$ solution drop.

7.2.1 Ca^{2+} diffusion and inverse ionotropic gelation kinetics

As for the case of external ionotropic gelation, the diffusion of calcium ions leading to the sol-gel transition was investigated by monitoring the advancement of the sol-gel front through the change in color of murexide dye upon Ca^{2+} complexation. However, differently from external ionotropic gelation, a spherical geometry was adopted and the shell thickness was monitored in time. Three representative pictures of growing capsules taken at different times (2.5, 15 and 30 min) from the beginning of the gelation process are shown in Fig. 7.15. The analysis of the pictures taken at different times allows the monitoring of the increase of the microcapsule volume and of the shell thickness. To account for deviations from the spherical shape, three diameters (D_1, D_2 and D_3 in Fig. 7.15) were measured in the three spatial dimensions and an average D value was considered. The uncertainty on diameter measurements was related to the not sharp sol-gel interface (about 1 mm along the gel growth direction) and to image contrast and calibration and was estimated to be around 20%. Knowing the microcapsule radius $\mathrm{R} = \mathrm{D}/2$ and the liquid core radius r, we determined the gel shell thickness as a function of time as the distance $\mathrm{r} = \mathrm{R} - \mathrm{r}$.

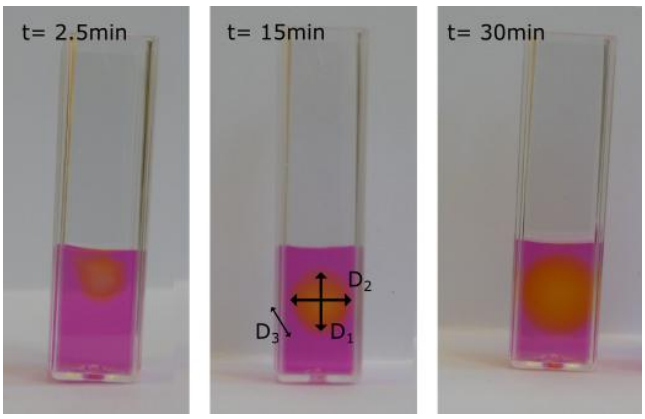

Fig 7.15: Diffusion front of Ca^{2+} ion in the incipient TOCN-Ca^{2+} hydrogel obtained by inverse ionotropic gelation. The images show the core-shell capsule growth induced by Ca^{2+} diffusion from the aqueous core. The pictures of the same sample were taken at 2.5 min, 15 min and 30 min (from left to right) after the contact between the $CaCl_2$-TiO_2 drop and the TOCN-murexide bulk solution (purple in the three images). The annulus, enlarging from left to right images, is the ionotropic gel shell formed upon diffusion of Ca^{2+} ions between TOCN crystallites.

Observing the plot of the thickness of the hydrogel shell against the square root of time ($t^{1/2}$), reported in Fig. 7.16, it appears that an initial linear relationship holds until a plateau value is reached. Indeed, in the case of inverse ionotropic gelation

the gelling agent availability is limited and the free diffusion model does not hold. Conversely, gelation proceeds until free Ca^{2+} disappears.

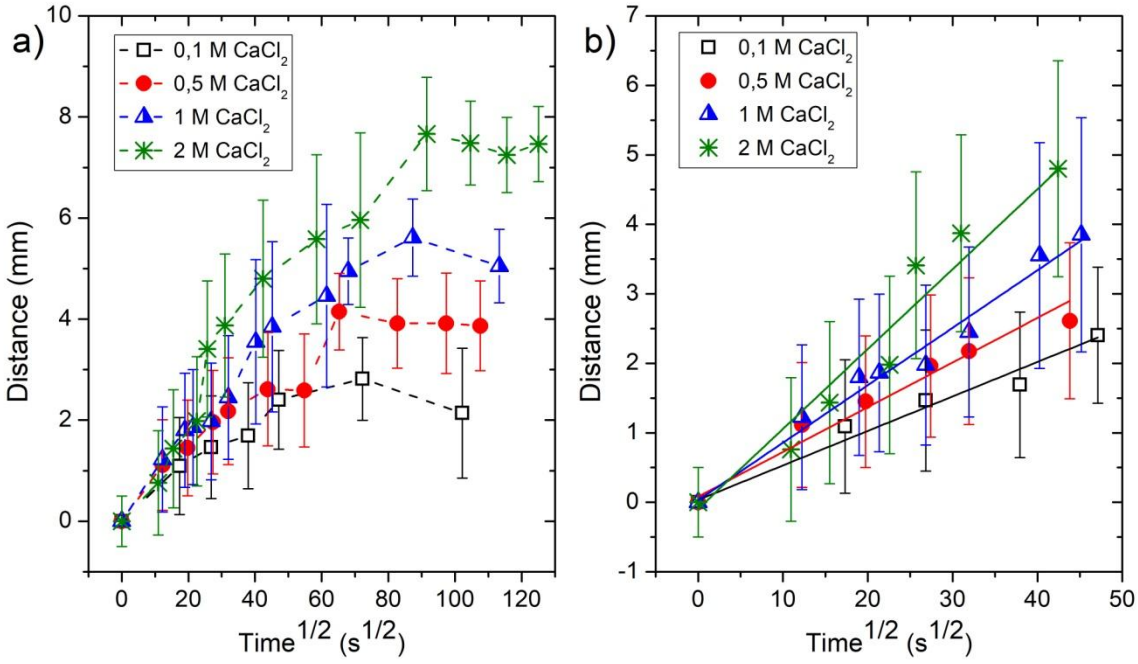

Fig 7.16: Gel growth measurements for inverse ionotropic gelation. (a) Sol-gel front distance from the inner liquid core as a function of square root of time for constant TOCN-Murexide solution concentrations (TOCN 8 mg mL^{-1}, murexide 20 μM) and different $CaCl_2$ concentrations. The points and errors are the mean value and SD, respectively. (b) Zoom on the short-times region characterized by a linear trend. The lines are linear fits performed on each set of data. The slopes resulting from the linear fits are (50 ± 4) μm $s^{-1/2}$, (64 ± 5) μm $s^{-1/2}$, (83 ± 4) μm $s^{-1/2}$ and (115 ± 10) μm $s^{-1/2}$ respectively for 0.1 M, 0.5 M, 1 M and 2 M $CaCl_2$ solutions.

Experimental data were analyzed performing a linear fit in the region 0-45 $s^{1/2}$ according to the experimental law $d = St^{1/2}$ in order to obtain the slope S (mm $s^{-1/2}$). Linear fits were performed with the software OriginLab using data's standard deviations as error bar sizes σ_i and calculating from them the weights W_i for the fitting procedure: $W_i = 1/\sigma_i^2$. The S values at different Ca^{2+} concentrations are reported in Fig. 7.17, together with an inset showing a representative plot of the d values versus $t^{1/2}$ and the corresponding linear fit.

Knowing the slope of the initial linear relationship, it is possible to design precisely the shell dimension by controlling the diffusion time. For example, core-shell capsules with shell thicknesses of (0.8 ± 0.1) mm, (1.9 ± 0.3) mm and (2.9 ± 0.3) mm were obtained by dropping 7 μL of 1 M $CaCl_2$ in a 8 mg mL^{-1} TOCN solution and leaving the Ca^{2+} diffusion to proceed in the TOCN bath for 3 min, 10 min and 20 min, respectively. After this time, the hydrogel

capsule was transferred in a water bath. The obtained shell thicknesses were in agreement with the values predicted through the experimental equation $d = St^{1/2}$ with S = (0.083 ± 0.004) mm $s^{-1/2}$ at 25 °C

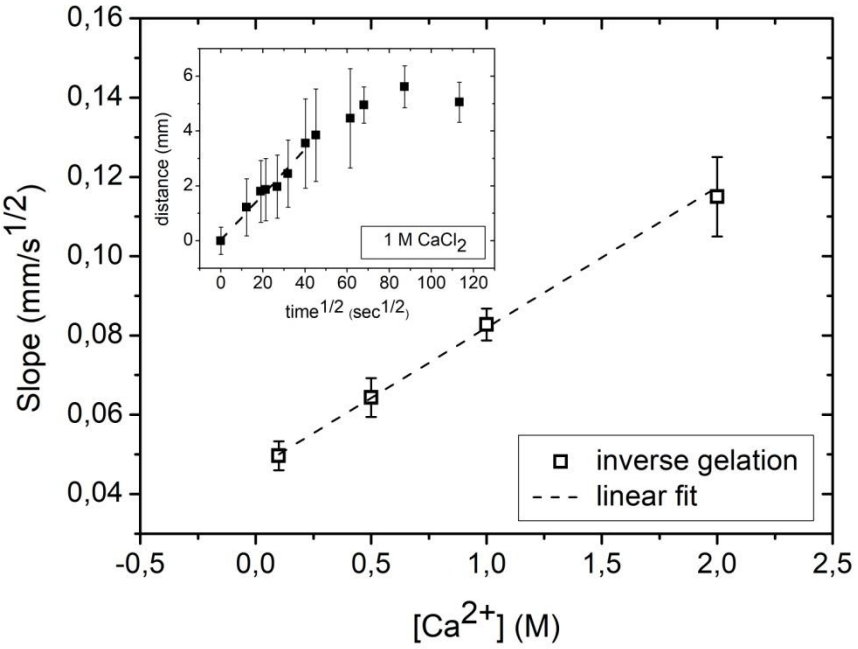

Fig 7.17: Slope S of the linear region of the plot of shell thickness versus $time^{1/2}$ of TOCN-Ca^{2+} microcapsules obtained by inverse ionotropic gelation at variable Ca^{2+} concentration. The shell TOCN concentration was (8 ± 1) mg mL^{-1} and murexide 20 μM in all the experiments. The Ca^{2+} concentration in the 7 μL $CaCl_2$ gelling core was 0.1 M, 0.5 M, 1 M, 2 M. In the inset an example of the advancement of murexide color change profile (distance) versus the square root of time for the case of 1 M $CaCl_2$ is reported. The dotted line is a linear fit performed on the experimental data in the 0-45 $s^{1/2}$ range.

7.3 Conclusions

In this Chapter, the ionotropic gelation process induced by the diffusion of Ca^{2+} into solutions of TOCNs was investigated in order to understand the mechanism and kinetics of hydrogel formation and use this strategy to fabricate microstructures with tunable size and shape. Here the main results for the case of both external ionotropic gelation and inverse ionotropic gelation are summarized:

1) External ionotropic gelation of TOCNs delivered in a Ca^{2+} bath forms filled hydrogel structures of various size and shape, depending on TOCN solution amount and delivery protocol. In particular, wires and beads with cross sections and diameters down to 800 μm can be obtained by simple extrusion

or dropping through a syringe needle powered by a pressure controller. Fig 7.18a shows the sizes of beads obtained by external ionotropic gelation as a function of the pulse time used to extrude the TOCN solution from a 400 μm nozzle at constant pressure. The minimum dimensions achievable in our experimental conditions are dictated by nozzle dimension and properties of TOCN solutions (in particular surface tension and viscosity), but could be further reduced by exploiting more complex delivery protocols (for example using a centrifugal force). On the contrary there is no theoretical limit on the maximum dimension achievable. For both external and inverse gelation, the process is driven by Ca^{2+} diffusion, as shown by the color shift profile of a Ca^{2+} sensitive indicator. In the case of external gelation, the diffusion process proceeds until equilibrium conditions are reached. The analysis of the Ca^{2+} reaction front propagation according to a diffusion-reaction model shows that free diffusion conditions of Ca^{2+} inside the incipient hydrogel network hold. Indeed measurements result in a diffusion coefficient of Ca^{2+} comparable to that in aqueous solutions, excluding any sieving effect of the incipient hydrogel. External ionotropic gelation is characterized by two distinct types of Ca^{2+} as ligand: a fraction of Ca^{2+} ions is tightly coordinated to carboxylates, as confirmed by FTIR spectroscopy, while a second fraction undergoes to un-specific binding. This last is released without compromising the hydrogel structure and stability in aqueous environments.

2) By inverse ionotropic gelation, instead, core-shell capsules can be obtained. Fig. 7.18b shows the capsule volume as a function of the moles of Ca^{2+} ions present in the starting $CaCl_2$ drop. In the case of inverse gelation, the hydrogel formation is again driven by Ca^{2+} dynamics, but in this case, the availability of Ca^{2+} ions is limited and the diffusion-reaction model does not hold. The core size is determined by the volume of the dropped Ca^{2+} solution and the dimension of the shell is controlled by the gelling time. In particular, the maximum shell thickness reached at equilibrium is determined by the Ca^{2+} availability.

3) The ionotropic gelation process of TOCNs, driven by the dynamics of Ca^{2+} diffusion, offers the opportunity of tailoring kinetic controlled hydrogel formation. Indeed, the measured apparent diffusion coefficient D_{app} (for external ionotropic gelation) or distance versus $time^{1/2}$ slope S (for inverse ionotropic gelation) enables to design gel structures with tunable thicknesses by simply controlling the diffusion time. Moreover, the simplicity and the flexibility of this approach suggest that it could be coupled to more sophisticated set-up to deliver the solutions (i.e. a dispositive operating under a centrifugal field or microfluidic systems), to allow the decrease of

the dimension or the fabrication of more complex geometries, such as multi-compartmentalized beads. This could open new perspectives to the application of these biocompatible hydrogel droplets in drug delivery and in high throughput systems for single cell analysis.

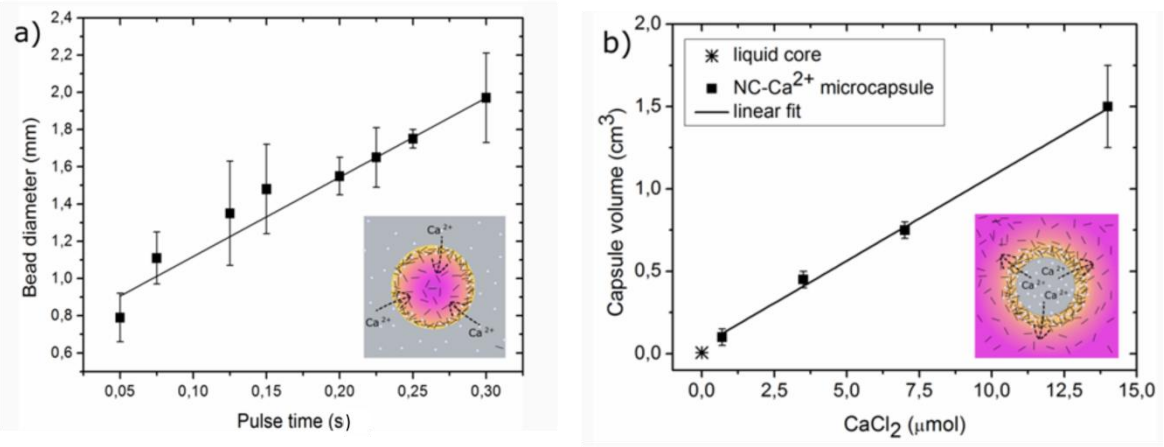

Fig 7.18: (a) Mean size of nanocellulose beads obtained by external ionotropic gelation as a function of pulse duration for a fixed pressure (350 mbar), using a TOCN concentration of 8 mg mL^{-1} and a 400 μm diameter extrusion nozzle. The points and error bars are the mean values and SD over the dimensions of 12 different beads, respectively. Sizes were estimated for each bead as the mean value between major axis and minor axis measured using an optical microscope with magnification 4X. (b) Final volume of TOCN-Ca^{2+} core-shell microcapsules obtained via inverse ionotropic gelation as a function of the amount of Ca^{2+} ions in the starting $CaCl_2$ solution drop. The microcapsules were obtained by dropping 7 μL of $CaCl_2$ solution (concentration 0.1 M, 0.5 M, 1 M and 2 M) in a 8 mg mL^{-1} TOCN solution. Volume measurements were done using a graduated cylinder, after 8 hours from the moment $CaCl_2$ drop and TOCN solution were put in contact. At this time the gelation process had gone to completion and the shell reached its constant maximum dimension. In the inset, two sketches of (a) external and (b) inverse ionotropic gelation processes are shown.

In conclusion, besides showing the efficiency of TOCNs as building blocks for hydrogel microstructures formation (with all the advantages peculiar of TOCN hydrogels that is high mechanical strength, toughness, and stability) these studies proved that Ca^{2+} induced gelation offers the opportunity of tailoring the TOCN hydrogel shape by simple, low-cost, pollutant-free procedure (without using surfactants, oils or other non-green chemicals).

CHAPTER 8:
Toxicity studies

In this Chapter we will discuss the biosafety of TOCN hydrogels fabricated by cation-induced gelation adding Na^{+}, Ca^{2+} and Mg^{2+} to sonicated TOCN solutions. In this regard, transparent and soft TOCN hydrogel membranes were fabricated, in view of their potential application as skin patches, in particular for photodynamic therapy of melanoma.

As already said in the introductory part (Section 1.5.2), hydrogels and, nanocelluloe hydrogels in particular, are good candidate materials for patches production, because of their high water content, softness and flexibility properties. However, even though nanocellulose precursor is essentially safe, thorough toxicity testing of hydrogels and all their components has not been widely executed (De France et al., 2017; Lin and Dufresne, 2014).
The results reported in this Chapter concerns the *in vitro* studies performed to evaluate the biosafety of TOCN hydrogel membranes (produced by crosslinking TOCNs with mono and divalent cations) and of its precursors (TOCN solutions and salt solutions) in cultures of malignant melanoma cells A375. The cytotoxicity was tested evaluating morphological changes, cell organelles integrity and cell survival with the tetrazolium salt reduction (MTT) assay. The tests were performed by addition of the hydrogel (or hydrogel components) to the cell culture medium and by incubation with a confluent monolayer of the melanoma cells. Considering that two important factors that can influence the performance of TOCN hydrogel membranes are their stability and their potential release of salts, four different post-gelation processing strategies were adopted and the results compared.
Moreover, taking into account the ISO 10993-5:2009 suggestions for the biological evaluation of medical devices (STANDARD, 2009), we evaluated the toxicity not only of the hydrogel device (both in direct and indirect contact with the cells) but also of each component material, including impurities, and constituents associated with processing. More into details, three types of tests were performed: toxicity tests of the molecular components of the device, direct contact assays and indirect contact assay. The results of the three tests are reported respectively in Sections 8.2, 8.3 and 8.4, while Section 8.1 gives some details of the samples preparation procedures.

8.1 Preparation and characterization of TOCN hydrogel membranes and their precursors

8.1.1 TOCN hydrogel membranes

Fig. 8.1 shows the visual aspect of the TOCN hydrogels evaluated in these toxicology studies. They consist of disk-shaped, about 4-5 mm thick, membranes and were obtained through ionotropic gelation, exploiting the diffusion of Na^{+}, Ca^{2+} and Mg^{2+} chloride salts added to sonicated TOCN solutions (8 mg mL^{-1}).

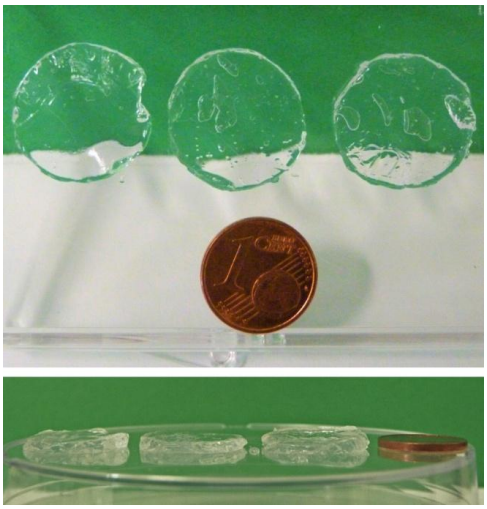

Fig. 8.1: Pictures of TOCN hydrogel membranes obtained by ionotropic gelation using 1M NaCl (left disk), $CaCl_2$ (central disk) and $MgCl_2$ (right disk). Top panel and down panel show respectively the top view and frontal view of the membranes.

Two important factors that can influence the performance of TOCN hydrogel membranes as medical devices are their stability and their potential release of salts. For this reason, after the gelation process, the hydrogel membranes were subjected to different procedures in order to remove the excess of salts and increase their stability in water. More into details, four different processing strategies were evaluated. The first one required a short washing (5 min) of the hydrogel membrane in water, while the second one involved a long-lasting incubation in water for 5 days (changing the 50 mL water once a day). The third strategy consisted of the conversion of hydrogels to alchoolgel by 5 days soakings in ethanol, followed by repetitive soakings in aqueous solution. Finally, following the fourth one, hydrogels were left 2 hours in water solution and then partially dried being placed for 1 h at 60°C.

The procedures are summarized in Table 8.1 (first column), together with the cations used for the gelation (second column) and the nomenclature we will use to

denote the samples (last column). Finally, in the third column the cation concentration estimated to be present in the hydrogel membrane at the end of the post-gelation strategy is reported. The concentration was estimated on the basis of the Ca^{2+} release studies reported in Chapter 7 (Section 7.1.3) and on the assumption that a similar release takes place for Na^{+} and Mg^{2+} too. More into details, the temporal evolution of the Ca^{2+} concentration inside TOCN hydrogels incubated in water (Fig. 7.12b) was fitted with an exponential decay: $C = y_0 + A\, e^{\frac{-t}{\tau}}$, where C and t are respectively the salt concentration in the hydrogel and the time of water incubation. The parameters y_0, A and τ resulting from the fit were used to estimate the Na^{+}, Ca^{2+}, Mg^{2+} concentration at time t, obtaining the data reported in the third column of table 8.1.

Table 8.1: Overview of the TOCN hydrogel membranes studied. Column one reports the procedure exploited after the gelation to increase hydrogels stability or reduce their salt content. Column two and three indicate respectively the cations used and their estimated concentration in the membrane after the post-gelation procedure. Finally, the last column shows the nomenclature we will use to denote the different samples.

Post-gelation procedure	Gelling agent	Cation Concentration in the hydrogel	Sample
a) 5 minutes rinsing in water	$Na^{+}/Ca^{2+}/Mg^{2+}$	125±17 mM	Rinsed-HM
b) 5 days soaking in water	$Na^{+}/Ca^{2+}/Mg^{2+}$	38±4 mM	Water-HM
c) 5 days soaking in ethanol	$Na^{+}/Ca^{2+}/Mg^{2+}$	38±4 mM	Ethanol-HM
d) 2 hours in water + 1h at 60°C	$Na^{+}/Ca^{2+}/Mg^{2+}$	54±16 mM	60°C-HM

The morphological appearance and the stability of the HMs were evaluated after each processing method and for each cation. The fast washings (procedure a) did not alter the compactness of the hydrogel membranes, while the prolonged washing (procedure b) caused a physical weakening of the membranes, which eventually become shapeless in the case of Na^{+}. The conversion to alchoolgel (procedure c) determined a slight decrease in volume (about 10% in diameter and 20% in thickness) which persisted after long time soaking in aqueous solution. Moreover, in the case of Ca^{2+} and Mg^{2+} HMs, it increased their compactness and stability for long term storage in aqueous solution: Ca^{2+} and Mg^{2+} ethanol-HMs soaked in water maintain the original shape and compactness for more than three months. In the case of Na^{+}, instead, the membranes are almost completely dissolved by long permanence in water both in the case of Na^{+}-water HMs and Na^{+}-ethanol HMs. Finally, the mild drying (procedure d) allowed water evaporation and

membranes compaction, independently of the cation used for gelation, increasing their long-term stability in aqueous environment.

8.1.2 TOCNs and TOCN films

In order to evaluate the toxicity of TOCN hydrogel precursors, TOCN aqueous solutions and TOCN films were considered.
TOCN films with thickness in the range of 10-12 μm were obtained by casting and drying an aqueous dispersion of TOCNs. The dried films were compact and flexible as shown in Fig. 8.2a. Moreover, if they were immersed again in aqueous solution, they became soft and pliable but kept their structure, without releasing visible amounts of the TOCNs components (Fig. 8.2b).

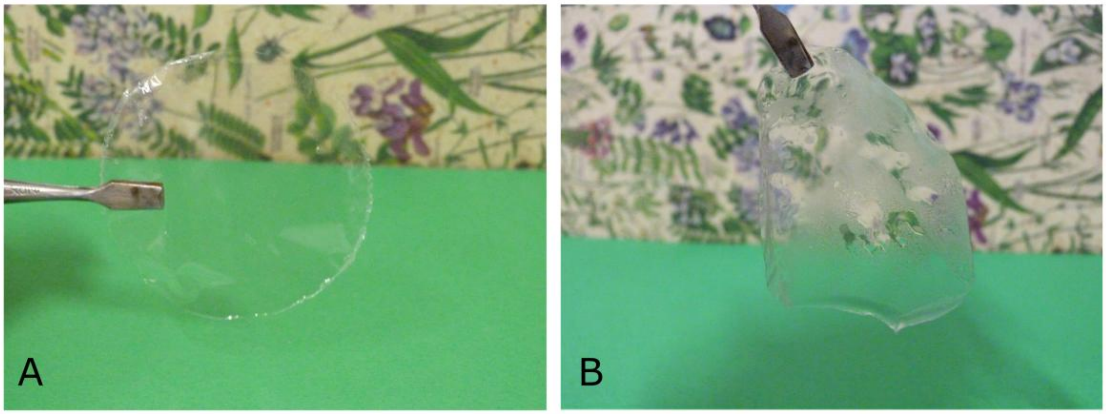

Fig. 8.2: Pictures of dry TOCN film (panel A) and of the same film after immersion in aqueous solution for 30 min (panel B).

With the purpose of investigating the possible cellular uptake of TOCNs (which could be released by the hydrogel membranes) through fluorescence microscopy, TOCNs were fluorescent labeled by covalently coupling them with FITC (Nielsen et al., 2010). Fig. 8.3a shows a representative example of the fluorescence excitation and emission spectra of the labeled TOCNs, after careful purification from unreacted FITC.
The quantum yield of fluorescein covalently bound to TOCNs was estimated according to a procedure outlined by Horiba Scientific (HORIBA Scientific, A guide to Recording Fluorescence Quantum Yields)) based on the comparative method (Lakowicz, 2006; Williams et al., 1983). In brief, UV-Vis absorption spectra and emission fluorescence spectra of FITC solutions in PBS at pH 7.4 were acquired at different known concentrations. The integrated fluorescence intensity at the different concentrations was calculated from the emission spectra and plotted as function of the absorbance at excitation wavelength (493 nm), evaluated from UV-

Vis spectra. The same steps were repeated for the FITC-labeled TOCN solution and the gradients of the integrated fluorescence/absorbance curves, which are proportional to the quantum yield of the samples, were estimated (Fig. 8.3b).

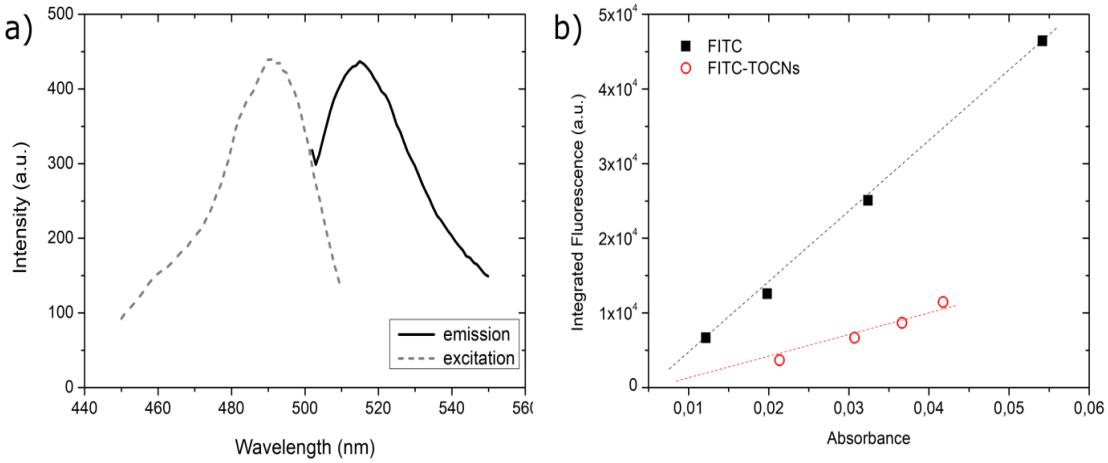

Fig. 8.3: (a) Typical excitation and emission spectra of a 0.8 mg mL^{-1} FITC-labeled TOCN solution (1.76 nmol/g FITC/TOCNs) at pH 7. (b) Integrated fluorescence intensity as a function of absorbance at 493 nm for FITC solutions and FITC-labeled TOCN solutions at different concentrations. From the gradients of the two curves that best fit the experimental data it is possible to estimate the Quantum Yield of the FITC grafted on TOCNs.

The unknown quantum yield of FITC on TOCNs was calculated from the following formula:

$$\Phi_{FITC-TOCN} = \Phi_{FITC}\left(\frac{Grad_{FITC-TOCN}}{Grad_{FITC}}\right)\left(\frac{n^2_{FITC-TOCN}}{n^2_{FITC}}\right) \quad \text{(Eq. 8.1)}$$

Where Φ_{FITC} is the quantum yield of FITC assumed to be equal to 0.75 (Zhang et al., 2014), $Grad_{FITC-TOCN}$ and $Grad_{FITC}$ the gradients of the curves and $n_{FITC-TOCN}$ and n_{FITC} the refractive indexes of the solvents.

Following this procedure, the estimated quantum yield for FITC on TOCNs was around 0.20±0.02.

The amount of FITC grafted on TOCNs was estimated acquiring the fluorescence spectrum of FITC-labeled TOCN solution, comparing the fluorescence intensity with a calibration curve obtained with FITC solutions in PBS at pH 7 at known concentrations and considering the measured quantum yield. The result was an estimated grafted FITC amount around 1.76 nmol/g.

8.2 Toxicity of TOCN hydrogel membranes precursors

Hydrogels toxicity could arise from hydrogels precursors themselves, which are loosely bound to the hydrogel network or are progressively released by degradation. In particular, toxicity could increase if chemical modification of the precursors and incorporation of reactive side groups onto these molecules have been performed (Kisiel et al., 2013). In our specific case of TOCN hydrogels, the precursors are the TOCNs bearing carboxylic groups in C6' position of the cellobiose units and the gelling cations.

8.2.1 TOCNs toxicity studies

We investigated the effect of TOCNs both in the form of individual nanocrystals in solution and in the form of compact, self-assembled layer (TOCN film). In the first case 5 mL of TOCN solution (concentration 8 mg mL^{-1}) were added to the cell culture containing 7 mL of cell medium. In the second case, the TOCN film was directly laid over a cell culture and 7mL of cell medium were added to cover the film surface. The results are reported in Fig. 8.4, which shows the cell survival after 24 hours of incubation in the presence of 3.3 mg mL^{-1} of TOCNs and of a TOCN film, with respect to the control (column C in Figure). No substantial toxicity was observed in both cases, being the viability percentage higher than 90%.

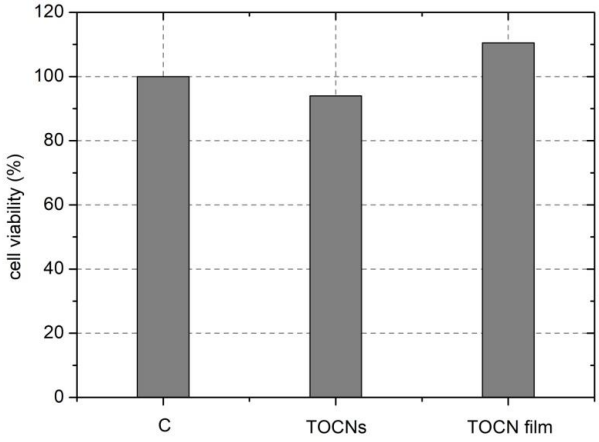

Fig. 8.4: Toxicity of TOCNs and TOCN films in terms of melanoma cell viability (%) after 24 hours of incubation, in the presence of 3.3 mg mL^{-1} of TOCN suspension and a TOCN film. The experiments were performed in triplicate and the SD of the mean was < 0.1% (not noticeable as error bar in the histogram).

To better investigate the interaction between TOCNs and melanoma cells, the trafficking and intracellular localization of the FITC-labeled TOCNs were investigated

by confocal microscopy. In particular, A375 cells were treated with three different concentrations of TOCNs in the cell culture medium: (0.13 ± 0.03) mg mL^{-1}, (0.4 ± 0.1) mg mL^{-1} and (0.53 ± 0.13) mg mL^{-1}. Fig. 8.5 shows some images obtained for the three different concentrations. FITC-labeled TOCNs and PI stained nuclei are visible respectively in green/yellow and red colors. At the lowest concentration, shown in panel A and A1 (magnification of A), TOCNs are visible only marginally in some cell membranes. Increasing the concentration (panel B and B1), it is possible to observe an increased positivity in the sub-membrane part as well as in the cytoplasm. Finally, at the highest concentration considered (panel C and C1), all the cells show FITC signal in the cytoplasm area. Moreover, as visible in the zoom-in image, numerous positive vesicles for TOCNs are present.
These data shows that, differently from other published data (Tang et al., 2017), the TOCNs here considered undergo substantial cell internalization. However, adverse effects were not observed for cells incubated with both TOCNs and FITC labeled TOCNs, in agreement with the results of the MTT assay shown in Fig. 8.4.

8.2.2 Gelling agents toxicity studies

As already said, the gelling agents used in this study are the chloride salts of Na^{+}, Ca^{2+} and Mg^{2+}. To evaluate the effects on cell cultures of their release from the hydrogel membranes, we firstly considered the worst case of complete membrane dissolution and release of the whole cation content. Moreover we considered the case of the post-gelation procedure for which the cation concentration in the hydrogel is the highest, i.e. the case of water-HMs, corresponding to a salt concentration around 125 mM (see Table 8.1). In this situation the maximum cation release in cell culture media is estimated to be around 160 μmoles, which corresponds to an increase of the final cation concentration in the cell culture medium of 19.6 mM.
It is important to remember here that Na^{+}, Ca^{2+} and Mg^{2+} are ubiquitous components of biological fluids and of the cell culture media (Na^{+}, in particular, plays a fundamental role to retain the osmotic pressure of the cells). Their concentrations in RPMI 1640 are respectively 90.75 mM, 0.42 mM and 0.41 mM, so only a significant leakage of these ions from the hydrogels is expected to produce toxicity. Fig. 8.6 shows the results of MTT tests on cells incubated with 19.6 mM NaCl, $CaCl_2$ and $MgCl_2$. The survival data show a modest toxicity of Na^{+} and Mg^{2+} and a higher toxicity of Ca^{2+}.

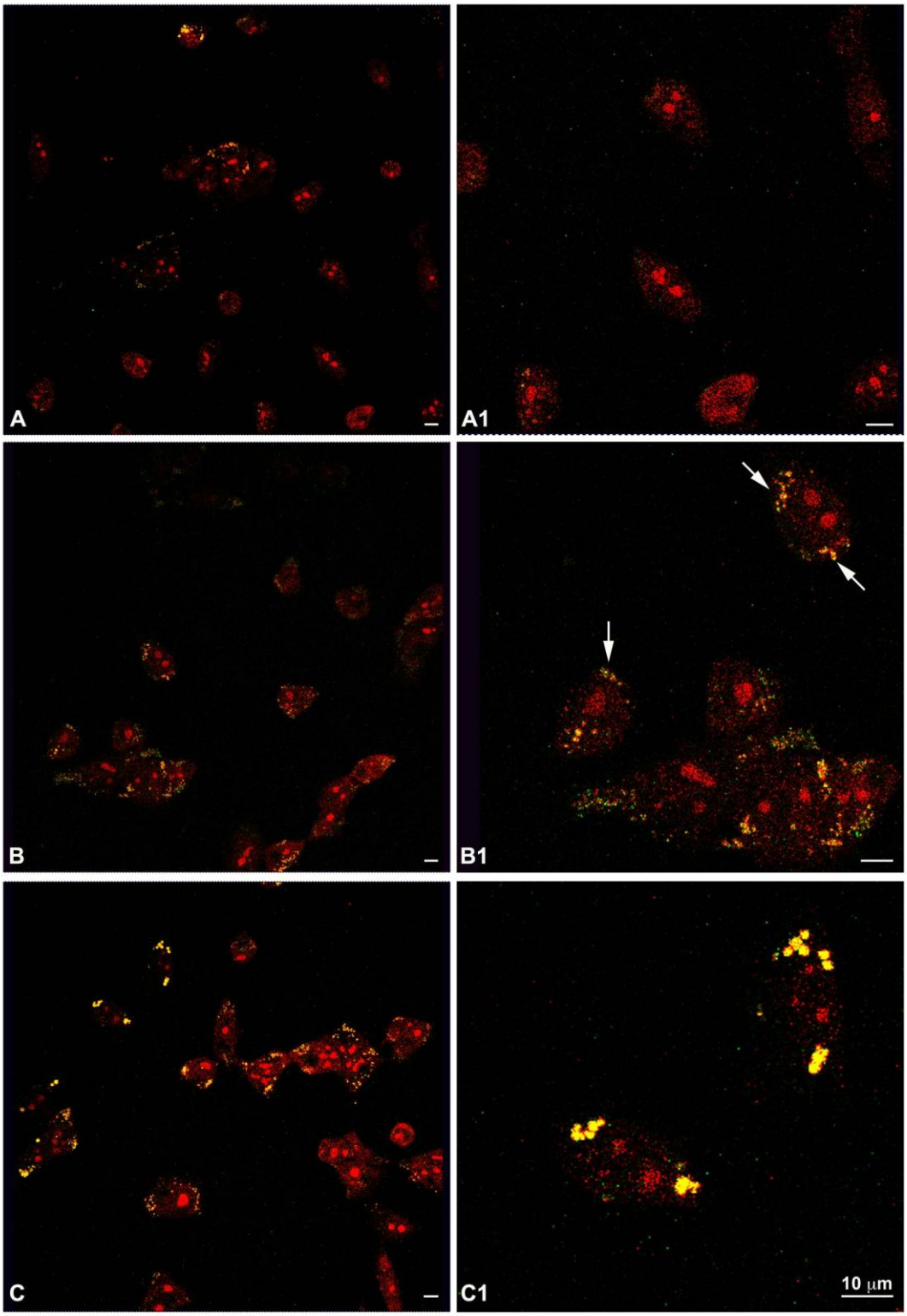

Fig. 8.5: Representative confocal fluorescent images of melanoma cells incubated with A) 0.13±0.03 $mgmL^{-1}$ B) 0.4±0.1 $mgmL^{-1}$ C) 0.53±0.13 $mgmL^{-1}$ FITC-labeled TOCNs. The scale bar is 10 μm in all the images. A1, B1, C1 are zoomed-in images of A, B, C respectively. All cells were treated for nuclear staining with PI, 1 μg/mL for 30 minutes and then incubated with FITC-labeled TOCNs for 24 h, at 37 °C in a 5% CO_2 atmosphere.

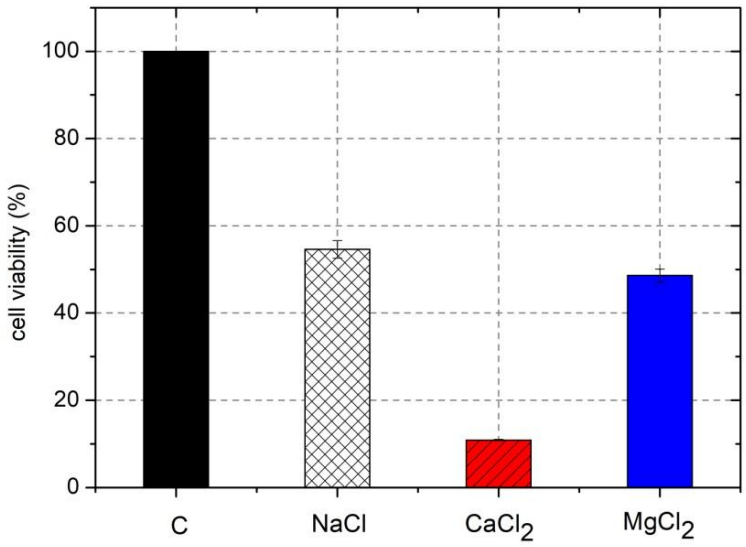

Fig. 8.6: Melanoma cell viability (%) after 24 hours of incubation in the presence of 19.6 mM NaCl, $CaCl_2$ and $MgCl_2$. The experiments were performed in triplicate and the SD is reported as error bar in the histogram.

The higher toxicity of Ca^{2+} with respect to Mg^{2+} in spite of their chemical similarity could be due to the role of Ca^{2+} as signaling molecule involved in all the mechanisms of cell death. To ensure adequate homeostasis, Ca^{2+} concentration is usually maintained within specific limits (Zhivotovsky and Orrenius, 2011). Moreover, the cytosolic concentration of Ca^{2+} is extremely low, while large Ca^{2+} gradients across plasma membrane should exist. As a consequence, the movement of a few Ca^{2+} molecules across plasma membranes results in a dramatic change of cytosolic Ca^{2+} and affects the binding of this ion to proteins, the function of which is consequently modified. Conversely, cytosolic Mg^{2+} concentration can be as high as in the mM range and an up-take of this ion does not perturb substantially the intracellular processes (Romani and Scarpa, 2000).
However, this toxicity is expected in the worst case of high salt content in the membranes (5 minute rinsing in water procedure) and its complete release, that is in the case of membrane disintegration.

8.3 Direct contact toxicity tests

Direct contact toxicity tests were performed directly placing the TOCN hydrogel membrane on the cell culture containing 7 mL of cell medium. Fig. 8.7 shows some representative images of the morphological changes induced by TOCN hydrogels on melanoma cells, with respect to control cells (panel A). These morphological perturbations are more evident for the cells lying under the membrane (panel B)

with respect to those in proximity of the membrane but not covered by it (panel C). In particular, in panel B is visible a remarkable inhibition of the growth and a cell body retraction. Moreover, other signs of cell suffering are detectable by the presence of surface blebs, not visible in the non-contact zone (panel C).

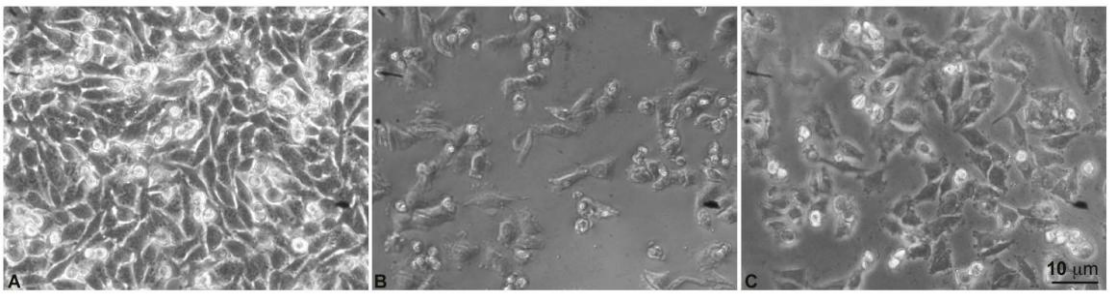

Figure 8.7: Phase Contrast Microscopy images of: (A) melanoma A375 cells (control), (B) A375 cells lying under a rinsed-HM, obtained using Ca^{2+} as gelling agent, (C) A375 cells incubated with the same membrane but not lying under it (as the area of the membrane is smaller than the area of the cell culture well). The membranes utilized were obtained using Ca^{2+} as gelling agent and were rinsed by short washings in water (Ca^{2+} rinsed-HM).

The decrease of cell survival is confirmed by the results of the MTT assay, which measured the survival of A375 melanoma cells evaluated after 24 h of contact with TOCN hydrogel membranes obtained using Ca^{2+} as gelling agent. It appears that the cell survival decreases down to 21% of the control cells in the case of rinsed-HMs (calcium concentration around 125 mM) and is only slightly higher (28%) in the case of water-HMs (calcium concentration around 38 mM).

The fact that TOCNs alone do not decrease the cell viability (see Fig. 8.4) and that this macroscopic effect is independent of careful rinsing and soaking the membranes in pure water (post-gelation procedure) suggests that the observed cells death or changes in morphology are related to a physical trauma due to hydrogel mechanical shearing. In fact, TOCN hydrogels are homogeneous and soft as indicated by their rheological parameters and by the presence of a pool of water in fast exchange with the surroundings (Chapter 6). These characteristics make the TOCN hydrogels easily injectable, suitable for *in vivo* applications such as drug and cell delivery or absorption of exudates and exchange of fluids. However, when utilized *in vitro* in cell cultures, the close contact between soft hydrogels and cell membranes can cause mechanical stresses (Pelham and Wang, 1997). Such stresses are reported to be responsible of morphological and then metabolic responses (La Rocca et al., 2014), which induce apoptosis of cancer cells (Cheng et al., 2009; Georges and Janmey, 2005). A recent research study reports the results of direct toxicity tests performed with hydrogels obtained by crosslinking coarse nanocellulose fibers with Ca^{2+} (Basu et al., 2017) and shows that these NCF hydrogels induce only small, but not quantified, disruptions of a fibroblast cell layer. The difference with respect to our situation is probably related to the reduced

adhesion and decreased susceptibility of normal cell lines to physical stress (La Rocca et al., 2014).
The hypothesis of cell death due to an hydrogel mechanical shearing effect is moreover supported by the warnings about possible physical trauma contained in the European Standards EN ISO 10993-5 for the evaluation of Biomedical devices by direct contact toxicity tests *in vitro* (Biological evaluation of medical devices - Part 5: Tests for *in vitro* cytotoxicity) (STANDARD, 2009).

8.4 Indirect contact toxicity tests

To perform toxicity tests in an indirect geometry, a simple but innovative set-up was obtained using a microporous cell culture insert (PET track-etched membrane 8.0 µm pore size) suspended over a confluent cell monolayer by small plastic supports, as shown in Chapter 5, Fig. 5.3.
The most popular approach to perform indirect toxicity tests is usually the agar overlay assay, where a sub-confluent cell culture is overlaid by a thin layer of agar on top which is placed the test material. This method suffers from several limitations, among which the slow diffusion of molecules through the agar membrane, so that only acute cytotoxic effects are detected (Pusnik et al., 2016). The main advantages of the new protocol used in our tests are the high porosity and the large pore size of the PET insert, which allow the free permeation of solutes (included micro-sized TOCNs eventually released by the hydrogel) and the fact that the support is hanging over the cell layer, so that any physical stress is prevented. In this way, the only toxic effect is eventually due to the leakage from the hydrogels.
Fig. 8.8 compares the results of the MTT assay for the case of Ca^{2+} hydrogel membranes both in direct and in indirect contact. Moreover two different post-gelation procedures were considered, corresponding to two different salt concentrations in the hydrogels (around 125 mM for the case of rinsed-HM and around 38 mM for the case of water-HM). It is possible to see that, once the coarse mechanical effect due to the direct contact is removed, a Ca^{2+} concentration-dependent toxicity emerges. The cell survival is infact similar between rinsed-HMs and water-HMs in the case of direct contact. However, in the case of indirect contact, the survival increases from 22% to 53% passing from rinsed HMs to water HMs, that is decreasing the Ca^{2+} content of the hydrogel membrane. This suggests that the mechanical shearing levels the cell survival to a minimum value, independently of Ca^{2+} toxicity, that indeed emerges when the first cause of death is removed. The cell population surviving in all situations (around 20-25%) probably corresponds to cells which can respond to stress by activation of efficient survival pathways.

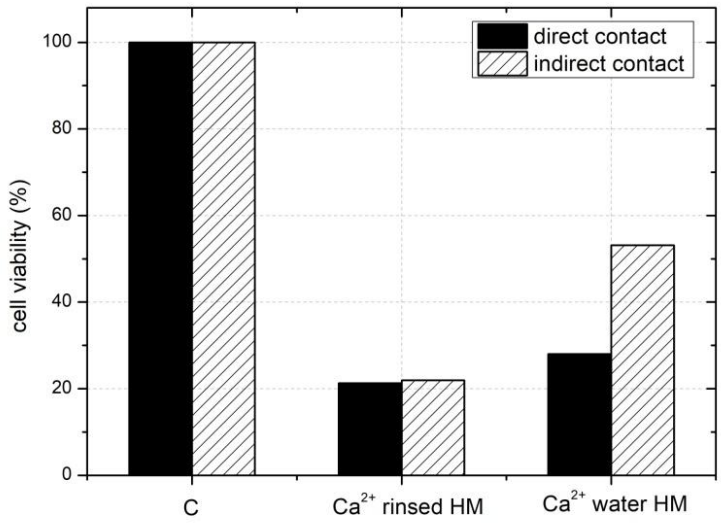

Fig. 8.8: melanoma cell survival at 24 h in response to direct (filled black column) and indirect (grey lines column) contact with Ca^{2+}-HMs subjected to two different washing processes. Rinsed-HM refers to membranes rinsed by 5 min washings in water and with a Ca^{2+} content estimated to be 125±17 mM. Water-HM refer to membranes left in water for 5 days after gelation, so that the estimated Ca^{2+} content in the hydrogel volume was lowered to 38 ± 4 mM. Column C refers to control cells. The experiments were performed in triplicate and the SD of the mean was < 0.1% (error bar not visible in figure).

After the comparison between direct and indirect contact for the case of Ca^{2+} rinsed and water HMs, indirect contact measurements were performed for all the samples obtained using different cations and different post-gelation strategies, as listed in table 8.1. The results are reported in Fig. 8.9.

Considering the case of Na^{+}-HM (white checked columns in figure), the high survival values (> 80% even after a short rinsing procedure: Na^{+} rinsed-HMs) confirm that Na^{+} is a safe gelling agent. However the obtained membranes are fragile and even dissolved after long contact with water.

On the contrary, hydrogels crosslinked by Ca^{2+} show a good stability in water and in the culture medium, but traces of Ca^{2+} are clearly toxic (red streaked columns in figure) and a survival comparable to the control has been obtained only after a long lasting incubation in water of the Ca^{2+}-HMs (Ca^{2+} water-HMs).

The Mg^{2+} -HMs gave the best performances, since these membranes combine quite low toxicity (blue columns in figure) with good stability. In fact, if Mg^{2+} rinsed-HMs produce a low cell survival (30±1 %), cell survival increases to about 85% after washing and thermal treatment (Mg^{2+} 60°-HM) and 98% after long-lasting soaking in water (Mg^{2+} water-HMs). Finally, when 1 μM STS was used as positive control, a vitality reduction higher than that induced by Ca^{2+} (30% of cell survival with respect to the control cells) was observed.

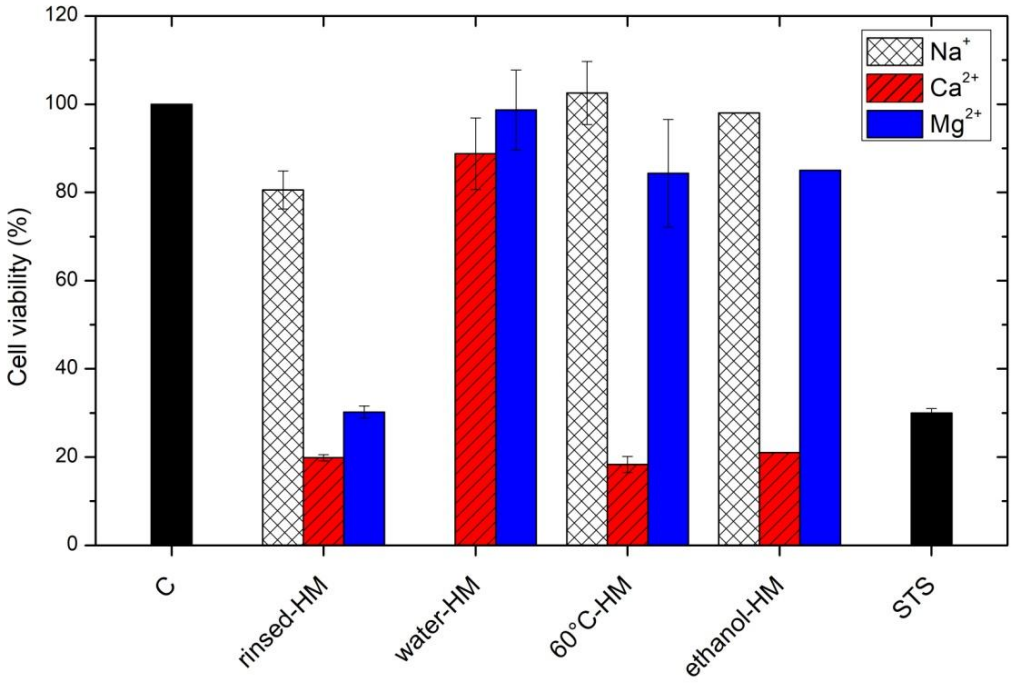

Fig. 8.9: Cell viability of A375 cells exposed (24 h) to HMs gelified by Na^+, Ca^{2+} and Mg^{2+} and undergoing different washing protocols: 5 min rinsing in water (rinsed-HM, salt concentration 125±17 mM), long-lasting incubation in water (water-HM, salt concentration 38 ± 4 mM), 2 hours soaking in water + partially drying (60°C-HM, salt concentration 54 ± 16 mM) and conversion to alchoolgel followed by repetitive soakings in aqueous solution (ethanol-HM, salt concentration 38 ± 4 mM). Measurements were repeated at least three times and the reported values and error bars are respectively the mean values and SD.

8.5 Conclusions

TOCN hydrogel membranes were produced by crosslinking TOCNs with mono and divalent cations and subjected to different post gelation strategies in order to remove the excess of salts and increase their stability in water. *In vitro* toxicity studies were performed on the membranes and on their precursors (TOCN solutions and salt solutions) in cultures of malignant melanoma cells A375, in view of a possible use of them as skin patches. Here are summarize the main results:

1) MTT assay and cell morphology observation demonstrate that TOCNs are not toxic to melanoma cells in culture. Furthermore, observations using confocal microscopy (Fig. 8.5) showed the cellular up-take of TOCNs, both in the area of the cell membrane and scattered in the cytoplasm. The presence

of the crystallites internalization further supports the quantitative data of Fig. 8.4, which demonstrates the non-toxicity of the hydrogel precursors and suggest the possible use of TOCNs as nanomaterial in biomedical applications. Indeed, most literature studies are focused on the use of nanocellulose as films or hydrogels and not as individual, nanometric crystallites. In this sense, further studies are required to better understand the interaction between TOCNs and cells and the fate of TOCNs inside cells both in *in-vitro* and *in-vivo* experiments.

2) The addition of NaCl, $CaCl_2$ and $MgCl_2$ salts (around 20 mM) to the culture medium decreased cell survival, being divalent Ca^{2+} cations more toxic than Na^{+} and Mg^{2+} (Fig. 8.6). The observed reduced cell survival appears to be concentration-dependent and can be ascribed in part to the unbalance of osmotic pressure which is more evident in the presence of Ca^{2+} cations.

3) Ca^{2+} crosslinked TOCN hydrogel membranes laid on top of a confluent monolayer of human melanoma malignant cells (A375) induced a severe reduction of cell viability, probably due to activation of programmed cell death as revealed by the positive control performed with STS which is an inducer of cell apoptosis. This apparent toxicity is to be ascribed to the physical stress of the hydrogel on the cell monolayer.

4) Cytotoxicity was decreased performing indirect contact toxicity tests. For this purpose, a method based on the use of a commercial insert with a microporous (8μm), permeable polyethylene terephthalate (PET) membrane was used. This set-up allows the free exchange of the molecules between cell monolayer and suspended membranes but avoids any shear effect. In this way, the only toxic effect is eventually due to the leakage from the hydrogels. By this approach, the specific toxicity of TOCN-HMs (obtained using different cations and subjected to different processing strategies) was investigated (fig 8.9).
   The best performances were those of Mg^{2+}-HMs, which combined low toxicity and good stability, while Na^{+}-HMs and Ca^{2+}-HMs showed respectively low toxicity but low stability or good stability but high toxicity.
   Among the washing protocols, a long-lasting incubation in aqueous solution reduces the unbound ions concentration in the HMs but weakens the hydrogel structure or eventually disrupts it in the case of Na^{+}-HMs. On the contrary a two days incubation in water followed by a partial drying or an intermediate washing step in ethanol reduce the unbound ions content and, at the same time, make all the HMs more stable and compact, irrespectively of the charge of the cation.

In conclusion, the performed toxicity studies showed that TOCN-HMs fabricated with cation–mediated gelation lack of cytotoxicity, in particular when the gelling cation is Na^{+} or Mg^{2+} , being Mg^{2+}-HMs also stable after long-term storage in aqueous solution. Moreover, TOCN crystallites were observed to undergo cellular internalization without significantly compromise cell survival. These evidences suggest both TOCN-HM and individual TOCN crystallites as good candidate materials for application in the biomedical field.

PART 3

Hybrid TEMPO-oxidized Cellulose Nanocrystals/Chitosan Hydrogels

CHAPTER 9:
Materials and Methods for TOCN/Cht hydrogels

In this chapter, the procedures utilized to prepare hybrid TOCN/chitosan (TOCN/Cht) hydrogels and the techniques used to investigate their structure and properties are reported. More into details, Section 9.1 describes the procedures followed to obtain TOCN/Cht solutions and hydrogels starting from aqueous TOCN and Cht solutions. Section 9.2 concerns, instead, the techniques used to characterize the hybrid hydrogel from a mechanical and structural point of view. Section 9.3 reports the experimental approaches exploited to study the enzymatic degradation and the release properties of TOCN/Cht hydrogels loaded with fluorescent labeled bovine serum albumin (FITC-BSA). Finally, in Section 9.4, the methods used to characterize the mucoadhesion of the hydrogels are described.
The rheological measurements, compression tests and mucoadhesion measurements were performed during my permanence at the Institute of Pharmacy of the Innsbruck University (Drug delivery and Powder Technology research Group).
All the results obtained with the techniques described in this Chapter will be reported in Chapter 10.

9.1 TOCN/Cht solutions and hydrogels preparation

9.1.1 TOCN/Cht solutions

TOCN/Cht solutions were obtained starting from chitosan solutions and aqueous TOCN solutions. TOCN solution, with a crystallite concentration around 4 g L^{-1} and neutral pH, was obtained following the same procedure described in PART 1, Chapter 2. Chitosan solution was prepared, instead, by dissolving low molecular weight chitosan in acidic aqueous solution. In particular, 1 g chitosan was added to 250 mL distilled water and 1 M HCl was added to the solution under agitation until a pH around 2 was obtained. The solution was kept in agitation for 2 hours to allow complete dissolution of chitosan and a clear, visually homogeneous chitosan solution with concentration around 4 g L^{-1} was obtained.

At this point, 125 mL of TOCN solution (0.5 g TOCN) was added slowly to chitosan solution under agitation, so that the weight ratio between nanocellulose and chitosan was 1:2. At this pH value, the most part of the carboxyl functional groups of TOCNs is in the neutral state, conversely, amino functionalities of chitosan are fully protonated. The resulting 4 g L^{-1} TOCN/Cht solution (pH around 2.3) was then stirred at 80°C until the desired final concentration was reached. All the solutions so obtained were homogeneous, almost transparent with jelly-like consistency.
To obtain a weight ratio between nanocellulose and chitosan equal to 1:3 and 1:1 the same procedure was used but different volumes of nanocellulose solutions were added to chitosan solution.

9.1.2 TOCN/Cht hydrogels

Hybrid TOCN/Cht hydrogels were prepared starting from TOCN/Cht solutions at the desired concentration (in the range 0.9 - 3.1 wt%) and using disodium succinate as crosslinker and stabilizing agent for Chitosan. In particular, for the mechanical characterization of hydrogels and the evaluation of their mucoadhesion properties, hydrogel samples were prepared by filling with TOCN/Cht solution 3 mL culture plates wells, covering the opened extremities with dialysis membrane (molecular weight cutoff 10000) and placing the wells in a 0.5 M disodium succinate solution for 12 hours.

To investigate the enzymatic degradation and the drug release properties of TOCN/Cht hydrogels, we prepared cylindrically shaped hydrogels. The cylindrical shape was chosen because of its simplicity and reproducibility of preparation and because it enables an easy evaluation of both longitudinal and transversal dimensions during the degradation studies. In this case, the TOCN/Cht solution was placed, with the aid of a syringe, in a teflon tube (6 mm internal diameter and 25 mm height) closed at the two extremities with a dialysis membrane (MW cutoff 10000). To promote the gelation, the tube was placed in 15 mL of 0.5 M disodium succinate solution. After 12 hours the tube was recovered from the solution and the inside gelled composite material was taken out from the tube, obtaining a self-standing TOCN/Cht hydrogel cylinder. Previously to measurements, the two faces of the cylinders, wrinkled because of the contact with the non rigid dialysis membrane, were cut to get a more defined and constant cylindrical geometry.
To study the drug release properties, the hybrid hydrogel was loaded with fluorescein isothiocyanate labeled bovine serum albumin (FITC-BSA). For the preparation of FITC-BSA solutions, 20 mg BSA were dissolved in 10 mL 0.1 M NaOH solution and stirred. After that, 1 mL FITC solution (1 g L^{-1} in DMSO) was added and the reaction mixture was left for 20 h at 5 °C in the dark. The resulting FITC-BSA complex was then separated from unreacted FITC using a column filled with

Sephadex G25 resin and further purified and concentrated by centrifugation at 4500 RPM for 45 min using a 20 mL Vivaspin (molecular weight cutoff 5000). An aqueous FITC-BSA solution with BSA and FITC concentration around 2 g L^{-1} and 14 μM, respectively, was obtained. The ratio between BSA and FITC molecules was estimated to be around 2:1 (assuming that the purification procedures do not lead to BSA losses). 2.1 mL FITC-BSA solution were added to 18 mL TOCN/Cht solution (1.7 wt%) and the solution was stirred at 40°C in the dark until a homogeneous dispersion with the desired concentration of the FITC-BSA and TOCN/Cht precursors was obtained. The hydrogel cylinders were obtained performing the procedure above reported in the dark to avoid fluorescence loss.

9.2 TOCN/Cht solutions and hydrogels characterization

The mechanical properties of TOCN/Cht solutions and hydrogels at different concentrations (0.9 wt% - 3 wt%) and different nanocellulose/chitosan weight ratios (1:3, 1:2, 1:1) were studied by rheology and compression tests, respectively. The structure and morphology of the hydrogels were investigated by microscopy (fluorescence microscopy and SEM).

9.2.1 TOCN/Cht solutions rheological characterization

Rheological measurements on TOCN/Cht solutions at different TOCN/Cht weight ratio and different total concentration were performed by a stress-controlled rheometer (Haake Mars Rheometer, 379-0200, Thermo ElectronGmbH, Karlsruhe, Germany) in cone-plate geometry (Rotor: C25/1° Ti, D= 25 mm, gap = 0.052 mm). To determine the linear viscoelastic region, stress sweep SS tests were performed in the range 0.01-500 Pa at fixed frequency f = 1 Hz. Frequency sweep FS tests were performed in the frequency range 0.05-50 Hz keeping the stress constant, τ = 1 Pa. The temperature was fixed at T= 25±1 °C. Both SS tests and FS tests were done in triplicate. To allow a comparison, rheological measurements were performed on pure TOCN and pure Cht solutions too. TOCN solutions were characterized under the same conditions of TOCN/Cht solution. In particular, the pH was brought around 2.3 by addition of 1 M HCl.

9.2.2 TOCN/Cht hydrogels compression tests

To mechanical characterize the TOCN/Cht hydrogels at different TOCN/Cht weight ratio and total concentration, a TA-XT2i Texture Analyzer was used. The hydrogel samples were prepared filling with TOCN/Cht solution a 3 mL well, covering the

opened extremity with a dialysis membrane (molecular weight cutoff 10000) and placing the well in a 0.5 M disodium succinate solution for 12 hours. Afterwards the dialysis membrane was removed and the resulting hydrogel cylinders (16 mm height, 16 mm diameter) were compressed three times with a 10-15 s recovery time in between. The trigger force, test velocity and compression distance were fixed to 0.098 N, 0.5 mm s^{-1} and 2 mm respectively. The measurements were performed at room temperature and using a 10 mm diameter cylindrical probe. Measurements were done firstly on the top face of the hydrogel cylinder (named T), then the hydrogel was overturned and measurements were done on its bottom face (named B). Finally, the cylinder was cut in half and its central part was evaluated (named C). All the measurements were performed in triplicate and with the cylinders placed in the wells.

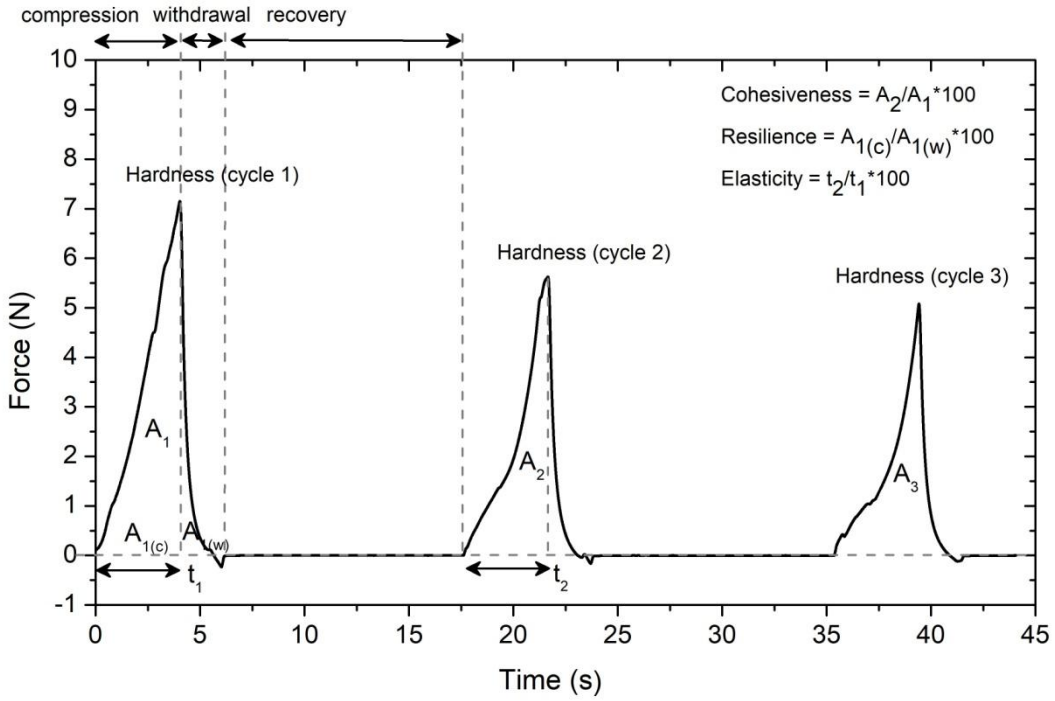

Fig 9.1: Example of force versus time curve obtained in TPA experiments. The samples were subjected to three compression cycles with a 10-15 s recovery time in between (trigger force 0.098 N, test velocity 0.5 mm s^{-1} and compression distance 2 mm) using a 10 mm diameter cylindrical probe. The main quantities extrapolated from the curve and used to characterize the hydrogel samples are reported in figure. A_1, A_2, A_3 refer to the areas (N s) under the curve for the first, second and third compression cycles, $A_{(c)}$ and $A_{(w)}$ to the area respectively under the compression and withdrawal portion of the curve, t stands for time.

Fig. 9.1 shows a representative example of the Force/Time curve obtained through the performed compression tests. Different parameters, related to the mechanical properties of the sample, can be determined from it. In particular, we focused our attention to the following quantities (Stable Micro Systems web site):

- The hardness of the material, that is the maximum force required to obtain a 2 mm deformation;
- The cohesiveness, that is the % ratio between the area under the curve for a compression cycle with respect to the previous one (A_2/A_1 in Fig 9.1) and tells how well the samples withstand subsequent deformations;
- The resilience, which is the % ratio between the area up to the maximum value and the area during the withdrawal step during the same cycle ($A_{1(c)}/A_{1(w)}$ in Fig 9.1) and shows the ability of the hydrogel to recover its original position during the first compression;
- The elasticity, defined as the time required to achieve a compression with respect to the time required for the previous one, in percentage (t_2/t_1 in Fig 9.1).

Another parameter that can be obtained from compression experiments is the Young Modulus E, which measures the stiffness of a material and is defined as the ratio between the stress σ (in N m^{-2}) and the strain γ (in %) in the linear elasticity regime, for a sample subjected to an uniaxial deformation:

$$E = \frac{stress\ \sigma}{strain\ \gamma} \qquad \text{(Eq. 9.1)}$$

In our situation stress and strain can be determined from the Force versus Distance TPA curves, knowing the cross sectional area of the probe (A= 78.5 mm^2) and the initial height of the sample (h_0=16 mm):

$$\sigma = \frac{F}{A} \qquad \gamma = \frac{h_0 - h}{h_0} 100 \qquad \text{(Eq. 9.2)}$$

where F is the compression force and h the height of the sample at time t during the compression test. Fig. 9.2 shows an example of stress versus strain curve obtained for a TOCN/Cht hydrogel sample: the Young Modulus E was determined performing a linear fit in the linear range of deformation (strain 2-6%) and considering its slope.

9.2.3 Fluorescence Microscopy

Images of TOCN/Cht hydrogel cylinders with fluorescent-labeled TOCN were acquired using a LEICA MZ16AF stereomicroscope.

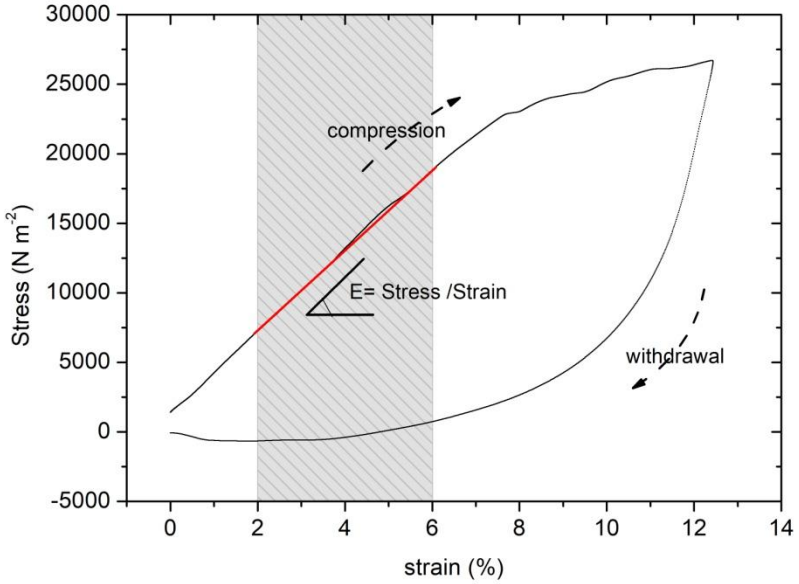

Fig. 9.2: Example of stress versus strain curve obtained from a compression test on a TOCN/Cht hydrogel sample. The Young Modulus of the material was determined evaluating the slope of the curve in the linear range of deformation (gray region in figure, corresponding to 2 - 6% strain). The red line is a linear fit in the considered region.

To prepare fluorescein isothiocyanate (FITC)-labeled TOCNs, 0.75 mL of 2 mM FITC were added to 5 mL of a 0.1 M NaOH aqueous suspension of TOCNs (3 g L^{-1}) (Nielsen et al., 2010) and then stirred for 6 days in the dark at RT.
The suspension was dialyzed against 400 mL NaOH (0.05M) for 7 days by changing the dialysis solution 4 times and then dialyzed against deionized water until pH 7.0 was reached. 2 mL of the resulting 1 g L^{-1} FITC-labeled TOCN solution were added to 7 mL of 1.62 wt% TOCN/Cht solution (2 : 1 weight ratio), which was then stirred and heated at 40°C in the dark, till reaching a final concentration of 2.3 wt%. The resulting FITC-labeled TOCN/Cht solution was placed in Teflon tubes (6 mm an 4 mm internal diameter) closed at the two extremities with a dialysis membrane (molecular weight cutoff 10000) and placed in 15 mL 0.5 M disodium succinate solution in the dark for 12 hours. Before microscope analysis the hydrogels were washed in distilled water for 1 hour.

9.2.4 Scanning Electron Microscopy (SEM)

SEM images of TOCN/Cht hydrogels were acquired using a Zeiss Supra 60 Field Emission Scanning Electron Microscope at the Biotech Laboratories (Engineering Department, University of Trento). TOCN/Cht hydrogel cylinders (concentration 2.1 wt%, Cht:TOCN weight ratio 2:1) were prepared following the procedure explained

in Subsection 9.1.2. To enable the observation of both surface and inside structure of the hydrogels, they were fractured in liquid nitrogen and then freeze dried. After lyophilisation they were sputtered with an ultrathin layer of gold before measurements.

9.3 TOCN/Cht hydrogels enzymatic degradation and release studies

To investigate the release kinetics of TOCN/Cht hydrogels and evaluate their relation with hydrogels degradation, FITC-BSA loaded TOCN/Cht hydrogel cylinders (Cht:TOCN weight ratio 2:1, concentration around 2.7 wt%) were incubated in 15 mL PBS solution (pH 7.4) at 37°C with 3 g L^{-1} lysozyme. To evaluate the contribution of degradation to the release process, blank samples were also prepared, by incubating TOCN/Cht cylinders in 15 mL PBS solution at 37°C without enzyme.
Moreover, pure TOCN samples (concentration 2 wt%) were investigated for comparison. In this case, the hydrogels were prepared using 0.5 M $CaCl_2$ as crosslinker agent and the release and degradation processes were evaluated in 15 mL 0.1 M HEPES solution (pH 7.4) at 37°C both in presence and absence of 3 g L^{-1} lysozyme. We used HEPES buffer solution for TOCN hydrogels incubation, instead of PBS, to avoid the formation of calcium phosphate due to the interaction between Ca^{2+} ions released by the hydrogles and PBS phosphates.
At fixed times, hydrogel cylinders were taken from incubation solutions and measurements (FITC-BSA release, weight loss and dimensions loss) were done. Measurements were performed in triplicate and the results were expressed as mean value and SD over the three measurements.

9.3.1 Release kinetics

For FITC-BSA release measurements, fluorescence spectra of the incubation solutions were acquired using a Varian Cary Eclipse Fluorescence Spectrophotometer. Emission spectra were acquired in the range 505-600 nm by exciting the sample at 498 nm. A calibration curve was acquired to relate the fluorescence intensity signal to the FITC concentration in PBS. The release was then expressed as percentage with respect to the maximum expected signal in the case of complete FITC-BSA release. At the end of the experiments, the cylinders were disintegrated by sonication to check the correctness of the maximum release expected.

9.3.2 Weight loss measurements

To evaluate the weight loss due to enzymatic degradation of chitosan, the hydrogel cylinders were weighted using an analytic Mettler Toledo balance with resolution 0.1 mg. The weight loss at time t was then express as the difference between the initial weight of the cylinder W_0 and the weight at time t: $W_{loss} = W_0 - W_t$. The main source of error in this experimental procedure is related to the presence of excess and evaporating water, which was estimated around 0.012 ± 0.04 g during the measurement, corresponding to a percentage error around 5-10%.

9.3.3 Dimensions loss measurements

The changes in the dimensions of hydrogel cylinders were evaluated acquiring photographs of the cylinders at different times and analyzing them with the software ImageJ. In particular, the changes in height and diameter were considered and expressed as losses with respect to the initial height and diameter, respectively. To account for the non uniformity of heights and diameters, which was particularly evident at long times as a consequence of the non uniform degradation, three values of heights and diameters were measured for each image and the mean value and SD were considered.

9.4. Mucoadhesion properties of TOCN/Cht hydrogels

The mucoadhesiveness of TOCN/Cht hydrogels on porcine intestinal mucosa (provided by a local slaughterhouse) were evaluated using a Texture Analyzer. The exploitation of a Texture Analyzer is indeed a well assessed method for the characterization of the mucoadhesion properties of a material through the measurement of the detachment force and the total work of adhesion from an experimental force-distance curve (Woertz et al., 2013).
For this purpose, TOCN/Cht hydrogel cylinders were prepared in 3 mL culture plates wells starting from TOCN/Cht solutions with different total concentrations (in the range 0.9-3 wt%) and TOCN:Cht weight ratios (1:1, 1:2 and 1:3). After gelation the cylinders were cut in sections resulting in hydrogel disks with dimensions of around 16 mm in diameter and 4 mm in height. A sketch of the exploited experimental apparatus is reported in Fig. 9.3a.

The disks were attached to the upper moving arm of the instrument using the dedicated gel mucoadhesion probe, which consists of an inverted cone shape with machined concentric grooves (as shown in the inset of Fig. 9.3b). The porcine intestine was cut in 3x3 cm pieces, opened and fixed on the bottom working surface of the instrument. The hydrogel disks were attached to the mucosa with a force of 50 mN for 60 s. Afterwards the disks were raised up from the mucosa at a rate of 0.1 mm s^{-1}. Fig. 9.3b shows an example of the experimentally obtained Force versus Distance curve, from which the maximum adhesion force and total work of adhesion were evaluated measuring the peak force value and the area under the curve.

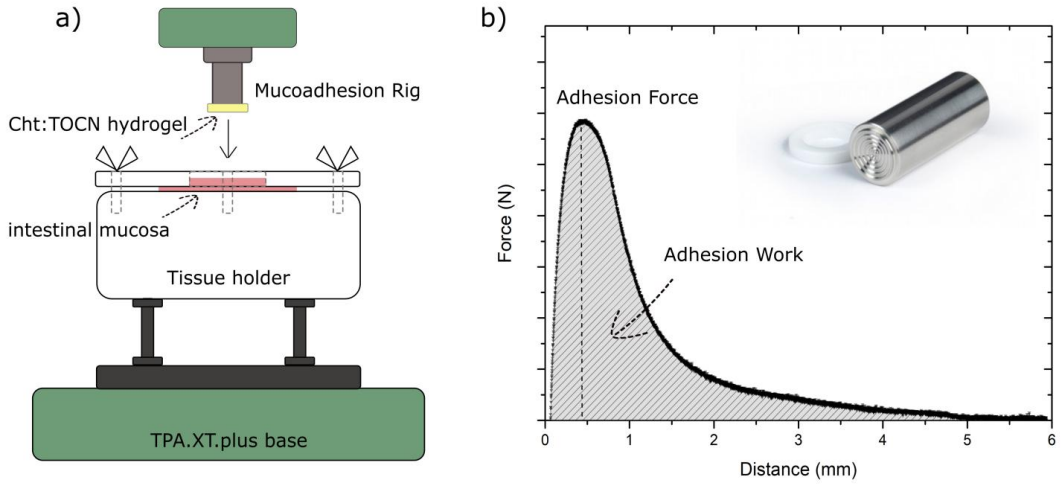

Fig 9.3: (a) Sketch view of the experimental setup used to perform mucoadhesion measurements with the Texture Analyzer instrument. The porcine intestinal mucosa is fixed on a tissue holder at the base of the instrument, while the TOCN/Cht hydrogel disk is attached to the upper moving arm of the instrument using the dedicated probe. The probe is lowered down to press the mucosa with a 50 mN force for 60 s and then raised up at a rate of 0.1 mm s^{-1}. (b) Typical force versus distance curve obtained while the hydrogel is raised up from the mucosa and graphical definition of adhesion force and adhesion work. In the inset a picture of the gel mucoadhesion probe is shown.

Chapter 10:
TOCN/Cht HYDROGELS

Here we report the results obtained studying hybrid TOCN/Cht hydrogels, with the purpose of understanding the individual role of TOCN and Cht as components of a potential hydrogel delivery system.
The first section (Section 10.1) shows the preliminary rheological and mechanical studies performed on TOCN/Cht solutions and hydrogels at different concentration and TOCN/Cht weight ratios. Since the characterization of material's structure is the starting point to understand the properties of the final product, the structural features of the hydrogel matrix and surface were studied using microscopy techniques, as reported in Section 10.2.
Section 10.3 reports instead the results of the enzymatic degradation and release kinetics studies performed on drug-loaded TOCN/Cht hydrogels (at fixed concentration and TOCN/Cht weight ratio) incubated in buffer solution. A medium-sized protein such as BSA was chosen as protein drug model and functionalized with fluorescence FITC to follow its release via fluorescence spectroscopy, while lysozyme was utilized as a representative example of human digestive enzymes. Finally, in section 10.4, the attempts performed to evaluate the mucoadhesion properties of TOCN/Cht hydrogels at different concentration and TOCN/Cht weight ratios are described. For all the experiments, the results obtained for TOCN/Cht hydrogels were compared with the case of pure TOCN hydrogels.

To make the presentation and discussion of the results more clear, in Fig. 10.1 a schematic summary of the experimental procedures exploited is reported. In particular, the red stars highlight the measurements performed on the different TOCN:Cht materials, a more technical description of which is reported in Chapter 9.

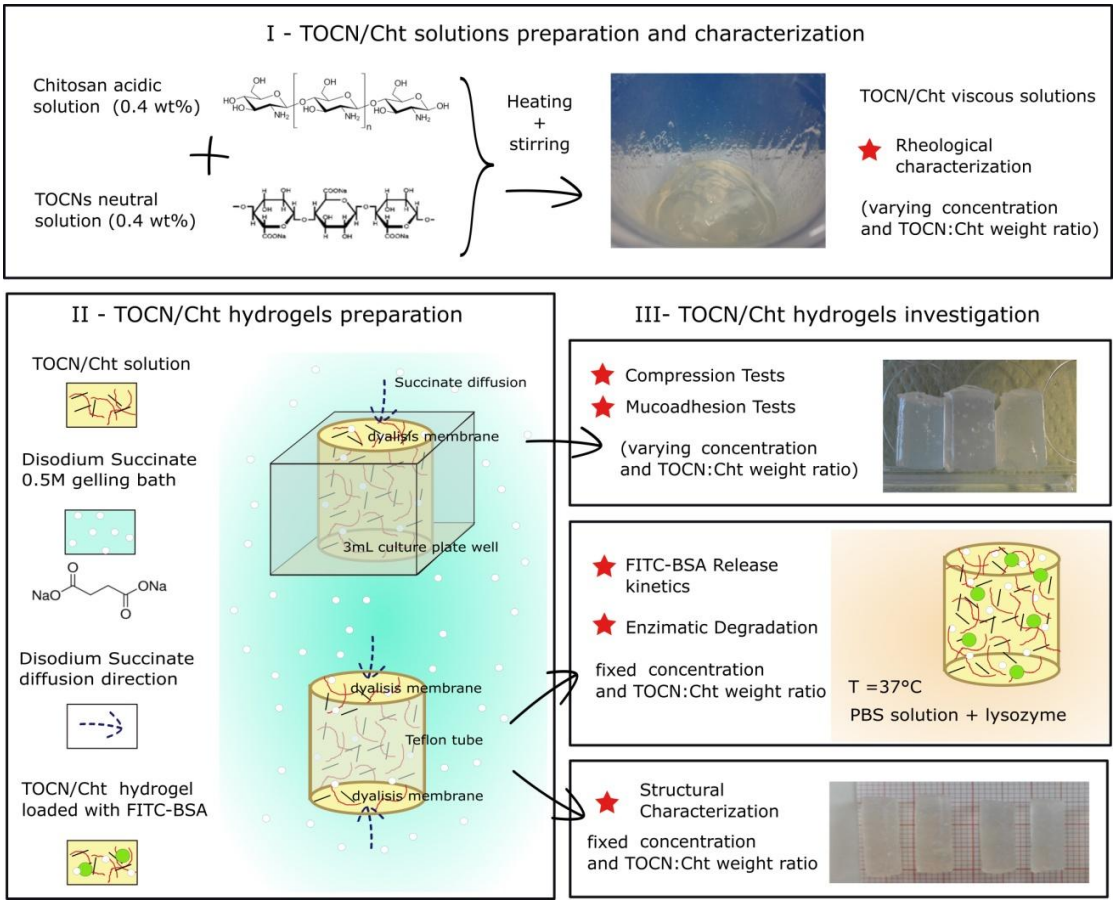

Fig 10.1: Scheme of the experimental procedures followed and experimental techniques used to prepare and characterize hybrid TOCN/Cht hydrogels. In particular, part I reports how TOCN/Cht solutions were prepared starting from the individual components, part II schematically shows how hydrogel cylinders were obtained exploiting disodium succinate as crosslinker and stabilizing agent. Finally part III briefly reports the techniques used to mechanically and structurally characterize the TOCN/Cht hydrogels and study the release and degradation properties of FITC-BSA loaded TOCN/Cht hydrogels incubated in PBS solution with Lysozyme. A more detailed description of the procedures and experimental techniques utilized is reported in Chapter 9.

10.1 TOCN/Cht Solutions and Hydrogels mechanical characterization

The viscoelastic and mechanical properties of the hybrid solutions and hydrogels were evaluated exploiting rheology and compression tests, respectively. The influence of total concentration and ratio between chitosan and TOCN weights were evaluated and the results were compared with the case of pure TOCNs and chitosan materials. In Table 10.1 the investigated concentrations (Chitosan, TONCs and total)

and ratios are summarized. As visible, the samples and experiments were divided into three blocks to allow a systematic study the influence of different variables. In the first part, the total concentration was varied in the range 0.9 - 2.8 wt%, keeping fixed the TOCN:Cht weight ratio to 0.5. The concentration range was chosen in such a way to obtain manageable solutions and self-standing hydrogels: concentrations smaller than 0.9 wt% did not lead to strong enough hydrogels while concentrations higher than 2.8 wt% resulted in solutions too viscous to be managed in an easy and reproducible manner. In the second and third part, instead, the TOCN:Cht weight ratio was varied keeping fixed respectively the TOCNs concentration and the total concentration.

Table 10.1: Summary of the different samples prepared and studied, in terms of TOCN:Cht weight ratios, Chitosan, TOCNs and total concentration. The samples and experiments were divided into three parts, by varying one parameter at a time (yellow columns) and keeping fixed the other one (gray column). Samples of pure TOCN and pure Chitosan were considered for comparison.

	TOCN/Cht ratio	Cht conc wt%	TOCN conc wt%	tot conc wt%
PART 1	0.5	0.6	0.3	0.9 ± 0.1
	0.5	1.0	0.5	1.5 ± 0.1
	0.5	1.4	0.7	2.1 ± 0.1
	0.5	1.9	0.9	2.8 ± 0.1

	TOCN/Cht ratio	Cht conc wt%	TOCN conc wt%	tot conc wt%
PART 2	pure TOCN	0.00	0.75	0.75 ± 0.05
	1	0.70	0.70	1.4 ± 0.1
	0.5	1.47	0.73	2.2 ± 0.1
	0.33	2.33	0.78	3.1 ± 0.1

	TOCN/Cht ratio	Cht conc wt%	TOCN conc wt%	tot conc wt%
PART 3	1	0.70	0.70	1.4 ± 0.1
	0.5	0.93	0.47	1.4 ± 0.2
	0.33	1.05	0.35	1.4 ± 0.2
	pure Cht	1.40	0.00	1.4 ± 0.1

10.1.1 Rheology of TOCN/Cht solutions

The influence of TOCN:Cht weight ratios and concentrations on the viscoelastic properties of TOCN/Cht solutions were investigated by SS and FS rheological tests. Fig. 10.2 shows an example of SS and FS curves obtained for a solution with a TOCN:Cht weight ratio equal to 0.5 and a total concentration equal to 2.2±0.1 wt%.

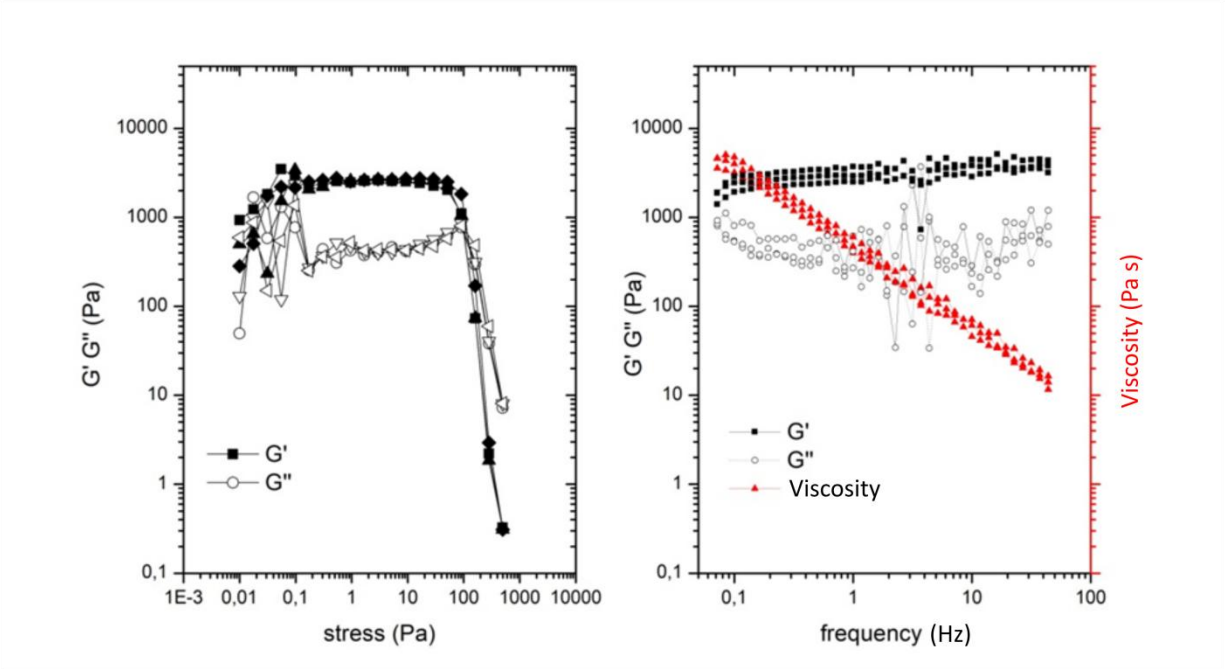

Fig. 10.2: Example of SS test (left panel) and FS test (right panel) for a TOCN/Cht solution with a TOCN:Cht weight ratio of 0.5 and 2.2±0.1 wt% total concentration. G' and G'' refer to elastic modulus and viscous modulus respectively. Rheological measurements were performed using a cone-plate geometry (Rotor: C25/1° Ti) with a 0.052 mm gap and temperature fixed at T=25±1 °C. Measurements were performed in triplicate.

SS tests enabled to find the linear viscoelastic region, that is the stress range in which elastic modulus G' and viscous modulus G'' are quite constant and the tests can be carried out without destroying the structure of the sample. From FS tests it is clear that the sample behaves as a structured (gelled) system, being G'>G'' in the considered frequency range and both of them quite independent from frequency. Moreover, the sample shows a shear thinning profile, with viscosity decreasing increasing the shear rate. Different values but similar trends were obtained for all the tested samples, apart from the case of pure chitosan, which showed instead the typical flow properties of solutions (not constant G', G'' in the considered ranges and very low viscosity values).

In Table 10.2 the main parameters obtained from SS curves and FS curves for the different tested samples are reported. In particular the reported G', G'' and viscosity values were evaluated from FS curves performing a linear fit in the 0.1-50 Hz frequency range and extrapolating from it the values at 1 Hz frequency. The last

column reports instead the stress value for which the gel-like structure of the sample is destroyed, that is the stress value for which G'' becomes equal or larger than G' (obviously this parameter cannot be evaluated for liquid samples like Cht solutions).

Table 10.2: Rheological parameters obtained through stress sweep curves ($Stress_{G'=G''}$) and through frequency sweep curves (G', G'', Viscosity). The first and second column report the TOCN:Cht ratio and concentration of the considered samples. Column three, four, and five show the elastic modulus G', viscous modulus G'' and Viscosity values at 1 Hz evaluated from linear fits performed in the frequency range 0.1- 50 Hz. The last column report the stress value after which G'' becomes larger than G' and the gel-like structure of the material is destroyed. Values and uncertainties are the mean value and standard deviation over three measurements, respectively.

	TOCN/Cht ratio	$conc_{tot}$ (wt%)	G' (Pa)	G'' (Pa)	Viscosity (Pa*s)	$Stress_{G'=G''}$ (Pa)
PART 1	0.5	0.9 ± 0.1	66 ± 8	4 ± 1	11 ± 1	29 ± 8
	0.5	1.5 ± 0.1	366 ± 22	53 ± 5	60 ± 4	70 ± 19
	0.5	2.1 ± 0.1	1021 ± 62	145 ± 28	174 ± 2	124 ± 33
	0.5	2.8 ± 0.1	2626 ± 174	316 ± 45	428 ± 24	220 ± 60
PART 2	pure TOCN	0.75 ± 0.05	19950 ± 1277	3412 ± 308	3263	1210 ± 267
	1	1.4 ± 0.1	2103 ± 63	282 ± 8	277	221 ± 61
	0.5	2.2 ± 0.1	2956 ± 507	409 ± 61	483	125 ± 35
	0.33	3.1 ± 0.1	2460 ± 76	351 ± 41	404	125 ± 35
PART 3	1	1.4 ± 0.1	1994 ± 161	222 ± 41	323	217 ± 57
	0.5	1.4 ± 0.2	571 ± 193	60 ± 28	92	89 ± 25
	0.33	1.4 ± 0.2	207 ± 37	29 ± 13	33	89 ±24
	pure Cht	1.4 ± 0.1	0.0019 ± 0.0005	0.037±0.001	0.074	

As visible in Table, G'>G'' for all the considered samples, independently from concentration and TOCN:Cht weight ratios, apart from the case of pure chitosan. The dependence of G', G'' and viscosity values on samples concentrations and weight ratios between TOCN and chitosan are reported in Fig. 10.3.

As shown in Fig. 10.3a, the rheological properties of the samples, increase with the total concentration following approximately a quadratic law. Considering the dependence on TOCN:Cht weight ratio, it appears that the G', G'' and viscosity values increase increasing the relative weight of TOCNs with respect to chitosan at constant total concentration (Fig. 10.2d) while they remain quite constant if the TOCN concentration is kept constant (Fig. 10.2b). These observations suggest that the gel-like behavior of the samples is mainly due to TOCNs, which act as reinforcing agent in the hybrid TOCN/Cht material. As a comparison the case of pure TOCN

samples at concentration 0.75 wt% and pH around 2.3 is reported in Fig. 10.3c (Pure TOCN), showing an increase of the G' value of an order of magnitude with respect to hybrid TOCN/Cht samples.

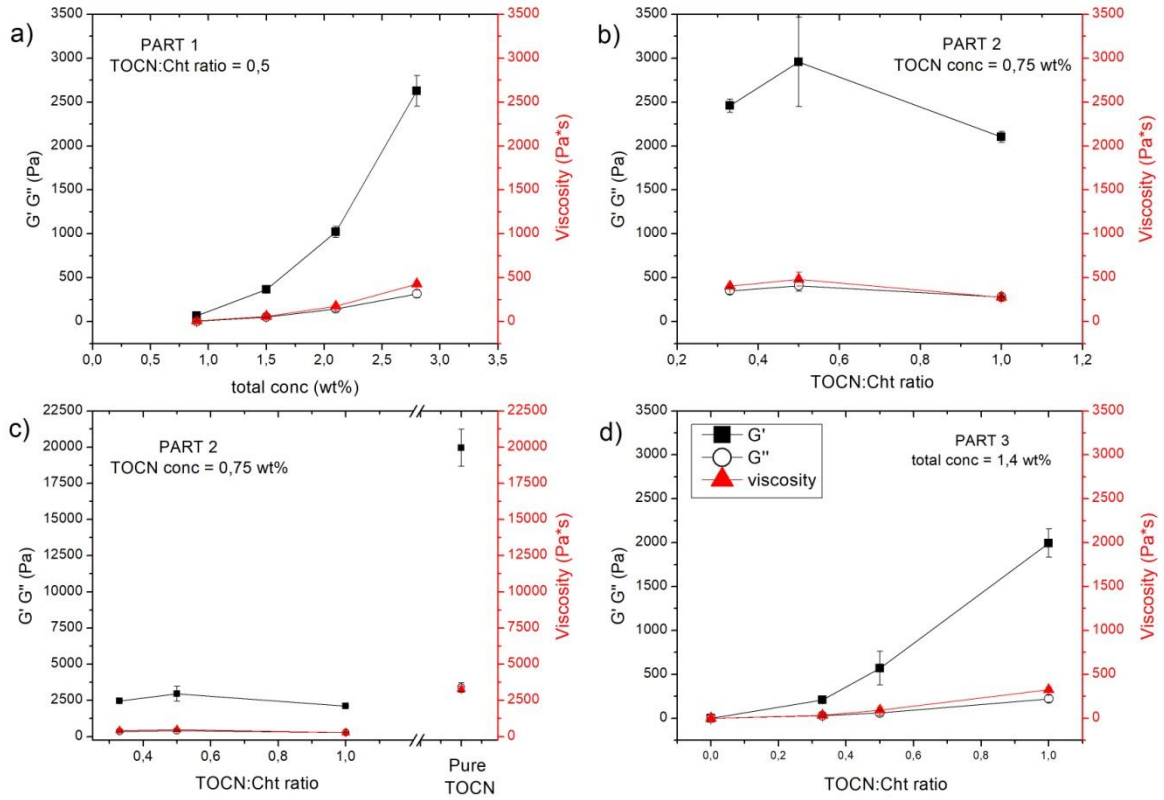

Fig. 10.3: Rheological parameters (Elastic Modulus G', Viscous modulus G'' and Viscosity) of TOCN/Cht solutions as a function of: total concentration at fixed TOCN:Cht weight ratio (a), TOCN:Cht ratio at fixed TOCN concentration (b), TOCN:Cht ratio at fixed total concentration (d). Panel (c) shows a comparison between TOCN/Cht hybrid solutions (TOCN concentration 0.75wt% + variable amounts of Cht solution) and a pure TOCN solution at the same pH and concentration (pH around 2.3 and concentration 0.75wt%). The reported values and error bars are the mean value and SD over three replicated measurements, respectively. Rheological measurements were performed using a cone-plate geometry (Rotor: C25/1° Ti) with a 0.052 mm gap and temperature fixed at T=25±1 °C.

These findings confirm the reinforcement capability of TOCN crystallites (Aitomäki and Oksman, 2014; Lee et al., 2014; Mondal, 2017) and the impressive mechanical properties of TOCN hydrogels spontaneously formed in acidic conditions (Saito et al., 2011; Way et al., 2012).

Despite the gel-like rheological behavior shown by TOCN/Cht samples, self-standing hydrogels could not be obtained simply by mixing TOCN solutions and chitosan solutions. For this reason we exploited disodium succinate as a crosslinker and stabilizing agent, being it able to electrostatic interact with the amino groups of chitosan and to originate well shaped and stable hydrogels. The incubation in the disodium succinate solution is expected to increase the pH inside the hydrogel and,

probably, deprotonates some of the carboxylic groups of TOCN. It is also expected that a small and flexible molecule such as disodium succinates diffuses in the hydrogel matrix and crosslinks chitosan chains more easily than the rigid and large TOCN crystallites.

10.1.2 Compression tests on TOCN/Cht hydrogels

Physical properties such as hardness, cohesiveness and elasticity are important factors for the protection of encapsulated drugs during hydrogel migration from the oral cavity to the intestine and were thus evaluated by texture profile analysis (TPA). Texture Analyzers are commonly used to study the mechanical properties of hyrogels, quantifying their deformation under compression (Singh et al., 2018; Jones et al., 1997, 1996).

As schematically shown in Fig. 10.1 (panel I,) TOCN/Cht hydrogels with malleable and cylindrical shapes were prepared using 3 mL polystyrene culture plate wells as moulds. The wells were covered with dialysis membrane and placed in 0.5 M Disodium Succinate solution, enabling Disodium Succinate to diffuse during the moulding process, interact with TOCN/Cht and stabilize the structures.

The hydrogel cylinders were subjected to axial compression tests, keeping the maximum deformation smaller than 13%. This upper limit was determined by the brittleness of the samples at low TOCN:Cht ratios and concentrations, the surface of which is visibly perturbed when undergoing deformations higher than 13%. Measurements were performed on both cylinder sides (being the top side and bottom side in contact, during the gelation process, respectively with the gelling solution through the dialysis membrane and with the well). Then, by cutting out the cylinders in two parts, the physical properties inside the bulk of the composite were tested too (central part).

Fig. 10.4 shows the results in terms of hardness obtained for samples with different concentrations and TOCNC:Cht weight ratios. In particular, panel a) refers to measurements on hydrogels with fixed TOCN:Cht weight ratios and variable total concentrations, panel b) and panel c) to tests on samples with different TOCN:Cht weight ratios and fixed TOCN concentration and total concentration, respectively. Finally, to allow a comparison, panel d) shows the results for pure TOCN hydrogels obtained starting from neutral TOCN solutions crosslinked with 0.5 M calcium chloride.

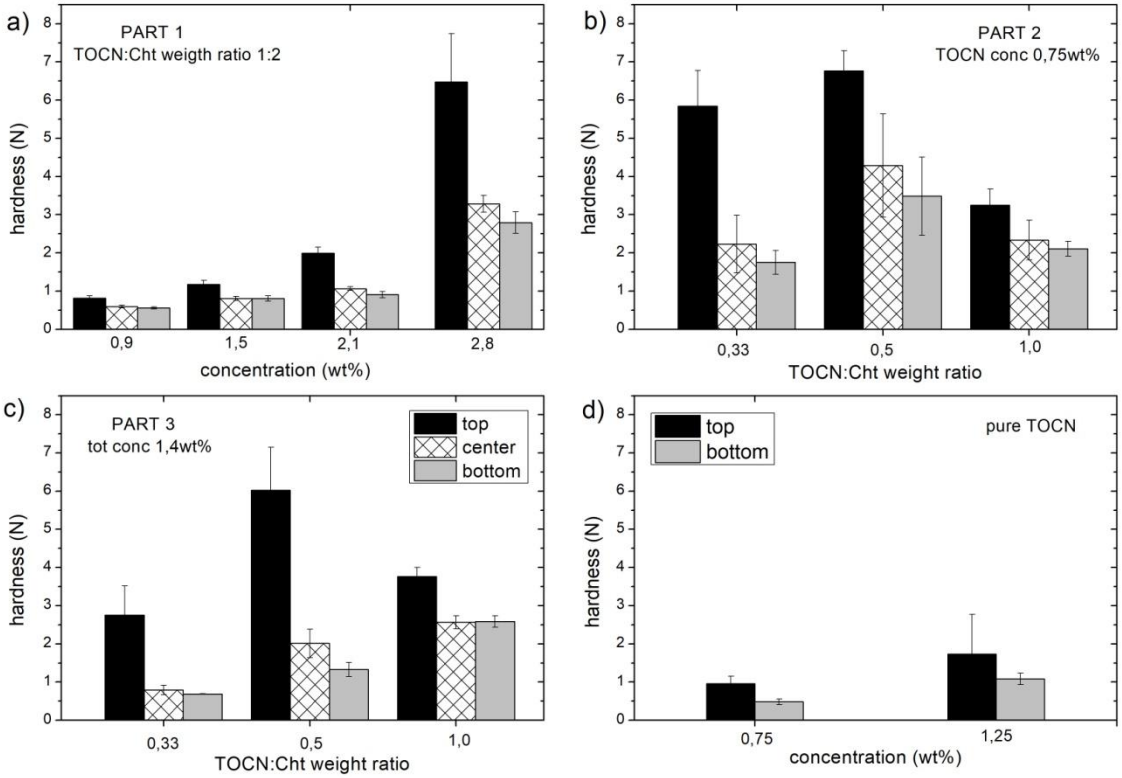

Fig. 10.4: Results of compression tests performed on TOCN/Cht hydrogels at different concentrations and TOCN:Cht weight ratios (figure a-b-c) and on TOCN hydrogels at two different concentrations (figure d). TOCN/Cht hydrogels and TOCN hydrogels were obtained using respectively 0.5 M disodium succinate solution and 0.5 M calcium chloride solution as stabilizing agents. Different columns refer to the hardness values obtained for the different hydrogel layers tested: top (meaning the up side of the cylinder, which was in contact with the gelling solution through the dialysis membrane during the gelation process), center (meaning the central part of the cylinder) and bottom (meaning the face of the cylinder, which was far from the gelling solution and in contact with the bottom of the well). The measurements were performed at least in triplicate and the reported values and error bars are the resulting mean values and SD.

The comparison with pure Cht samples was not possible because, in absence of the reinforcing nanocellulose crystallites, Cht solutions are not able to form durable, self-standing hydrogel structures in the considered concentration range, even in presence of crosslinker agents. Indeed, while cylinders of TOCN/Cht hydrogels or TOCN hydrogels soaked in PBS are stable for months, Cht cylinders almost immediately dissolve.

The different behavior of chitosan can be ascribed to the bigger dimensions and smaller surface to areas of chitosan molecules with respect to TOCN crystallites, which reduce both the degree of possible arrangements achievable and the ability of chitosan molecules to interact among them and with the surrounding water and

salt molecules. The result is a less structured and less viscous material, as shown by rheological measurements too.
An first interesting property emerging from Fig. 10.4 is the fact that the hardness values are always higher for the top face of the hydrogel, that is the one in contact with the dialysis membrane and closer to the disodium succinate solution during the gelation process, with respect to those resulting from measurements performed on a central section and on the bottom face of the hydrogels. This is probably due to a progressively more hindered and slow diffusion of disodium succinate moving away from the hydrogel exposed surface, which reflects in the formation of a material with weaker mechanical properties at higher distances from the interface with the gelling solution. A similar behavior was reported in a literature study, which investigates the formation of cylindrical chitosan hydrogels upon diffusion of OH^- ions from an external bath. In this study, the observed different mechanical properties are ascribed to the diverse porosity and orientation structures created by chitosan at different distances from the hydrogel surface, as a consequence of the decreased diffusion of OH^- (Nie et al., 2016, 2015).

The trends of the hardness values for the top hydrogels surface as a function of the considered concentration and weight ratio parameters are shown in Fig. 10.5, where the hardness values for the three compression cycles are also compared. As visible, there are not significant differences among the three cycles, suggesting that the hydrogel structure is not disrupted by the first compression and the samples are able to withstand subsequent deformations without losing their organization. Considering the dependence on concentrations and weight ratios, panel a) shows that the hardness increases with the total concentration of the two precursors following a non-monotonic trend similar to that observed for the rheological parameters of the starting TOCN/Cht solutions (Fig. 10.3a). Differently, hardness values do not show a clear dependence on TOCN:Cht weight ratios, even if the maximum strength was always measured for the case of 0.5 TOCN:Cht weight ratio (Panel b) and c)). While in the case of the starting TOCN/Cht solutions the main contribution to the mechanical strength of the samples (evaluated through G', G'', viscosity values) was given by TOCNs, in this case the introduction of a chitosan crosslinker agent clearly contributes to the mechanical properties. As a consequence, both the TOCNs reinforcing capability and the presence of crosslinked chitosan contribute to the hydrogel hardness. The result is a clear increase of the mechanical properties with the total concentration, as the contributions of TOCNs and Cht sum up, and a more complex dependence on TOCN:Cht weight ratio, because the two contributions are in competition among them.

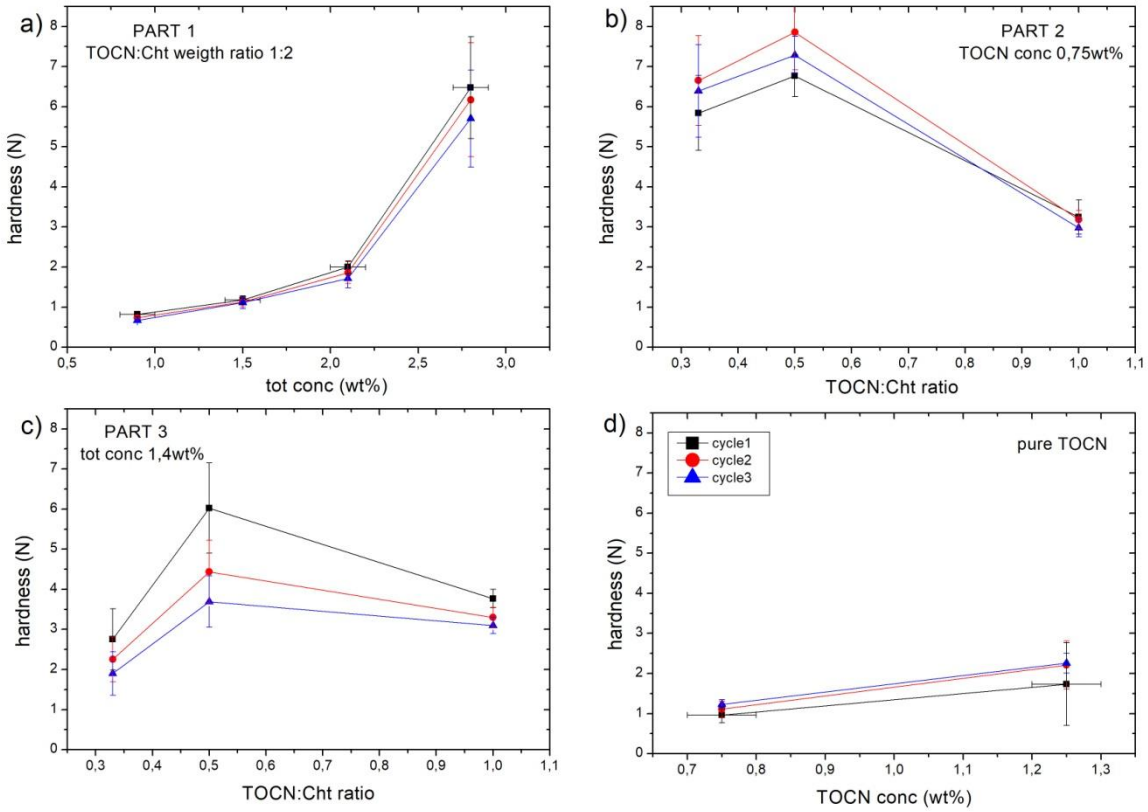

Fig. 10.5: Hardness of TOCN/Cht and TOCN hydrogels at different concentrations and TOCN:Cht weight ratios. TOCN/Cht and TOCN hydrogels were stabilized with 0.5 M disodium succinate solution and 0.5 M calcium chloride solution respectively. Cycle 1, cycle 2 and cycle 3 refer to the subsequent compression cycles to which the hydrogel cylinders were subjected. The measurements were performed at least in triplicate and the reported values and error bars are the resulting mean values and SD.

The increase of hardness with concentration is coherent with the results reported in literature both for chitosan hydrogels (Hurler et al., 2012) and other materials (Jones et al., 1996; Karavana et al., 2012). A quantitative comparison of the numerical values is made difficult by the fact that the TPA results partially depend on the test parameters such as compression speed and distance (Rosenthal, 2010). However, it appears that the hardness of hybrid TOCN/Cht hydrogels (at total concentration 2.7 wt%) is an order of magnitude higher with respect to that reported for pure chitosan hydrogels (at concentration 5 wt%) and around three times higher than that of glycerol-reinforced chitosan hydrogels (at concentration 2.5 wt%) (Hurler et al., 2012).

The Elasticity, Cohesiveness and Resilience values obtained from compression tests measurements on the top face of hydrogel samples are reported in Fig. 10.6.

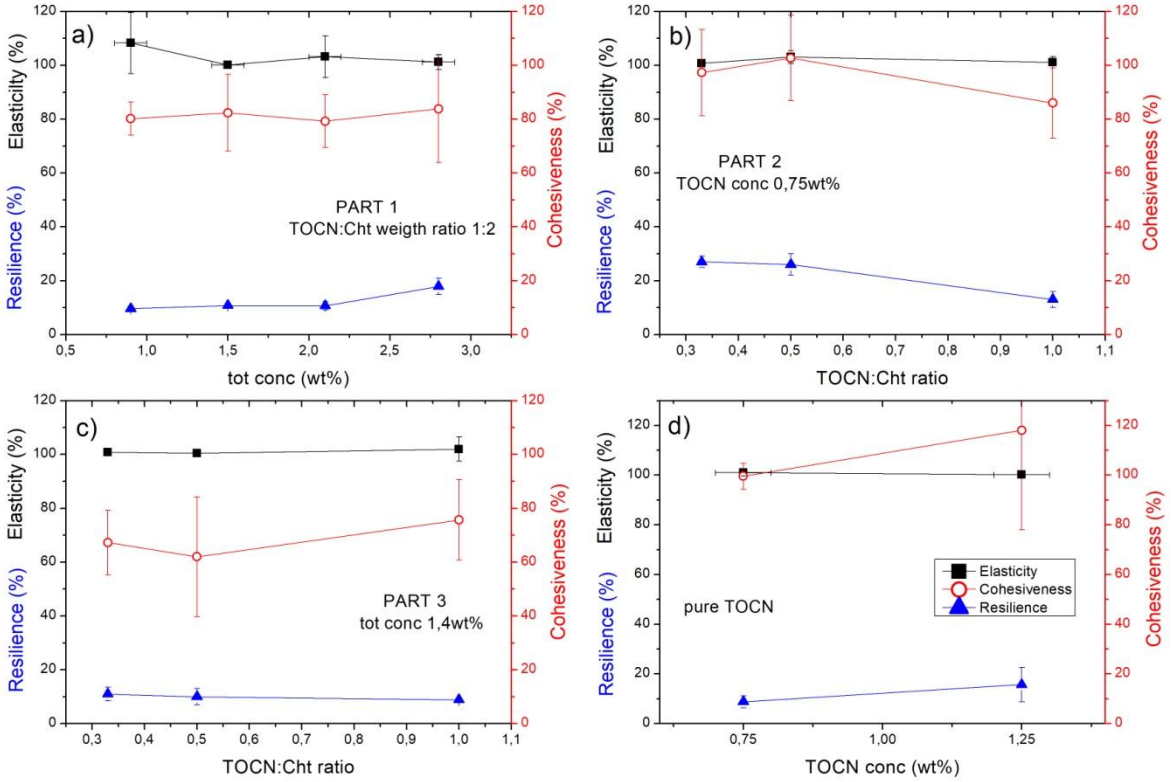

Fig. 10.6: Elasticity, Resilience and Cohesiveness percentage values, as defined in Chapter 9, Section 9.2.2, obtained through compression tests on TOCN/Cht hydrogels (figure a, b, c) and TOCN hydrogels (figure d) as a function of concentration or TOCN:Cht weight ratios. TOCN/Cht and TOCN hydrogels were stabilized with 0.5 M disodium succinate solution and 0.5 M calcium chloride solution respectively. The measurements were performed at least in triplicate and the reported values and error bars are the resulting mean values and SD.

From this figure it appears that all the plotted parameters are quite independent from both concentrations and TOCN:Cht weight ratios. In particular, the Resilience values are always lower than 30%, the Elasticity values always approach 100% and the Cohesiveness values appear to be between 60% and 100%. Cohesiveness measures the effect of repeated stresses on the structural properties of the sample and the degree of difficulty in breaking down the hydrogels structure (Lau et al., 2000; Sanderson, 1990). The high values obtained indicate a strong structuring of the hydrogel, which is able to stand subsequent compressions without being disrupted. Elasticity and Resilience are both related to the ability of a deformed material to return to its original position after the deforming force is removed (Mazzuca et al., 2014). In our situation, high Elasticity values and low Resilience values show the flexibility of the tested samples, which are capable of recover the initial structure completely and in a small period of time.

We conclude this Section reporting in Fig. 10.7b the Young Modulus obtained through compression tests on TOCN/Cht hydrogel samples at fixed 0.5 TOCN:Cht weight ratio and variable total concentrations. The reported values were estimated from the slope of the linear region of the stress-strain curves, as shown in Fig. 10.7a. The obtained trends are coherent with both the results of rheological measurements on Cht:TOCN solutions (Fig 10.3a) and the hardness values found for the hydrogels (Fig. 10.5a).

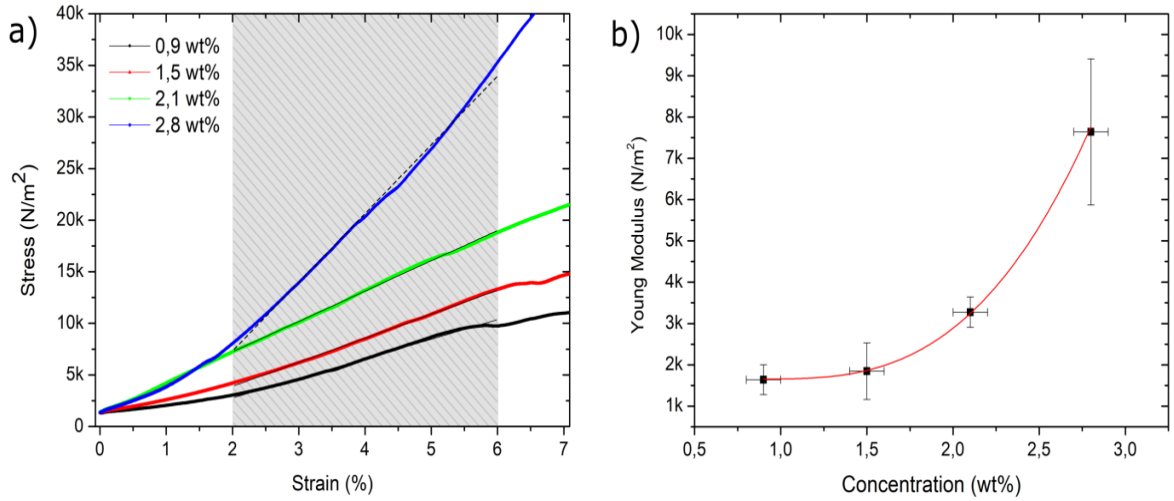

Fig 10.7: (a) Examples of axial stress-strain curves obtained through compression tests on TOCN/Cht hydrogel samples (TOCN:Cht weight ratio fixed to 0.5 and variable total concentrations, as reported in the legend) during the first compression cycle. The gray region highlights the linear deformation range from which the Young Modulus E of the samples was evaluated. (b) Young Modulus E as a function of the total concentration for TOCN/Cht (0.5 weight ratio) hydrogel samples. The values were obtained from the slopes of the linear fits performed on the stress-strain curves in the 2% - 6% deformation region. Measurements were performed at least in triplicate and the obtained mean value and SD were assumed as experimental value and uncertainty.

To sum up, the high values of hardness and Young modulus and the linear relationship between stress and strain, which holds till to stress values of the order of 10-50 kPa (depending on TOCN/Cht concentration), support the presence of a rather stable hydrogel network, able to withstand stresses higher than those in the digestive tract without collapse. At the same time, their highly elastic character renders them easy to be handled without risk of breakage or permanent deformation.

10.2 TOCN/Cht Hydrogels morphology and structure

The structure and homogeneity of TOCN/Cht hydrogels (concentration 2.3 wt% and TOCN:Cht weight ratio 0.5) were studied by microscopy techniques. TOCN/Cht hydrogels cylinders were prepared, as explained in Chapter 9 and schematically shown in Fig. 10.1, using, as moulds, Teflon tubes closed at the two extremities with a dialysis membrane (molecular weight cutoff 10000). The cylinders were stabilized by the diffusion of disodium succinate during the moulding process.

In the case of fluorescence microscopy images, around 2% of the TOCNs forming the hydrogel cylinders were previously fluorescent-labeled with FITC as explained in Chapter 9, Section 9.2.3. Fig. 10.8 shows some fluorescence microscopy images of hydrogel cylinders. In particular, panel (a) is a lateral image of the entire cylinders, while panel (b) and (c) show respectively a cross-section view and a lateral view and of a cylinder slice.

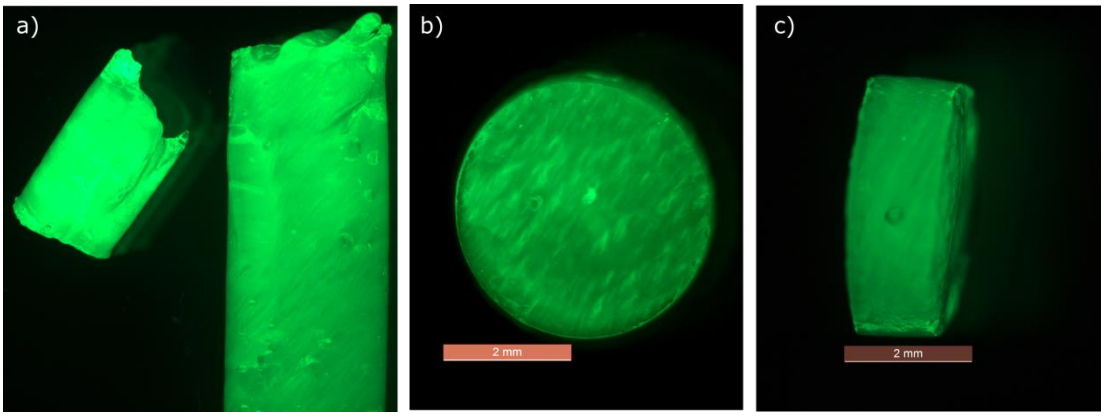

Fig. 10.8: Fluorescence microscopy images of TOCN/Cht hydrogel cylinders. The green colour is due to FITC-labeled TOCNs. (a) Lateral view of two cylinders, where the irregularity of two faces (top part of the image) is due to the contact with the wrinkled dialysis membrane. Cross section (b) and lateral view (c) of a cylinder slice.

The irregular aspect of the cylinders faces visible at the top of panel (a) is due to their contact with the wrinkled dialysis membrane during the stabilization in disodium succinate solution. To have a more regular cylindrical geometry and facilitate the subsequent measurements, the two faces were usually cut before degradation and release tests obtaining more flat faces (as the one visible in the left, bottom part of panel (a)). As qualitatively visible from the fluorescence intensity, the TOCNs are quite homogeneously distributed in all the hydrogel volume.

To investigate both the external and internal structure of TOCN/Cht hydrogels (concentration 2.1 wt% and TOCN:Cht weight ratio 0.5) through SEM microscopy, the cylindrical samples were fractured in liquid nitrogen, freeze dried and sputtered with an ultrathin layer of gold. In Fig. 10.9 and 10.10 are reported some representative imaged of the internal structure and external surface, respectively.

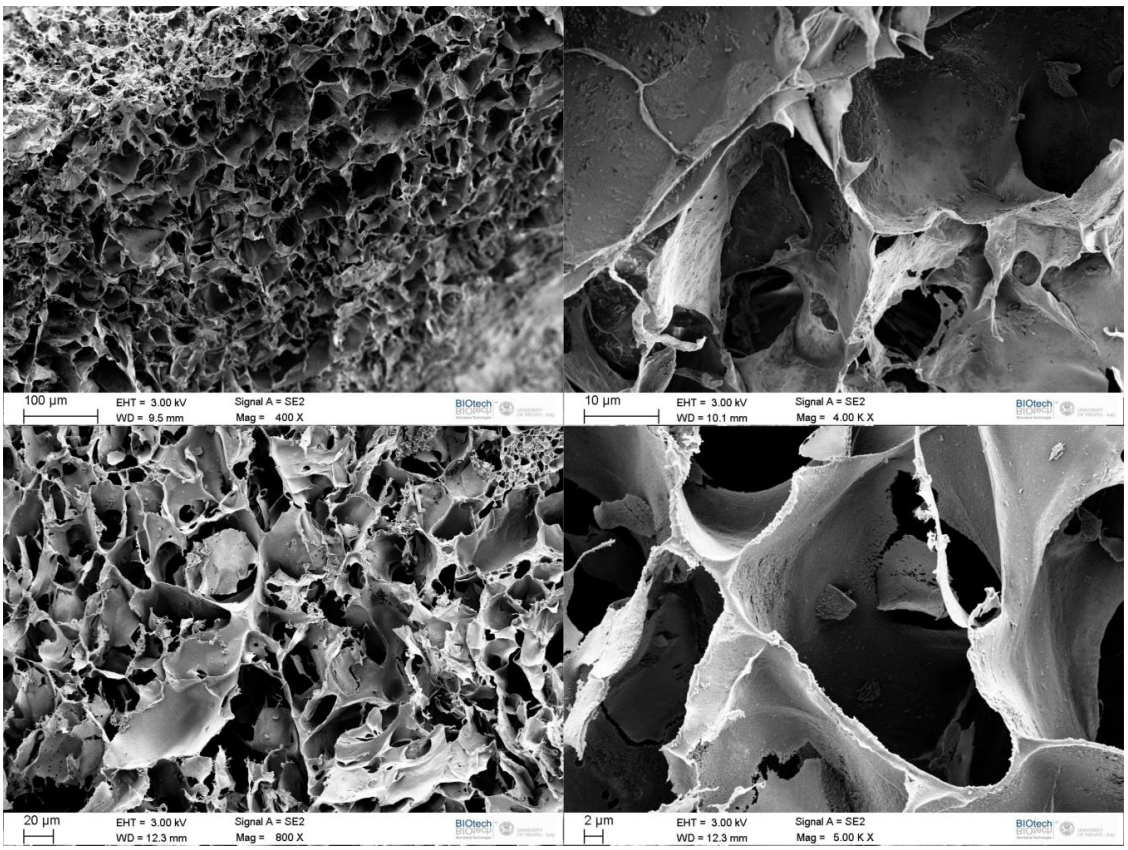

Fig. 10.9: SEM images of the internal porous structure of TOCN/Cht hydrogel cylinders (concentration 2.1 wt%, TOCN:Cht weight ratio 0.5). Cylindrical hydrogel samples were fractured in liquid nitrogen, freeze dried and sputtered with an ultrathin layer of gold before measurements.

As visible in Fig. 10.9 and Fig. 10.10, the arrangement of chitosan and cellulose nanocrystals on hydrogel surface is remarkably different from that assumed in the inside. Indeed, the matrix structure of the hydrogel shows a porous architecture with pore size around 10 - 50 µm. On the contrary, the hydrogel surface is characterized by a more compact organization, with appearance of a continuous film, covering the underlying porous structure.

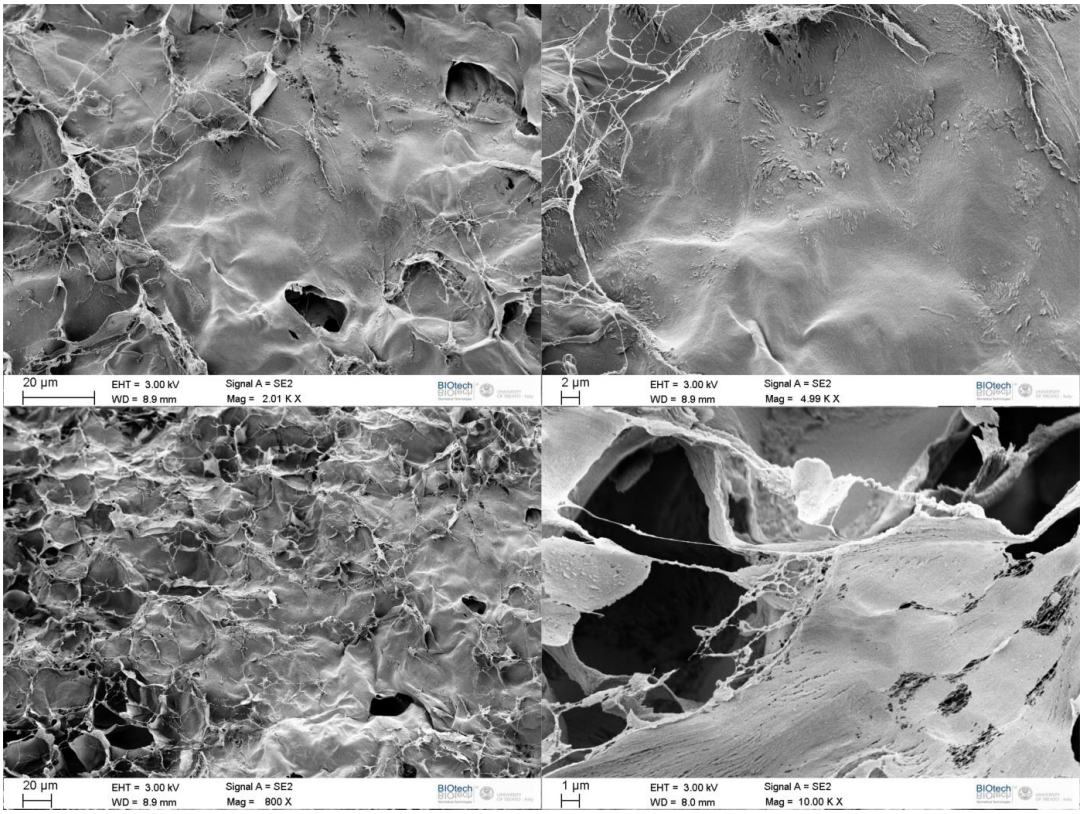

Fig. 10.10: SEM images of the film-like structure observed on the external hydrogel surface (in contact with the Teflon tube during the incubation in disodium succinate) of TOCN/Cht hydrogel cylinders (concentration 2.1 wt%, TOCN:Cht weight ratio 0.5). Cylindrical hydrogel samples were fractured in liquid nitrogen, freeze dried and sputtered with an ultrathin layer of gold before measurements.

10.3 Release kinetics and biodegradability

In this Section, we focus on the results obtained investigating the behavior of cylindrical TOCN/Cht hydrogels loaded with fluorescent-labeled BSA and incubated in PBS solution both in presence and absence of lysozyme. Measurements were performed to study both BSA release kinetics and TOCN/Cht scaffold degradation, in order to evaluate the potential use of TOCN/Cht hydrogels as gastro-intestinal drug delivery systems. Fixed TOCN/Cht concentration and weight ratio were considered (2.7 wt% total concentration and 0.5 TOCN:Cht weight ratio). Pure TOCN hydrogels (concentration around 2 wt%) were investigated for comparison.

10.3.1 Biodegradability of TOCN and composite TOCN/Cht hydrogel scaffolds

It is well known that chitosan can be enzymatically degraded in vivo by lysozyme, a polyanionic protein commonly present in various human body tissues and fluids (Lee et al., 1995; Onishi and Machida, 1999; Vårum et al., 1997).
Fig. 10.9 shows the degradation *in vitro*, of TOCN and TOCN/Cht hydrogel cylinders incubated in HEPES solution and PBS solution, respectively, at 37°C and in presence of 3 mg mL^{-1} lysozyme enzyme. The hydrogels degradation was evaluated measuring their weight loss at different incubation times and comparing the results with those obtained in absence of enzyme.

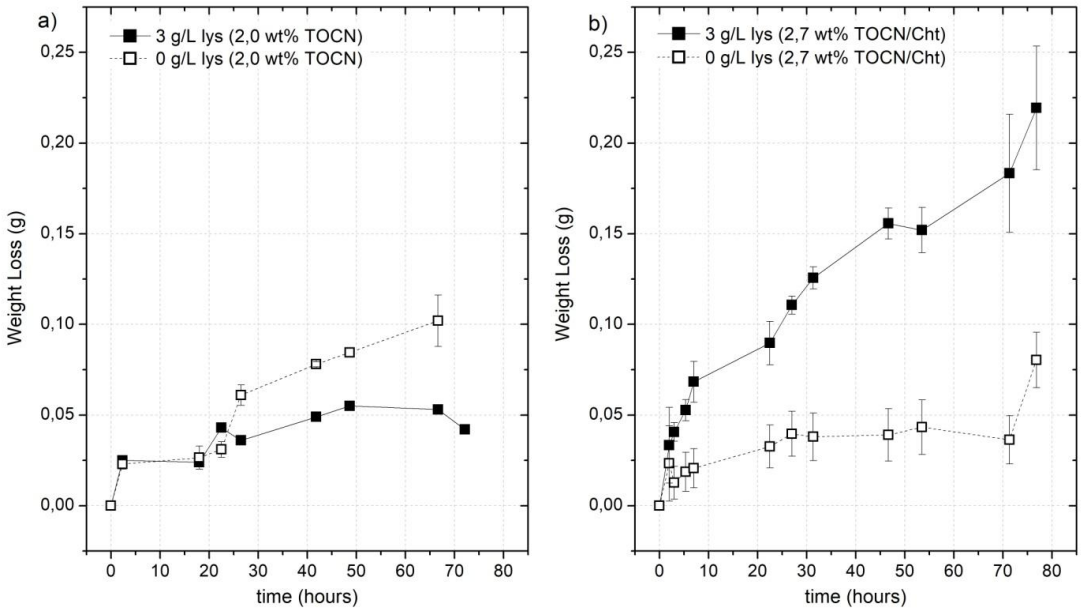

Fig. 10.11: Weight loss for TOCN hydrogel cylinders (a) and TOCN/Cht hydrogels (b) incubated in 20 mL HEPES solution and PBS solution both in presence and absence of lysozyme enzyme at 37°C. TOCN/Cht hydrogels were obtained from a 0.5 TOCN:Cht weight ratio solution (total concentration 2.7 wt%) using a 0.5 M disodium succinate solution as crosslinker. For TOCN hydrogel cylinders instead, a 2.0 wt% TOCN solution and a 0.5 M crosslinker $CaCl_2$ solution were used. The initial weight of the cylinders was around 0.4- 0.6 g. Error bars refer to the SD over 3 repeated measurements.

As expected, pure TOCN hydrogels are stable in solution both in absence and presence of lysozyme (Panel a). The small (0.05-0.1 g) weight loss detected is probably due to the partial and progressive spoiling of the samples consequent to their frequent handling during the long-lasting experiments. On the contrary, a significant weight reduction was noticed in the case of hybrid TOCN/Cht hydrogels incubated in presence of lysozyme (Panel b). Indeed, after 3 days incubation, the measured weight loss was approx. 0.22 g (corresponding to around 50% of the

initial weight), while the corresponding weight loss in absence of enzyme was approx. 0.075 g (corresponding to around 15% of the initial weight).
The timing of the degradation process was of the order of days, in accord with the results reported in literature for crosslinked chitosan hydrogels of similar dimensions, incubated in 1mg ml^{-1} PBS solutions (Hong et al., 2007; Jin et al., 2009). In particular, Jin *et al*. followed the degradation process for 21 days and reported a final weight loss between 20% and 60%, depending on hydrogel concentration (in the range 1-3 wt%), while Hong *et al*. observed a complete shape loss after 8 days for 1% chitosan hydrogels.

Changes in hydrogel shapes and dimensions were monitored in parallel to weight loss measurements. Fig. 10.12 shows some pictures of the TOCN/Cht samples before and after 3 days incubation in PBS solution, both with and without lysozyme. For completeness, the pictures of pure TOCN cylinders incubated in HEPES solution in presence of lysozyme are reported too. Coherently with weight loss measurements, only the TOCN/Cht cylinders incubated in presence of lysozyme undergo a significant degradation process, as shown by their progressive dimensions reduction and loss of shape. From these pictures it appears also that the degradation process of TOCN/Cht cylinders catalyzed by lysozyme is preferentially oriented along the cylinder axis.

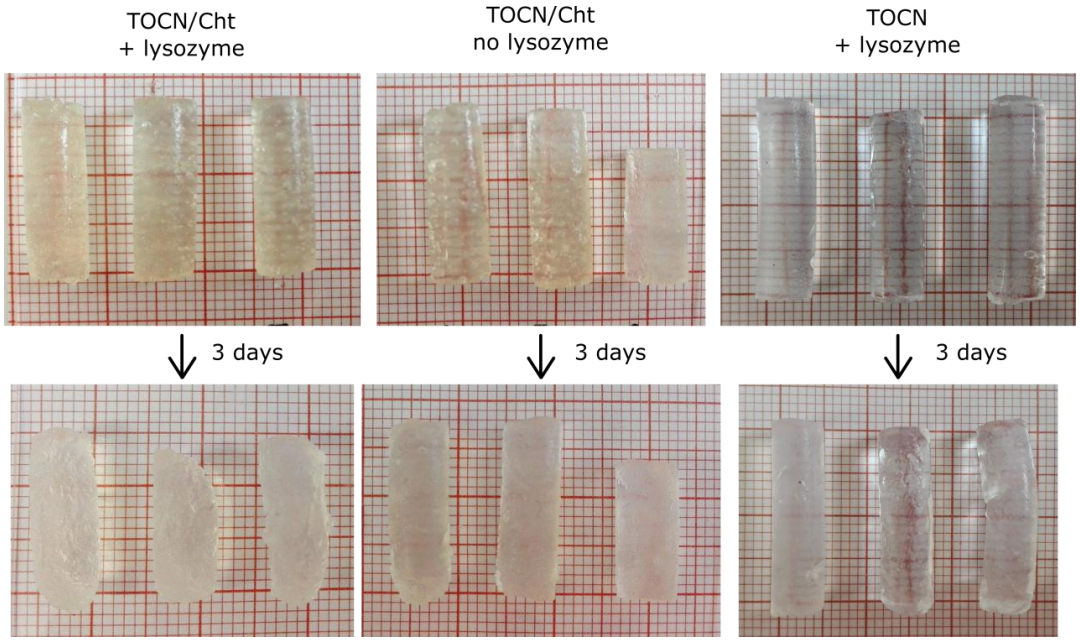

Fig. 10.12: Pictures of TOCN/Cht hydrogel cylinders (TOCN:Cht weight ratio 0.5, total concentration 2.7 wt%) before and after 3 days incubation in PBS solution both in presence and absence of lysozyme (3 g L^{-1}). In the last column, two pictures of pure TOCN hydrogels (concentration 2 wt%) before and after incubation in HEPES solution in presence of lysozyme (3 g L^{-1}) are reported.

To get more quantitative information, the height H and diameter D of the cylindrical samples were measured in time and their dimensions losses (expresses as difference ΔD and ΔR with respect to the starting diameter D and height H) calculated. These data are reported in Fig. 10.13 for the case of TOCN/Cht cylinders in presence and absence of lysozyme.

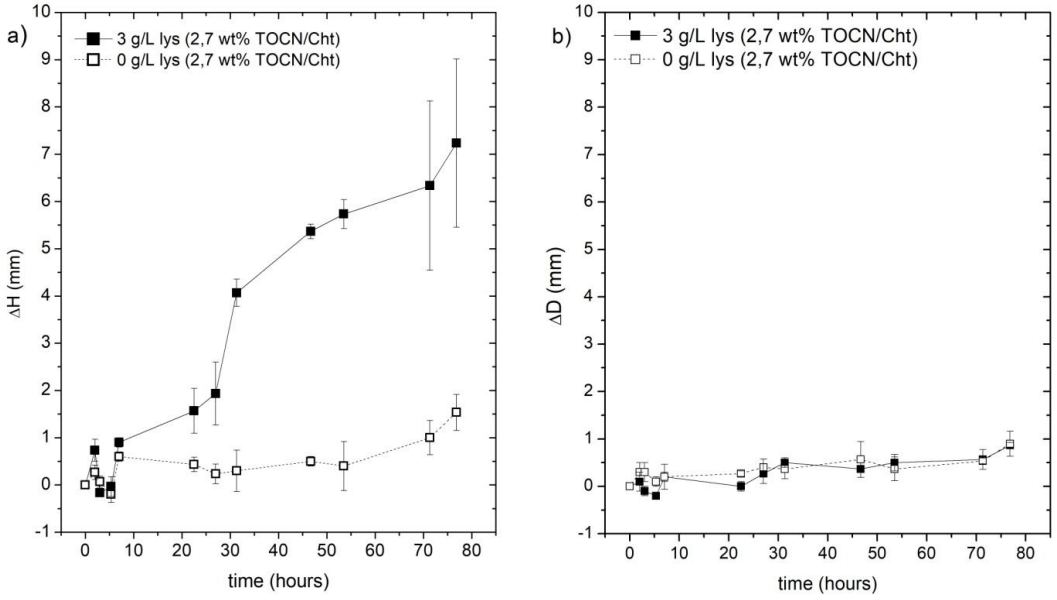

Fig. 10.13: Dimensions variations for TOCN/Cht hydrogels (TOCN:Cht ratio 0.5, total concentration 2.7 wt%) in PBS solution both in presence and absence of lysozyme. Left and right panel refer to the height reduction and diameter reduction of TOCN/Cht hydrogel cylinders, respectively. The initial height and diameter of the cylinders were around 15-20 mm and 6-7 mm, respectively. The reported points and error bars refer to the mean value and SD over 3 repeated measurements.

From both Fig. 10.12 and 10.13 it appears that, while the cylinders height progressively decreases, the diameter does not undergo significant variations. In principle, a spatially-oriented degradation process could be due to a preferential access of the catalyst to the catalysis sites from the two cylinder faces or to a reduced permeability of the composite at the lateral cylinder interface. In this regard, we must take into consideration that: a) the degradation process is enzyme-catalysed, where the water soluble and strongly basic lysozyme (pI 10.4) must diffuse inside the quasi-solid hydrogel matrix; b) the gelation process occurs inside a mould, which is a Teflon tube, open at the two extremities to allow the diffusion of the hydrogel stabilizer (that is succinate). A gradient of negatively charged succinate could be present along the cylinder axis and favour the access of the positive lysozyme from the two extremities. This hypothesis is supported by the results of the compression tests (Section 10.1.2), which showed that hydrogel mechanical properties and structure are strongly related to direction and easiness of diffusion of sodium succinate. The second important question is the difference between the

sol-gel transition at the interface with respect to the process occurring in the bulk. We can expect that the two polysaccharides, and in particular the rigid rod-like TOCN, gel at the interphase in a more ordered manner, following a self-orientation process driven by the presence of the Teflon mould. This hypothesis is proven by the SEM images, which show a compact film-like layer on the lateral cylinder surface, while the porous network is directly exposed at the cylinder bases. Film compactness and, probably, an increased presence of TOCN hinders lysozyme penetration and slow down the lateral corrosion of the cylinders.

10.3.2 Release profile of BSA from TOCN and composite hydrogels

Fig. 10.10 shows the cumulative releases from TOCN hydrogels (panel a) and TOCN/Cht hydrogels (panel b) loaded with FITC-BSA, both in presence (black squares) and absence (empty circles) of lysozyme.

Comparing panel (a) with panel (b), it appears that the release kinetics obtained with hybrid TOCN/Cht hydrogels are significantly different from those obtained for pure TOCN hydrogels. Indeed, the relatively fast release observed in the latter case is substituted by a slower, delayed release in the case of TOCN/Cht samples, since the time required to obtain a 50% release shifts from 9-10 hours to 30-50 hours.
Moreover, the release profile changes too. While the experimental curves obtained for TOCN hydrogels can be fitted according to Higuchi model (Siepmann and Peppas, 2011), suggesting a diffusion-controlled drug release, the release profile of TOCN/Cht hydrogels shows a sigmoidal, biphasic pattern, with an acceleration from time equal to approx. 20 hours.
According to different literature works, sigmoidal release profiles of small molecules from hydrogel materials can be described combining the diffusion of the drug through the hydrogel scaffold with other two phenomena: polymer degradation and a non uniform distribution of the drug within the hydrogel (Chen et al., 2017; Raman et al., 2005). In our specific situation it is reasonable that both the processes contribute. Indeed, the TOCN/Cht cumulative release is slightly higher in the case of hydrogel incubation in lysozyme, i.e. in the case of enzymatic degradation, however, a sigmoidal profile was obtained in the absence of lysozyme too.

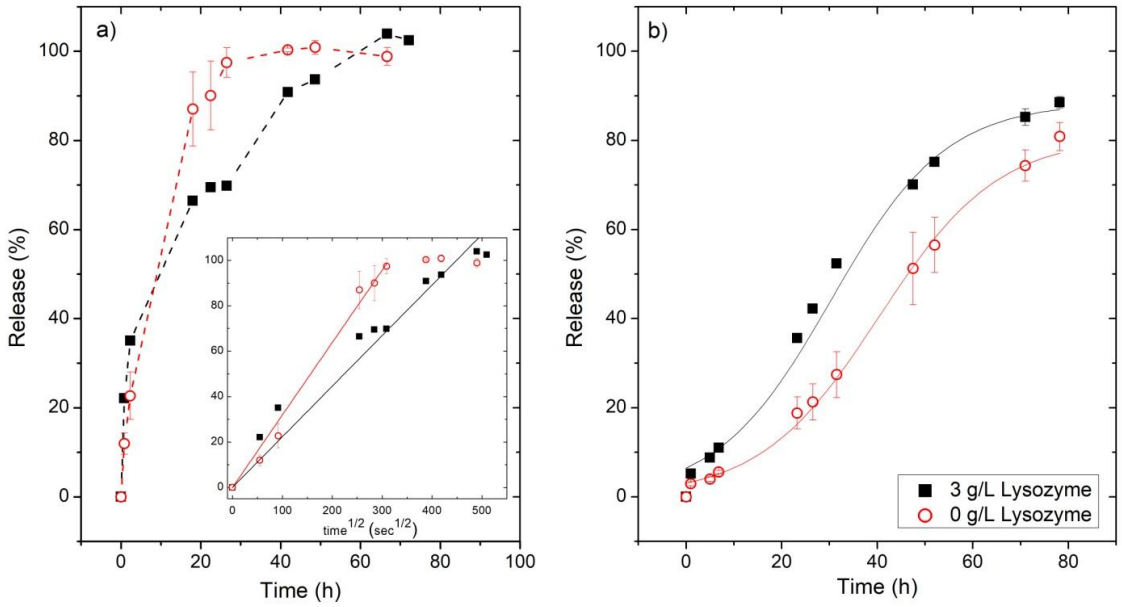

Fig. 10.14: Cumulative release of FITC-labeled BSA from: TOCN hydrogels (a) and TOCN/Cht hydrogels (b). TOCN hydrogel cylinders were obtained starting from a 2.0 wt% TOCN solution, using a 0.5 M $CaCl_2$ solution as crosslinker, while TOCN/Cht hydrogels were obtained from a 2.7 wt% TOCN/Cht solution, using 0.5 M disodium succinate solution as crosslinker. The time course of the fluorescence released in the buffer at 37°C was monitored in 20 mL HEPES solution or PBS solution for respectively TOCN hydrogels and TOCN/Cht hydrogels. Error bars refer to the SD over 3 repeated measurements. Dotted lines are guides for the eyes, while continuous lines are fits performed on the experimental data. In particular, as shown in the inset of panel (a), a linear relationship between cumulative release and square root of time was assumed valid for TOCN hydrogels at short times, according to the Higuchi model (Siepmann and Peppas, 2011). In the case of hybrid TOCN/Cht hydrogels, instead, data were fitted using a sigmoidal function $y = a/(1 + \exp(-k(x - x_c))$.

10.4 Mucoadhesion studies on Cht:TOCN hydrogels

As last Section of this Chapter, I report the results of some mucoadhesion measurements performed on TOCN/Cht hydrogels. Chitosan mucoadhesion properties have been widely studied and documented (Bonferoni et al., 2009; Ganguly and Dash, 2004). The cationic nature of chitosan, due to the presence of amino groups, protonated at low pH values, provides strong electrostatic interaction with negatively charged components of mucus, such as sialic acid and epithelial surfaces. Moreover, hydrogen bonding and hydrophobic interaction are supposed to positively affect chitosan mucoadhesion too (M. Ways et al., 2018; Sogias et al., 2008).

Fig. 10.15 shows the results of the mucoadhesion tests performed on our TOCN/Cht hydrogels using a Texture Analyzer and measuring the detachment force and total work of adhesion. Among the numerous methods to quantify the mucoadhesion properties of pharmaceutical dosage forms, the use of a Texture Analyzer is one of the most published techniques (Woertz et al., 2013).

It can be immediately observed from Fig. 10.15 that both adhesion force and adhesion work do not significantly change by varying the concentrations or TOCN:Cht weight ratios. Moreover, similar values are obtained for the case of pure TOCN hydrogels.

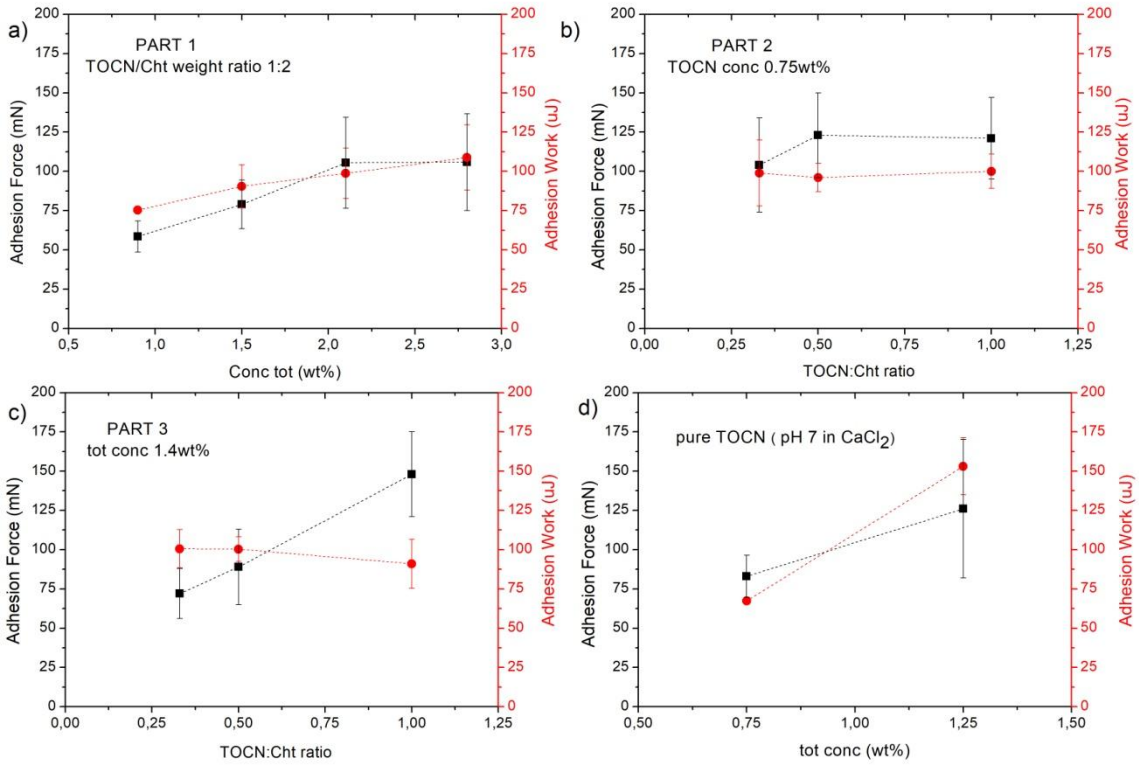

Fig 10.15: Mucoadhesion Force and Mucoadhesion Work for Cht:TOCN hydrogels as a function of: Cht:TOCN total concentration keeping fixed the Cht:TOCN ratio (a); Cht:TOCN weight ratio keeping fixed TOCN concentration (b); Cht:TOCN weight ratio keeping fixed the total concentration (c). Panel (d) shows the mucoadhesion Force and Work obtained for TOCN hydrogels at two different total concentration (the TOCN hydrogels were obtained at neutral pH using calcium chloride as a crosslinker). The reported values and error bars are mean values and SD over at least 6 measurements.

A quantitative comparison of the obtained values with results reported in literature for other chitosan-based devices is hardly feasible, because they strongly depend on the particular parameters and geometries used in the experiments (Woertz et al., 2013). Indeed, this method allows to get an idea of the high-low-no mucoadhesive

potential of a formulation, but rarely enables to compare absolute values due to major differences in the experimental set-ups. For example, Jones *et al.* demonstrated that mucoadhesion force increases increasing the contact time between tested gels and mucosa (Jones et al., 1997).
The obtained adhesion work (around 0.08-0.15 mJ) is similar to the 0.05 mJ value reported in literature for lyophilized or air dried solutions of chitosan (Grabovac et al., 2005) and not-crosslinked carboxymethylcellulose (Hägerström and Edsman, 2001). However, the measured adhesion force (around 0.05-0.15 N) is much lower than that reported for chitosan gels crosslinked by glutaraldehyde by Alsarra *et al*., 2009 (around 8 N).
The quite poor adhesion performances shown by our samples and the fact that they seem not to depend neither on total concentration nor on hydrogel composition, are partially related to the non optimal experimental conditions, which did not allow us to use higher contact times or pressing forces. Indeed, the wet nature of the hydrogels together with their compactness and lack of spreadability rendered the cohesion between the hydrogel and the instrument moving arm very poor, forcing us to perform measurements at low contact times and pressing forces. In this sense, in order to obtain more significant results, a different experimental protocol should be developed, which meets the specific mechanical and structural properties of the tested samples. After that, a possible evolution could be the chemical modification of chitosan with thiol groups, which are known to increase both gelling and mucoadhesion properties of chitosan (Bernkop-Schnürch et al., 2003; Esquivel et al., 2015).

10.5 Conclusions

In this section hybrid TOCN/Cht hydrogels were investigated, with the purpose of obtaining a hydrogel material, which can be digested by human enzymes and used as protein therapeutics delivery system in the gastrointestinal tract. Here I summarize the main results obtained, in terms of mechanical properties, structural characterization, degradation properties and BSA release kinetics:

1) A mechanical characterization of both TOCN/Cht solutions and cylindrical TOCN/Cht hydrogels stabilized by disodium succinate was performed by rheological measurements and compression tests respectively. In both cases, the mechanical properties of the samples appeared to increase with the total concentration. Moreover, the increase of G', G'' and viscosity values with the relative weight of TOCNs with respect to chitosan (at constant total concentration) demonstrated the reinforcing capability of TOCNs in hybrid materials. The hardness and Young modulus values obtained through compression tests suggested that TOCNs and chitosan are

arranged in TOCN/Cht hydrogel cylinders forming a rather stable network, able to withstand stresses as high as 10-50 kPa without collapse. Moreover, the obtained high elasticity and low resilience values show that samples are capable of recovering the initial structure completely and in a small period of time. These results suggest on one side that samples are able to withstand stresses higher than those in the digestive tract, on the other side that they can be easily handled without risk of breakage or permanent deformation.

2) SEM images revealed that TOCN/Cht hydrogel cylinders are characterized by an inner porous architecture with pore size around 10-50 μm. However a more compact, film-like structure was observed on the lateral surface of the hydrogel cylinders. The presence of such an external shell was ascribed to the contact of chitosan and especially TOCNs with the hydrophobic Teflon tube used as a mould, which induced the formation of a thin interfacial film.

3) Weight reduction and dimensions reduction were detected in TOCN/Cht hydrogels incubated in presence of Lysozyme, showing that the material is slowly degraded by the tested digestive enzyme (50% of the weight lost in three days). On the contrary, pure TOCN hydrogels are stable in solution both in absence and presence of lysozyme. Curiously, the degradation process of TOCN/Cht cylinders is preferentially oriented along the cylinder axis. This fact could be due to a favored access of the positive lysozyme from the two extremities of the cylinders as consequence of the presence of a negatively charged succinate gradient along the cylinder axis or to a different structure of the hydrogel at the lateral interface with respect to that in the bulk, which hinders lysozyme penetration and slow down the lateral corrosion of the cylinder. The first hypothesis is supported by the results of the compression tests, which showed that hydrogel mechanical properties are strongly related to direction and easiness of diffusion of sodium succinate, getting worse moving away from hydrogel surface. The second hypothesis is instead proven by SEM images, which showed the presence of a compact film-like layer on the lateral cylinder surface.

4) Release kinetics studies showed that the fast, diffusion-controlled release profile obtained for pure TOCN hydrogels is substituted by a slower release with sigmoidal profile in the case of TOCN/Cht samples. The observed biphasic pattern was noticed for TOCN/Cht incubated both in presence and absence of enzyme and could be due to the combination of drug diffusion with polymer degradation and a non uniform initial distribution of the drug within the hydrogel.

In conclusion, it was demonstrated that the combination of TOCNs with low molecular weight chitosan enables to obtain hybrid hydrogels with the desired mechanical properties for being used as protein delivery system in the gastrointestinal tract. However, further studies are required to better investigate and eventually enhance the material mucoadhesion properties. Another interesting aspect to be further investigated is the observed presence of a preferential degradation direction, related to a different structural organization of TOCNs and Cht in different areas of the hydrogels, which could allow to design delivery systems with spatially controlled degradation and release properties.

Chapter 11
Final Remarks

11.1: Conclusions

The aim of this thesis was the isolation of cellulose nanocrystals and the investigation of their assembly processes through weak interactions to produce hydrogel and film structures. TEMPO-oxidized cellulose nanocrystals (TOCNs) with a rod-like shape and dimensions around 3-5 nm in diameter and some hundred nanometers in lengths were obtained, starting from cellulose pulp, by a two step process consisting in an oxidation reaction followed by a sonication treatment.

The self-assembly of TOCNs in dry conditions resulted in the formation of transparent, flexible films. Both optical measurements and microscopy images showed the dense nature of the films, characterized by a layered, highly packed arrangement of TOCNs. The low porosity was confirmed by PALS analysis, which estimated the cross-section of pores equal to approx 0.31 nm, and is at the origin of TOCN-films excellent gas barrier properties. Indeed, a selective transport of gas molecules according to a size-sieving effect was observed, which is in agreement with the estimated porosity of the films.

Turning to consider TOCNs assembly in aqueous solutions, it was observed that, despite their non-polymeric and rigid nature, TOCNs are able to form supramolecular hydrogel structures with good mechanical properties. In particular, weak hydrogels are obtained by non exhaustive sonication of TOCN solutions, while a clearer gel-like behavior is observed if sonication is followed by salt addition thanks to the strong electrostatic interactions generated by hydrogen bonds and between cations and carboxyl groups. The influence of sonication and cations addition (in particular, Na^{+}, Ca^{2+} and Al^{3+} were considered here) on the sol-gel process and on TOCNs assembly and interaction with water were studied in details. It was demonstrated through rheology and NMR that cation valence and concentration affect hydrogels mechanical properties and three dimensional architecture. Moreover, their stability and elasticity resulted to strongly depend on the duration of the sonication treatment. These results showed that hydrogels with tunable structures and mechanical properties can be obtained by changing both cation valence and sonication pre-treatment.
In order to better understand and control the mechanism and kinetics of TOCN hydrogels formation, a ionotropic gelation strategy was exploited and Ca^{2+} was used

as gelling agent. By external ionotropic gelation of TOCNs delivered in a Ca^{2+} bath, filled hydrogel structures of various size and shape (beads, wires and membranes) were obtained, while inverse ionotropic gelation resulted in the formation of core-shell capsules. For both external and inverse ionotropic gelation, the process was driven by Ca^{2+} diffusion and by its interaction with TOCNs carboxylic groups. The diffusion process was studied using a Ca^{2+} sensitive indicator and it was demonstrated that in the case of external gelation free diffusion conditions for Ca^{2+} inside the incipient hydrogel network hold. Considering instead the interaction properties, FTIR spectroscopy showed that a fraction of Ca^{2+} ions is tightly coordinated to carboxylates, while a second fraction undergoes to un-specific binding and could be released without compromising hydrogel structure and stability in water. It was demonstrated that the control of the TOCNs ionotropic gelation processes, driven by the dynamics of Ca^{2+} diffusion, offers the opportunity of fabricate hydrogel microstructures with tunable size and shape simply controlling the diffusion time.

In view of a possible use of TOCN hydrogels as skin patches, *in vitro* toxicity studies in cultures of malignant melanoma cells A375 were performed. Taking into account the ISO 10993-5:2009 suggestions for the biological evaluation of medical devices, experiments were done both on TOCN hydrogel membranes (obtained adding NaCl, $CaCl_2$ and $MgCl_2$ salts) and on their precursors (TOCN solutions and salt solutions). For this purpose, a set-up based on the use of an insert with a microporous and permeable PET membrane was used, which allows the free exchange of the molecules between cell monolayer and suspended hydrogel but avoids any shear effect. MTT assays and cell morphology observation demonstrated that TOCN hydrogels fabricated with Na^{+} or Mg^{2+} cation-mediated gelation lack of cytotoxicity. In addition, Mg^{2+}-hydrogels are also stable after long-term storage in aqueous solution. Moreover, confocal microscopy images showed up-take of TOCNs inside the vesicles both in the area of the cell membrane and in the cytoplasm. The cells capability of crystallites internalization supports the non-toxicity of TOCNs and suggests possible interesting uses of TOCNs as nanomaterial in biomedical applications.

Finally, hybrid TOCN/Cht hydrogels were produced and their structure, degradation and release properties were investigated in view of their possible use as enzymatically degradable material in the biomedical field. It was demonstrated that the combination of TOCNs with low molecular weight chitosan enables to obtain hybrid hydrogels with the desired properties for being used as drug delivery systems in the gastrointestinal tract. In particular, rheological measurements showed that TOCNs act as reinforcing agent contributing to the mechanical properties of the samples, while the presence of Cht renders the material degradable by digestive enzymes. Moreover, it was observed that the degradation

takes place along a preferential direction, probably related to TOCNs and chitosan assembly. Indeed, as observed through SEM images, the internal porous structure of the hydrogel cylinders is externally covered by a film-like layer, which hinders lysozyme penetration from the lateral surface.

11.2: Future Perspectives

Considering TOCNs in dry conditions, an interesting future perspective could be the development of hybrid nanocomposite films with tuned properties, by addition of different kinds of nanoadditives like TiO_2 nanoparticles to TOCN solutions. This could lead to obtain innovative materials for gas separation/purification or advanced packaging applications.

Another future development of this thesis work concerns the study of TOCNs interaction with cells, in view of the possible exploitation of TOCNs in the biomedical field not only as hydrogels but also as individual crystallites. In this sense, further experiments, both *in-vitro* and *in-vivo,* are required to better investigate the interaction between crystallites and cells. Moreover, the toxicity of TOCNs and TOCN hydrogels could be evaluated on different, non malignant, cell lines too (measurements already in progress).

Finally, regarding hybrid TOCN/chitosan hydrogels, it would be interesting to further investigate the observed phenomenon of directional degradation, as it could lead to the design of delivery systems with spatially controlled degradation and release properties. Furthermore, the mucoadhesive behavior of TOCN/chitosan hydrogels could be studied more into details through ad-hoc experiments and eventually optimized.

Acknowledgments

I realize now that these years of PhD have passed in a flash, so full of experiences, challenges and encounters to forget sometimes the pass of time. During these three years, I could get in contact with a lot of people with different scientific backgrounds and knowledges and had the chance to ''steal'' something to each of them: competences, experiences but also stories and emotions. I think that this opportunity has enriched me both as a scientist and as a person and I am truly grateful to each of them for this.

Some persons, in particular, have to be mentioned, as this thesis work would not exist without them.

First of all, I want to sincerely thanks my tutor, Prof. Marina Scarpa, for her tireless and constant support both from a scientific and human point of view. Her expert supervision, endless curiosity and comprehension have been a fundamental reference point in these years. I need to thanks also Prof. Paolo Bettotti for having always been available with preciuos suggestions and for his enthusiasm for research.
I am grateful also to the numberous collaborators, which accompanied my research for a more or less long period. In particular, a sincere thanks to Prof. Romano Lapasin, Prof. Mario Grassi and Dr. Michela Abrami from Trieste for their interest in our work and for being always available for discussion and confrontation. I have to express my gratitude also to Dr. Stefania Meschini and Evelin Pellegrini from Rome, for sharing their competences in the cellular field and for their warm hospitality. My sincere gratitude also to my collaborators from the Department of Physics in Trento, Prof. Riccardo Checchetto and Dr. David Roilo in particular, who showed curiosity in nanocellulose and shared their research experience in a very professional manner.
Finally special thanks to Prof. Andreas Bernkop-Schnürch from Innsbruck, who hosted me in his laboratories during my training period abroad, and to his research group, for assisting me and providing me with instrumentation and help every time I needed.

E infine grazie alla mia famiglia, che mi ha sempre appoggiata e sostenuta anche nei momenti più impegnativi, ed alle persone che mi hanno accompagnata e mi sono state vicine in questi anni.

APPENDIX to Chapter 7
Reaction-diffusion models

Analytical model for the reaction front as a function of time

Reaction-diffusion systems showing a reaction front which evolves in time are characteristic of many physical, chemical and biological processes (Cencini et al., 2003; Kondo and Miura, 2010). In 1988 Racz and Galfi (Gálfi and Rácz, 1988) proposed an analytical model (known as ''mean field model'') for the reaction front in the case of a chemical reaction $A_{(diffusing)} + B_{(diffusing)} \rightarrow C_{(inhert)}$, where the reagents A and B (initially separated in space) react to produce the inert species C and the reaction kinetics is of second order. Aim of the model is to obtain a scaling description for the center and width of the reaction front and for the production rate of C starting from a couple of reaction-diffusion equations.

Later on, Leger *et al.* (Léger et al., 1999) experimentally studied the case $A_{(diffusing)} + B_{(static)} \rightarrow C_{(inhert)}$ and demonstrated that the results obtained by Racz and Galfi for the movement of the reaction front as a function of time is independent of the reaction orders or the number of diffusing reactants (one or two) as long as the two species are initially separated and there is no relative advection of them.

In particular, the model can be used to describe the ionotropic gelation process of TOCNs in presence of Ca^{2+} ions, where $A_{(diffusing)}$ = Ca^{2+} ions, $B_{(static)}$ = TOCN and $C_{(inhert)}$ = TOCN-Ca^{2+} hydrogel.

Here we recall how, from the model, the characteristic distance versus time$^{1/2}$ relationship observed experimentally can be analytically obtained and how the apparent diffusion coefficient is introduced. The mathematical description of the considered reaction-diffusion process is given by the following set of reaction-diffusion equations:

$$\frac{\partial a}{\partial t} = D_a \frac{\partial^2 a}{\partial x^2} - kab \qquad \text{(Eq. A1)}$$

$$\frac{\partial b}{\partial t} = D_b \frac{\partial^2 b}{\partial x^2} - kab \qquad \text{(Eq. A2)}$$

where a, b are the concentrations of the reactants A and B, D_a and D_b the diffusion constants and k the reaction rate constant. The model is developed in 1D, where x is the spatial coordinate, and considering, as an initial condition, A, B separated and with constant densities: $a = a_0$ and $b = 0$, for $x < 0$ and $a = 0$ and $b = b_0$ for $x > 0$. For simplicity we consider $D_a = D_b = D$ (same conclusions can be obtained in the case $D_a \neq D_b$). We introduce the units $l = \sqrt{D/(ka_0)}$, $\tau = 1/(ka_0)$ and a_0 to measure lengths, time and concentration, so that the only control parameter remains $q = b_0/a_0$. Subtracting Eq. (A2) from Eq. (A1), we obtain a diffusion equation for $u = a - b$:

$$\frac{\partial u}{\partial t} = D\frac{\partial^2 u}{\partial x^2} \qquad \text{(Eq. A3)}$$

that can be solved with the initial conditions $u = 1$ ($x < 0$) and $u = -q$ ($x > 0$) obtaining:

$$u(x,t) = \frac{1-q}{2} + \frac{1+q}{2}\,\mathrm{erf}\left(\frac{x}{2\sqrt{t}}\right) \qquad \text{(Eq. A4)}$$

Where $\mathrm{erf}(x) = \frac{1}{\sqrt{\pi}}\int_{-x}^{x} e^{-t^2} dt$ is the Error Function. We introduce now a reference point x_f, assumed as the center of the reaction zone, where a = b and the production rate of C is expected to be the largest. This point can be determined from Eq. (A4) by requiring $a(x_f, t) = b(x_f, t)$, that is $u(x_f, t) = 0$. The time dependence of x_f is:

$$x_f = \sqrt{2D_f t} \qquad \text{(Eq. A5)}$$

where D_f is the ''diffusion constant'' of the front (or apparent diffusion coefficient) given by the equation:

$$\mathrm{erf}\left(\sqrt{D_f/2}\right) = (1-q)/(1+q) \qquad \text{(Eq. A6)}$$

Steady state model for gel growth kinetics

In order to explain the experimentally observed kinetics and obtain the real diffusion coefficient of Ca^{2+} ions through the TOCN hydrogel, a model is required that relates front propagation kinetics and Ca^{2+} diffusion. Different models exist in literaure depending on the particular experimental conditions and geometry (Bjørnøy et al., 2016; Braschler et al., 2011; Nobe et al., 2005; Potter et al., 1994). Here we report a model based on the theory developed by Braschler *et al.*, (Braschler et al., 2011) who studied the Ca^{2+}-induced gelation of alginate systems

both analytically and experimentally by following the sol-gel front propagation using fluorescence intensity signals. The presented reaction-diffusion model is essentially based on two mechanisms: the chemical reaction between TOCNs and Ca^{2+} ions and the diffusion of the reactants (in particular the flux J_C of Ca^{2+} ions, as we assume the diffusion of TOCNs negligible). In Fig. A1 a schematic view of the 1D reaction-diffusion system with the main quantities considered in the model is shown.

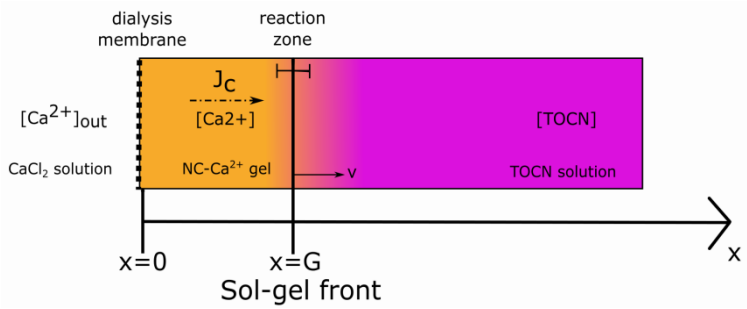

Fig. A1: Schematic view of the reaction-diffusion system involved in the proposed model.

To reach the reaction front and promote the gelation of TOCN solution by chemically reacting with it, Ca^{2+} ions have to diffuse through the already formed gel. The concentration of free TOCNs in the gel can be assumed to be very low, so that negligible reaction takes place in it. The transport of free Ca^{2+} ions through the gel is studied as a linear diffusion process. The advancement of the reaction front is determined by the flux of Ca^{2+} ions J_c and the stoichiometry of the TOCN-Ca^{2+} reaction.

In the hypothesis that the Ca^{2+} ions flux converts a known amount of TOCNs and that the flux of nanocellulose $J_{NC} = v\,[TOCN]$ consumed by the reaction is equal to the flux of Ca^{2+} ions J_C reaching the reaction zone, we have:

$$J_c = R\,J_{TOCN} = R\,v\,[TOCN] \qquad \text{(Eq. A7)}$$

where R is a factor taking into account the TOCN-Ca^{2+} reaction stoichiometry, v is the advancing speed of the reaction front and $[TOCN]$ the bulk nanocellulose concentration. As there is little free TOCN in the hydrogel region, the reaction rate is very low and the transport of Ca^{2+} ions through the gel is regulated by the linear diffusion equation:

$$D_c \frac{\partial^2[Ca^{2+}]}{\partial x^2} - \frac{\partial[Ca^{2+}]}{\partial t} \approx 0 \qquad \text{(Eq. A8)}$$

where D_c is the Ca^{2+} diffusion coefficient in the gel, $[Ca^{2+}]$ the calcium concentration and x the spatial coordinate of the gel growth in1D (as illustrated in Fig. A1). To solve Eq. (A8), two boundary conditions are required. The first one is obtained from the fact that the concentration of free Ca^{2+} ions is low in the reaction zone (x = G), that is:

$$[Ca^{2+}]_{x=G} \approx 0 \qquad \text{(Eq. A9)}$$

The problem of a mobile boundary, which advances with a speed given by the diffusive transport of a reactant whose concentration is zero at the reaction front is known as Stefan problem (Hilhorst et al., 1996). The second boundary condition arises from Fick's law of diffusion at the dialysis membrane (x = 0) and results to be:

$$\left(\frac{\partial[Ca^{2+}]}{\partial x}\right)_{x=0} = \frac{[Ca^{2+}]_{(x=0)} - [Ca^{2+}]_{out}}{L} \qquad \text{(Eq. A10)}$$

where L is the thickness of the dyalisis membrane and $[Ca^{2+}]_{out}$ the bulk concentration of Ca^{2+} ions outside the dyalisis membrane (x < 0). An approximated analytical solution of Eq. A8 with boundary conditions given by Eq. (A9) and Eq. (A10) can be obtained in the hypothesis that $\frac{\partial[Ca^{2+}]}{\partial t} = 0$ (steady-state concentration gradient for the Ca^{2+} ions). This assumption is known as Kim's model and is typically used in alginate gel growth studies (Kim, 1990). In this approximation, the concentration of free Ca^{2+} ions in the gel is:

$$[Ca^{2+}] = [Ca^{2+}]_{out}\frac{x}{G+L} \qquad \text{(Eq. A11)}$$

meaning a constant flux J_c through the gel:

$$J_c = D_c\frac{[Ca^{2+}]_{out}}{G+L} \qquad \text{(Eq. A12)}$$

Combining Eq. (A7) with Eq. (A12) and considering that $v = \frac{\partial G}{\partial t}$ we obtain:

$$\frac{\partial G}{\partial t} = \frac{D_c\theta}{G+L} \qquad \text{(Eq. A13)}$$

where we have introduced $\theta = \frac{[Ca^{2+}]_{out}}{R\,[TOCN]}$ as a shorthand notation for the ratio between the bulk Ca^{2+} concentration $[Ca^{2+}]_{out}$ and the nanocellulose crystallites concentration $[TOCN]$ multiplied by the factor R, which accounts for both the carboxylic content of TEMPO-oxidized TOCNs and the stoichiometry of the TOCN-Ca^{2+} reaction. The solution of Eq. (A13) gives an expression for the temporal progression of the reaction front in the x-direction:

$$G(t) = \sqrt{2D_c\theta\,t + L^2} - L \approx \sqrt{2D_c\theta\,t} \qquad \text{(Eq. A14)}$$

Eq. (A14) confirms the characteristic dependence of front propagation G(t) on $t^{1/2}$. Moreover it allows to estimate Ca^{2+} ions diffusion coefficient in the gel starting from the slope of the curve $K = \frac{G(t)}{\sqrt{t}}$ or from the apparent diffusion coefficient $D_f = \frac{G(t)^2}{2t}$.

Bibliography

Abdul Khalil, H.P.S., Davoudpour, Y., Saurabh, C.K., Hossain, M.S., Adnan, A.S., Dungani, R., Paridah, M.T., Islam Sarker, M.Z., Fazita, M.. N., Syakir, M.., Haafiz, M.K.M., 2016. A review on nanocellulosic fibres as new material for sustainable packaging: Process and applications. *Renew. Sustain. Energy Rev.* **64**, 823–836.

Abitbol, T., Rivkin, A., Cao, Y., Nevo, Y., Abraham, E., Ben-Shalom, T., Lapidot, S., Shoseyov, O., 2016. Nanocellulose, a tiny fiber with huge applications. *Curr. Opin. Biotechnol.* **39**, 76–88.

Aitomäki, Y., Oksman, K., 2014. Reinforcing efficiency of nanocellulose in polymers. *React. Funct. Polym.* **85**, 151–156.

Alentiev, A.Y., Shantarovich, V.P., Merkel, T.C., Bondar, V.I., Freeman, B.D., Yampolskii, Y.P., 2002. Gas and Vapor Sorption, Permeation, and Diffusion in Glassy Amorphous Teflon AF1600. *Macromolecules* **35**, 9513–9522.

Almeida, A.P.C., Canejo, J.P., Fernandes, S.N., Echeverria, C., Almeida, P.L., Godinho, M.H., 2018. Cellulose-Based Biomimetics and Their Applications. *Adv. Mater.* **30**, 1703655.

Alsarra, I. A., Hamed, A., Mahrous, G. M., El Maghraby, G., Al-Robayan, A. A., Alanazi, F. K., 2009. Mucoadhesive Polymeric ydrogels for Nasal Delivery of Acyclovir. *Drug Dev. Ind. Pharm*. **35**:352-362.

Anjum, S., Arora, A., Alam, M.S., Gupta, B., 2016. Development of antimicrobial and scar preventive chitosan hydrogel wound dressings. *Int. J. Pharm.* **508**, 92–101.

Atta-ur-Rahman T. I., 1986. Nuclear magnetic resonance: basic principles. Springer-Verlag, New York

Aulin, C., Gällstedt, M., Lindström, T., 2010. Oxygen and oil barrier properties of microfibrillated cellulose films and coatings. *Cellulose* **17**, 559–574.

Aulin, C., Karabulut, E., Tran, A., Wågberg, L., Lindström, T., 2013a. Transparent Nanocellulosic Multilayer Thin Films on Polylactic Acid with Tunable Gas Barrier Properties. *ACS Appl. Mater. Interfaces* **5**, 7352–7359.

Aulin, C., Karabulut, E., Tran, A., Wågberg, L., Lindström, T., 2013b. Correction to Transparent Nanocellulosic Multilayer Thin Films on Polylactic Acid with Tunable Gas Barrier Properties. *ACS Appl. Mater. Interfaces* **5**, 10395–10396.

Banerjee, A., Lee, J., Mitragotri, S., 2016. Intestinal mucoadhesive devices for oral delivery of insulin. *Bioeng. Transl. Med.* **1**, 338–346.

Basu, A., Lindh, J., Ålander, E., Strømme, M., Ferraz, N., 2017. On the use of ion-crosslinked nanocellulose hydrogels for wound healing solutions: Physicochemical properties and application-oriented biocompatibility studies. *Carbohydr. Polym.* **174**, 299–308.

Bayer, T., Cunning, B.V., Selyanchyn, R., Nishihara, M., Fujikawa, S., Sasaki, K., Lyth, S.M., 2016. High Temperature Proton Conduction in Nanocellulose Membranes: Paper Fuel Cells. *Chem. Mater.* **28**, 4805–4814.

Bechtold, T., Manian, A.P., Öztürk, H.B., Paul, U., Široká, B., Široký, J., Soliman, H., Vo, L.T.T., Vu-Manh, H., 2013. Ion-interactions as driving force in polysaccharide assembly. *Carbohydr. Polym.* **93**, 316–323.

Belbekhouche, S., Bras, J., Siqueira, G., Chappey, C., Lebrun, L., Khelifi, B., Marais, S., Dufresne, A., 2011. Water sorption behavior and gas barrier properties of cellulose whiskers and microfibrils films. *Carbohydr. Polym.* **83**, 1740–1748.

Bernkop-Schnürch, A., Hornof, M., Zoidl, T., 2003. Thiolated polymers--thiomers: synthesis and in vitro evaluation of chitosan-2-iminothiolane conjugates. *Int. J. Pharm*. **260**, 229–237.

Bettotti, P., Maestri, C.A., Guider, R., Mancini, I., Nativ-Roth, E., Golan, Y., Scarpa, M., 2016. Dynamics of Hydration of Nanocellulose Films. *Adv. Mater. Interfaces* **3**, 1500415.

Bjørnøy, S.H., Mandaric, S., Bassett, D.C., Åslund, A.K.O., Ucar, S., Andreassen, J.-P., Strand, B.L., Sikorski, P., 2016. Gelling kinetics and in situ mineralization of alginate hydrogels: A correlative spatiotemporal characterization toolbox. *Acta Biomater.* **44**, 243–253.

Boddupalli, B.M., Mohammed, Z.N.K., Nath, R.A., Banji, D., 2010. Mucoadhesive drug delivery system: An overview. *J. Adv. Pharm. Technol. Res.* **1**, 381–387.

Bonferoni, M.C., Sandri, G., Rossi, S., Ferrari, F., Caramella, C., 2009. Chitosan and its salts for mucosal and transmucosal delivery. *Expert Opin. Drug Deliv.* **6**, 923–939.

Bonilla, M.R., Lopez-Sanchez, P., Gidley, M.J., Stokes, J.R., 2016. Micromechanical model of biphasic biomaterials with internal adhesion: Application to nanocellulose hydrogel composites. *Acta Biomater.* **29**, 149–160.

Borysiak, S., Grząbka-Zasadzińska, A., 2016. Influence of the polymorphism of cellulose on the formation of nanocrystals and their application in chitosan/nanocellulose composites. *J. Appl. Polym. Sci.* **133**, 42864.

Braschler, T., Valero, A., Colella, L., Pataky, K., Brugger, J., Renaud, P., 2011. Link between Alginate Reaction Front Propagation and General Reaction Diffusion Theory. *Anal. Chem.* **83**, 2234–2242.

Buwalda, S.J., Vermonden, T., Hennink, W.E., 2017. Hydrogels for Therapeutic Delivery: Current Developments and Future Directions. *Biomacromolecules* **18**, 316–330.

Catalan, J., Rydman, E., Aimonen, K., Hannukainen, K., Suhonen, S., Vanhala, E., Moreno, C., Meyer, V., Perez, D., Sneck, A., Forsstrom, U., Hojgaard, C., Willemoes, M., Winther, J. R., Vogel, U., Wolff, H., Alenius, H., Savolainen, K. N., Norppa, H., 2017. Genotoxic and inflammatory effects of nanofibrillated cellulose in murine lungs. *Mutagenesis*, **32**, 23-31.

Cencini, M., Lopez, C., Vergni, D., 2003. Reaction-diffusion systems: front propagation and spatial structures, in: The Kolmogorov Legacy in Physics. Springer, pp. 187–210.

Chami Khazraji, A., Robert, S., 2013. Interaction Effects between Cellulose and Water in Nanocrystalline and Amorphous Regions: A Novel Approach Using Molecular Modeling. *J. Nanomater.* **2013**, 1–10.

Chang, C., Zhang, L., 2011. Cellulose-based hydrogels: Present status and application prospects. *Carbohydr. Polym*. **84,** 40–53.

Checchetto, R., Gratton, L.M., Miotello, A., Cestari, C., 1995. Hydrogen permeation apparatus with thermal desorption spectroscopy capabilities. *Meas. Sci. Technol.* **6**, 1605–1611.

Chen, Q., Liu, P., Nan, F., Zhou, L., Zhang, J., 2014. Tuning the Iridescence of Chiral Nematic Cellulose Nanocrystal Films with a Vacuum-Assisted Self-Assembly Technique. *Biomacromolecules* **15**, 4343–4350.

Chen, W., Palazzo, A., Hennink, W.E., Kok, R.J., 2017. Effect of Particle Size on Drug Loading and Release Kinetics of Gefitinib-Loaded PLGA Microspheres. *Mol. Pharm*. **14**, 459–467.

Chen, W., Yu, H., Lee, S.-Y., Wei, T., Li, J., Fan, Z., 2018. Nanocellulose: a promising nanomaterial for advanced electrochemical energy storage. *Chem. Soc. Rev.* **47**, 2837–2872.

Chen, X., Mao, S.S., 2007. Titanium dioxide nanomaterials: synthesis, properties, modifications, and applications. *Chem. Rev.* **107**, 2891–2959.

Cheng, G., Tse, J., Jain, R.K., Munn, L.L., 2009. Micro-Environmental Mechanical Stress Controls Tumor Spheroid Size and Morphology by Suppressing Proliferation and Inducing Apoptosis in Cancer Cells. *PLoS ONE* **4**, e4632.

Chui, M. M., Phillips R. J., McCarthy M. J., 1995. Measurement of the porous microstructure of hydrogels by nuclear magnetic resonance. *J. Coll. Inter. Sci.* **174**, 336-344.

Cohen, Y., Ramon, O., Kopelman, I.J., Mizrahi, S., 1992. Characterization of inhomogeneous polyacrylamide hydrogels. *J. Polym. Sci. Part B Polym. Phys.* **30**, 1055–1067.

Consolati, G., Quasso, F.,. In Polymer Physics: From Suspensions to Nanocomposites and Beyond; Utracki, L. A., Jamieson, A. M., Eds.; John Wiley and Sons: Hoboken, NJ, 2010; pp 393-420.

Coviello, T., Matricardi, P., Alhaique, F., Farra, R., Tesei, G., Fiorentino, S., Asaro, F., Milcovich, G., Grassi, M., 2013. Guar gum/borax hydrogel: Rheological, low field NMR and release characterizations. *Express Polym. Lett.* **7**, 733–746.

Crank, J., Crank, E.P.J., 1979. The Mathematics of Diffusion. Clarendon Press.

D'Ayala, G.G., Malinconico, M., Laurienzo, P., 2008. Marine Derived Polysaccharides for Biomedical Applications: Chemical Modification Approaches. *Molecules* **13**, 2069–2106.

De France, K.J., Hoare, T., Cranston, E.D., 2017. Review of Hydrogels and Aerogels Containing Nanocellulose. *Chem. Mater*. **29**, 4609–4631.

De Greef, T.F., Meijer, E.W., 2008. Materials science: supramolecular polymers. *Nature* **453**, 171–173.

Deacon, G., 1980. Relationships between the carbon-oxygen stretching frequencies of carboxylato complexes and the type of carboxylate coordination. *Coord. Chem. Rev.* **33**, 227–250.

Dong, H., Snyder, J.F., Tran, D.T., Leadore, J.L., 2013a. Hydrogel, aerogel and film of cellulose nanofibrils functionalized with silver nanoparticles. *Carbohydr. Polym.* **95**, 760–767.

Dong, H., Snyder, J.F., Williams, K.S., Andzelm, J.W., 2013b. Cation-Induced Hydrogels of Cellulose Nanofibrils with Tunable Moduli. *Biomacromolecules* **14**, 3338–3345.

Draper, N.R. and Smith H., 1966. Applied Regression Analysis. John Wiley & Sons, New York, USA.

Duan, J., Han, C., Liu, L., Jiang, J., Li, J., Li, Y., Guan, C., 2015. Binding Cellulose and Chitosan via Intermolecular Inclusion Interaction: Synthesis and Characterisation of Gel. *J. Spectrosc*. 2015, 1–6.

Dufresne, A., 2012. Nanocellulose: From Nature to High Performance Tailored Materials, 2 edition. De Gruyter GmbH, Berlin/Boston

Dumanli, A.G., van der Kooij, H.M., Kamita, G., Reisner, E., Baumberg, J.J., Steiner, U., Vignolini, S., 2014. Digital color in cellulose nanocrystal films. *ACS Appl. Mater. Interfaces* **6**, 12302–12306.

Eldrup, M., Lightbody, D., Sherwood, J.N., 1981. The temperature dependence of positron lifetimes in solid pivalic acid. *Chem. Phys*. **63**, 51–58.

Endes, C., Camarero-Espinosa, S., Mueller, S., Foster, E.J., Petri-Fink, A., Rothen-Rutishauser, B., Weder, C., Clift, M.J.D., 2016. A critical review of the current knowledge regarding the biological impact of nanocellulose. *J. Nanobiotechnology* **14**, 78.

Espino-Pérez, E., Domenek, S., Belgacem, N., Sillard, C., Bras, J., 2014. Green Process for Chemical Functionalization of Nanocellulose with Carboxylic Acids. *Biomacromolecules* **15**, 4551–4560.

Esquivel, R., Juárez, J., Almada, M., Ibarra, J., Valdez, M.A., 2015. Synthesis and Characterization of New Thiolated Chitosan Nanoparticles Obtained by Ionic Gelation Method. *Int. J. Polym. Sci.,* **vol. 2015.**

Evmenenko, G., Theunissen, E., Mortensen, K., Reynaers, H., 2001. SANS study of Evmenenko, G., Theunissen, E., Mortensen, K., Reynaers, H., 2001. SANS study of surfactant ordering in k-carrageenan/cetylpyridinium chloride complexes. *Polymer* **42**, 2907-2913

EVONIK Industries , 2015. AEROXIDE®, AERODISP® and AEROPERL® Titanium Dioxide as Photocatalyst - Technical Information 1243. https://www.aerosil.com/sites/lists/RE/DocumentsSI/TI-1243-Titanium-Dioxide-as-Photocatalyst-EN.pdf. accessed 2018-09-02.

Flory, P. J., 1953. Principles of polymer chemistry. Cornell University Press. New York, USA.

Fras, L.,Laine, J., Stenius, P., Stana-Kleinschek, K., Ribitish, V., Dolecek, V., 2004. Determination of dissociable groups in natural and regenerated cellulose fibers by different titration methods. *J. Appl. Polym. Sci.*, **92**, no. 5, pp. 3186-3195.

Fukuzumi, H., Fujisawa, S., Saito, T., Isogai, A., 2013a. Selective Permeation of Hydrogen Gas Using Cellulose Nanofibril Film. *Biomacromolecules* **14**, 1705–1709.

Fukuzumi, H., Saito, T., Isogai, A., 2013b. Influence of TEMPO-oxidized cellulose nanofibril length on film properties. *Carbohydr. Polym*. **93**, 172–177.

Fukuzumi, H., Saito, T., Iwamoto, S., Kumamoto, Y., Ohdaira, T., Suzuki, R., Isogai, A., 2011. Pore Size Determination of TEMPO-Oxidized Cellulose Nanofibril Films by Positron Annihilation Lifetime Spectroscopy. *Biomacromolecules* **12**, 4057–4062.

Fukuzumi, H., Saito, T., Iwata, T., Kumamoto, Y., Isogai, A., 2009. Transparent and High Gas Barrier Films of Cellulose Nanofibers Prepared by TEMPO-Mediated Oxidation. *Biomacromolecules* **10**, 162–165.

Gálfi, L., Rácz, Z., 1988. Properties of the reaction front in an A+ B→ C type reaction-diffusion process. *Phys. Rev. A* **38**, 3151.

Ganguly, S., Dash, A.K., 2004. A novel in situ gel for sustained drug delivery and targeting. *Int. J. Pharm.* **276**, 83–92.

García, A., Gandini, A., Labidi, J., Belgacem, N., Bras, J., 2016. Industrial and crop wastes: A new source for nanocellulose biorefinery. *Ind. Crops Prod.* **93**, 26–38.

Gauvin, R., Parenteau-Bareil, R., Dokmeci, M.R., Merryman, W.D., Khademhosseini, A., 2012. Hydrogels and microtechnologies for engineering the cellular microenvironment. *Wiley Interdiscip. Rev. Nanomed. Nanobiotechnol*. **4**, 235–246.

Georges, P.C., Janmey, P.A., 2005. Cell type-specific response to growth on soft materials. *J. Appl. Physiol.* **98**, 1547–1553.

Giese, M., Blusch, L.K., Khan, M.K., MacLachlan, M.J., 2015. Functional Materials from Cellulose-Derived Liquid-Crystal Templates. *Angew. Chem. Int. Ed.* **54**, 2888–2910.

Grabovac, V., Guggi, D., Bernkop-Schnurch, A., 2005. Comparison of the mucoadhesive properties of various polymers. *Adv. Drug Deliv. Rev.* **57**, 1713–1723.

Grande, R., Trovatti, E., Carvalho, A.J.F., Gandini, A., 2017. Continuous microfiber drawing by interfacial charge complexation between anionic cellulose nanofibers and cationic chitosan. *J. Mater. Chem. A* **5**, 13098–13103.

Grassi, M., Lapasin, R., Pricl, S., 1996. A study of the rheological behavior of scleroglucan weak gel systems. *Carbohydr. Polym.* **29**, 169-181.

Habibi, Y., Lucia, L.A., Rojas, O.J., 2010. Cellulose Nanocrystals: Chemistry, Self-Assembly, and Applications. *Chem. Rev.* **110**, 3479–3500.

Hägerström, H., Edsman, K., 2001. Interpretation of mucoadhesive properties of polymer gel preparations using a tensile strength method. *J. Pharm. Pharmacol.* **53**, 1589–1599.

Haynes, W. M. 2014-2015. Handbook of Chemistry and Physics, CRC Press: Boca Raton, FL.

Halib, N., Perrone, F., Cemazar, M., Dapas, B., Farra, R., Abrami, M., Chiarappa, G., Forte, G., Zanconati, F., Pozzato, G., Murena, L., Fiotti, N., Lapasin, R., Cansolino, L., Grassi, G., Grassi, M., 2017. Potential Applications of

Nanocellulose-Containing Materials in the Biomedical Field. *Materials (Basel).* **10** (8). E977.

He, X., Hwang, H.-M., 2016. Nanotechnology in food science: Functionality, applicability, and safety assessment. *J. Food Drug Anal*. **24**, 671–681.

Hilhorst, D., Van der Hout, R., Peletier, L. A., 1996. The fast reaction limit for a Reaction-Diffusion System. *Math. Anal. Appl.*, **199**, 349-373.

Hoeng, F., Denneulin, A., Bras, J., 2016. Use of nanocellulose in printed electronics: a review. *Nanoscale* **8**, 13131–13154.

Hong, Y., Song, H., Gong, Y., Mao, Z., Gao, C., Shen, J., 2007. Covalently crosslinked chitosan hydrogel: Properties of in vitro degradation and chondrocyte encapsulation. *Acta Biomater.* **3**, 23–31.

HORIBA Scientific. A guide to Recording Fluorescence Quantum Yields. http://www.horiba.com/scientific/products/fluorescence-pectroscopy/application-notes/quantum-yields/ (accessed 6.1.18).

Horkay, F., Hecht, A.M., Zrínyi, M., Geissler, E., 1996. Effect of Cross-links on the Structure of Polymer Gels. *Polym. Gels Netw*. **4**, 451–465.

Hua, K., Carlsson, D.O., Ålander, E., Lindström, T., Strømme, M., Mihranyan, A., Ferraz, N., 2014. Translational study between structure and biological response of nanocellulose from wood and green algae. *RSC Adv* **4**, 2892–2903.

Hugenschmidt, C., Löwe, B., Mayer, J., Piochacz, C., Pikart, P., Repper, R., Stadlbauer, M., Schreckenbach, K., 2008. Unprecedented intensity of a low-energy positron beam. *Nucl. Instrum. Methods Phys. Res. Sect. Accel. Spectrometers Detect. Assoc. Equip.* **593**, 616–618.

Hurler, J., Engesland, A., Poorahmary Kermany, B., Škalko-Basnet, N., 2012. Improved texture analysis for hydrogel characterization: Gel cohesiveness, adhesiveness, and hardness. *J. Appl. Polym. Sci.* **125**, 180–188.

Ikkala, O., ten Brinke, G., 2002. Functional materials based on self-assembly of polymeric supramolecules. *Science* **295**, 2407–2409.

Isogai, A., Hänninen, T., Fujisawa, S., Saito, T., 2018. Review: Catalytic oxidation of cellulose with nitroxyl radicals under aqueous conditions. Prog. Polym. Sci. 86, 122–148.

Isogai, A., Saito, T., Fukuzumi, H., 2011. TEMPO-oxidized cellulose nanofibers. *Nanoscale* **3**, 71–85.

Jasińska, B., Kozioł, A.E., Goworek, T., 1996. Ortho-positronium lifetimes in nonspherical voids. *J. Radioanal. Nucl. Chem*. **210**, 617–623.

Jhon, M.S., Andrade, J.D., 1973. Water and hydrogels. *J. Biomed. Mater. Res*. **7**, 509–522.

Jin, R., Moreira Teixeira, L.S., Dijkstra, P.J., Karperien, M., van Blitterswijk, C.A., Zhong, Z.Y., Feijen, J., 2009. Injectable chitosan-based hydrogels for cartilage tissue engineering. *Biomaterials* **30**, 2544–2551.

Jones, D.S., Woolfson, A.D., Brown, A.F., 1997. Textural, viscoelastic and mucoadhesive properties of pharmaceutical gels composed of cellulose polymers. *Int. J. Pharm.* **151**, 223–233.

Jones, D.S., Woolfson, A.D., Djokic, J., 1996. Texture profile analysis of bioadhesive polymeric semisolids: Mechanical characterization and investigation of

interactions between formulation components. *J. Appl. Polym. Sci.* **61**, 2229–2234.

Jonoobi, M., Oladi, R., Davoudpour, Y., Oksman, K., Dufresne, A., Hamzeh, Y., Davoodi, R., 2015. Different preparation methods and properties of nanostructured cellulose from various natural resources and residues: a review. *Cellulose* **22**, 935–969.

Jorfi, M., Foster, E.J., 2015. Recent advances in nanocellulose for biomedical applications. J. Appl. Polym. Sci. 132, n/a-n/a.

Jr, R.M.B., 1996. The Biosynthesis of Cellulose. *J. Macromol. Sci. Part A* **33**, 1345–1373.

Kamida, K., Okajima, K., Matsui, T., Kowsaka, K., 1984. Study on the Solubility of Cellulose in Aqueous Alkali Solution by Deuteration IR and ^{13}C NMR. *Polym. J.* **16**, 857–866.

Karavana, S.Y., Rençbe, S., Şenyiğit, Z.A., Baloğlu, E., 2012. A New In-Situ Gel Formulation of Itraconazole for Vaginal Administration. *Pharmacol. Amp Pharm.* **03**, 417–426.

Kargarzadeh, H., Ahmad, I., Thomas, S., Dufresne, A., 2017. Handbook of Nanocellulose and Cellulose Nanocomposites, 2 Volume Set. John Wiley & Sons.

Kean, T., Thanou, M., 2010. Biodegradation, biodistribution and toxicity of chitosan. *Adv. Drug Deliv. Rev.* **62**, 3–11.

Khademhosseini, A., Vacanti, J. P., Langer, R., 2009. Progess in Tissue Engineering. *Scientific American,* **300**, 64-71.

Kim, H.-S., 1990. A kinetic study on calcium alginate bead formation. *Korean J. Chem. Eng*. **7**, 1–6.

Kirkegaard, P., Pedersen, N.J., Eldrup, M., 1989. PATFIT-88: a data-processing system for positron annihilation spectra on mainframe and personal computers. Risø National Laboratory, Roskilde, Denmark.

Kisiel, M., Martino, M.M., Ventura, M., Hubbell, J.A., Hilborn, J., Ossipov, D.A., 2013. Improving the osteogenic potential of BMP-2 with hyaluronic acid hydrogel modified with integrin-specific fibronectin fragment. *Biomaterials* **34**, 704–712.

Klemm, D., Heublein, B., Fink, H.-P., Bohn, A., 2005. Cellulose: Fascinating Biopolymer and Sustainable Raw Material. *Angew. Chem. Int. Ed.* **44**, 3358–3393.

Klemm, D., Kramer, F., Moritz, S., Lindström, T., Ankerfors, M., Gray, D., Dorris, A., 2011. Nanocelluloses: A New Family of Nature-Based Materials. *Angew. Chem. Int. Ed*. **50**, 5438–5466.

Koenig, S. H., Hallenga, K., Shporer, M., 1975. Protein-water interaction studied by solvent ^{1}H, ^{2}H, and ^{17}O magnetic relaxation. *Proc. Nat. Acad. Sci. USA* **72**, 7, 2667-2671.

Kondo, S., Miura, T., 2010. Reaction-Diffusion Model as a Framework for Understanding Biological Pattern Formation. *Science* **329,** 1616–1620.

Kong, M., Chen, X.G., Xing, K., Park, H.J., 2010. Antimicrobial properties of chitosan and mode of action: A state of the art review. *Int. J. Food Microbiol.* **144**, 51–63.

Kopeček, J., 2007. Hydrogel biomaterials: a smart future? Biomaterials 28, 5185–5192.

Kumar, M.N.V.R., Muzzarelli, R.A.A., Muzzarelli, C., Sashiwa, H., Domb, A.J., 2004. Chitosan Chemistry and Pharmaceutical Perspectives. *Chem. Rev.* **104**, 6017–6084.

La Rocca, R., Tallerico, R., Talib Hassan, A., Das, G., Tadepally, L., Matteucci, M., Liberale, C., Mesuraca, M., Scumaci, D., Gentile, F., Cojoc, G., Perozziello, G., Ammendolia, A., Gallo, A., Kärre, K., Cuda, G., Candeloro, P., Di Fabrizio, E., Carbone, E., 2014. Mechanical Stress Downregulates MHC Class I Expression on Human Cancer Cell Membrane. *PLoS ONE* **9**, e111758.

Lagerwall, J.P.F., Schütz, C., Salajkova, M., Noh, J., Park, J.H., Scalia, G., Bergström, L., 2014. Cellulose nanocrystal-based materials: from liquid crystal self-assembly and glass formation to multifunctional thin films. *NPG Asia Mater.* **6**, e80.

Lakowicz, J.R., 2006. Principles of Fluorescence Spectroscopy, 3rd ed. Springer US.

Lapasin, R., Pricl, S., 1995. Rheology of Industrial Polysaccharides: Theory and Applications. Chapman & Hall, London, GB.

Lasseuguette, E., Roux, D., Nishiyama, Y., 2008. Rheological properties of microfibrillar suspension of TEMPO-oxidized pulp. *Cellulose* **15**, 425–433.

Lau, M.H., Tang, J., Paulson, A.T., 2000. Texture profile and turbidity of gellan/gelatin mixed gels. *Food Res. Int.* **33** (8), 665-671.

Laufer, G., Kirkland, C., Cain, A.A., Grunlan, J.C., 2012. Clay-chitosan nanobrick walls: completely renewable gas barrier and flame-retardant nanocoatings. *ACS Appl. Mater. Interfaces* **4**, 1643–1649.

Lavoine, N., Desloges, I., Dufresne, A., Bras, J., 2012. Microfibrillated cellulose – Its barrier properties and applications in cellulosic materials: A review. *Carbohydr. Polym*. **90**, 735–764.

Lee, K.-Y., 2018. Nanocellulose and Sustainability: Production, Properties, Applications, and Case Studies. CRC Press.

Lee, K.-Y., Aitomäki, Y., Berglund, L.A., Oksman, K., Bismarck, A., 2014. On the use of nanocellulose as reinforcement in polymer matrix composites. *Compos. Sci. Technol.* **105**, 15–27.

Lee, K.Y., Ha, W.S., Park, W.H., 1995. Blood compatibility and biodegradability of partially N-acylated chitosan derivatives. *Biomaterials* **16**, 1211–1216.

Lee, Y.-A.L., Zhang, S., Lin, J., Langer, R., Traverso, G., 2016. A Janus Mucoadhesive and Omniphobic Device for Gastrointestinal Retention. *Adv. Healthc. Mater.* **5** (10).

Léger, C., Argoul, F., Bazant, M.Z., 1999. Front dynamics during diffusion-limited corrosion of ramified electrodeposits. *J. Phys. Chem. B* **103**, 5841–5851.

Leong, J.-Y., Lam, W.-H., Ho, K.-W., Voo, W.-P., Lee, M.F.-X., Lim, H.-P., Lim, S.-L., Tey, B.-T., Poncelet, D., Chan, E.-S., 2016. Advances in fabricating spherical alginate hydrogels with controlled particle designs by ionotropic gelation as encapsulation systems. *Particuology* **24**, 44–60.

Li, B., Xu, W., Kronlund, D., Määttänen, A., Liu, J., Smått, J.-H., Peltonen, J., Willför, S., Mu, X., Xu, C., 2015a. Cellulose nanocrystals prepared via formic acid hydrolysis followed by TEMPO-mediated oxidation. *Carbohydr. Polym.* **133**, 605–612.

Li, F., Mascheroni, E., Piergiovanni, L., 2015b. The Potential of NanoCellulose in the Packaging Field: A Review. *Packag. Technol. Sci.* **28**, 475–508.

Li, R., Zhang, L., Xu, M., 2012. Novel regenerated cellulose films prepared by coagulating with water: Structure and properties. *Carbohydr. Polym.* **87**, 95–100.

Li, Y., Li, X., Chen, C., Zhao, D., Su, Z., Ma, G., Yu, R., 2016. A rapid, non-invasive and non-destructive method for studying swelling behavior and microstructure variations of hydrogels. *Carbohydr. Polym*. **151**, 1251–1260.

Lin, N., Dufresne, A., 2014. Nanocellulose in biomedicine: Current status and future prospect. *Eur. Polym. J.* **59**, 302–325.

Liu, D., Wang, S., Ma, Z., Tian, D., Gu, M., Lin, F., 2014. Structure–color mechanism of iridescent cellulose nanocrystal films. *RSC Adv.* **4**, 39322–39331.

Liu, H., Sale, K.L., Simmons, B.A., Singh, S., 2011. Molecular dynamics study of polysaccharides in binary solvent mixtures of an ionic liquid and water. *J. Phys. Chem.* B **115**, 10251–10258.

M. Ways, T., Lau, W., Khutoryanskiy, V., 2018. Chitosan and Its Derivatives for Application in Mucoadhesive Drug Delivery Systems. *Polymers* **10**, 267.

Majoinen, J., Kontturi, E., Ikkala, O., Gray, D.G., 2012. SEM imaging of chiral nematic films cast from cellulose nanocrystal suspensions. *Cellulose* **19**, 1599–1605.

Mallon, P. E. and Schrader, D. M., 2003. Application to Polymers, in: Principles and Applications of Positron and Positronium Chemistry. World Scientific, pp. 253–280.

Mariano, M., El Kissi, N., Dufresne, A., 2014. Cellulose nanocrystals and related nanocomposites: Review of some properties and challenges. *J. Polym. Sci. Part B Polym. Phys*. **52**, 791–806.

Martin-Martinez, F.J., 2018. Designing nanocellulose materials from the molecular scale. Proc. Natl. Acad. Sci. U. S. A. 115, 7174–7175.

Mazzuca, C., Micheli, L., Cervelli, E., Basoli, F., Cencetti, C., Coviello, T., Iannuccelli, S., Sotgiu, S., Palleschi, A., 2014. Cleaning of Paper Artworks: Development of an Efficient Gel-Based Material Able to Remove Starch Paste. *ACS Appl. Mater. Interfaces* **6**, 16519–16528.

McKee, J.R., Hietala, S., Seitsonen, J., Laine, J., Kontturi, E., Ikkala, O., 2014. Thermoresponsive Nanocellulose Hydrogels with Tunable Mechanical Properties. *ACS Macro Lett.* **3**, 266–270.

Medronho, B., Duarte, H., Alves, L., Antunes, F., Romano, A., Lindman, B. 2015. Probing cellulose amphiphilicity. *Nord. Pulp Pap. Res. J.* **30**, 058–066.

Medronho, B., Lindman, B., 2015. Brief overview on cellulose dissolution/ regeneration interactions and mechanisms. *Adv. Colloid Interface Sci*. **222**, 502–508.

Mills, A.P., Wilson, R.J., 1982. Transmission of 1 - 6-keV positrons through thin metal films. *Phys. Rev. A* **26**, 490–500.

Milroy, C.A., Manthiram, A., 2016. Bioelectronic Energy Storage: A Pseudocapacitive Hydrogel Composed of Endogenous Biomolecules. *ACS Energy Lett*. **1**, 672–677.

Mittal, N., Ansari, F., Gowda.V, K., Brouzet, C., Chen, P., Larsson, P.T., Roth, S.V., Lundell, F., Wågberg, L., Kotov, N.A., Söderberg, L.D., 2018. Multiscale

Control of Nanocellulose Assembly: Transferring Remarkable Nanoscale Fibril Mechanics to Macroscale Fibers. *ACS Nano* **12**, 6378–6388.

Mondal, S., 2017. Preparation, properties and applications of nanocellulosic materials. *Carbohydr. Polym.* **163**, 301–316.

Moon, R.J., Martini, A., Nairn, J., Simonsen, J., Youngblood, J., 2011. Cellulose nanomaterials review: structure, properties and nanocomposites. *Chem. Soc. Rev.* **40**, 3941.

Müller, A., Zink, M., Hessler, N., Wesarg, F., Müller, F.A., Kralisch, D., Fischer, D., 2014. Bacterial nanocellulose with a shape-memory effect as potential drug delivery system. *RSC Adv* **4**, 57173–57184.

Muzzarelli, R.A.A., 1997. Human enzymatic activities related to the therapeutic administration of chitin derivatives. *Cell. Mol. Life Sci.* **53**, 131–140.

Nakamoto, k., 1989. Infrared and Raman Spectra of Inorganic and Coordination Compounds: Part A: Theory and Applications in Inorganic Chemistry, Wiley-Interscience: New York, USA.

Nara, M., Torii, H., Tasumi, M., 1996. Correlation between the Vibrational Frequencies of the Carboxylate Group and the Types of Its Coordination to a Metal Ion: An *ab Initio* Molecular Orbital Study. *J. Phys. Chem.* **100**, 19812–19817.

Nečas, D., Klapetek, P., 2012. Gwyddion: an open-source software for SPM data analysis. *Open Phys*. **10**.

Nechyporchuk, O., Belgacem, M.N., Bras, J., 2016a. Production of cellulose nanofibrils: A review of recent advances. *Ind. Crops Prod.* **93**, 2–25.

Nechyporchuk, O., Belgacem, M.N., Pignon, F., 2016b. Current Progress in Rheology of Cellulose Nanofibril Suspensions. *Biomacromolecules* **17**, 2311–2320.

Nie, J., Lu, W., Ma, J., Yang, L., Wang, Z., Qin, A., Hu, Q., 2015. Orientation in multi-layer chitosan hydrogel: morphology, mechanism, and design principle. *Sci. Rep.* **5**.

Nie, J., Wang, Z., Hu, Q., 2016. Chitosan Hydrogel Structure Modulated by Metal *Ions. Sci. Rep*. **6**.

Nielsen, L.J., Eyley, S., Thielemans, W., Aylott, J.W., 2010. Dual fluorescent labelling of cellulose nanocrystals for pH sensing. *Chem. Commun*. **46**, 8929.

Nishiyama, Y., 2018. Molecular interactions in nanocellulose assembly. *Phil Trans R Soc A* **376**, 20170047.

Nishiyama, Y., Langan, P., Chanzy, H., 2002. Crystal Structure and Hydrogen-Bonding System in Cellulose Iβ from Synchrotron X-ray and Neutron Fiber Diffraction. *J. Am. Chem. Soc*. **124**, 9074–9082.

Nishiyama, Y., Sugiyama, J., Chanzy, H., Langan, P., 2003. Crystal Structure and Hydrogen Bonding System in Cellulose Iα from Synchrotron X-ray and Neutron Fiber Diffraction. *J. Am. Chem. Soc*. **125,** 14300–14306.

Nobe, M., Dobashi, T., Yamamoto, T., 2005. Dynamics in Dialysis Process for Liquid Crystalline Gel Formation. *Langmuir* **21**, 8155–8160.

Nogi, M., Handa, K., Nakagaito, A.N., Yano, H., 2005. Optically transparent bionanofiber composites with low sensitivity to refractive index of the polymer matrix. *Appl. Phys. Lett.* **87**, 243110.

Nyström, G., 2018. Assembly, Aggregation and Gelation in Nanocellulose Dispersions. *Proc Natl Acad Sci U S A* , **115** (28), 7174-7175.

Onishi, H., Machida, Y., 1999. Biodegradation and distribution of water-soluble chitosan in mice. *Biomaterials* **20**, 175–182.

Pääkkö, M., Ankerfors, M., Kosonen, H., Nykänen, A., Ahola, S., Osterberg, M., Ruokolainen, J., Laine, J., Larsson, P.T., Ikkala, O., Lindström, T., 2007. Enzymatic hydrolysis combined with mechanical shearing and high-pressure homogenization for nanoscale cellulose fibrils and strong gels. *Biomacromolecules* **8**, 1934–1941.

Padera, F., 2013. Measuring Absorbance and Refractive Index of Thin Films with the PerkinElmer Lambda 950/1050 High Performance UV-Vis/NIR Spectrometers. Application note PerkinElmer Inc. Shelton, CT, USA.

Papageorgiou, S.K., Kouvelos, E.P., Favvas, E.P., Sapalidis, A.A., Romanos, G.E., Katsaros, F.K., 2010. Metal–carboxylate interactions in metal–alginate complexes studied with FTIR spectroscopy. *Carbohydr. Res.* **345**, 469–473.

Pasqui, D., De Cagna, M., Barbucci, R., 2012. Polysaccharide-Based Hydrogels: The Key Role of Water in Affecting Mechanical Properties. *Polymers* **4**, 1517–1534.

Paterson, R., Yampol'Skii, Y.P., Fogg, P.G.T., Bokarev, A., Bondar, V., Ilinich, O., Shishatskii, S., 1999. IUPAC-NIST Solubility Data Series 70. The Solubility of Gases in Glassy Polymers. *J. Phys. Chem. Ref. Data* **28**, 1255–1450.

Patil, J.S., Kamalapur, M.V., Marapur, S.C., Kadam, D.V., 2010. Ionotropic gelation and polyelectrolyte complexation: the novel techniques to design hydrogel particulate sustained, modulated drug delivery system: a review. *Dig. J. Nanomater. Biostructures* **5**, 241–248.

Patil, P., Chavanke, D., Wagh, M., 2012. A review on ionotropic gelation method: novel approach for controlled gastroretentive gelispheres. *Int J Pharm Pharm Sci* **4**, 27–32.

Pelham, R.J., Wang, Y. l, 1997. Cell locomotion and focal adhesions are regulated by substrate flexibility. Proc. Natl. Acad. Sci. U. S. A. 94, 13661–13665.

Peppas, N.A., Hilt, J.Z., Khademhosseini, A., Langer, R., 2006. Hydrogels in Biology and Medicine: From Molecular Principles to Bionanotechnology. Adv. Mater. **18**, 1345–1360.

Peppas, N.A., Sahlin, J.J., 1996. Hydrogels as mucoadhesive and bioadhesive materials: a review. *Biomaterials* **17**, 1553–1561.

Persin, Z., Stana-Kleinschek, K., Foster, T.J., van Dam, J.E.G., Boeriu, C.G., Navard, P., 2011. Challenges and opportunities in polysaccharides research and technology: The EPNOE views for the next decade in the areas of materials, food and health care. *Carbohydr. Polym*. **84**, 22–32.

Picard, G., Simon, D., Kadiri, Y., LeBreux, J.D., Ghozayel, F., 2012. Cellulose Nanocrystal Iridescence: A New Model. *Langmuir* **28**, 14799–14807.

Plackett, 2014. A review of nanocellulose as a novel vehicle for drug delivery. *Nord. Pulp Pap. Res. J*. **29**, 105–118.

Poelman, D., Smet, P.F., 2003. Methods for the determination of the optical constants of thin films from single transmission measurements: a critical review. *J. Phys. Appl. Phys*. **36**, 1850–1857.

Pollard, F.H., Martin, J.V., 1956. The spectrophotometric determination of the alkaline-earth metals with murexide, eriochrome black T and with o-cresolphthalein complexone. *The Analyst* **81**, 348.

Pönni, R., Vuorinen, T., Kontturi, E., 2012. Proposed nano-scale coalescence of cellulose in chemical pulp fibers during technical treatments. *BioResources* **7**, 4.

Poonguzhali, R., Basha, S.K., Kumari, V.S., 2017. Synthesis and characterization of chitosan-PVP-nanocellulose composites for in-vitro wound dressing application. *Int. J. Biol. Macromol.* **105**, 111–120.

Potter, K., Balcom, B. J., Carpenter, A., Hall, L., 1994. The gelation of sodium alginate with calcium ions studied by magnetic resonance imaging (MRI). *Carbohydr. Res.* **257**, 117-126.

Pusnik, M., Imeri, M., Deppierraz, G., Bruinink, A., Zinn, M., 2016. The agar diffusion scratch assay - A novel method to assess the bioactive and cytotoxic potential of new materials and compounds. *Sci. Rep*. **6**, 20854.

Qiu, X., Hu, S., 2013. "Smart" Materials Based on Cellulose: A Review of the Preparations, Properties, and Applications. *Materials* **6**, 738–781.

Raman, C., Berkland, C., Kim, K. (Kevin), Pack, D.W., 2005. Modeling small-molecule release from PLG microspheres: effects of polymer degradation and nonuniform drug distribution. *J. Control. Release* **103**, 149–158.

Rhim, J.-W., Park, H.-M., Ha, C.-S., 2013. Bio-nanocomposites for food packaging applications. *Prog. Polym. Sci.* **38**, 1629–1652.

Riva, G.H., García-Estrada, J., Vega, B., López-Dellamary, F., Hérnandez, M.E., Silva, J.A., 2015. Cellulose-Chitosan Nanocomposites -Evaluation of Physical, Mechanical and Biological Properties, in: Poletto, M., Ornaghi, H.L. (Eds.), Cellulose - Fundamental Aspects and Current Trends. InTech.

Rodionova, G., Lenes, M., Eriksen, Ø., Gregersen, Ø., 2011. Surface chemical modification of microfibrillated cellulose: improvement of barrier properties for packaging applications. *Cellulose* **18**, 127–134.

Romani, A.M., Scarpa, A., 2000. Regulation of cellular magnesium. *Front. Biosci.* **5**, D720-734.

Rosenthal, A.J., 2010. Texture Profile Analysis- how important are the parameters? *J. Texture Stud.* **41**, 672–684.

Saito, T., Isogai, A., 2004. TEMPO-mediated oxidation of native cellulose. The effect of oxidation conditions on chemical and crystal structures of the water-insoluble fractions. *Biomacromolecules*, **5**, 1983-1989.

Saito, T., Kimura, S., Nishiyama, Y., Isogai, A., 2007. Cellulose Nanofibers Prepared by TEMPO-Mediated Oxidation of Native Cellulose. *Biomacromolecules* **8**, 2485–2491.

Saito, T., Nishiyama, Y., Putaux, J.-L., Vignon, M., Isogai, A., 2006. Homogeneous Suspensions of Individualized Microfibrils from TEMPO-Catalyzed Oxidation of Native Cellulose. *Biomacromolecules* **7**, 1687–1691.

Saito, T., Uematsu, T., Kimura, S., Enomae, T., Isogai, A., 2011. Self-aligned integration of native cellulose nanofibrils towards producing diverse bulk materials. *Soft Matter* **7**, 8804.

Salas, C., Nypelö, T., Rodriguez-Abreu, C., Carrillo, C., Rojas, O.J., 2014. Nanocellulose properties and applications in colloids and interfaces. *Curr. Opin. Colloid Interface Sci*. **19**, 383–396.

Sampath, U.G.T.M., Ching, Y.C., Chuah, C.H., Singh, R., Lin, P.-C., 2017. Preparation and characterization of nanocellulose reinforced semi-interpenetrating polymer network of chitosan hydrogel. *Cellulose* **24**, 2215–2228.

Sanderson, G.R., 1990. Gellan Gum, in: Harris, P. (Ed.), Food Gels, Elsevier Applied Food Science Series. Springer Netherlands, Dordrecht, pp. 201–232.

Saxena, I.M., Brown, R.M., 2005. Cellulose biosynthesis: current views and evolving concepts. *Ann. Bot.* **96**, 9–21.

Schurz, J., 1991. Rheology of polymer solutions of the network type. *Prog. Polym. Sci.* **16**, 1–53.

Sehaqui, H., Zhou, Q., Ikkala, O., Berglund, L.A., 2011. Strong and Tough Cellulose Nanopaper with High Specific Surface Area and Porosity. *Biomacromolecules* **12**, 3638–3644.

Shahidi, F., Arachchi, J.K.V., Jeon, Y.-J., 1999. Food applications of chitin and chitosans. *Trends Food Sci. Technol.* **10**, 37–51.

Shimizu, M., Saito, T., Fukuzumi, H., Isogai, A., 2014. Hydrophobic, Ductile, and Transparent Nanocellulose Films with Quaternary Alkylammonium Carboxylates on Nanofibril Surfaces. *Biomacromolecules* **15**, 4320–4325.

Siepmann, J., Peppas, N.A., 2011. Higuchi equation: Derivation, applications, use and misuse. *Int. J. Pharm.,* **418** (1), 6–12.

Singh, P., Medronho, B., Alves, L., da Silva, G.J., Miguel, M.G., Lindman, B., 2017. Development of carboxymethyl cellulose-chitosan hybrid micro- and macroparticles for encapsulation of probiotic bacteria. *Carbohydr. Polym.* **175**, 87–95.

Singh T. R. R., Laverty, G., Donnelly, R., 2018. Hydrogels: Design, Synthesis and Application in Drug Delivery and Regenerative Medicine. CRC Press.

Skjåk-Bræk, G., Grasdalen, H., Smidsrod, O., 1989. Inhomogeneous Polysaccharide Ionic Gels. *Carbohydr. Polym.* **10**, 31-54.

Sogias, I.A., Williams, A.C., Khutoryanskiy, V.V., 2008. Why is Chitosan Mucoadhesive? *Biomacromolecules* **9**, 1837–1842.

Sperr, P., Egger, W., Kögel, G., Dollinger, G., Hugenschmidt, C., Repper, R., Piochacz, C., 2008. Status of the pulsed low energy positron beam system (PLEPS) at the Munich Research Reactor FRM-II. *Appl. Surf. Sci.* **255**, 35–38.

Stable Micro Systems, Products, TA.XTplus Texture Analyser. Web site accessed 2018.09.02 http://texturetechnologies.com/resources/texture-profile-analysis

STANDARD, 2009. UNI EN ISO 10993-5. Biological evaluation of medical devices. Part 5: Tests for in vitro cytotoxicity

Stendahl, J.C., Rao, M.S., Guler, M.O., Stupp, S.I., 2006. Intermolecular Forces in the Self-Assembly of Peptide Amphiphile Nanofibers. *Adv. Funct. Mater.* **16**, 499–508.

Stokke, B. T., Draget, K. I., Smidsrød, O., Yuguchi, Y., Urakawa, H., Kajiwara, K., 2000. Small-Angle X-ray Scattering and Rheological Characterization of Alginate Gels. 1. Ca−Alginate Gels. *Macromolecules* **33**(5), 1853-1863.

Suttiponparnit, K., Jiang, J., Sahu, M., Suvachittanont, S., Charinpanitkul, T., Biswas, P., 2010. Role of Surface Area, Primary Particle Size, and Crystal Phase on Titanium Dioxide Nanoparticle Dispersion Properties. *Nanoscale Res. Lett.* **6**, 27.

Syverud, K., Stenius, P., 2009. Strength and barrier properties of MFC films. *Cellulose* **16**, 75–85.

Tammelin, L. E., Mogensen, S.,1952. Microquantitative dtermination of calcium as Murexide Complex in the presence of magnesium, *Acta Chem. Scand*. **6**, 988-992.

Tang, J., Sisler, J., Grishkewich, N., Tam, K.C., 2017. Functionalization of cellulose nanocrystals for advanced applications. *J. Colloid. Interface Sci.* **494**, 397–409.

Tao, S.J., 1972. Positronium Annihilation in Molecular Substances. *J. Chem. Phys*. **56**, 5499–5510.

Toivonen, M.S., Kurki-Suonio, S., Schacher, F.H., Hietala, S., Rojas, O.J., Ikkala, O., 2015. Water-Resistant, Transparent Hybrid Nanopaper by Physical Cross-Linking with Chitosan. *Biomacromolecules* **16**, 1062–1071.

Udeni Gunathilake, T., Ching, Y., Chuah, C., 2017. Enhancement of Curcumin Bioavailability Using Nanocellulose Reinforced Chitosan Hydrogel. *Polymers* **9**, 64.

Ul-Islam, M., Khattak, W.A., Kang, M., Kim, S.M., Khan, T., Park, J.K., 2013. Effect of post-synthetic processing conditions on structural variations and applications of bacterial cellulose. *Cellulose* **20**, 253–263.

Usov, I., Nyström, G., Adamcik, J., Handschin, S., Schütz, C., Fall, A., Bergström, L., Mezzenga, R., 2015. Understanding nanocellulose chirality and structure–properties relationship at the single fibril level. *Nat. Commun.* **6**, 7564.

Vanhamme, L., Sundin, T., Hecke, P.V., Huffel, S.V., 2001. MR spectroscopy quantitation: a review of time-domain methods. *NMR Biomed*. **14**, 233–246.

Vårum, K.M., Myhr, M.M., Hjerde, R.J.N., Smidsrød, O., 1997. In vitro degradation rates of partially N-acetylated chitosans in human serum. *Carbohydr. Res.* **299**, 99–101.

Vo, L., Navard, P., 2016. Treatments of plant biomass for cementitious building materials – A review. *Constr. Build. Mater*. **121**, 161–176.

Wang, X., Yao, C., Wang, F., Li, Z., 2017. Cellulose-Based Nanomaterials for Energy Applications. *Small* **13**, 1702240.

Way, A.E., Hsu, L., Shanmuganathan, K., Weder, C., Rowan, S.J., 2012. pH-Responsive Cellulose Nanocrystal Gels and Nanocomposites. *ACS Macro Lett.* **1**, 1001–1006.

Whitesides, G.M., Boncheva, M., 2002. Beyond molecules: Self-assembly of mesoscopic and macroscopic components. *Proc. Natl. Acad. Sci.* **99**, 4769–4774.

Williams, A.T.R., Winfield, S.A., Miller, J.N., 1983. Relative fluorescence quantum yields using a computer-controlled luminescence spectrometer. *The Analyst* **108**, 1067.

Woertz, C., Preis, M., Breitkreutz, J., Kleinebudde, P., 2013. Assessment of test methods evaluating mucoadhesive polymers and dosage forms: An overview. *Eur. J. Pharm. Biopharm*. **85**, 843–853.

Wu, Q., Meng, Y., Wang, S., Li, Y., Fu, S., Ma, L., Harper, D., 2014. Rheological behavior of cellulose nanocrystal suspension: Influence of concentration and aspect ratio. *J. Appl. Polym. Sci.* **131**, 40525.

Wu, Z.L., Kurokawa, T., Sawada, D., Hu, J., Furukawa, H., Gong, J.P., 2011. Anisotropic Hydrogel from Complexation-Driven Reorientation of Semirigid Polyanion at Ca^{2+} Diffusion Flux Front. *Macromolecules* **44**, 3535–3541.

Yampolskii, Y., Shantarovich, V., 2006. Positron Annihilation Lifetime Spectroscopy and Other Methods for Free Volume Evaluation in Polymers, in: Materials Science of Membranes for Gas and Vapor Separation. Wiley-Blackwell, pp. 191–210.

Yang, C.H., Wang, M.X., Haider, H., Yang, J.H., Sun, J.-Y., Chen, Y.M., Zhou, J., Suo, Z., 2013. Strengthening Alginate/Polyacrylamide Hydrogels Using Various Multivalent Cations. *ACS Appl. Mater. Interfaces* **5**, 10418–10422.

Yang, J., Li, J., 2018. Self-assembled cellulose materials for biomedicine: A review. *Carbohydr. Polym.* **181**, 264–274.

Yang, J., Xu, F., Han, C.-R., 2017. Metal Ion Mediated Cellulose Nanofibrils Transient Network in Covalently Cross-linked Hydrogels: Mechanistic Insight into Morphology and Dynamics. *Biomacromolecules* **18** (3), 1019–1028.

Young, M., 2000. Optics and Lasers: Including Fibers and Optical Waveguides, 5th ed, Advanced Texts in Physics. Springer-Verlag, Berlin Heidelberg.

Zander, N.E., Dong, H., Steele, J., Grant, J.T., 2014. Metal Cation Cross-Linked Nanocellulose Hydrogels as Tissue Engineering Substrates. *ACS Appl. Mater. Interfaces* **6**, 18502–18510.

Zennaro, L., Magro, M., Vianello, F., Rigo, A., Mariotto, G., Giarola, M., Froner, E., Scarpa, M., 2013. Stable Aqueous Solutions of Naked Titanate Nanotubes. *Chem. Phys. Chem*. **14**, 2786–2792.

Zhang, K., Liimatainen, H., 2018. Hierarchical Assembly of Nanocellulose-Based Filaments by Interfacial Complexation. *Small* **0**, 1801937.

Zhang, X.-F., Zhang, J., Liu, L., 2014. Fluorescence Properties of Twenty Fluorescein Derivatives: Lifetime, Quantum Yield, Absorption and Emission Spectra. *J. Fluoresc.* **24**, 819–826.

Zheng, G., Cui, Y., Karabulut, E., Wågberg, L., Zhu, H., Hu, L., 2013. Nanostructured paper for flexible energy and electronic devices. *MRS Bull.* **38**, 320–325.

Zhivotovsky, B., Orrenius, S., 2011. Calcium and cell death mechanisms: A perspective from the cell death community. *Cell Calcium* **50**, 211–221.

Zhou, Y., Fu, S., Zhang, L., Zhan, H., Levit, M.V., 2014. Use of carboxylated cellulose nanofibrils-filled magnetic chitosan hydrogel beads as adsorbents for Pb(II). *Carbohydr. Polym*. **101**, 75–82.